Investigation of Metal and Semiconductor Nanoparticle/2D Layer Decorated TiO_2 Nanostructures for Visible Light Photo(electro)-catalysis and Optoelectronic Applications

A Thesis Submitted to
Indian Institute of Technology Guwahati
For the Degree of

Doctor of Philosophy

By

KAMAL KUMAR PAUL

Department of Physics
Indian Institute of Technology Guwahati
Guwahati-781039, India

November 2018

Dedicated to

…..My beloved Parents

Department of Physics
Indian Institute of Technology Guwahati
Guwahati-781039, India

STATEMENT

The work contained in the thesis entitled "**Investigation of Metal and Semiconductor Nanoparticle/2D Layer Decorated TiO_2 Nanostructures for Visible Light Photo(electro)-catalysis and Optoelectronic Applications**" has been carried out by me at Indian Institute of Technology Guwahati under the supervision of **Prof. P. K. Giri**, Professor, Department of Physics, Indian Institute of Technology Guwahati. This work has not been submitted elsewhere for the award of any degree.

Kamal Kumar Paul

Roll No. - **136121028**

Senior Research Fellow
Department of Physics
Indian Institute of Technology Guwahati
Guwahati-781039, India

Prof. P. K. Giri
Professor
Department of Physics
Indian Institute of Technology Guwahati
Guwahati-781039, India
Phone: ***+91 361 2582703****, Fax:* ***+91 361 2690762***
Email: ***giri@iitg.ac.in***

CERTIFICATE

This is to certify that the work contained in the thesis entitled "***Investigation of Metal and Semiconductor Nanoparticle/2D Layer Decorated TiO_2 Nanostructures for Visible Light Photo(electro)-catalysis and Optoelectronic Applications***" has been carried out by **Mr. Kamal Kumar Paul** at Indian Institute of Technology Guwahati under my supervision. This work has not been submitted elsewhere for the award of any degree.

Prof. P. K. Giri
Thesis supervisor

ACKNOWLEDGEMENT

The entire PhD journey would not have been possible without the constant help, support and encouragement of many people. Here I take this opportunity to acknowledge them.

The first person who deserves to be mentioned is my supervisor Prof. P. K. Giri, without whom this PhD journey would not have even started. I owe my sincerest gratitude to him for giving me the opportunity to work under his guidance. His fruitful discussion, kind support, constant encouragement and useful suggestions made the completion of my PhD possible. His vast knowledge and strong technical expertise have helped me in getting an excellent background in the semiconductor technology, identifying the opportunities in this field and preparing for the challenges. I am thankful for giving me the complete freedom in my work and providing the essential arrangements, laboratory facilities and moral support throughout my PhD work to achieve the goal.

I express my sincere gratitude to my Doctoral Committee members, Dr. Charudatt Y Kadolkar, Dr. Subhash Thota, and Prof. Md. Qureshi for their regular review of my work, constructive criticism and valuable suggestions.

I am thankful to our Head of the Department of Physics, other faculty members of Physics, members of the Central Instruments Facilities and Centre for Nanotechnology for providing me a research friendly environment with up-to-date research facilities. I am immensely grateful to Indian Institute of Technology Guwahati for providing the fellowship, good accommodation in this beautiful campus and having pleasant working environment. A special thanks to the scientific/technical officers, Dr. Sidananda Sarma, Indrajit Talukdar, Kaustubh Acharya, Dr. Kula K. Senapati, Chandan Borgohain and Madhurjya Borah for their help and co-operation to complete my work. Junior technical superintendent Sujit Deb, Ashim Malakar and Milan Mahadani, deserve a special mention who helped in the characterization of my samples. I am also thankful to Central Workshop, Department of Mechanical Engineering for the fabrication of essential components used in my experimental setup. I would like to thank specially Prof. Minoru Fujii, Dr. Sugimoto from Kobe University, Japan, Prof. Tharangattu N. Narayanan from Tata Institute of Fundamental Research, India, Dr. Wolfgang Theis and Dr. Neil V. Rees from University of Birmingham, UK for providing the opportunity to use some of their laboratory facilities.

Life in the lab have always been exciting due to the amazing labmates that I was fortunate to have. I should not forget to mention a few of them. I express my sincere gratitude to my seniors Dr. Biswajit Choudhury, Dr. Batakrushna Santara, Dr. Ramesh Ghosh, Ravi K. Biroju, Dr. Biswajit Karmakar, Dr. Sk. Md. Obaidullah, Dr. Rajender Gone, Jitendra Kumar and Somorjit Singh for their help in research and their good company. Thanks to my labmates Larionette, Joydip, Ruma, Sumaiya, Abhilasha and Neda for their support and help to bring the thesis in reality. I should not forget to mention Randeep, Shaad, Adil, Sanjib and Santanu from other LAB for their cheerful and enjoyable company and the moral support during my depression. I would like to thank Somnath, Arindam, Bhaskar and Sudipta as well.

Last but not the least my acknowledgements to the blessings of my father Late Shyam Pada Paul and mother Malina Paul without whose support and encouragement this journey would not have been possible at all for me. I am highly grateful to Ramkrishna Sengupta (Mama) and Late Dipika Sengupta (Mami), whose constant motivation has enabled me to pursue higher studies. I am really fortunate to have friends like Litan and Spandana in my life who were always been there for me during the hard time and motivated me go through the thick and thin. I am immensely thankful to China Madam, Ranjit Sir, Subodh Dhar, Shyamal (dada) and Sampa (didi) for their constant support and encouragement.

Kamal Kumar Paul

IIT Guwahati

CONTENTS

SYNOPSIS

Shape tailored transition metal oxide nanostructures are being extensively studied due to their promising applications in diverse range of fields. Among these, titanium dioxide (TiO_2) has been explored extensively due to its unique physicochemical properties e.g., strong oxidizing capacity, non-toxicity, biocompatibility, abundant availability etc. TiO_2 generally exists in four distinct polymorphs: rutile, anatase, brookite and monoclinic B (TiO_2(B)) phases. Despite its metastability, TiO_2(B) has a very open framework structure with lower density and larger specific capacity, which is advantageous for various applications.

Mesoporous TiO_2 nanostructures with various dimensionality (0D-3D) possess large surface area (high aspect ratio), lower axial resistance (especially in 1D TiO_2) providing the direct path of carrier transport and their easy collection, which facilitate the efficient photocatalysis and multifunctional optoelectronic applications. Over the past decades, several approaches have been developed for the synthesis of shape tailored TiO_2 nanostructures. A relatively simple, cost effective and versatile technique, i.e., hydrothermal method has been developed recently and it has emerged as a powerful tool to grow nanostructures with various dimensionalities and distinct surface morphology, simply by adjusting the growth parameters including reaction temperature, pH of the solvent and reaction duration. Additionally, the hydrothermally grown TiO_2 nanostructures have exotic physical and chemical characteristics promising for the diverse range of applications including energy and environment, Li-ion battery, sensors, optoelectronic application etc.

One of the major limitation of TiO_2 as a photocatalyst is that it is a large band gap (~3.2 eV) material and can utilize only the UV light (wavelength < 400 nm) that contributes less than 5% of the incident solar light. Additionally, in homogeneous TiO_2 nanostructure, recombination process of photogenerated excitons is random and thus highly probable before it reaches the surface to initiate redox reactions and this makes it inefficient for photocatalysis and other optoelectronic applications. To tune the electronic band structure and light harvesting window of TiO_2 extending to the visible-NIR region in order to enhance the charge separation, several strategies have been explored including defect engineering, doping with metal and non-metal ions, exploring the localized surface plasmon resonance (LSPR) by introducing plasmonic nanoparticles, (Ag, Au, Pd) and formation of type-II heterostructures (HSs) with narrow band gap semiconductors (Ag_2O, MoS_2, CdS) etc.

Binary/ternary HSs on shape tailored mesoporous TiO_2 template with plasmonic NPs or suitable narrow band gap semiconductors (type-II HSs) have been found to be attractive for its additional structural complexity and functionality arising from the heterojunction of different materials. However, the selection of suitable material, formation of high quality interface and control of external coating are still challenging. Our study focuses on the growth of multijunction plasmonic HSs and hot electron injection mediated interfacial charge separation for the efficient visible light photodegradation of hazardous chemicals. In addition, mesoporous TiO_2 nanostructures coupled with edge-exposed few-layer MoS_2 and its selective decoration with platinum NPs at the edge/defect sites are investigated for the optimum photoelectrocatalytic hydrogen evolution reaction. The energy band engineering, tuning of defect and doping level, manipulation of optical absorption and catalytically active functionalities are the powerful approach to improve the performance as solar light driven photocatalyst/ photoelectrocatalyst.

Next, TiO_2, being an indirect large band gap material, is highly unfavorable for the light emission and broadband efficient photodetection. For the first time, we report ultra-high yield photoluminescence (PL) emission from the self-grown fluorine doped TiO_2 quantum dots (QDs) on the TiO_2 nanostructures. Further, we study the in-situ formation of 1L-MoS_2@TiO_2 heterojunction, which shows complete conversion of trions to neutral excitons and thus giving rise to the ultra-high PL emission. Under reverse bias, the p-n heterojunction photodetector shows high, broadband and ultra-fast photoresponse. Our results contain key step for the development of practical commercial devices for visible light photocatalysis, light emission and broadband photodetection.

This thesis presents a systematic study on the controlled growth of shape tailored TiO_2 nanostructures and its various plasmonic and type-II HSs with tunable photophysical and photochemical properties for the applications of hydrogen generation, environmental cleaning, light emission and broadband photodetection. We believe that these studies are very significant to address the current challenges of energy and environmental issues, and multifunctional optoelectronic applications. The complete thesis work has been organized into eight chapters as detailed below:

Chapter 1 presents a brief account of the key properties, growth strategies for shape tailored TiO_2 nanostructures and their potential utilization in different technological applications, such as photocatalysis, photoelectrocatalysis, photodetector, solar cell and

chemical sensor etc. Fundamental issues with the pristine TiO_2 nanostructures and its limitations to become a next generation candidate for the real life applications are discussed. Recent progress and the lacunae on the fabrication of shape tailored (0D, 1D, 2D and 3D) TiO_2 nanostructure based hybrids with plasmonic metal nanoparticles/suitable semiconductors NPs/ 2D semiconductor for photocatalytic, photoelectrocatalytic, light emitting and broadband photodetection applications are presented. The chapter ends with a motivation for the present work.

Chapter 2 presents a detailed investigation on the controlled growth of Ag_2O-nanoparticle (NP) decorated porous monoclinic B-phase TiO_2 (TiO_2(B)) nanorods (NRs) grown by a solvothermal route. The as-grown TiO_2(B) NRs are found to be mesoporous in nature and the Ag_2O NPs are uniformly decorated over its surface, since the pores work as nucleation sites for the growth of Ag_2O NPs. Ag_2O NP decorated TiO_2 NRs show ultrahigh rate of photodegradation of organic dyes under visible light illumination. Optimization of size and number density of Ag_2O NPs over the porous sites of TiO_2(B), their coupling, band bending and interfacial charge transfer are discussed. Highly stable visible light photodegradation of TiO_2(B)/Ag_2O HSs has been investigated using aqueous methyl orange (anionic) and methylene blue (cationic) as the reference dyes with one order enhanced efficiency than pristine components. Enhanced visible light absorption, band bending induced efficient charge separation and the Coulombic interaction between the dye molecules and catalyst surface are discussed in details to demonstrate the fast photocatalysis. This work provides valuable insights on the controlled growth of TiO_2 based hybrid photocatalysts for its cutting edge application in hydrogen production and environmental cleaning.

Chapter 3 presents the origin of multi-step sequential degradation rate of organic dye, Rhodamine-B (RhB), under visible light illumination on Ag NPs decorated anatase TiO_2 NRs grown by a solvothermal route. Presence of intrinsic defects and localized surface plasmon resonance (LSPR) in the optimized Ag@TiO_2 HS facilitate strong optical absorption in the entire visible region. The role of hot electron generation and fast interfacial charge migration for the enhanced visible light photocatalysis are discussed in details with the steady state and time resolved photoluminescence and photoconductivity studies. The degradation kinetics of HSs follows a sequential rate process with two distinct exponential decay functions with two rate constants. Ultra-fast N-de-ethylation of RhB, photoreduction of Ag^+ ions into metallic Ag NPs during the photocatalysis and thus the enhanced plasmonic effect

on Ag NPs demonstrate the faster rate constant (>2 fold) in the 2nd degradation zone than the 1st zone. This study offers new insights in designing and understanding the mechanism of advanced photocatalysis with multi rate constants by oxygen vacancy enriched Ag@TiO_2 nano-heterostructures.

Chapter 4 presents evidence of plasmonic hot electron injection and efficient interfacial charge transfer in ternary plasmonic photocatalyst of Ag-TiO_2(B)-C_3N_4 and Au-TiO_2(B)-C_3N_4 through the photoresponse study with plasmonic excitations and the resulting superior visible light photocatalytic activity. Close inter-particle separation of plasmonic NPs in the HSs, as revealed from the TEM analysis, possess numerous plasmonic hot spots for the generation of hot electrons that are excited to the conduction band of TiO_2 followed by an interfacial migration to 2D-C_3N_4 (CN) network. Steady state PL and TRPL studies reveal very fast charge transfer through the interfaces of the ternary systems, making it very promising for the visible light photodegradation of RhB (visible light absorbing dye) as well as phenol (UV absorbing dye) with high reusability. The monochromatic photoexcitation at wavelengths corresponding to the plasmonic absorption peaks (470 nm, 510 nm for Ag NPs and 545 nm for Au NPs) possesses highly enhanced photocurrent due to hot electron injection from plasmonic NPs to TiO_2-CN integrated network facilitating enhanced photocatalysis.

In chapter 5, we demonstrate an enhanced visible light photoelectrocatalytic hydrogen evolution reaction (HER) in acidic media by the edge-exposed few-layer MoS_2 nanoflowers (NFs) over the porous TiO_2(B) nanobelts (NBs) grown via a low temperature in-situ hydrothermal process. A selective decoration of minimal platinum (Pt) NPs (1.4 wt%) on the edge/defect sites of MoS_2 and porous sites of TiO_2(B) enhances the photoelectrocatalytic HER activity synergistically, beyond that of commercial Pt/C electrodes. The high density of electrons in S-doped TiO_2 migrates to the MoS_2 layer inducing n-type doping in it and thus TiO_2 acts as an efficient photocathode in the photoelectrocatalysis. Quantitative XPS analysis reveals that the catalytically active bridging S_2^{2-}/apical S^{2-} increases up to ~72% after the formation of the ternary system (Pt@MoS_2/TiO_2(B)) demonstrating nearly 13 fold higher exchange current density as compared to the binary system (MoS_2/TiO_2). Interestingly, we observe an absorption in the entire visible region from the ternary system and the PL study reveals the lower recombination dynamics. The ternary system shows lowest Tafel slope and charge transfer resistance (R_{ct}) with high stability as revealed by the chronopotentiometric measurements. This study will be valuable to fabricate the photocathode for efficient HER

with maximally edge-exposed and catalytically active sites of MoS_2 marginally-loaded with Pt NPs.

Chapter 6 presents a new approach to achieve tunable and high PL quantum yield (QY) from the self-grown spherical TiO_2 quantum dots (QDs) on fluorine doped TiO2 (F-TiO_2) nanoflowers, which are mesoporous in nature, synthesized by a simple solvothermal process followed by a post growth rapid thermal annealing (RTA) under vacuum. The strong PL emission from F-TiO_2 QDs centered at ~485 nm is associated with shallow and deep traps, and we measured a record high PL QY of ~5.76% at room temperature. Size distribution and doping of F-TiO_2 nanocrystals (NCs) are successfully tuned by simply varying the HF concentration during synthesis. Optimized post-growth RTA under vacuum transforms the arbitrary shaped F-TiO_2 NCs into spherical QDs with smaller sizes demonstrating a dramatic enhancement (~163 times) in the PL intensity. ESR and XPS confirm the high density of oxygen vacancy defects (Ti^{3+} and F^{+} centers) on the surface of TiO_2 NCs, while low temperature and time resolved PL studies reveal that the ultrafast radiative recombination in the TiO_2 QDs results in highly efficient PL emission. This work is important for the design of highly stable, biologically inert and highly fluorescent TiO_2 QDs/flowers without any capping agent, significant for emerging applications in bioimaging, energy and environmental cleaning.

Chapter 7 presents an in-situ chemical vapor deposition (CVD) growth of MoS_2@TiO_2 core-shell heterojunction with single layer MoS_2 (1L-MoS_2) as shell and 3D TiO_2 nanoflower (NF) as core for multifunctional optoelectronic applications. In this work, we reveal an easy technique to switch the trions in 1L-MoS_2 into neutral excitons by developing a core-shell heterojunction with TiO_2 in order to demonstrate a giant PL enhancement (~up to 83 fold) from 1L-MoS_2 shell at room temperature. The Raman and XPS analyses reveal a heavy p-doping effect in 1L-MoS_2 lattice due to the migration of excess electrons from MoS_2 to TiO_2, resulting in the enormous PL enhancement suppressing the nonradiative recombination, as verified from the low temperature PL study. A mild oxygen plasma treatment verifies further the charge transfer induced p-doping effect in 1L-MoS_2 and thus the huge PL enhancement.

Next, 1L-MoS_2@TiO_2 p-n heterojunction system acts as a high performance broadband photodetector owing to the favorable band alignment and high absorption coefficient in the wide spectral range. The heterojunction photodetector offers a record high

responsivity with two prominent peaks at 370 nm (~35.9 A W^{-1}) and at 570 nm (~18.5 A W^{-1}) at an applied reverse bias of 5 V. An ultra-fast photoresponse (a few μs) as well as extremely high detectivity having two major peaks of 1.98×10^{13} and 1.09×10^{13} Jones at 370 nm and 570 nm, respectively, are demonstrated for the heterojunction photodetector. We evaluate various device parameters to realize the superiority of the p-n junction photodetector operated at a reverse bias. This work offers a detailed insights to understand and fabricate the next generation multifunctional optoelectronic devices based on the 1L-MoS_2 and TiO_2 heterojunction.

Chapter 8 presents the summary and highlights of the contributions of the present thesis. Future scope of work on shape tailored TiO_2 nanostructures, their plasmonic and 2D HSs for the environment, energy, light emitting and broadband photodetection applications are presented at the end.

LIST OF PUBLICATIONS:

A. In Peer-Reviewed Journals:

1. Kamal Kumar Paul, N. Sreekanth, Ravi K. Biroju, Alexander J Pattison, Daniel Escalera-López, Anku Guha, Tharangattu N. Narayanan, Neil Vaughan Rees, Wolfgang Theis and P. K. Giri, "Strongly enhanced visible light photoelectrocatalytic hydrogen evolution reaction in an n-doped MoS_2/TiO_2(B) heterojunction by selective decoration of platinum nanoparticles at the MoS_2 edge sites." ***J. Mater. Chem. A***, 6, 22681 (2018).

2. Kamal Kumar Paul, Larionette P. L. Mawlong and P. K. Giri, "Trion inhibited strong excitonic emission and broadband giant photoresponsivity from chemical vapor deposited monolayer MoS_2 grown in-situ on TiO_2 nanostructure" ***ACS Appl. Mater. Interfaces,*** 10, 42812 (2018).

3. Kamal Kumar Paul, N Sreekanth, Ravi K Biroju, Tharangattu N Narayanan and P. K. Giri, "Solar Light Driven Photoelectrocatalytic Hydrogen Evolution and Dye Degradation by Metal-Free Few-Layer MoS_2 Nanoflower/TiO_2(B) Nanobelts Heterostructure" ***Sol. Energy Mater Sol. Cells.***, 185, 364 (2018).

4. Kamal Kumar Paul, Subhadip Jana and P. K. Giri, "Tunable and High Photoluminescence Quantum Yield from Self-Decorated TiO_2 Quantum Dots on Fluorine Doped Mesoporous TiO_2 Flowers by Rapid Thermal Annealing" ***Part. Part. Syst. Charact.***, 35, 1800198 (2018).

5. Kamal Kumar Paul and P. K. Giri, "Role of Surface Plasmons and Hot Electrons on the Multi-Step Photocatalytic Decay by Defect Enriched Ag@TiO_2 Nanorods under Visible Light" ***J. Phys. Chem. C.***, 121, 20016 (2017).

6. Kamal Kumar Paul, Ramesh Ghosh and P. K. Giri, "Mechanism of Strong Visible Light Photocatalysis by Ag_2O-Nanoparticle-Decorated Monoclinic TiO_2(B) Porous Nanorods" ***Nanotechnology***, 27, 315703 (2016).

7. Kamal Kumar Paul and P. K. Giri, "Shape Tailored TiO_2 Nanostructures and Its' Hybrids for Advanced Energy and Environmental Applications: A Review" ***J. Nanosci. Nanotechnol.***, 19, 307–331 (2019)

8. Biswajit Choudhury, Kamal Kumar Paul, Dirtha Sanyal, Anil Hazarika, P. K. Giri, "Evolution of Nitrogen-Related Defects in Graphitic Carbon Nitride Nanosheets Probed by Positron Annihilation and Photoluminescence Spectroscopy" ***J. Phys. Chem. C.***, 122, 9209 (2018).

9. Larionette P L Mawlong, Kamal Kumar Paul, P. K. Giri, "Direct CVD Growth of Monolayer MoS_2 on TiO_2 Nanorods and Evidence for Doping Induced Strong Photoluminescence Enhancement" ***J. Phys. Chem. C.***, 122, 15017 (2018).

10. Kamal Kumar Paul and P. K. Giri, "Plasmonic Metal and Semiconductor Nanoparticle Decorated TiO_2-Based Photocatalysts for Solar Light Driven Photocatalysis" A chapter in ***Encyclopedia of Interfacial Chemistry.,*** DOI: 10.1016/B978-0-12-409547-2.13176-2, **Elsevier**, 786 (2018).

B. Manuscripts under Review:

1. Kamal Kumar Paul, P. K. Giri, H. Sugimoto, Minoru Fujii and B. Choudhury, "Trap State Mediated Plasmonic Hot Electron Injection and Efficient Charge Separation in Ag-TiO_2(B) and Au-TiO_2(B) Nanorods decorated over g-C_3N_4 Nanosheets with Superior Visible Light Photocatalytic Performance." ***Sol. Energy Mater Sol. Cells.,*** **(under Review).**

C. Conference Papers Presented:

1. Kamal Kumar Paul and P. K. Giri, *'Enhanced Visible Light Photocatalytic Activity of Ag_2O Decorated Nanoporous TiO_2(B) Nanorods Heterostructure'*, International conference on nanoscience, nanotechnology and advanced materials **(NANOS-2015)**, *Gitam University, Vizag, India, 14-17 December, 2015* ***(Best Poster Award)*****.**
2. Kamal Kumar Paul and P. K. Giri, *'Enhanced Visible Light Absorption and Photocatalytic Activity of Pd Nanoparticle Decorated CuO/TiO_2 Nanobelts Heterostructure',* Recent Advances in Nanoscience and Nanotechnology **(NCRANNT-2016),** *NEHU, Shillong, India, 8-9 September, 2016.*
3. Kamal Kumar Paul and P. K. Giri, '*Surface Plasmon Induced Enhanced Visible Light Photocatalytic Activity of Silver Nanoparticle Decorated TiO_2 Nanorods Heterostructure',* International Conference on Emerging Trends in Nanomaterials Science & Technology **(ICETNMST-2017),** *NIT Nagaland, India, 4-6 January, 2017.*
4. Kamal Kumar Paul and P. K. Giri, *'Role of Surface Plasmons and Hot Electrons on the Strong Visible Light Photocatalysis by Ag@TiO_2 Nanostructures',* International Conference on Materials for Advanced Technologies **(ICMAT-2017)**, *Singapore, 18-23 June, 2017.*
5. Kamal Kumar Paul and P. K. Giri, *'High Adsorption and Solar Light Driven Strong Photocatalysis of RhB by Pt@MoS_2/TiO_2(B) Nanobelt Heterostructures',* International Conference on Materials for Advanced Technologies **(ICMAT-2017)**, *Singapore, 18-23 June, 2017.*
6. Kamal Kumar Paul and P. K. Giri, *'High Photoluminescence Quantum Yield in F-doped TiO_2 Quantum Dots Decorated on TiO_2 Nanoflowers Induced by Rapid Thermal Annealing',* International Conference on Advanced Nanomaterial and Nanotechnology **(ICANN-2017)**, *IIT Guwahati, India, 18-21 December, 2017.*
7. Kamal Kumar Paul and P. K. Giri, *'Solar Light Driven Photo-electrocatalytic Hydrogen Evolution by Pd Nanoparticle Decorated CuO Nanocrystal/TiO_2(B) Nanobelt Heterostructure',* Conference on Advances in Catalysis for Energy and Environment **(CACEE-2018),** *TIFR Mumbai, India, 10-12 January, 2018.*
8. Kamal Kumar Paul and P. K. Giri, *'Enhanced Visible Light Photocatalysis by Fluorine Doped Faceted TiO_2 Nanoflowers Hierarchically Designed with Vacancy-Rich TiO_2 Nanocrystals Grown by Vacuum Annealing'*, International conference on Optoelectronic and Nanomaterials for Advanced Technology **(iCONMAT-2019)**, *Cochin University of Science and Technology, Kerala, India, 3-5 January, 2019* ***(Best Poster Award)*****.**

D. Workshops Attended:

1. *INUP Familiarization workshop on 'Nanofabrication Technologies', Tezpur University, 25-26 April, 2015.*
2. *'National workshop on MEMS/NEMS and Theranostic devices (NWNTD-2015)', IIT Guwahati, 16-17 March, 2015.*
3. *'National Workshop on Advanced Probing Techniques in TEM', IIT Guwahati, 15-16 February, 2016.*
4. *'2nd National Workshop on MEMS/NEMS and Theranostic devices (NWNTD-2016', IIT Guwahati 21-22 March, 2016.*
5. *'3rd National Workshop on MEMS/NEMS and Theranostic devices (NWNTD-2017', IIT Guwahati 21-23 March, 2017.*
6. *'5th National Workshop on MEMS/NEMS and Theranostic devices (NWNTD-2019', IIT Guwahati 21-23 March, 2019.*

LIST OF ABBREVIATIONS

Abbreviation	***Description***
0D	Zero dimensional
1D	One dimensional
2D	Two dimensional
3D	Three dimensional
1L	Single Layer
CVD	Chemical Vapor Deposition
DRS	Diffuse Reflectance Spectroscopy
EDS	Energy Dispersive X-ray Spectroscopy
ESR	Electron Spin Resonance
FESEM	Field Emission Scanning Electron Microscopy
FETEM	Field Emission Transmission Electron Microscopy
FTIR	Fourier Transform Infrared Spectroscopy
FWHM	Full Width at Half Maxima
HER	Hydrogen Evolution Reaction
HRTEM	High Resolution Transmission Electron Microscopy
HS	Heterostructure
NB	Nanobelt
NC	Nanocrystal
NF	Nanoflower
NIR	Near Infrared
NP	Nanoparticle
NR	Nanorod
NT	Nanotube
NW	Nanowire
O_V	Oxygen vacancy
PEC	Photoelectrocatalysis
PL	Photoluminescence
QC	Quantum Confinement

QD	Quantum Dot
RHE	Reversible Hydrogen Electrode
RTA	Rapid Thermal Annealing
SAED	Selected Area Electron Diffraction
SPR	Surface Plasmon Resonance
STEM	Scanning Transmission Electron Microscopy
TEM	Transmission Electron Microscopy
TRPL	Time Resolved Photoluminescence
UV-Vis	Ultraviolet Visible
XPS	X-ray Photoelectron Spectroscopy
XRD	X-ray Diffraction

Corrigendum

Synopsis:

1. Page ix: Para 1, Line 2: Replace “its” by “their”.
2. Page ix: Para 3, Line 6: Replace “application” by “applications”.
3. Page ix: Para 3, Line 10: Replace “HSs” by “heterostructures (HSs)”.
4. Page xi: Para 2, Line 1: Replace “details” by “detailed”.
5. Page xiii: Para 2, Line 1: Replace “novel” by “new”.

Chapter 1:

1. Page 1: Line 2: Delete the word “novel”.
2. Page 1: Line 3: The word “various” is moved to the beginning of the sentence.
3. Page 1: Line 6: Replace “its” by “their”.
4. Page 2: Section 1.1., Para 2, Line 2: Replace “details” by “detailed”.
5. Page 14: Section 1.5.1., Line 5: Replace “its” by “their”.
6. Page 14: Section 1.5.1., Line 8: Delete “A” in the beginning of the sentence.
7. Page 16: Line 1: Replace the word “novel” by “unique”.
8. Page 20: Section 1.5.4., Line 5: Replace “The main two steps” by “The two main steps”.
9. Page 20: Section 1.5.4., Line 7: Replace “following the” by “followed by”.
10. Page 24: Section 1.8., Line 10: Replace “novel” by “highly efficient”.

Chapter 2:

1. Page 33: Section 2.1., Line 1: Replace “its” by “their”.
2. Page 59: Delete Reference 23.

3. Chapter 3:

1. Page 75: Table 3.3 caption: Replace “Degradation performance” by “two stage degradation”.
2. Page 75: Table 3.3: Replace “compartment” by “stage”.

Chapter 4:

1. Page 89: Para 1, Line 4: Replace “hybrids” by “hybrid”.

Chapter 5:

1. Page 121: Section 5.2.3., Line 7: Replace “was” by “were”.
2. Page 121: Section 5.3.1., Line 11: Replace “limit of FESEM” by “limit of the FESEM”.
3. Page 135: Para 3, Line 8: Replace “photocatalysts” by “photoelectrocatalysts”.
4. Page 137: Table 5.2: Replace “photocatalysts” by “photoelectrocatalysts”.

Chapter 6:

1. Page 145: Section 6.1., Line 9: Replace “doping” by “dopings”.
2. Page 145: Section 6.1., Line 11: Replace “was” by “were”.
3. Page 146: Section 6.1., Line 5: Replace “novel” by “various optoelectronic”.

Chapter 7:

1. Page 177: Section 7.2.1.2., Para 2, Line 4: Replace “purged” by “used to purge”.
2. Page 178: Section 7.2.1.2., Line 1: Replace “Furnace” by “The furnace”.

Chapter 8:

1. Page 205: Section 8.1., Line 11: Replace “novel” by “unique”.

Chapter 1

Introduction

Over the past decades, significant advancement in nanoscience and nanotechnology has been achieved with the development of nanomaterials with exotic properties, utterly different from their bulk counterparts. Various shape tailored nanostructured materials including metal and semiconductors are being developed at different dimensionalities (0D, 1D, 2D and 3D) over the range up to few hundreds of nanometer, through different chemical and physical techniques. The materials with nanoscale dimensionality have drawn great attention due to the variation of their properties with the shape, size, composition etc. High aspect ratio (surface to volume ratio) and strong quantum size effect are the two critical features of a nanomaterial, leading to a modification of its characteristic properties including structural, electrical, optical (bandgap, absorption/emission) and various physicochemical (particle size, surface area, chemical reactivity, etc.) properties. By introducing additional structural complexities through heterostructure (HS) formation (plasmonic, semiconductor-semiconductor HS), doping and defect creation, desired photophysical properties can be tuned selectively. It is of fundamental interest to have a detailed understanding of the promising growth strategies of nanoscale heterostructures and the dependence of its properties on the size, shape, surface morphology and interface band alignment. The suitable physicochemical and photophysical properties of a nanoheterostructure open up vast opportunities for diverse advanced applications up to the industrial scale. In this chapter, we briefly review the important features of titanium dioxide (TiO_2) nanostructures, various techniques for the growth of shape-controlled TiO_2 nanostructures and the fundamental issues related to the respective growth mechanism. The growth of TiO_2 based various HSs is also presented, and the recent advancements of its applications in the energy, environmental and optoelectronics (photocatalysis, photoelectrocatalysis, photovoltaics, photodetector, sensor, etc.) are discussed. The existing challenges along with the focus of the present thesis and the outline of the thesis are described at the end of the chapter.

1.1. Crystal Structure of TiO_2

Titania (TiO_2) is a well-known semiconductor possessing wide bandgap and diverse range of applications.[1-4] TiO_2 generally exists in three distinct polymorphs (phases): rutile, anatase, and brookite, where anatase and rutile phases have a tetragonal crystal structure and brookite has the orthorhombic crystal structure. In each polymorph, titanium cations are found to be six-fold coordinated to oxygen anions, which forms distorted TiO_6 octahedra. The crystal structure of TiO_2 differs with phase due to the distinct spatial arrangement of the TiO_6 octahedra building blocks. While anatase has corner sharing TiO_6 octahedra, in rutile phase edge sharing is observed, and the brookite shows both the sharing.[5] The crystal structure of rutile, anatase and brookite phases with their polyhedral representation of TiO_6 octahedra are shown in **Fig. 1.1(a-c)**, respectively. Among the different crystal phases, rutile is considered to be the most stable (thermodynamically) bulk phase. At the nanoscale, anatase and brookite are generally regarded as quite stable due to their low surface energy, although there is debate on it in the literature.[6, 7] Additionally, another exotic crystal phase of pure TiO_2 also exists in nature, known as TiO_2(B). This monoclinic polymorph showed in **Fig. 1.1(d)** is the uncommon phase in nature, usually synthesized by a chemical route at high temperature and pressure.

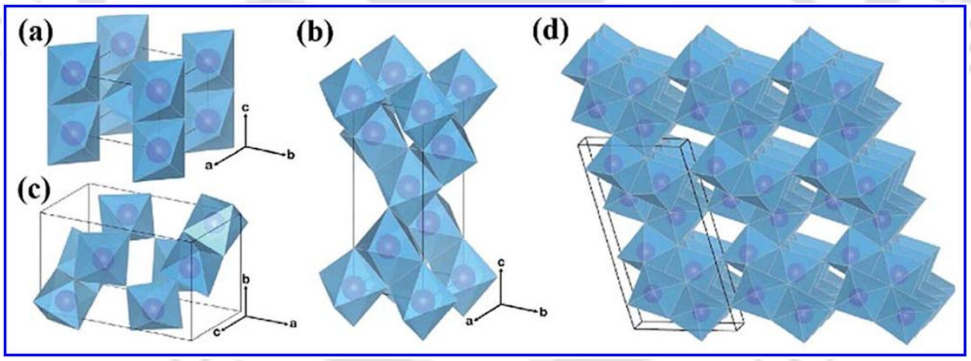

Fig. 1.1. A schematic representation of various of TiO_2 polymorphs: (a) rutile; (b) anatase; (c) brookite; and (d) TiO_2(B). Each purple sphere represents Ti atom, and the blue octahedra represent TiO_6 blocks. Oxygen atoms at the corner of the octahedra are omitted for clarity of representation. Adopted from Ref. [5].

In 1980, Marchand et al.[8] reported the synthesis of pure TiO_2(B) nanostructure by hydrolysis of potassium-titanate for the first time. The detailed experimental results asserted that the crystal phases are determined by the experimental conditions and also post-growth treatments (synthesis method, pH of the medium, annealing duration and annealing temperature).[9-11] The details of the crystal structure, space group, lattice parameter, density and cell volume of various polymorphs are presented in **Table 1.1**.

Table 1.1. *Various polymorphs of TiO_2 with their crystal structure, space group, lattice constant, density and cell volume. Adopted from Ref.* [5]

TiO_2 Polymorph	*Crystal structure*	*Space group*	*Lattice parameter (Å)*			*Density (g/cm^3)*	*Cell volume (Å)*
			a	**b**	**c**		
Rutile	Tetragonal	$P4_2/mnm$	4.6	4.6	2.94	4.27	62.1
Anatase	Tetragonal	$I4_1/amd$	3.78	3.78	9.53	3.90	136.0
Brookite	Orthorhombic	Pbca	9.17	5.44	5.13	4.15	256.0
TiO_2(B)	Monoclinic	C2/m	12.17	3.73	6.54	3.73	284.2

In spite of having the identical chemical formula with other polymorphs, TiO_2(B) has a very open framework structure. Thus, it possess the lowest packing density and highest cell volume as compared to the other phases, see **Table 1.1**. Despite the stability issue of the B-phase TiO_2, the larger specific capacity are extremely advantageous in the applications of photocatalysis, solar cells and energy storage.[12-14] In this thesis, a major portion of the work deals with the TiO_2(B) nanostructure and its heterostructures for energy and environmental applications. We also consider anatase/rutile TiO_2 nanostructures in some cases.

1.2. Band Structure of TiO_2

During the past few decades, shape tailored TiO_2 nanostructures with different polymorphs have been drawing intense attention in the basic scientific research as well as the advanced technological applications due to their interesting physicochemical properties.[1, 15, 16] Investigation of the electronic band structure of a material is one of the fundamental interest in order to predict its suitability for a particular application.

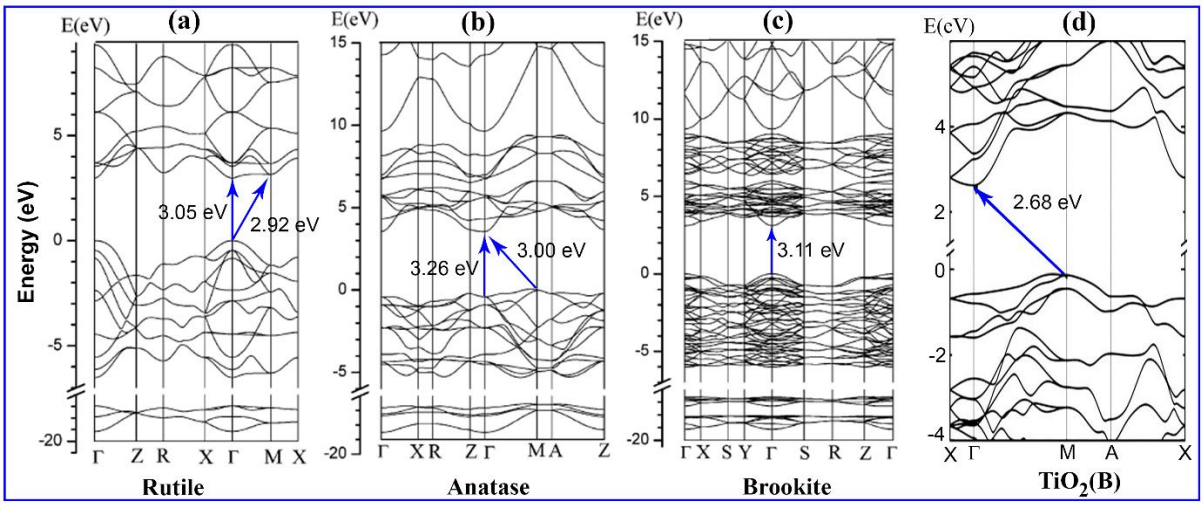

Fig. 1.2. Band structure of different polymorphs of TiO_2: (a) rutile, (b) anatase, (c) brookite and (d) TiO_2(B), calculated from the first-principles density functional theory. The arrow in each case shows the transition from valence band maximum to conduction band minimum. Adopted from Ref. [17-19]

The nature of the bandgap transition varies with the phases of TiO_2. According to the experimental and theoretical studies rutile TiO_2 possesses both the direct and indirect bandgap of 3.0 eV, while the anatase TiO_2 has an indirect bandgap of 3.2 eV.[20, 21] Experimental studies suggest that the brookite TiO_2 has both the direct and indirect bandgap ranging from 3.1-3.4 eV.[22-24] Various experimental studies predict the indirect bandgap of TiO_2(B) as 3.05 eV and 3.2 eV.[25] The bandgap of all the TiO_2 polymorphs lies in the UV region irrespective of the nature of optical transition. The effective bandgap as well as the optical absorption properties can be tuned by defect engineering. The oxygen vacancy and Ti interstitial defects may introduce an additional localized states within the bandgap of TiO_2, which in turn leading to the visible light absorption. The Ti^{3+} formed with the oxygen vacancy introduce a shallow donor state just below the conduction band, which also contribute to the visible light response. The anion and cation doping also introduce additional defect states, resulting in redshift of optical absorption edge absorb the visible light.[26]

Theoretical studies on rutile TiO_2 have estimated the direct band gap as 3.05 eV and indirect band gap as 2.92 eV ($\Gamma_V \rightarrow M_C$)[17], as shown in **Fig. 1.2(a)**. Wang et al.[17] also reported the direct band gap of 3.26 eV and the indirect band gap of 3.0 eV for the anatase phase (see **Fig. 1.2(b)**). Zhang et al.[18] calculated the direct band structure of brookite with a band gap value of 3.1 eV, as shown in **Fig. 1.2(c)** by a hybrid density functional theory (DFT) calculation. Yahia et al.[19] observed an indirect nature of B-phase TiO_2 with a band gap of 2.68, as shown in **Fig. 1.2(d)**.

It can be noted that the TiO_2 is a wide band gap material and is active only under the ultraviolet (UV) region of the solar spectrum, limiting its applications involving solar light. The sensitization of visible/solar light can be realized by the modification of electronic band structure, introducing some defects or doping in the TiO_2 lattice. After the creation of oxygen vacancy, the electrons located at the oxygen vacancy states may form a donor level just below the conduction band, as shown in **Fig. 1.3**.[27]

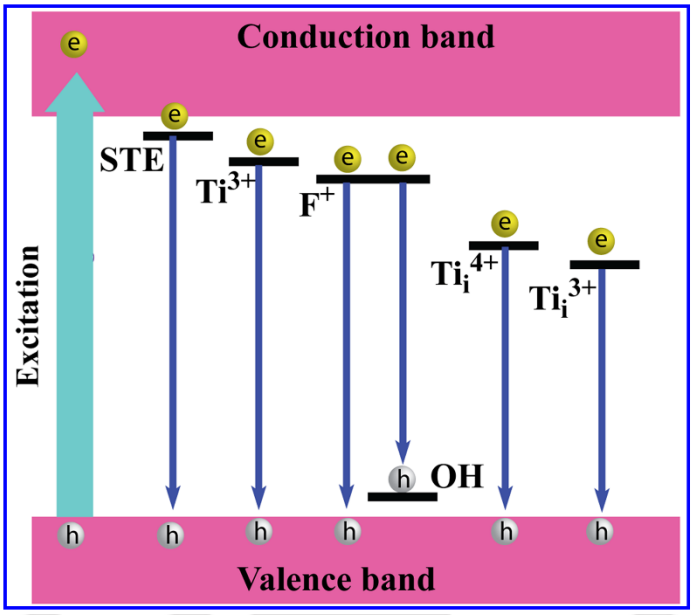

Fig. 1.3. Schematic band diagram showing the presence of various defect states and the corresponding optical transitions. Adopted from Ref. [27]

Further investigation by some sophisticated experimental techniques (ultraviolet photoemission spectroscopy and electron energy loss spectroscopy) reveals that the energy levels of localized donor states resulting from the oxygen vacancies lie at ~0.7–1.0 eV below the conduction band of TiO_2 nanostructures.[28, 29] Self-trapped exciton (STE) state lies just below the conduction band of TiO_2. Singly ionized oxygen vacancy (F^+) also shows a defect state below the conduction band (**Fig. 1.3**).[30] Additionally, the oxygen vacancy may cause the redistribution of the excess electrons in the vicinity of Ti atoms near the vacancy site and form a donor state below the conduction band (Ti^{3+}).[31] The Ti interstitial defects (Ti_i^{4+} and Ti_i^{3+}) forming a localized state at the bottom of the conduction band are shown in **Fig. 1.3**.

Defect engineered black TiO_2 nanostructure is an emerging substantial material for the different promising applications and thus the investigation on its photophysical properties is of fundamental interest. The defect engineering by growing the black TiO_2 is reported to be achieved by various thermal treatment in hydrogen atmosphere.[32] Chen et al.[33] investigated the DOS of the valence band in black TiO_2 by analyzing the valence band XPS spectra. They showed that the energy corresponding to the valence band maximum blue-shifts from 1.26 eV to –0.92 eV after the formation of black TiO_2 nanocrystals, and thus narrowed down the optical bandgap. The conduction band tail may extend below the conduction band minimum due to the

defect engineering and thus optical bandgap decreases from ~3.3 eV to ~2.18 eV, as shown in **Fig. 1.4(a)**. The DOS of the black TiO_2 nanocrystals is shown in **Fig. 1.4(b)**, clearly depicting the additional states within the bandgap.

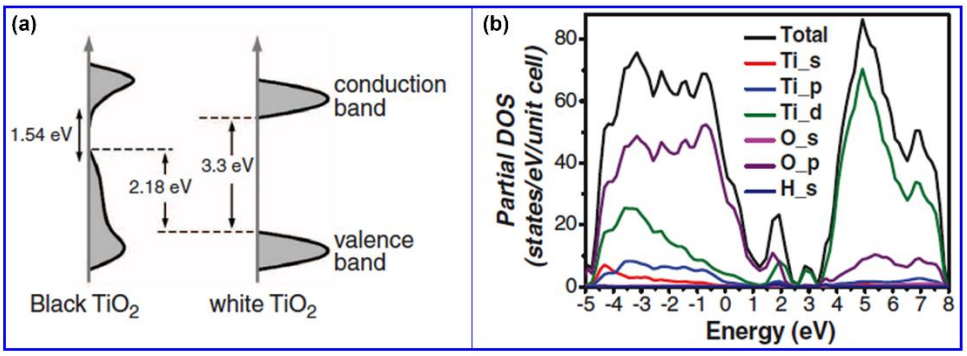

Fig. 1.4. (a) Schematic representation of the DOS of black TiO_2 (disorder-engineered) nanocrystals along with the unmodified TiO_2 nanocrystals. (b) The DOS of black TiO_2 nanocrystals. Adopted from Ref. [33]

1.3. Fabrication of TiO_2 Nanostructures

Over the past decades, numerous chemical and physical techniques have been developed for the fabrication of shape tailored TiO_2 nanostructures and their suitable HSs with narrow bandgap materials as well as plasmonic nanoparticles, aimed at dedicated advanced applications. TiO_2 nanostructures are usually grown considering the following precursors: commercial TiO_2 powder, Ti foil/Ti powder, titanium isopropoxide ($Ti(OCH(CH_3)_2)_4$), titanium butoxide ($Ti(OC_4H_9)_4$), titanium tetrachloride ($TiCl_4$), titanium tetrafluoride (TiF_4) etc. The commonly used growth techniques of TiO_2 nanostructures and TiO_2 based HSs are briefly discussed below.

1.3.1. Sol-gel and Template Assisted Method

One of the key synthesis processes involving wet chemistry method is the sol-gel synthesis of TiO_2 at low temperature and it enables easy control of surface morphology of TiO_2 nanostructures. This process involves the transformation of a sol (colloidal solution) into a gel by the hydrolysis and polymerization reaction. Further processing of the gel can produce a compact, thin film of various TiO_2 nanostructures.[1] Joo et al.[34] have prepared 3.4 nm (diameter) × 38 nm (length) sized TiO_2 nanocrystals from the sol-gel reaction between titanium(IV) isopropoxide and oleic acid at 270 °C. Various TiO_2 nanostructures are reported with the typical sol-gel process by varying the precursor material, pH of the solution, growth temperature and solvent.[35-37] The template-assisted method is also extensively used to fabricate the 1D TiO_2 nanostructures. An anodic aluminium oxide (AAO) nanoporous membrane consisting of a parallel straight array

of nanopores with well controllable dimension (diameter and length), is usually considered as a template. Finally, the template is removed by chemical etching, and 1D TiO_2 nanostructures remain on the substrate. Sander et al.[38] fabricated dense, thermally stable and well-aligned TiO_2 nanotubes (NTs) by sequential ALD (atomic layer deposition) process with $TiCl_4$ as the precursor material using the template-assisted method. A combination of sol-gel and template-assisted method produces better control over the growth of 1D TiO_2 nanostructures.[39-41]

1.3.2. Hydrothermal Method

Hydrothermal method is the most widely used chemical synthesis route for the fabrication of shape tailored TiO_2 nanostructures including various 0D and 1D architectures. Usually, the reaction is conducted in a stainless steel chamber with a Teflon liner under high temperature with autogenous pressure. The shape, size, crystallinity and facet orientation of the nanomaterials can be controlled simply by varying the growth parameters, such as temperature, stirring, reaction duration, solvent and pH of the solution.[42-44] It is probably the simplest method for tuning the surface morphology at the lowest production cost. Kasuga et al.[45, 46] discovered a template-free new route to fabricate TiO_2 NTs with diameter ~8 nm and length ~100 nm. Afterwards, many research articles have reported on the growth of TiO_2 NTs [47, 48], nanowires (NWs)[49, 50], nanorods (NRs)[51], nanobelts (NBs)[52, 53], nanosheets[54-57], (001) facet dominated anatase TiO_2 nanocrystals[58-62]. Dinh et al.[63] demonstrated the TiO_2 nanocrystal growth with various shapes: rhombic, truncated rhombic, spherical, dog-bone, truncated and elongated rhombic, etc. by using a modified hydrothermal route.[64] Depending upon the solvent used, the synthesis procedure can generally be divided into two methods: first, acid hydrothermal method where the reactants are titanium salts and concentrated hydrochloric acid (HCl) and second, alkali-hydrothermal method where the reactants are TiO_2 nanoparticles and concentrated sodium hydroxide (NaOH) solution. These two methods have different reaction mechanisms, which produces different morphological features of TiO_2. During the alkali-hydrothermal process, layered sodium titanate ($Na_2Ti_4O_9$) is produced at an intermediate reaction stage. As the Na^+ ions are residing between the edge-shared TiO_6 octahedral layers, it can be easily replaced by protons (H^+ ion) in a dilute acidic medium. Thus, hydrogen titanate ($H_2Ti_5O_{11}.H_2O$) is formed first, and the interlayer distance becomes enlarged because of the larger intercalated size effect of H_2O molecules causing weaker static interaction between neighboring TiO_6 octahedral sheets. Thus, hydrogen titanate can easily be exfoliated to form nanosheets which in turn curl up from the edges to form TiO_2 NTs to

minimize the high surface tension.[65-70] The proposed growth mechanism and steps of the shape evolution TiO_2 nanostructures are depicted in **Fig. 1.5**.

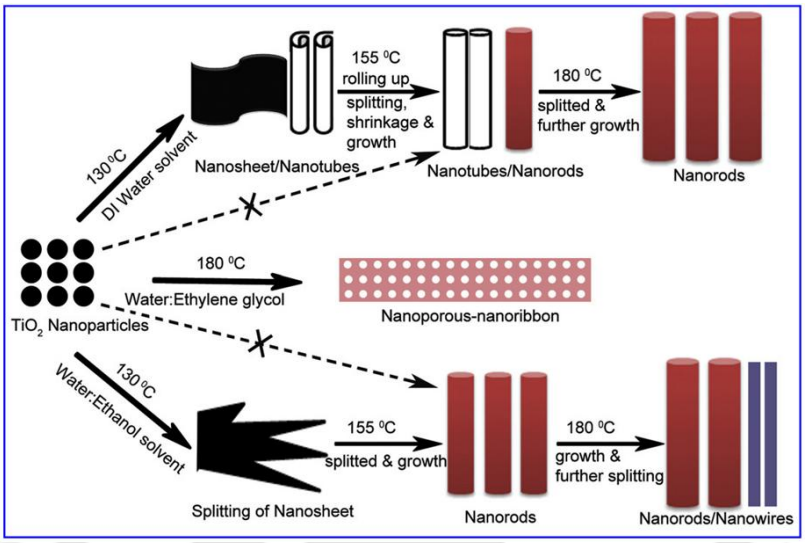

Fig. 1.5. Schematic of the shape evolution of TiO_2 nanostructure during the hydrothermal process using different solvents and different growth temperatures. Adopted from Ref. [67]

Fabrication of 3D hierarchical flower-like nanostructures has attracted much attention due to their plenty of active sites, high surface area and greater pore volume leading to the superior adsorption and catalytic applications. As the average surface formation energy is maximum for (001) facet (0.90 J m^{-2}) which is nearly double of the (101) facet (0.44 J m^{-2}), these facets are highly catalytically active and are very promising for the future generation energy and environmental applications.[57, 71-73] The growth of 3D hierarchical nanoporous spheres composed of ultrathin anatase TiO_2 nanosheets (thickness ~3 nm) with nearly 100% exposed (001) facets is recently reported.[74] A fluoride mediated self-transformation based fabrication of hollow TiO_2 microspheres and core-shell TiO_2 microspheres have been widely reported.[75-78] The 3D morphology evolution by dissolution and recrystallization is fully determined by the reaction species, temperature, and duration of nucleation. The synthesis, formation mechanism and necessary characterization of 3D TiO_2 nanostructures are discussed thoroughly by Ong et al.[44]

1.3.3. Solvothermal Method

Like the hydrothermal process, the solvothermal method is also a common growth process for various shaped TiO_2 nanostructures. The working principle of the solvothermal method is very similar to the hydrothermal process. The only difference is the use of an organic solvent (ethanol, ethylene glycol, n-hexane, etc.) in the solvothermal method, while only water is used as a

reaction solution in the hydrothermal method.[79-85] As the solvent plays an important role to determine the surface morphology, crystallinity and chemical composition, one can tune the above properties by varying the solvent, which makes the solvothermal technique more versatile than the hydrothermal process. By choosing an organic solvent with a high boiling point, the solvothermal reaction temperature can be elevated higher than that of the hydrothermal process.[86] The solvothermal growth of TiO_2 NWs[87], nanoribbons[11, 27], nitrogen and fluorine co-doped TiO_2 NBs[77, 79], 3D single crystals[55, 88] and 3D hierarchical superstructures[73] has been reported for use in the high-performance Li-ion battery materials, solar light-driven photocatalysis and dye-sensitized solar cells.[87, 89]

Despite having huge versatility and advantages of the hydrothermal and solvothermal method over the other growth processes, it has still some disadvantages. First, the nanostructures grown by this method are not always uniform in size and shape. Second, the size of the as-grown 1D nanostructures are generally too small for the better performance in practical applications. Third, the reaction rate is very slow, and it takes a long time to grow the desired materials. Fourth, the growth of monolayer 2D materials (MoS_2, $MoSe_2$, WS_2, etc.) is not well controllable by this method.

1.3.4. Electrochemical Anodization Method

Well-aligned vertical TiO_2 NT arrays can be easily grown on the Ti foil by an electrochemical anodization method with high repeatability. The anodic oxidation, surface feature and structure of the NT are significantly influenced by the electrochemical etching and chemical dissolution. Thus, the surface morphology, porosity, length, inner diameter and the wall thickness of the NTs can be tuned by varying the electrolyte, applied anodization voltage, pH of the electrolyte, reaction duration and temperature.[90-92] High purity Ti foil and Pt foil are usually used as a working electrode and counter electrode, respectively, while fluorine ion based electrolytes ($KF/HF/NH_4F+H_2O$) are used for the growth of the vertical TiO_2 NTs. The TiO_2 NTs synthesized by this method is very promising for the photoanode material due to its high performance, stability and easy synthesis procedure. Several works in the literature have reported the controlled growth of well-aligned TiO_2 NTs by this technique.[60, 93-98]

However, despite the advantages, the electrochemical anodization process suffers from some drawbacks, such as its growth only on the Ti foil substrate and only tube-like structure forms with low crystallinity.

1.3.5. Electrospinning Method

In 2003, Li et al.[99] synthesized TiO_2 nanofibers having diameter ~55 nm by electrospinning method for the first time. In this process, a polymer solution is injected from a needle of a syringe-like chamber under the influence of a strong electric field, as shown in **Fig. 1.6(a)**. Due to the continuous gathering electric charges, the polymer solution starts stretching to form ultralong and hollow nanofibers (see **Fig. 1.6(b)**). Enormous attention is being given to this method due to the easy formation of single-phase and highly crystalline TiO_2 nanofibers, including easy morphological manipulation upon heating (see **Fig. 1.6(c)**).[100-102]

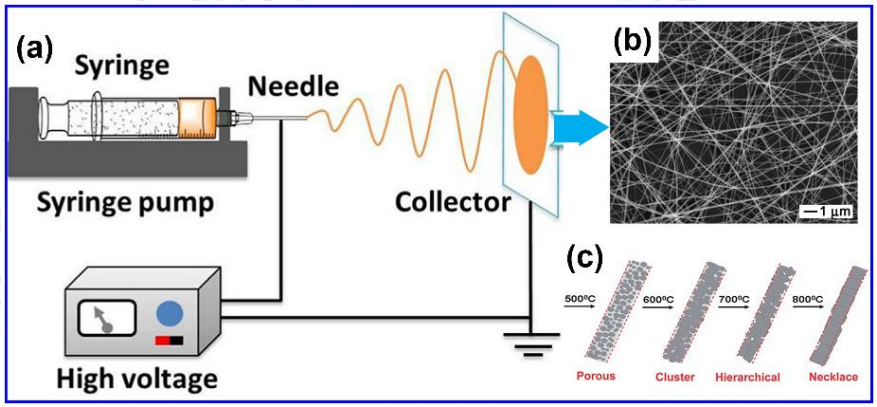

Fig. 1.6. (a) Schematic of an electrospinning setup. (b) SEM image of TiO_2/PVP nanofibers grown from an ethanol solution. (c) Change in the surface morphology of the nanofibers after thermal treatment. Adopted from Ref. [99, 100]

1.3.6. Vapor Deposition Technique

Vapor deposition is a high temperature assisted technique involving the material in a vapor phase which is allowed to condense to form crystalline solid-phase material. If the vapor deposition process involves the chemical reaction/gas source to grow the desired material, it is referred to as chemical vapor deposition (CVD) process, if not, it is termed as physical vapor deposition (PVD) process.

High quality and nonvolatile solid film can be deposited on a substrate by the CVD technique, which involves the chemical reaction of constituent materials in the vapor phase. Though the chemical based growth mechanism of TiO_2 is now firmly established, the synthesis of pure TiO_2 nanostructure by a physical method is not yet well explored. In a typical synthesis, Ti precursor is vaporized in the low-temperature zone of the furnace which is further carried by the carrier gas (O_2/N_2/H_2) into the high-temperature zone, following the growth of TiO_2 nanostructures on the substrate. The phase, morphology and growth orientation of the TiO_2

nanostructure can be controlled by the experimental parameters.[103] Lee et al.[104] developed high density (001) facet dominated TiO_2 nanosheets on a silicon substrate via CVD method in anatase and rutile phases induced by the H_2 autoignition, as shown in **Fig. 1.7**.

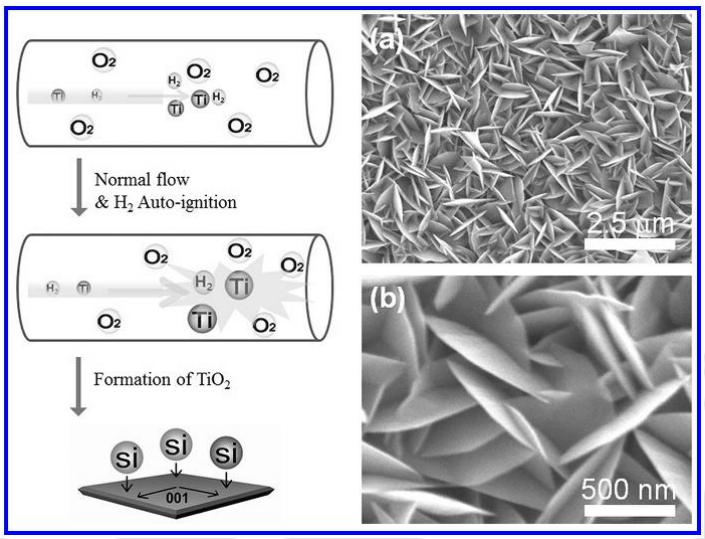

Fig. 1.7. Schematic representation along with the FESEM micrographs of (001) facet dominated anatase TiO_2 nanosheets grown by CVD method. Adopted from Ref. [104]

Unlike the CVD process, PVD process does not involve any chemical reactions for the growth of desired material. In this process, solid source material is evaporated by high power heating, laser ablation and other techniques, followed by the condensation on the substrate material to grow the final thin film. In a typical synthesis of TiO_2 nanostructure from the Ti powder source, it is thermally evaporated at ~1050 °C and the vapor is carried by the carrier gas O_2/N_2 to the low temperature zone (~850 °C) where Au/Ti/Si substrate (Au and Ti coated Si substrate) is placed.[105] The growth of TiO_2 follows the vapour-liquid-solid phase, where the vaporized source is deposited on the substrate and during condensation, it is liquefied first and then converted into the solid phase. Despite the several advantages of CVD and PVD techniques, both the processes involve high power source for the evaporation, the release of toxic and hazardous gases to the environment, lack of versatility and cost effectiveness.

1.4. TiO_2 Based Heterostructures

After the groundbreaking work by Honda in 1972 on the electrochemical water splitting by TiO_2 under the UV irradiation, TiO_2 HSs with different materials are being extensively studied to exploit the multifunctional properties of the heterojunction.[15] The TiO_2 surface can be

engineered by the following ways: (a) doping with metal and non-metal elements, (b) plasmonic HSs, (c) type-II HSs with narrow bandgap semiconductor and (d) core-shell HSs. The poor performance index of the pristine TiO_2 nanostructures hinders its multifunctional applications up to the industrial scale. Thus, the design and effective synthesis strategies may lead to the significant improvement in the required applications to realize the future demands of the society. Therefore, the surface modification of TiO_2 nanostructure by forming the suitable HSs may pave the way to its enhanced/superior photocatalysis, photoelectrocatalysis, gas sensing, photovoltaics, and optoelectronics applications.

Controlled incorporation of a suitable secondary element into the TiO_2 lattice may introduce additional energy band in between the forbidden region of TiO_2 nanostructured materials and thus can sensitize the enhanced visible light absorption and suppressed recombination of the photogenerated electrons and holes. The first report on the successful doping of nitrogen into TiO_2 by a sputtering method in a nitrogen-rich environment showed extended optical absorption band from UV to visible region, resulting in the superior visible light photocatalytic activity.[106] Following this work, several reports have been published on the doping of TiO_2 nanostructure with various non-metal ions, such as nitrogen (N)[107], carbon (C)[108], sulfur (S)[109, 110] and fluorine (F)[111, 112] etc., fabricated by various methods including hydrothermal, sputtering and thermal treatment method. Besides the individual doping, a few works in the literature concentrated on the co-doping with N and F, or N and S.[89, 113] Doping with the ions of a transition metals, such as Fe, V and Cu, has also been explored for the improvement of the photoelectron conversion efficiency under the solar light illumination.[114-117]

The most promising approach for the enhancement of visible light absorption, high charge separation at the interface and hence the superior energy and environmental applications is to decorate the TiO_2 nanostructures with noble metal nanoparticles such as Au, Ag, Pd, Pt, Cu, etc.[118-126] Among the various existing fabrication strategies (photoreduction method, plasma sputtering, electrodeposition, wet impregnation method, electrospinning, vapor-thermal method and hydrothermal method)[121, 127-130] of plasmonic noble metal nanoparticles (NPs) growth on TiO_2 nanostructures, the hydrothermal method has been established to be the most versatile method in controlling the shape, size and dispersion over the TiO_2 template.[98]

The discovery of semiconductor HS by Herbert Kroemer and Zhores I. Alferov opens up a wide research window in the field of high-speed optoelectronics, photocatalysis and energy storage applications. The band position and their alignment at near the interface primarily determine the catalytic as well as the optoelectronic properties of a semiconductor heterojunction. Among the various semiconductor heterojunctions, a type-II (staggered type) band arrangement of TiO_2 with a suitable semiconductor develops a band bending at the heterojunction resulting to a built-in electric field, which actually drives the photogenerated electrons and holes in two opposite directions. The formation of heterojunction by coupling an n-type semiconductor (say, TiO_2) with a p-type semiconductor (say, Cu_2O, Ag_2O)[131, 132] develops an electric field from n-type to p-type semiconductor, which increases the carrier separation efficiency at the interface. Though numerous fabrication techniques have been developed for the synthesis of semiconductor HSs including physical (sputtering, physical vapor deposition) and chemical (hydrothermal, sol-gel, sonochemical, electrodeposition, microwave and chemical vapor deposition) approaches, hydrothermal technique is extremely popular due to its low cost and versatility for the shape tuning and multifaceted advantages over the other processes. Liu et al.[133] synthesized a type-II heterojunction composed of TiO_2(B)/anatase core-shell NW. A variety of semiconductors including Ag_2O NPs[132, 134], few-layer MoS_2 nanosheets[135-138], CdS NPs[139], CdS quantum dots (QDs)[140], CdSe[141], CdS/CdSe[142], C_3N_4[143], Sn_3O_4[144], RuO_2[145], Bi_2MoO_6[146], Copper(II) phthalocyanine[147], ZnO[148], $ZnIn_2S_4$[149] have also been explored in the development of type-II HSs with TiO_2 nanostructure.

Based on the TiO_2 nanostructure, different metal and semiconductor decorated core-shell HSs have been reported by several groups mainly focusing on the application in photocatalytic hydrogen evolution and dye-sensitized solar cells (DSSCs). Liu et al.[77] showed a new facile method consisting of electrospray and hydrothermal treatment to grow mesoporous core-shell TiO_2 microspheres composed of tiny anatase TiO_2 nanocrystals and dominated by high-energy facets. The superior photocatalytic activity of the various core-shell HSs Au@TiO_2[150], TiO_2(B)/anatase[133] and TiO_2@MoS_2[135] has also been investigated.

1.5. Application of TiO_2 Nanostructure and Its Heterostructures

A solid TiO_2 powder is generally used as one of the most excellent white pigments in sunscreen, paints, toothpaste, ointments, food coloring etc. due to its several advantageous properties, e.g.

non-toxicity, biocompatibility, UV-absorbing property, low cost and whiteness. Among the other metal oxide semiconductors, TiO_2 with its suitable HSs is being studied extensively as an efficient photocatalyst, photoelectrocatalyst, and energy storage materials, owing to its unique stability against photo/chemical corrosion, high oxidizing and reducing ability. In the past few decades, various strategies including the HS formation with TiO_2 have been explored in order to improve its performance index for various potential applications, such as photocatalysis in environmental cleaning[131, 132, 151], photo-/electro-catalysis in H_2 generation[120, 135, 136, 150], lithium ion batteries[4, 152-157], sensors[3, 158-160], dye-sensitized solar cell[161-166], photodetection[163, 167-170], self-cleaning and antifogging[171, 172]. Some of the potential applications of TiO_2 based HSs are elaborated below:

1.5.1. Photocatalysis: Hydrogen Production and Environmental Remediation

With the fast technological advancement, the energy crisis is increasing as well as the huge amount of wastewater and heavily toxic gases from the various factories are destroying the biodiversity and introducing non-curable diseases in the human life. Solar light-driven photocatalysis is regarded as one of the most promising solutions to the energy and environment problems. Among the various semiconductor photocatalysts, TiO_2 nanostructures have proved their extremely high potential as a photocatalyst towards the commercialization. TiO_2 shows appreciably good photocatalytic activity irrespective of the nature of the medium of catalytic reaction: in aqueous pollutants, air pollutants or the CO_2 reduction from the hydrocarbon fuels. Photocatalysis mainly utilizes the oxidation (OH^-, H_2O, hydrocarbons, etc.) and reduction (O_2, H^+, etc.) reaction by the photogenerated electron-hole pairs in a semiconductor in order to produce O_2/H_2 gas as well as decompose the pollutants from water/air, as shown in **Fig. 1.8(a)**.[173] With the exposure of light in a semiconductor (energy>band gap), the photogenerated excitons need to migrate to the surface/interface to initiate redox reactions. In a homogeneous semiconductor (TiO_2), the migration process is random and thus the excited electrons and holes have plenty of chances to recombine, causing low photocatalytic efficiency, while in a suitable HS the migration can be channelized resulting in the superior visible light photocatalytic activity (see **Fig. 1.8(b)**). Additionally, the bare TiO_2 nanostructure is active only under the UV irradiation (wide band gap: ~3.2 eV) leading to the low photocatalytic efficiency under solar light.[173]

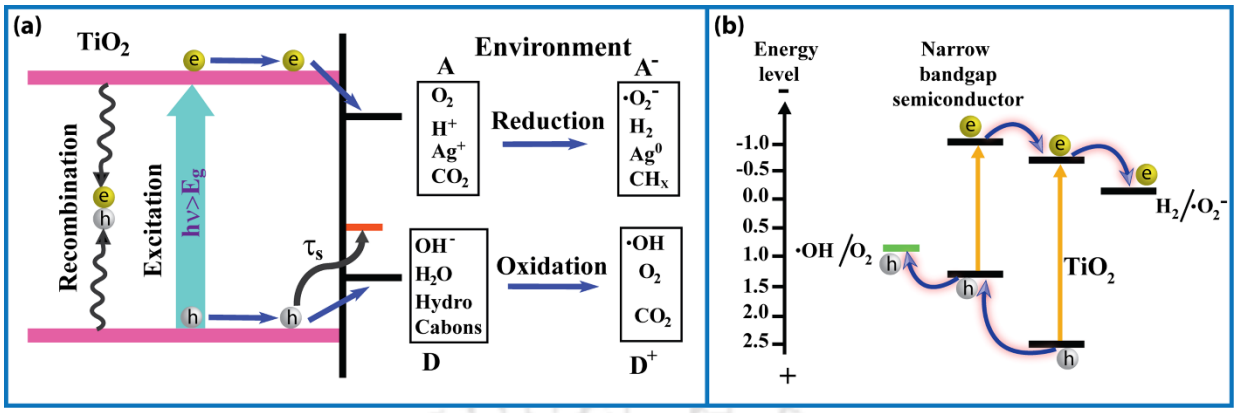

Fig. 1.8. (a) Schematic representation of photocatalysis at a TiO_2 nanostructure/aqueous medium interface. Acceptors (A) are reduced, and donors (D) are oxidized by the photogenerated electrons and holes, respectively. Bare TiO_2 possesses high recombination probability leading to the low catalytic efficiency. (b) Semiconductor heterojunction for open-circuit photocatalytic H_2 evolution in an aqueous solution. Adopted from Ref. [174]

Though the shape tailored TiO_2 architectures having high specific surface area, exposed high energy facets and low axial resistivity have shown better results in degradation as well as hydrogen evolution, it is still necessary to modify the electronic arrangement in the nanostructure by incorporating several techniques to make it efficient up to the industrial scale. Several modification strategies have been explored, such as: (i) doping with metal and non-metal elements, (ii) loading noble metal NPs to drive surface plasmon resonance and create hot electrons and (iii) fabrication of staggered type (type-II) HSs with another semiconductor for synergic absorption and efficient interfacial charge separation to achieve higher solar light-driven photocatalytic activity. **Fig. 1.9** shows the valence band and conduction band positions of commonly used photocatalysts indicating the suitability of HS formation to further improve the performance. Introduction of doping element causes narrowing of the effective band gap of the TiO_2, which facilitates the visible light sensitization and thus, dramatically enhanced photocatalytic activity under visible light irradiation.[106-112] These results mainly demonstrate the incorporation of additional energy band, enhanced visible light absorption, lower recombination rates, making the TiO_2 nanostructures suitable to be commercially used. A properly designed TiO_2 HS with noble metal NPs may drive the localized surface plasmon resonance (LSPR) excitation following the light absorption and eventually, the plasmons may decay non-radiatively in a femtosecond time scale, generating hot electrons in the conduction band of TiO_2. After the migration of these electrons from the plasmonic material to the TiO_2 in contact forms a metal-semiconductor Schottky junction which may accelerate the rate of photocatalysis.[125, 126]

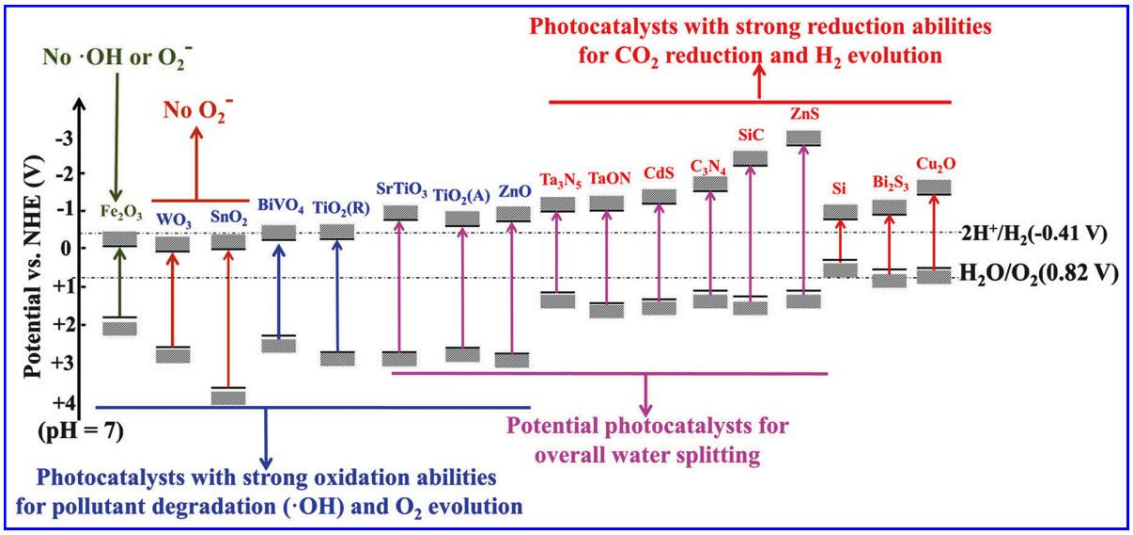

Fig. 1.9. Band edge position of several frequently used semiconductors and the potential applications in typical photocatalysis, using the normal hydrogen electrode (NHE) as a reference. Adopted from Ref. [175]

Wu et al.[176] recently developed a unique strategy for the bottom-up synthesis of AuNR/TiO_2 nanodumbbell like structures with spatially separated Au and TiO_2 regions. The as-prepared Au NRs are exposed on their sidewall which acts as the optical window for the incident light as well as it offers a fast lane transfer of the photogenerated hot electrons to the TiO_2 side, making the AuNR/TiO_2 HSs highly efficient for the H_2 generation under visible/NIR light. Shen and co-workers[177] developed a new magnetically separable plasmonic 3D sandwich-structured $Fe_3O_4/SiO_2/Au/TiO_2$ photocatalyst, which shows easy magnetic separability, higher absorption in the visible region and enhanced photocatalytic activity under the illumination of simulated sunlight. Additionally, a variety of TiO_2 based type-II HSs have been developed (discussed in **Section 1.3**) and extensively studied for the superior visible light photocatalysis.[132-138] A summary of the reported visible light photocatalytic/photoelectrocatalytic H_2 generation by various catalysts are presented in **Table 1.2**. However, choosing a suitable HS (noble metal free) with high performance stability is still challenging. A satisfactory broad light absorbing material (up to infrared region) for efficient photocatalysis still needs to be investigated. Multifunctional heterostructured material for various real life applications is not explored yet.

1.5.2. Photoelectrocatalysis: Hydrogen Production and Environmental Remediation

Electrolysis is a well-known technique for the production of high purity H_2 at the cathode and O_2 at the anode, by directly applying current to an aqueous solution. Limited ion mobility, diffusion of bubbles and entropy may be responsible for the high overpotential. Thus, in order to reduce the overpotential and improve the performance, many strategies have been explored including the UV light exposure to the working electrode and use noble metal Pt/Pd co-catalyst. However, negligible visible light response and the scarcity of noble-metal co-catalysts are still the main challenges for its practical use. Following the groundbreaking work of Fujishima and Honda on the photoelectrochemical reaction[15], tremendous efforts have been made to develop suitable heterojunction of TiO_2 with another semiconductor/metal NPs, leading to the visible light sensitization and thus the improved H_2 evolution. **Fig. 1.10** shows a schematic representation of the photoelectrocatalytic H_2 evolution and the possible charge separation in a type-II semiconductor HS. Therefore, H_2 is directly generated from the solar energy. In a typical process, semiconductor HS generates electron-hole pairs after absorbing the solar light. Afterwards, the applied potential facilitates the movement of the electrons in the conduction band towards the cathode via the external circuit and react with water to form H_2. The evolution of H_2 involves the following chemical reaction:

$$TiO_2 \xrightarrow{h\nu} e^- + h^+ \qquad (1.1)$$

At the anode (TiO_2 electrode)

$$2H_2O + 4h^+ \longrightarrow O_2 + 4H^+ \qquad (1.2)$$

At the cathode (Pt electrode)

$$2H^+ + 2e^- \longrightarrow H_2 \qquad (1.3)$$

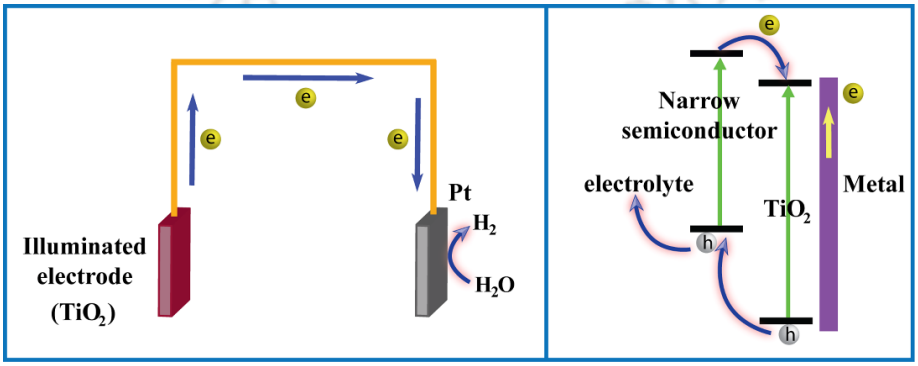

Fig. 1.10. Schematic illustration of type-II heterojunction for photoelectrochemical H_2 evolution with the working electrode (semiconductor HS) as a photoanode and Pt as a cathode at an applied bias.

Various types of heterojunctions integrated with TiO_2 nanostructures have been reported for the advancement in HER activity, such as MoS_2@TiO_2[178], TiO_2/Pt/MoS_2[179] etc.

In addition to the H_2 generation, photoelectrocatalysis shows higher degradation efficiency of pollutants as compared to the photocatalysis. In this case, a low bias voltage applied to the TiO_2 electrode can transfer the photocarriers through the external circuit inhibiting their fast recombination. Thus, plenty of active species (hydroxyl, superoxide radicals) present on the TiO_2 surface accelerates the catalytic efficiency.[180-182] However, the catalytic performance and the stability of noble metal free co-catalyst are much lower than that of the conventional Pt/Pd co-catalyst. Additionally, proper visible light responsive material needs to be investigated to realize the efficient solar light driven catalysis.

Table 1.2. *Summary of the reported visible light photocatalytic (PC)/photoelectrocatalytic (PEC) performance of TiO_2 nanostructure and TiO_2 based HSs.*

TiO_2 HS components	Visible light intensity	Water splitting H_2 generation efficiency		Ref.
		PC (mmol h^{-1} g^{-1})	PEC (μmol h^{-1} cm^{-2})	
TiO_2 NT	150 W		8.3	[183]
Black TiO_2 NCs	1 Sun power	10.00		[33]
TiO_2 NR/CuO/Cu	300 W	0.85		[184]
Ag/TiO_2 NT	100 mW cm^{-2}	0.54		[185]
Pt/TiO_2 NT	320 mW cm^{-2}		492	[186]
CdS/TiO_2 NT	300 W	20.00		[187]
C_3N_4/N/TiO_2 nanofibers	300 W	8.40		[188]
CuO/TiO_2 NT	-	100.00		[189]
MoS_2/TiO_2 NW	-	16.70		[137]
Au/TiO_2 nanosheets/Pd	100 mW cm^{-2}	3.00		[190]
CdS/TiO_2 microsphere/Ru	-	3.2		[191]
AuNR/TiO_2	-	11.6		[176]
CdSe/TiO_2 core-shell	Air mass 1.5G filter	0.44		[192]
rGO/TiO_2	300 W	14.0		[193]

1.5.3. Photodetector

TiO_2 based photodetector has recently drawn a great deal of research interest due to its diverse applications such as biological research, optical communication, astronomical studies and missile launch detection. TiO_2 nanostructures, especially vertically aligned TiO_2 NT arrays grown by electrochemical anodization have been recognized as highly promising for optoelectronic nano-devices.[194] **Fig. 1.11(a)** shows a schematic representation of a front-illuminated TiO_2 photodetector, transferred on a transparent FTO (fluorine-doped tin oxide) glass, showing excellent spectral responsivity (~176 A/W) at 350 nm. Under dark condition, oxygen molecules are adsorbed on the NT surface by trapping the surface electrons from the n-type TiO_2, leading to a formation of the depletion region and thus lower photoconductivity. Under UV illumination, the photogenerated holes discharge the adsorbed oxygen ion and limit the recombination, leading to enhanced photoconductivity (see **Fig. 1.11(b)**).[167, 195] Being a wide bandgap material, the TiO_2 photodetector shows high sensitivity only in the UV region, and the photoresponse is quite slow due to various surface defects and trap centers. Several approaches have been reported to broaden the spectral responsivity up to the visible region by forming a heterojunction with silicon[169, 170], composite with polymer[168], N_2 ion implantation[196], etc. However, the spectral responsivity in the visible region is usually low.

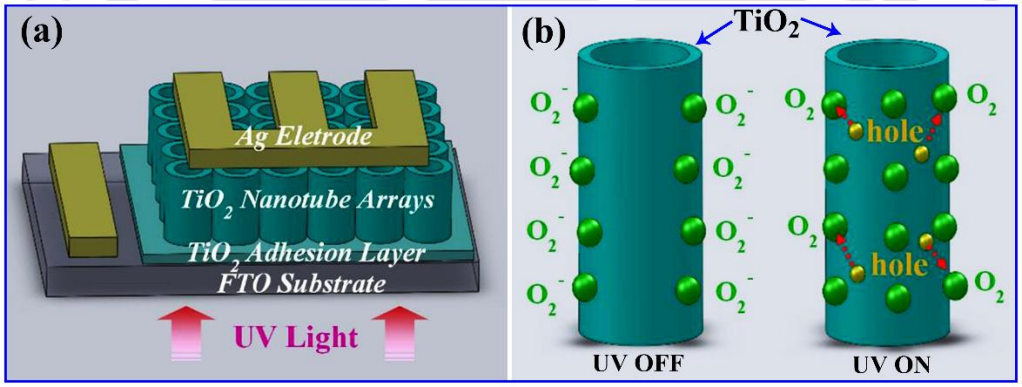

Fig. 1.11. Schematic representation of (a) a front-illuminated TiO_2 NT photodetector configuration, (b) adsorption and desorption of oxygen molecules on the surface of the TiO_2 NT under dark and UV light illumination, respectively. Adopted from Ref. [194]

1.5.4. Sensor: Gas Sensor and Biosensor

A TiO_2 based gas sensor can detect the presence of various gases even at the very low concentration, depending on the change in electrical conductivity of the sensor exposed to a gas environment. Both the oxidative gas (O_2, NO_2) as well as the reductive gas (H_2, CO, NH_3, H_2S)

can be detected by the TiO_2 based gas sensor monitoring the decrease and increase in the conductivity, respectively. The two main steps of the sensing mechanism are as follows: first, physisorption of gas molecules on TiO_2 surface by the van der Waals interaction and the dipole interaction, followed by chemisorption through the strong chemical bond between the gas molecule and the surface atoms of TiO_2; second, exchange interaction of the electrons between the TiO_2 based sensing material and the gas molecules, leading to its transformation into the outer signals. Oxygen vacancy on the TiO_2 surface plays a major role in both the above-mentioned processes. In an ambient atmosphere, the surface vacancies in TiO_2 form anionic oxygen, resulting in the reduction in the n-type doping density, which eventually forms a depletion region and band bending near the surface. After the adsorption on TiO_2 surface, the reducing gas (H_2, CO, NH_3 and H_2S) may inject the electrons into the TiO_2 surface, reducing the depletion region and band bending, which results in the improved conductivity (see **Fig. 1.11**, **Section 1.3.3**). On the contrary, oxidative gas after the adsorption on the TiO_2 surface extracts electrons from the anionic oxygen, increasing the depletion region, which results in the lower conductivity.[3] Typical response curves in CO sensing by various TiO_2 films are shown in **Fig. 1.12(a)**.

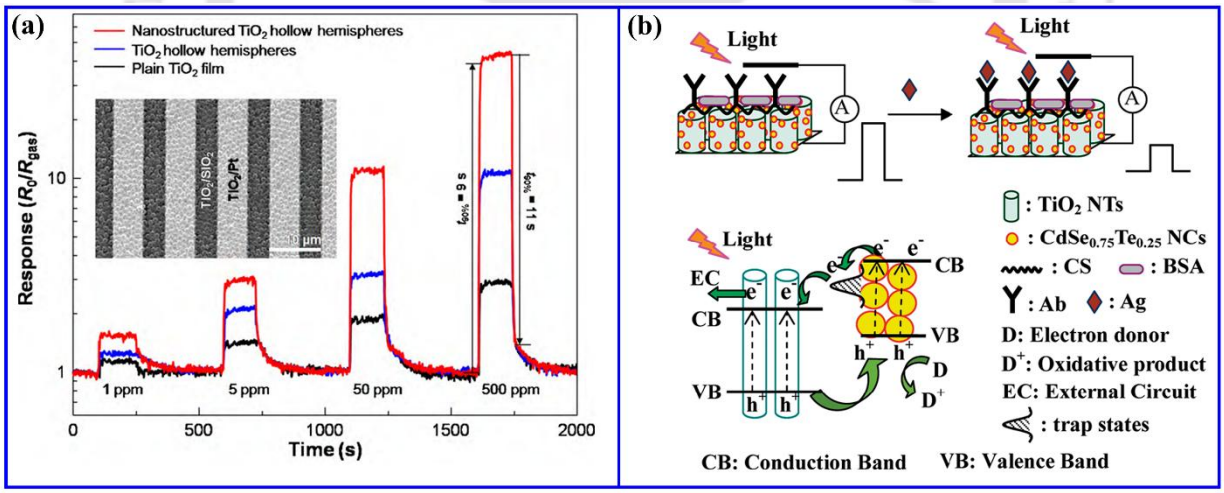

Fig. 1.12. (a) Typical response curves of gas (CO) sensor with plain TiO_2 film, TiO_2 hollow hemispheres, and nanostructured TiO_2 hollow hemispheres. CO gas concentration is varied in the range 1−500 ppm at 250 °C. The inset shows an SEM image of TiO_2 film on a Pt interdigitated electrodes. Adopted from Ref. [197]. (b) Scheme illustration of the immunosensor and the charge transport in $CdSe_{0.75}Te_{0.25}/TiO_2$ electrodes. Adopted from Ref. [198].

TiO_2 based nanostructure having low cost, high stability, and biocompatibility has also been extensively investigated as a biosensor, which is based on the conversion of biological response into a quantified electrical/optical signal detected by several conventional techniques. A

biosensor can be utilized to analyze a variety of biomaterials such as body fluids, cell cultures and food samples. Depending on the sensing mechanism, a biosensor can be categorized as (i) amperometric (current), (ii) potentiometric (voltage) and (iii) optical biosensor (SPR and fluorescence-based).[3] Prior to the sensing measurement, surface of the TiO_2 based sensor is usually modified with enzyme, antibody, antigen, hemoglobin, and bacteria. With the variation of the conductive properties of the medium between the electrodes, electrochemical reaction generates measurable current and potential in the amperometric and potentiometric biosensors, respectively. Additionally, an optical biosensor based on the SPR, electrochemiluminescence and fluorescence is also feasible to analyze the bio-samples with ultrahigh sensitivity, fast response time, higher selectivity and better stability. The biomolecules first bind with the target, which modifies the optical properties of the electrode surface, leading to a change in the optical signal proportionately with the target concentration.[3] In order to avoid severe damage to the biomolecules caused by the UV light (<400 nm), TiO_2 biosensor can be sensitized up to the visible light by integrating with some narrow bandgap material $CdSe_xTe_{1-x}$, as reported by Kang et al.[198]. They have demonstrated a trap state mediated advantageous electron injection and hole recovery system illustrated in **Fig. 1.12(b)**, resulting in the high photocurrent at $CdSe_{0.75}Te_{0.25}/TiO_2$ electrode and ultrahigh detection limit up to pM (picomolar). However, the stability and reusability of the TiO_2 based sensors are of major concern.

1.5.5. Dye-Sensitized Solar Cells

Fast exhaustion of the limited fossil fuel reservoir and the inevitable pollution encouraged the scientific community to investigate the environment-friendly renewable energy sources. Solar cell offers one of the most satisfactory solutions to realize the ever-rising global energy demand. Besides the solid state junction solar cell, DSSC has also been recognized as a promising approach, explored extensively to achieve higher efficiency with low production cost. Typically, a DSSC is constructed on FTO substrate with a TiO_2 film coated by a monolayer dye molecules (D149), redox electrolyte (I^-/I^{3-}), and counter electrode (Pt/FTO glass), as shown in **Fig. 1.13(a)**.[199] Highly ordered one-dimensional TiO_2 nanostructure-based DSSC was found to be more efficient than the TiO_2 NPs because of the larger electron diffusion length and lower recombination probability. Many approaches have been explored to increase the overall conversion efficiency such as tuning the TiO_2 morphology, back/front illumination, and choosing the appropriate dye.[200, 201] The working principle of a DSSC including the sensitization of TiO_2

by solar light and easy transport to the external circuit are shown schematically in **Fig. 1.13(b)**. Lin et al. have demonstrated the higher conversion efficiency of a DSSC with a hierarchical rutile TiO_2 nanostructure (~8.6%) than the commercial anatase TiO_2 (Dyesol-S) (7.6%), as shown in **Fig. 1.13(c)**.[199] However, long term stability is one of the important issues in this technology.

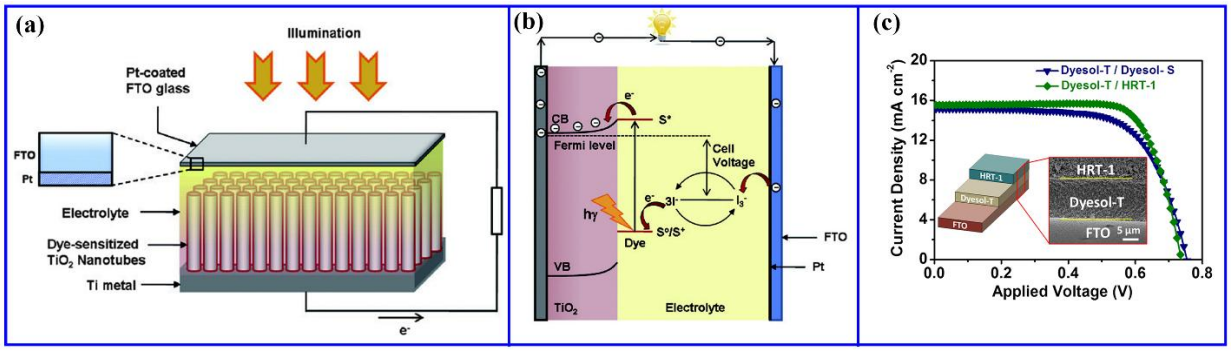

Fig. 1.13. (a) Schematic illustration of a typical DSSC using TiO_2 NTs grown on Ti substrate. (b) Schematic representation of the working principle of a typical DSSC. Adopted from Ref. [202] (c) Comparison of the photovoltaic performance of the hierarchical rutile TiO_2 architectures (HRT) and commercial anatase titania (Dyesol-S) as a light scattering layer. Adopted from Ref. [199]

1.6. Challenges in Fabrication and Applications of TiO_2 Based Heterostructures

In the last few decades, TiO_2 nanostructures and TiO_2 based various HSs have been extensively explored for diverse range of applications, and few of these have reached up to the commercial production. Still, there are many unresolved issues and challenges, that need to be addressed and there are plenty of room for further improvement in order to fulfil the future demands. After the successful synthesis of 1D TiO_2 NT[45], extensive research has been carried out especially by the hydrothermal/solvothermal method to manipulate the shape, surface morphology and electronic structure of TiO_2. The above approach including the formation of suitable heterojunction has broadened the absorption window of TiO_2 up to the visible-infrared region as well as suppressed the charge recombination probability, leading to the superior visible light photocatalysis, photoelectrocatalysis and solar cell applications. However, the growth of TiO_2 nanostructures with controlled dimensionalities (size, shape, layer number, etc.), pores distribution and intrinsic defects/doping remains a challenge for exploiting their wide spread applications. The solar light harvesting capability and the charge extraction efficiency of a TiO_2 based HS can be improved further to make it commercially viable. Though visible light induced photocatalysis has been widely studied, the insight of the mechanism and the rate kinetics of photocatalytic degradation

are still not fully understood. Furthermore, photocatalytic or photoelectrocatalytic H_2 evolution is still determined by the amount of noble metal co-catalysts (Pt/Pd) integrated with the TiO_2 nanostructure. Thus, search for a noble metal-free alternative co-catalyst or minimization of the noble metal co-catalyst loading without compromising the performance are challenging. TiO_2 is a nontoxic, biocompatible and inexpensive material which may be suitable for the biomarker, but the manipulation of its electronic structure (indirect bandgap) to make it fluorescent is really challenging. Additionally, fabrication of single layer transition metal dichalcogenide (MoS_2, WS_2, $MoSe_2$, etc.) on the TiO_2 interface directly by a physical technique (chemical vapor deposition) is very challenging, and this heterojunction is highly promising for the energy and optoelectronic applications. A huge possibility of exploiting TiO_2 based HSs for visible light photocatalysis, photoelectrocatalysis, light emission and photodetection applications still remains open to us.

1.7. Focus of the Present Thesis

Despite the significant advancement, there are still several challenges on the fabrication of well-controlled shape tailored TiO_2 nanostructures and various suitable heterojunctions for their applications in the diverse area of nanotechnology. In the present thesis, we have attempted the growth of various shape tailored TiO_2 nanostructures and their HSs with other semiconductors including 2D materials and noble metals NPs and investigated their photophysical properties. The main objectives of the present thesis are as follows:

- Fabrication of mesoporous TiO_2(B) NRs, NBs via a simple hydrothermal process and their HSs with various semiconductors (Ag_2O, MoS_2, C_3N_4, etc.) and noble metal NPs (Ag, Au, Pt, etc.).
- Study the morphology and photophysical properties of the metastable TiO_2(B) based various HSs, and investigation on the stability upon photocatalytic and photoelectrocatalytic reactions.
- Investigation of the photodegradation kinetics of commonly used dyes using a sequential decay model, for the first time.
- Investigation on the trap state mediated hot electron injection from Ag/Au NP to TiO_2(B) by the photoresponse study with monochromatic photoexcitation.

- Growth of few-layer MoS_2 on mesoporous TiO_2(B) NBs and selective decoration of marginal amount of Pt NPs on the edge/defect sites of the MoS_2 layer and porous sites of TiO_2(B).
- Investigation on the synergic role of MoS_2 and Pt co-catalysts together over the conventional Pt co-catalyst in photoelectrocatalytic H_2 evolution reaction.
- Growth of 3D TiO_2 NFs with self-grown TiO_2 QDs on its surface by a hydrothermal process and their shape evolution.

  Quantitative analysis of the tunable visible PL and the origin of high PL quantum yield of TiO_2 QDs/F-TiO_2 NFs on the basis of surface defects, quantum confinement and doping.
- Fabrication of high-quality core-shell heterojunction between single-layer MoS_2 (shell) and 3D TiO_2 NF (core) by in-situ CVD technique. We attempt to understand the growth mechanism of single-layer MoS_2 over a large area on various substrates.
- Investigation on the switching of the trions in MoS_2 into neutral excitons by the formation of MoS_2@TiO_2 p-n heterojunction, and controlled oxygen plasma treatment.
- The application of MoS_2@TiO_2 p-n heterojunction in efficient light emission and broadband fast photodetection.

1.8. Organization of the Thesis

The complete thesis work is presented in eight chapters. This chapter, i.e., **Chapter 1** presents a summary of the various growth strategies including latest developments, key properties and the promising applications of TiO_2 nanostructures and its heterostructures. **Chapter 2** presents a controlled growth of Ag_2O NPs on mesoporous TiO_2(B) NRs, and its ultra-high visible light photocatalysis. **Chapter 3** provides a detailed investigation of the origin of the multi-step sequential photocatalytic degradation of dyes under visible light illumination by Ag NPs decorated TiO_2 NRs. **Chapter 4** discusses about trap state mediated direct hot electron injection from Ag/Au NP to TiO_2(B)-C_3N_4 network in the ternary hybrids Ag-TiO_2(B)-C_3N_4 and Au-TiO_2(B)-C_3N_4 by visible light photocatalysis. In **Chapter 5**, we demonstrate the fabrication of highly efficient ternary heterojunction consisting of few-layer MoS_2 nanoflowers grown on mesoporous TiO_2(B) NB and Pt NPs, selectively decorated on the edge/defect sites of the MoS_2 layer. The superior visible light photoelectrocatalytic hydrogen evolution reaction by the ternary

system is investigated. In **Chapter 6**, self-grown TiO_2 nanocrystals with tunable size on TiO_2 NFs are demonstrated and high photoluminescence quantum yield from the TiO_2 QDs/TiO_2 NFs is investigated. **Chapter 7** presents an in-situ CVD growth of single layer MoS_2@TiO_2 core-shell heterojunction and high PL emission as well as broadband photodetection. **Chapter 8** summarizes the major findings and important conclusions of the present thesis and future directions of work.

References

1. X. Chen and S. S. Mao, *Chem. Rev.*, 2007, **107**, 2891-2959.
2. A. L. Linsebigler, G. Lu and J. T. Yates, *Chem. Rev.*, 1995, **95**, 735-758.
3. J. Bai and B. Zhou, *Chem. Rev.*, 2014, **114**, 10131-10176.
4. T. Song and U. Paik, *J. Mater. Chem. A*, 2016, **4**, 14-31.
5. Y. Zhang, Z. Jiang, J. Huang, L. Y. Lim, W. Li, J. Deng, D. Gong, Y. Tang, Y. Lai and Z. Chen, *RSC Adv.*, 2015, **5**, 79479-79510.
6. M. Altomare, M. V. Dozzi, G. L. Chiarello, A. Di Paola, L. Palmisano and E. Selli, *Catal. Today*, 2015, **252**, 184-189.
7. J. Muscat, V. Swamy and N. M. Harrison, *Phys. Rev. B*, 2002, **65**, 224112.
8. R. Marchand, L. Brohan and M. Tournoux, *Mater. Res. Bull.*, 1980, **15**, 1129-1133.
9. H. Zhang and J. F. Banfield, *J. Phys. Chem. B*, 2000, **104**, 3481-3487.
10. Z. Yang, B. Wang, H. Cui, H. An, Y. Pan and J. Zhai, *J. Phys. Chem. C*, 2015, **119**, 16905-16912.
11. B. Santara, P. K. Giri, K. Imakita and M. Fujii, *Nanoscale*, 2013, **5**, 5476.
12. A. G. Dylla, P. Xiao, G. Henkelman and K. J. Stevenson, *J. Phys. Chem. Lett.*, 2012, **3**, 2015-2019.
13. D. Yang, H. Liu, Z. Zheng, Y. Yuan, J.-c. Zhao, E. R. Waclawik, X. Ke and H. Zhu, *J. Am. Chem. Soc.*, 2009, **131**, 17885-17893.
14. J. Dai, J. Yang, X. Wang, L. Zhang and Y. Li, *Appl. Surf. Sci.*, 2015, **349**, 343-352.
15. A. Fujishima and K. Honda, *Nature*, 1972, **238**, 37-38.
16. G. K. Mor, O. K. Varghese, M. Paulose, K. Shankar and C. A. Grimes, *Sol. Energy Mater. Sol. Cells*, 2006, **90**, 2011-2075.
17. H. Wang and J. P. Lewis, *J. Phys. Condens. Matter*, 2006, **18**, 421.
18. Y.-f. Zhang, W. Lin, Y. Li, K.-n. Ding and J.-q. Li, *J. Phys. Chem. B*, 2005, **109**, 19270-19277.
19. M. B. Yahia, F. Lemoigno, T. Beuvier, J.-S. Filhol, M. Richard-Plouet, L. Brohan and M.-L. Doublet, *J. Chem. Phys.*, 2009, **130**, 204501.
20. L. Kavan, M. Grätzel, S. E. Gilbert, C. Klemenz and H. J. Scheel, *J. Am. Chem. Soc.*, 1996, **118**, 6716-6723.
21. H. Tang, K. Prasad, R. Sanjinès, P. E. Schmid and F. Lévy, *J. Appl. Phys.*, 1994, **75**, 2042-2047.
22. A. Di Paola, M. Bellardita and L. Palmisano, *Catalysts*, 2013, **3**, 36.
23. W. Hu, L. Li, G. Li, C. Tang and L. Sun, *Cryst. Growth Des.*, 2009, **9**, 3676-3682.
24. M. Koelsch, S. Cassaignon, J. F. Guillemoles and J. P. Jolivet, *Thin Solid Films*, 2002, **403-404**, 312-319.
25. W. Li, C. Liu, Y. Zhou, Y. Bai, X. Feng, Z. Yang, L. Lu, X. Lu and K.-Y. Chan, *J. Phys. Chem. C*, 2008, **112**, 20539-20545.

26. S. Wendt, P. T. Sprunger, E. Lira, G. K. H. Madsen, Z. Li, J. Ø. Hansen, J. Matthiesen, A. Blekinge-Rasmussen, E. Lægsgaard, B. Hammer and F. Besenbacher, *Science*, 2008, **320**, 1755-1759.
27. B. Santara, P. K. Giri, K. Imakita and M. Fujii, *J. Phys. Chem. C*, 2013, **117**, 23402.
28. M. Nolan, S. D. Elliott, J. S. Mulley, R. A. Bennett, M. Basham and P. Mulheran, *Phys. Rev. B*, 2008, **77**, 235424.
29. V. E. Henrich, G. Dresselhaus and H. J. Zeiger, *Phys. Rev. Lett.*, 1976, **36**, 1335-1339.
30. H.-Y. Lee, S. J. Clark and J. Robertson, *Phys. Rev. B*, 2012, **86**, 075209.
31. E. Finazzi, C. D. Valentin, G. Pacchioni and A. Selloni, *J. Chem. Phys.*, 2008, **129**, 154113.
32. X. Chen, L. Liu and F. Huang, *Chem. Soc. Rev*, 2015, **44**, 1861-1885.
33. X. Chen, L. Liu, P. Y. Yu and S. S. Mao, *Science*, 2011, **331**, 746-750.
34. J. Joo, S. G. Kwon, T. Yu, M. Cho, J. Lee, J. Yoon and T. Hyeon, *J. Phys. Chem. B*, 2005, **109**, 15297-15302.
35. D.-S. Lee and T.-K. Liu, *J. Sol-Gel Sci. Technol.*, 2002, **25**, 121-136.
36. Y. Zhu, L. Zhang, C. Gao and L. Cao, *J. Mater. Sci.*, 2000, **35**, 4049-4054.
37. C. Su, B. Y. Hong and C. M. Tseng, *Catal. Today*, 2004, **96**, 119-126.
38. M. S. Sander, M. J. Côté, W. Gu, B. M. Kile and C. P. Tripp, *Adv. Mater.*, 2004, **16**, 2052-2057.
39. A. S. Attar, M. S. Ghamsari, F. Hajiesmaeilbaigi, S. Mirdamadi, K. Katagiri and K. Koumoto, *Mater. Chem. Phys.*, 2009, **113**, 856-860.
40. Q. Jijun, Y. Weidong, G. Xiangdong and L. Xiaomin, *Nanotechnology*, 2006, **17**, 4695.
41. Y. Lin, G. S. Wu, X. Y. Yuan, T. Xie and L. D. Zhang, *J. Phys. Condens. Matter*, 2003, **15**, 2917.
42. M. Lahav and L. Leiserowitz, *Chem. Eng. Sci.*, 2001, **56**, 2245-2253.
43. M. A. Lovette, A. R. Browning, D. W. Griffin, J. P. Sizemore, R. C. Snyder and M. F. Doherty, *Ind. Eng. Chem. Res.*, 2008, **47**, 9812-9833.
44. W.-J. Ong, L.-L. Tan, S.-P. Chai, S.-T. Yong and A. R. Mohamed, *Nanoscale*, 2014, **6**, 1946-2008.
45. T. Kasuga, M. Hiramatsu, A. Hoson, T. Sekino and K. Niihara, *Langmuir*, 1998, **14**, 3160-3163.
46. T. Kasuga, M. Hiramatsu, A. Hoson, T. Sekino and K. Niihara, *Adv. Mater.*, 1999, **11**, 1307-1311.
47. G. Armstrong, A. R. Armstrong, J. Canales and P. G. Bruce, *Chem. Commun.*, 2005, DOI: 10.1039/B501883H, 2454-2456.
48. D. V. Bavykin, V. N. Parmon, A. A. Lapkin and F. C. Walsh, *J. Mater. Chem.*, 2004, **14**, 3370-3377.
49. Y. Xie, C. Xia, H. Du and W. Wang, *J. Power Sources*, 2015, **286**, 561-570.
50. J.-Y. Liao, B.-X. Lei, H.-Y. Chen, D.-B. Kuang and C.-Y. Su, *Energy Environ. Sci.*, 2012, **5**, 5750-5757.
51. B. Liu and E. S. Aydil, *J. Am. Chem. Soc.*, 2009, **131**, 3985-3990.
52. D. Sarkar and K. K. Chattopadhyay, *ACS Appl. Mater. Interfaces*, 2014, **6**, 10044-10059.
53. M. Li, Y. Jiang, R. Ding, D. Song, H. Yu and Z. Chen, *J. Electron. Mater.*, 2013, **42**, 1290-1296.
54. F. Wang, G. Zhang, Z. Zhao, H. Tan, W. Yu, X. Zhang and Z. Sun, *RSC Adv.*, 2015, **5**, 9861-9864.
55. H. G. Yang, G. Liu, S. Z. Qiao, C. H. Sun, Y. G. Jin, S. C. Smith, J. Zou, H. M. Cheng and G. Q. Lu, *J. Am. Chem. Soc.*, 2009, **131**, 4078-4083.
56. Q. Xiang, J. Yu and M. Jaroniec, *Chem. Commun.*, 2011, **47**, 4532-4534.
57. M. Liu, L. Piao, W. Lu, S. Ju, L. Zhao, C. Zhou, H. Li and W. Wang, *Nanoscale*, 2010, **2**, 1115-1117.
58. J. Yu, J. Fan and K. Lv, *Nanoscale*, 2010, **2**, 2144-2149.
59. W. Wang, H. Zhang, R. Wang, M. Feng and Y. Chen, *Nanoscale*, 2014, **6**, 2390-2396.
60. X. Han, Q. Kuang, M. Jin, Z. Xie and L. Zheng, *J. Am. Chem. Soc.*, 2009, **131**, 3152-3153.
61. B. Yan, P. Zhou, Q. Xu, X. Zhou, D. Xu and J. Zhu, *RSC Adv.*, 2016, **6**, 6133-6137.
62. F. Tian, Y. Zhang, J. Zhang and C. Pan, *J. Phys. Chem. C*, 2012, **116**, 7515-7519.
63. C.-T. Dinh, T.-D. Nguyen, F. Kleitz and T.-O. Do, *ACS Nano*, 2009, **3**, 3737-3743.
64. D. Wu, Z. Gao, F. Xu, J. Chang, S. Gao and K. Jiang, *CrystEngComm*, 2013, **15**, 516-523.
65. S. H. Lim, J. Luo, Z. Zhong, W. Ji and J. Lin, *Inorg. Chem.*, 2005, **44**, 4124-4126.
66. A. Nakahira, T. Kubo and C. Numako, *Inorg. Chem.*, 2010, **49**, 5845-5852.

67. B. Santara and P. K. Giri, *Mater. Chem. Phys.*, 2013, **137**, 928-936.
68. D. L. Morgan, H.-Y. Zhu, R. L. Frost and E. R. Waclawik, *Chem. Mater.*, 2008, **20**, 3800-3802.
69. S.-i. Tanaka, N. Hirose and T. Tanaki, *J. Electrochem. Soc.*, 2005, **152**, C789-C794.
70. X. Peng and A. Chen, *Adv. Func. Mater.*, 2006, **16**, 1355-1362.
71. Y. Fan, C. Ma, B. Liu, H. Chen, L. Dong and Y. Yin, *Mater. Sci. Semicond. Process.*, 2014, **27**, 47-50.
72. Z. Lai, F. Peng, Y. Wang, H. Wang, H. Yu, P. Liu and H. Zhao, *J. Mater. Chem.*, 2012, **22**, 23906-23912.
73. G. Li, J. Liu, J. Lan, G. Li, Q. Chen and G. Jiang, *CrystEngComm*, 2014, **16**, 10547-10552.
74. J. S. Chen, Y. L. Tan, C. M. Li, Y. L. Cheah, D. Luan, S. Madhavi, F. Y. C. Boey, L. A. Archer and X. W. Lou, *J. Am. Chem. Soc.*, 2010, **132**, 6124-6130.
75. S. Liu, J. Yu and M. Jaroniec, *J. Am. Chem. Soc.*, 2010, **132**, 11914-11916.
76. J. Yu, Q. Xiang, J. Ran and S. Mann, *CrystEngComm*, 2010, **12**, 872-879.
77. B. Liu, K. Nakata, M. Sakai, H. Saito, T. Ochiai, T. Murakami, K. Takagi and A. Fujishima, *Langmuir*, 2011, **27**, 8500-8508.
78. G. Tian, Y. Chen, W. Zhou, K. Pan, C. Tian, X.-r. Huang and H. Fu, *CrystEngComm*, 2011, **13**, 2994-3000.
79. Q. Jia, W. Que and J. Zhang, *Phys. Status Solidi A*, 2011, **208**, 2313-2316.
80. C. T. Nam, J. L. Falconer, L. M. Duc and W.-D. Yang, *Mater. Res. Bull.*, 2014, **51**, 49-55.
81. P. Wang, Y. Ao, C. Wang, J. Hou and J. Qian, *Mater. Lett.*, 2013, **101**, 41-43.
82. N. T. Q. Hoa and D. N. Huyen, *J. Mater. Sci. - Mater. Electron.*, 2013, **24**, 793-798.
83. Y. Chen, G. Tian, Z. Ren, C. Tian, K. Pan, W. Zhou and H. Fu, *Eur. J. Inorg. Chem.*, 2011, **2011**, 754-760.
84. N. Erdogan, A. Ozturk and J. Park, *Ceram. Int.*, 2016, **42**, 5985-5994.
85. B. Gomathi Thanga Keerthana, T. Solaiyammal, S. Muniyappan and P. Murugakoothan, *Mater. Lett.*, 2018, **220**, 20-23.
86. K. Das, S. K. Panda and S. Chaudhuri, *J. Cryst. Growth*, 2008, **310**, 3792-3799.
87. Q. Wang, Z. Wen and J. Li, *Inorg. Chem.*, 2006, **45**, 6944-6949.
88. C. Z. Wen, Q. H. Hu, Y. N. Guo, X. Q. Gong, S. Z. Qiao and H. G. Yang, *Chem. Commun.*, 2011, **47**, 6138-6140.
89. Z. He, W. Que, J. Chen, X. Yin, Y. He and J. Ren, *ACS Appl. Mater. Interfaces*, 2012, **4**, 6816-6826.
90. S. Yoriya, M. Paulose, O. K. Varghese, G. K. Mor and C. A. Grimes, *J. Phys. Chem. C*, 2007, **111**, 13770-13776.
91. S. P. Albu, A. Ghicov, J. M. Macak, R. Hahn and P. Schmuki, *Nano Lett.*, 2007, **7**, 1286-1289.
92. K. Shankar, J. I. Basham, N. K. Allam, O. K. Varghese, G. K. Mor, X. Feng, M. Paulose, J. A. Seabold, K.-S. Choi and C. A. Grimes, *J. Phys. Chem. C*, 2009, **113**, 6327-6359.
93. J. M. Macak, K. Sirotna and P. Schmuki, *Electrochim. Acta*, 2005, **50**, 3679-3684.
94. R. Hahn, J. M. Macak and P. Schmuki, *Electrochem. Commun.*, 2007, **9**, 947-952.
95. G. Xie, K. Zhang, B. Guo, Q. Liu, L. Fang and J. R. Gong, *Adv. Mater.*, 2013, **25**, 3820-3839.
96. M. Paulose, H. E. Prakasam, O. K. Varghese, L. Peng, K. C. Popat, G. K. Mor, T. A. Desai and C. A. Grimes, *J. Phys. Chem. C*, 2007, **111**, 14992-14997.
97. J. S. Kim, H. S. Han, S. Shin, G. S. Han, H. S. Jung, K. S. Hong and J. H. Noh, *Int. J. Hydrogen Energy*, 2014, **39**, 17473-17480.
98. M. Ye, J. Gong, Y. Lai, C. Lin and Z. Lin, *J. Am. Chem. Soc.*, 2012, **134**, 15720-15723.
99. D. Li and Y. Xia, *Nano Lett.*, 2003, **3**, 555-560.
100. L. Zhu, M. Hong and G. W. Ho, *Nano Energy*, 2015, **11**, 28-37.
101. P. Du, L. Song, J. Xiong, N. Li, Z. Xi, L. Wang, D. Jin, S. Guo and Y. Yuan, *Electrochim. Acta*, 2012, **78**, 392-397.
102. Y. Yang, H. Wang, Q. Zhou, M. Kong, H. Ye and G. Yang, *Nanoscale*, 2013, **5**, 10267-10274.

103. J.-J. Wu and C.-C. Yu, *J. Phys. Chem. B*, 2004, **108**, 3377-3379.
104. W.-J. Lee and Y.-M. Sung, *Cryst. Growth Des.*, 2012, **12**, 5792-5795.
105. J.-M. Wu, H. C. Shih and W.-T. Wu, *Chem. Phys. Lett.*, 2005, **413**, 490-494.
106. R. Asahi, T. Morikawa, T. Ohwaki, K. Aoki and Y. Taga, *Science*, 2001, **293**, 269.
107. X. Hou, C.-W. Wang, W.-D. Zhu, X.-Q. Wang, Y. Li, J. Wang, J.-B. Chen, T. Gan, H.-Y. Hu and F. Zhou, *Solid State Sci.*, 2014, **29**, 27-33.
108. F. Wang and D. Li, *Mater. Lett.*, 2015, **158**, 119-122.
109. S. W. Shin, J. Y. Lee, K.-S. Ahn, S. H. Kang and J. H. Kim, *J. Phys. Chem. C*, 2015, **119**, 13375-13383.
110. Y. Komai, K. Okitsu, R. Nishimura, N. Ohtsu, G. Miyamoto, T. Furuhara, S. Semboshi, Y. Mizukoshi and N. Masahashi, *Catal. Today*, 2011, **164**, 399-403.
111. Z. Hua, Z. Dai, X. Bai, Z. Ye, H. Gu and X. Huang, *J. Hazard. Mater.*, 2015, **293**, 112-121.
112. R. Ramanathan and V. Bansal, *RSC Adv.*, 2015, **5**, 1424-1429.
113. Q. Xiang, J. Yu and M. Jaroniec, *Phys. Chem. Chem. Phys.*, 2011, **13**, 4853-4861.
114. J. Yu, Q. Xiang and M. Zhou, *Appl. Catal. B Environ.*, 2009, **90**, 595-602.
115. J.-N. Nian, S.-A. Chen, C.-C. Tsai and H. Teng, *J. Phys. Chem. B*, 2006, **110**, 25817-25824.
116. S. N. R. Inturi, T. Boningari, M. Suidan and P. G. Smirniotis, *Appl. Catal. B Environ.*, 2014, **144**, 333-342.
117. Y. Su, Z. Wu, Y. Wu, J. Yu, L. Sun and C. Lin, *J. Mater. Chem. A*, 2015, **3**, 8537-8544.
118. Y.-C. Pu, G. Wang, K.-D. Chang, Y. Ling, Y.-K. Lin, B. C. Fitzmorris, C.-M. Liu, X. Lu, Y. Tong, J. Z. Zhang, Y.-J. Hsu and Y. Li, *Nano Lett.*, 2013, **13**, 3817-3823.
119. L. Sun, J. Li, C. Wang, S. Li, Y. Lai, H. Chen and C. Lin, *J. Hazard. Mater.*, 2009, **171**, 1045-1050.
120. J. Yu, L. Qi and M. Jaroniec, *J. Phys. Chem. C*, 2010, **114**, 13118-13125.
121. B. Cheng, Y. Le and J. Yu, *J. Hazard. Mater.*, 2010, **177**, 971-977.
122. T. Montini, V. Gombac, L. Sordelli, J. J. Delgado, X. Chen, G. Adami and P. Fornasiero, *ChemCatChem*, 2011, **3**, 574-577.
123. P. Zhang, T. Song, T. Wang and H. Zeng, *RSC Adv.*, 2017, **7**, 17873-17881.
124. MurdochM, G. I. N. Waterhouse, M. A. Nadeem, J. B. Metson, M. A. Keane, R. F. Howe, LlorcaJ and IdrissH, *Nat Chem*, 2011, **3**, 489-492.
125. B. Chen, W. Zhang, X. Zhou, X. Huang, X. Zhao, H. Wang, M. Liu, Y. Lu and S. Yang, *Nano Energy*, 2013, **2**, 906-915.
126. J. Li, T. Zhao, T. Chen, Y. Liu, C. N. Ong and J. Xie, *Nanoscale*, 2015, **7**, 7502-7519.
127. C.-H. Lin, J.-H. Chao, W.-J. Tsai, M.-J. He and T.-J. Chiang, *Phys. Chem. Chem. Phys.*, 2014, **16**, 23743-23753.
128. M. Ghaffari, M. B. Cosar, H. I. Yavuz, M. Ozenbas and A. K. Okyay, *Electrochim. Acta*, 2012, **76**, 446-452.
129. S. H. Nam, H.-S. Shim, Y.-S. Kim, M. A. Dar, J. G. Kim and W. B. Kim, *ACS Appl. Mater. Interfaces*, 2010, **2**, 2046-2052.
130. D. Yang, Y. Sun, Z. Tong, Y. Tian, Y. Li and Z. Jiang, *J. Phys. Chem. C*, 2015, **119**, 5827-5835.
131. X. Xu, Z. Gao, Z. Cui, Y. Liang, Z. Li, S. Zhu, X. Yang and J. Ma, *ACS Appl. Mater. Interfaces*, 2016, **8**, 91-101.
132. D. Sarkar, C. K. Ghosh, S. Mukherjee and K. K. Chattopadhyay, *ACS Appl. Mater. Interfaces*, 2013, **5**, 331.
133. B. Liu, A. Khare and E. S. Aydil, *ACS Appl. Mater. Interfaces*, 2011, **3**, 4444-4450.
134. W. Zhou, H. Liu, J. Wang, D. Liu, G. Du and J. Cui, *ACS Appl. Mater. Interfaces*, 2010, **2**, 2385.
135. W. Zhou, Z. Yin, Y. Du, X. Huang, Z. Zeng, Z. Fan, H. Liu, J. Wang and H. Zhang, *Small*, 2013, **9**, 140-147.
136. H. Li, Y. Wang, G. Chen, Y. Sang, H. Jiang, J. He, X. Li and H. Liu, *Nanoscale*, 2016, **8**, 6101-6109.

137. M. Shen, Z. Yan, L. Yang, P. Du, J. Zhang and B. Xiang, *Chem. Commun.*, 2014, **50**, 15447-15449.
138. C. Wang, C. Shao, X. Zhang and Y. Liu, *Inorg. Chem.*, 2009, **48**, 7261-7268.
139. Z. Shao, W. Zhu, Z. Li, Q. Yang and G. Wang, *J. Phys. Chem. C*, 2012, **116**, 2438-2442.
140. Y. Xie, G. Ali, S. H. Yoo and S. O. Cho, *ACS Appl. Mater. Interfaces*, 2010, **2**, 2910-2914.
141. Y. Liu, L. Zhao, M. Li and L. Guo, *Nanoscale*, 2014, **6**, 7397-7404.
142. H.-S. Rao, W.-Q. Wu, Y. Liu, Y.-F. Xu, B.-X. Chen, H.-Y. Chen, D.-B. Kuang and C.-Y. Su, *Nano Energy*, 2014, **8**, 1-8.
143. Q. Zhang, X. Quan, H. Wang, S. Chen, Y. Su and Z. Li, *Sci. Rep.*, 2017, **7**, 3128.
144. G. Chen, S. Ji, Y. Sang, S. Chang, Y. Wang, P. Hao, J. Claverie, H. Liu and G. Yu, *Nanoscale*, 2015, **7**, 3117-3125.
145. J. Tian, X. Hu, N. Wei, Y. Zhou, X. Xu, H. Cui and H. Liu, *Sol. Energy Mater. Sol. Cells*, 2016, **151**, 7-13.
146. J. Tian, P. Hao, N. Wei, H. Cui and H. Liu, *ACS Catalysis*, 2015, **5**, 4530-4536.
147. M. Zhang, C. Shao, Z. Guo, Z. Zhang, J. Mu, T. Cao and Y. Liu, *ACS Appl. Mater. Interfaces*, 2011, **3**, 369-377.
148. F.-X. Xiao, *ACS Appl. Mater. Interfaces*, 2012, **4**, 7055-7063.
149. Q. Liu, H. Lu, Z. Shi, F. Wu, J. Guo, K. Deng and L. Li, *ACS Appl. Mater. Interfaces*, 2014, **6**, 17200-17207.
150. X.-F. Wu, H.-Y. Song, J.-M. Yoon, Y.-T. Yu and Y.-F. Chen, *Langmuir*, 2009, **25**, 6438-6447.
151. L. Pan, J.-J. Zou, S. Wang, Z.-F. Huang, A. Yu, L. Wang and X. Zhang, *Chem. Commun.*, 2013, **49**, 6593-6595.
152. G. Kim, C. Jo, W. Kim, J. Chun, S. Yoon, J. Lee and W. Choi, *Energy Environ. Sci.*, 2013, **6**, 2932-2938.
153. Y. Wang, M. Wu and W. F. Zhang, *Electrochim. Acta*, 2008, **53**, 7863-7868.
154. M. Søndergaard, Y. Shen, A. Mamakhel, M. Marinaro, M. Wohlfahrt-Mehrens, K. Wonsyld, S. Dahl and B. B. Iversen, *Chem. Mater.*, 2015, **27**, 119-126.
155. H. Wang, D. Ma, X. Huang, Y. Huang and X. Zhang, *Sci. Rep.*, 2012, **2**, 701.
156. W. Li, F. Wang, S. Feng, J. Wang, Z. Sun, B. Li, Y. Li, J. Yang, A. A. Elzatahry, Y. Xia and D. Zhao, *J. Am. Chem. Soc.*, 2013, **135**, 18300-18303.
157. M. Kim, J. Lee, S. Lee, S. Seo, C. Bae and H. Shin, *ChemSusChem*, 2015, **8**, 2363-2371.
158. O. Alev, E. Şennik, N. Kılınç and Z. Z. Öztürk, *Procedia Engineering*, 2015, **120**, 1162-1165.
159. B. Karunagaran, P. Uthirakumar, S. J. Chung, S. Velumani and E. K. Suh, *Mater. Charact.*, 2007, **58**, 680-684.
160. J. Nisar, Z. Topalian, A. De Sarkar, L. Österlund and R. Ahuja, *ACS Appl. Mater. Interfaces*, 2013, **5**, 8516-8522.
161. T. Oku, N. Kakuta, K. Kobayashi, A. Suzuki and K. Kikuchi, *Prog. in Nat. Sci.: Mater. Int.*, 2011, **21**, 122-126.
162. P. Sanjay, K. Deepa, J. Madhavan and S. Senthil, *Mater. Lett.*, 2018, **219**, 158-162.
163. M. Kaur and N. K. Verma, *J. Mater. Sci. Technol.*, 2014, **30**, 328-334.
164. E. Guo and L. Yin, *J. Mater. Chem. A*, 2015, **3**, 13390-13401.
165. R. Tang and L. Yin, *J. Mater. Chem. A*, 2015, **3**, 17417-17425.
166. F. Sauvage, F. Di Fonzo, A. Li Bassi, C. S. Casari, V. Russo, G. Divitini, C. Ducati, C. E. Bottani, P. Comte and M. Graetzel, *Nano Lett.*, 2010, **10**, 2562-2567.
167. H. Xue, X. Kong, Z. Liu, C. Liu, J. Zhou, W. Chen, S. Ruan and Q. Xu, *Appl. Phys. Lett.*, 2007, **90**, 201118.
168. H. Yangang, W. Gang, L. Haiguo, W. Mang and C. Hongzheng, *Nanotechnology*, 2010, **21**, 185708.

169. T. Ji, Q. Liu, R. Zou, Y. Zhang, L. Wang, L. Sang, M. Liao and J. Hu, *J. Mater. Chem. C*, 2017, **5**, 12848-12856.
170. T. Ji, Y. Cao, X. Peng, Y. Zhang, L. Sun, L. Wang, R. Zou, Y. Sivalingam, W. Han and J. Hu, *Appl. Surf. Sci.*, 2018, **449**, 358-362.
171. J.-B. Chemin, S. Bulou, K. Baba, C. Fontaine, T. Sindzingre, N. D. Boscher and P. Choquet, *Sci. Rep.*, 2018, **8**, 9603.
172. M. Faustini, L. Nicole, C. Boissière, P. Innocenzi, C. Sanchez and D. Grosso, *Chem. Mater.*, 2010, **22**, 4406-4413.
173. Z. Xuming, C. Yu Lim, L. Ru-Shi and T. Din Ping, *Rep. Prog. Phys.*, 2013, **76**, 046401.
174. X. Zhou, N. Liu and P. Schmuki, *ACS Catalysis*, 2017, **7**, 3210-3235.
175. X. Li, J. Yu and M. Jaroniec, *Chem. Soc. Rev*, 2016, **45**, 2603-2636.
176. B. Wu, D. Liu, S. Mubeen, T. T. Chuong, M. Moskovits and G. D. Stucky, *J. Am. Chem. Soc.*, 2016, **138**, 1114-1117.
177. J. Shen, Y. Zhu, X. Yang and C. Li, *J. Mater. Chem.*, 2012, **22**, 13341-13347.
178. B. Ma, P.-Y. Guan, Q.-Y. Li, M. Zhang and S.-Q. Zang, *ACS Appl. Mater. Interfaces*, 2016, **8**, 26794-26800.
179. S. Li, T. Pu, J. Wang, X. Fang, Y. Liu, S. Kang and L. Cui, *Int. J. Hydrog. Energy*, 2018, **43**, 16534-16542.
180. S. Singh, V. C. Srivastava and I. D. Mall, *J. Phys. Chem. C*, 2013, **117**, 15229-15240.
181. G. G. Bessegato, J. C. Cardoso and M. V. B. Zanoni, *Catal. Today*, 2015, **240**, 100-106.
182. R. Salazar, M. S. Ureta-Zañartu, C. González-Vargas, C. d. N. Brito and C. A. Martinez-Huitle, *Chemosphere*, 2018, **198**, 21-29.
183. M. Altomare, M. Pozzi, M. Allieta, L. G. Bettini and E. Selli, *Appl. Catal. B Environ.*, 2013, **136-137**, 81-88.
184. H. Hou, M. Shang, F. Gao, L. Wang, Q. Liu, J. Zheng, Z. Yang and W. Yang, *ACS Appl. Mater. Interfaces*, 2016, **8**, 20128-20137.
185. X. Yang, L. Wu, L. Du and X. Li, *Catal. Lett.*, 2015, **145**, 1771-1777.
186. Y. Lai, J. Gong and C. Lin, *Int. J. Hydrogen Energy*, 2012, **37**, 6438-6446.
187. L. Long, J. Li, L. Wu and X. Li, *Mater. Sci. Semicond. Process.*, 2014, **26**, 107-111.
188. C. Han, Y. Wang, Y. Lei, B. Wang, N. Wu, Q. Shi and Q. Li, *Nano Res.*, 2015, **8**, 1199-1209.
189. D. Praveen Kumar, M. V. Shankar, M. Mamatha Kumari, G. Sadanandam, B. Srinivas and V. Durgakumari, *Chem. Commun.*, 2013, **49**, 9443-9445.
190. W. Jiang, S. Bai, L. Wang, X. Wang, L. Yang, Y. Li, D. Liu, X. Wang, Z. Li, J. Jiang and Y. Xiong, *Small*, 2016, **12**, 1640-1648.
191. Y. Huang, J. Chen, W. Zou, L. Zhang, L. Hu, M. He, L. Gu, J. Deng and X. Xing, *Dalton Trans.*, 2016, **45**, 1160-1165.
192. S. Lee, K. Lee, W. D. Kim, S. Lee, D. J. Shin and D. C. Lee, *J. Phys. Chem. C*, 2014, **118**, 23627-23634.
193. D. Chen, L. Zou, S. Li and F. Zheng, *Sci. Rep.*, 2016, **6**, 20335.
194. L. Wang, W. Yang, H. Chong, L. Wang, F. Gao, L. Tian and Z. Yang, *RSC Adv.*, 2015, **5**, 52388-52394.
195. J. Zou, Q. Zhang, K. Huang and N. Marzari, *J. Phys. Chem. C*, 2010, **114**, 10725-10729.
196. W. Pengcheng, S. Xianyin, S. Shuyao, K. Zunjian, C. Li, L. Wenqing, X. Xiangheng and J. Changzhong, *Nanotechnology*, 2018, **29**, 184005.
197. H. G. Moon, Y.-S. Shim, H. W. Jang, J.-S. Kim, K. J. Choi, C.-Y. Kang, J.-W. Choi, H.-H. Park and S.-J. Yoon, *Sens. Actuator B-Chem.*, 2010, **149**, 116-121.
198. Q. Kang, L. Yang, Y. Chen, S. Luo, L. Wen, Q. Cai and S. Yao, *Anal. Chem.*, 2010, **82**, 9749-9754.
199. J. Lin, Y.-U. Heo, A. Nattestad, Z. Sun, L. Wang, J. H. Kim and S. X. Dou, *Sci. Rep.*, 2014, **4**, 5769.

200. K. Shankar, G. K. Mor, H. E. Prakasam, O. K. Varghese and C. A. Grimes, *Langmuir*, 2007, **23**, 12445-12449.
201. B.-X. Lei, J.-Y. Liao, R. Zhang, J. Wang, C.-Y. Su and D.-B. Kuang, *J. Phys. Chem. C*, 2010, **114**, 15228-15233.
202. P. Roy, D. Kim, K. Lee, E. Spiecker and P. Schmuki, *Nanoscale*, 2010, **2**, 45-59.

Chapter 2

Mechanism of Strong Visible-Light Photocatalysis by Ag_2O Nanoparticle Decorated Monoclinic $TiO_2(B)$ Porous Nanorods

In this chapter, controlled growth of Ag_2O-nanoparticle (NP) decorated monoclinic B-phase TiO_2 ($TiO_2(B)$) nanorods (NRs), and its ultra-high visible-light-photocatalysis are investigated. Uniformly distributed pores on $TiO_2(B)$ NRs surface act as nucleation sites for the growth of Ag_2O NPs resulting in the uniform decoration over the $TiO_2(B)$ surface. Optimization of size and number density of Ag_2O NPs over the porous sites of $TiO_2(B)$, strong coupling and easy interfacial charge transfer during photocatalysis are discussed. Highly stable visible light photodegradation by $Ag_2O/TiO_2(B)$ HSs has been investigated using aqueous methyl orange (anionic dye) and methylene blue (cationic dye) as the model pollutants with one order enhanced efficiency than pristine components. Enhanced visible light absorption, band bending induced efficient charge separation and the Coulombic interaction between the catalyst surface and dye molecules are discussed in details to demonstrate the fast photodegradation. Our results provide valuable insights into the controlled growth of TiO_2 based hybrid photocatalysts for its cutting-edge application in hydrogen production and environmental cleaning.

2.1. Introduction

Metal oxide semiconductors are being studied extensively in photocatalysis due to their potential applications in clean hydrogen energy production and environmental protection, including wastewater treatment, water splitting, CO_2 reduction, air purification, etc.[1] Among these, TiO_2 is one of the most suitable and promising semiconductor photocatalysts because of its high chemical stability, low cost, non-toxicity, high oxidizing power and good degradation efficiency.[2] However, regardless of various phases, band gap of TiO_2 falls in the UV region (wavelength < 400 nm), limiting its industrial applications, which requires maximum utilization of the visible and near-infrared (NIR) region of the solar spectrum. Additionally, in a homogeneous semiconductor recombination of the photogenerated electron-hole pairs simply by liberating heat (nonradiative transition) or light (radiative transition) is highly probable, which prevents their migration to the surface of the semiconductor causing low photocatalytic

efficiency.[3] Several strategies have been adopted to enhance the charge separation and the light absorption in TiO_2 in the visible region, including the heterostructure (HS) formation, metallization[4, 5], sensitization[6], impurity doping[7], defect engineering[8] etc. Nano-sized catalyst particles are usually hard to recover from a large volume of photocatalysis chamber as the NPs (e.g., P25) make a highly stable suspension in water.[9] TiO_2 photocatalyst with larger size (~ a few μm) usually segregate and can be used successfully for the multiple cycles. In spite of having stability issue, TiO_2(B) phase offers a comparatively open structure than that of the other polymorphs of TiO_2. The volume of a TiO_2 unit in TiO_2(B) is 35.27 $Å^3$, while that for rutile, brookite and anatase phases are 31.12 $Å^3$, 32.20 $Å^3$ and 34.02 $Å^3$, respectively. The porous structure of TiO_2(B) may be an ideal platform for the uniform decoration of Ag_2O NPs and thus the superior photocatalysis can be achieved under visible light illumination. Herein, a solvothermal method is considered for the synthesis of porous TiO_2(B) NRs and co-precipitation method for the surface decoration with Ag_2O NPs and its use in the efficient visible light photodegradation of methyl orange (MO) and methylene blue (MB) is investigated.

2.2. Experimental Details

2.2.1. Sample Preparation

2.2.1.1. Synthesis of TiO_2(B) NRs

In a typical synthesis, 1 g of precursor anatase TiO_2 powder (Merck, average particle size ~ 80 nm) was mixed with 48 ml of 10 M NaOH mixed solvent (DI water : Ethylene glycol = 1 : 1) under stirring for 1 h, followed by a solvothermal treatment in 100 ml Teflon-lined autoclave (Berghof, BR-100). The temperature inside the autoclave chamber was measured and maintained at 180 ºC under autogenous pressure and constant magnetic stirring at 500 rpm for 16h. The formed precipitates were washed thoroughly with DI water and obtained by centrifugation followed by a drying process at 80 °C. The obtained sodium titanate NRs were treated ultrasonically with 0.1 N HCl till the pH reduces to ~7, which allowed the complete exchange of Na^+ ion to H^+ ion. Afterwards, the precipitates were washed several times with DI water to obtain H-titanate NRs. Subsequently, the H-titanate NRs were calcined at 500 °C for 5 h using a high-temperature split type furnace (Indfurr, India). During the calcination process, the sample was dehydrated, and organic impurities were eliminated. The product obtained after calcination was pure TiO_2(B), as confirmed by XRD and micro-Raman analyses.

2.2.1.2. Growth of $Ag_2O/TiO_2(B)$ NRs Heterostructures

$Ag_2O/TiO_2(B)$ HSs with various weight ratios ranging from 1:3 to 3:1 were synthesized by a precipitation method. Typically for 1:1 weight ratio, 0.1 g of as-prepared $TiO_2(B)$ powder was dispersed in 50 ml of DI water under ultrasonic vibration, and then 0.145 g of $AgNO_3$ was dissolved into the above-suspended solution. The above mixture was then stirred magnetically for 30 min to reach adsorption equilibrium. Next, 50 ml of 0.2 M aqueous NaOH solution was added to the above mixture dropwise. The amount of NaOH was enough to form the precipitation of Ag_2O NPs from the $AgNO_3$. During this process, the Ag_2O NPs were coated on the $TiO_2(B)$ NRs, and final pH of the solution was measured to be 14. The $Ag_2O/TiO_2(B)$ HS was obtained by washing the precipitation with DI water for several times, filtration and drying process. Pure Ag_2O NPs were also synthesized as blank material for comparison. In this case, 0.85 g of $AgNO_3$ was dissolved in 50 ml of DI water and 50 ml of 0.05 M aqueous NaOH solution was dropped into the above solution. A summary of the samples studied with sample codes is provided in **Table 2.1**.

Table 2.1: *Sample specifications, optical absorption range and effective band gap of different HS samples.*

HS sample specifications		***Sample code***	***Absorption region***	***Effective band gap (eV)***
Weight ratio of				
TiO_2	**Ag_2O**			
1	0	$TiO_2(B)$	UV	2.80
2	1	TA1	UV-Vis-NIR	2.20
1	1	TA2	UV-Vis-NIR	1.68
1	2	TA3	UV-Vis-NIR	2.03
0	1	Ag_2O	UV-Vis-NIR	1.34

2.2.2. Visible Light Photocatalytic Measurements

Photocatalytic activity of pristine $TiO_2(B)$ NRs, Ag_2O NPs and various $Ag_2O/TiO_2(B)$ HSs has been evaluated considering the photodegradation of MO and MB as model dyes under visible light irradiation. In a typical experiment, 100 ml aqueous suspension of MO/MB (10 mg/L) and 20 mg of catalyst powders have been placed in a 250 ml beaker. Before visible light irradiation, the mixture of dye solution and photocatalyst were magnetically stirred under dark for 30 min.

This allowed the establishment of adsorption-desorption equilibrium between the interface of the photocatalysts and dye molecules under ambient conditions. A 250 W lamp (Lelesil Innovative Systems, Mumbai, India) having emission in the range 390-800 nm was used as the light source for visible light photocatalysis. The lamp is surrounded by a water-cooled quartz jacket that absorbs the heat generated from the high power lamp. This maintains a constant temperature of the whole environment, and it ensures that the degradation occurred only because of light irradiation instead of heat. At chosen irradiation intervals (10 min), 5 ml of solution was collected and centrifuged to remove the catalyst particles for further study. To estimate the residual concentration of the dye solution, UV-Vis absorbance was measured in a Shimadzu 2450 UV-Vis spectrophotometer.

2.2.3. Characterization Techniques

The crystal structure of the as-grown catalysts has been obtained from X-ray powder diffraction (XRD) pattern (Rigaku RINT 2500 TTRAX-III, Cu kα radiation). Crystallinity and phase composition of the as-synthesized NRs and NPs have been measured by micro-Raman spectroscopy (LabRam HR800, Jobin Yvon). Morphology, size and the elemental compositions of the as-synthesized TiO_2(B) NRs and Ag_2O/TiO_2(B) HSs have been studied by a field emission scanning electron microscope (FESEM) (Sigma, Zeiss) equipped with an energy dispersive X-ray (EDX) spectrometer. The high magnification surface morphologies and structures of the as-grown samples have been studied by a transmission electron microscope (TEM) (JEOL-JEM 2010 operated at 200 kV). Samples for TEM analysis have been prepared on a carbon-coated Cu grid of 400 meshes (Pacific Grid, USA). UV-Vis diffuse reflectance spectroscopy (DRS) measurements of the samples were recorded using a commercial spectrophotometer (PerkinElmer, UV win Lab). X-ray photoelectron spectroscopy (XPS) has been carried out using a PHI X-tool automated photoelectron spectrometer (ULVAC-PHI, Japan) with an Al Kα X-ray beam (1486.6 eV) at a beam current of 20 mA. The shift in the binding energy of various catalysts has been corrected using the C1s spectrum at 284.8 eV as a standard value.[10] The XPS measurement was performed in Kobe University, Japan. The room temperature steady-state photoluminescence (PL) spectra have been recorded by using a 405 nm diode laser excitation with the help of a single grating monochromator (Triax 550) and a cooled CCD detector (Jovin Yvon). Each spectrum was corrected for detector response after background subtraction. Time-resolved photoluminescence (TRPL) spectra have been recorded using a picosecond time-

resolved luminescence spectrometer (Edinburgh Instruments, Model: FSP920). Nitrogen adsorption-desorption isotherms have been conducted by Quantachrome autsorb-iQ MP analyzer at 77 K. Surface area of the catalysts has been determined using multipoint Brunauer–Emmett–Teller (BET) method and average pore size by Barett–Joyner–Halenda (BJH) model. Photocatalytic activity of the synthesized photocatalysts has been studied using a time programmable commercial photochemical reactor (Lelesil Innovative Systems, Mumbai, India), with a visible lamp source.

2.3. Results and Discussion

2.3.1. Morphology and Composition Studies

The growth of 1D porous TiO_2 nanostructures by a solvothermal process and its surface decoration by Ag_2O NPs have been discussed by several groups.[6, 11] It has been recognized that during the growth process, porous like TiO_2 NRs are formed under certain conditions. To understand the morphology and microstructural properties of as-synthesized TiO_2 NRs, Ag_2O NPs and their HS, we have performed FESEM analysis of the samples.

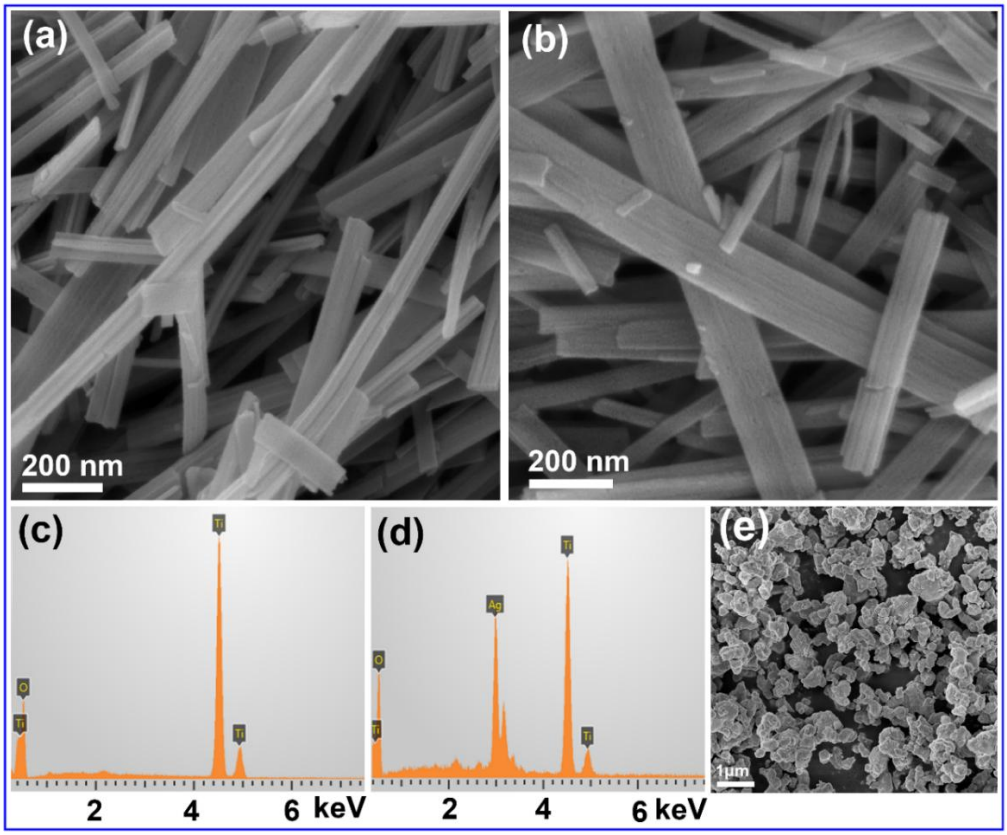

Fig. 2.1. FESEM images of (a) pristine TiO_2(B) NRs and (b) TA2 HS. (c, d) the corresponding EDX spectra. (e) FESEM image of bare Ag_2O NPs.

Fig. 2.1(a) shows the FESEM image of pristine TiO_2 NRs with diameter ~40-180 nm and lengths up to a few micrometres, while **Fig. 2.1(b)** shows the FESEM image of TA2 HS (see **Table 2.1**). Since the size of the as-grown Ag_2O NPs is very small (~5.3 nm for TA2 as revealed from the TEM analysis), even in the presence of the Ag_2O NPs, the surface of the TiO_2 NRs appears to be smooth in the FESEM image due to resolution limit. EDX analysis of as-grown TiO_2 NRs reveals that it is composed of only Ti and O elements with 1:2.24 atomic ratio, as shown in **Fig. 2.1(c)**. EDX analysis of the sample TA2 in **Fig. 2.1(d)** confirms that the HS consists of Ti, Ag and O elements. **Fig. 2.1(e)** shows the FESEM image of the bare Ag_2O NPs. The size of the Ag_2O NPs varies from 100-600 nm, which is much larger than the NPs decorated on the TiO_2 NR surface. In the case of HS samples, the presence of numerous small pores on the surface of TiO_2 NRs serves as the nucleation sites for the growth of small Ag_2O NPs, which minimizes the probability of aggregation.

TEM images are acquired for the pristine TiO_2 NRs and its HSs to investigate the high-resolution surface features to confirm the nanoporous nature of pristine TiO_2 NRs and its surface decoration with Ag_2O NPs. **Fig. 2.2(a)** shows the TEM image of a pristine TiO_2 NR, while **Fig. 2.2(b)** depicts the TEM image of the sample TA2. It is clear from **Fig. 2.2(a)** that the surface of the pristine TiO_2 NRs is rough in nature due to the presence of uniformly distributed pores on the NRs. Note that the porous regions are primarily the nucleation sites for the Ag_2O NPs grown by the precipitation method. The pores on the surface of the TiO_2 NR provide a noble stage to grow Ag_2O NPs, which are strongly attached with TiO_2 NRs. **Fig. 2.2(b)** confirms the uniform decoration of Ag_2O NPs on the surface of TiO_2 NRs, though some exposed regions still show the ultrafine pores on it. The pores on the pristine TiO_2 NRs have an average diameter ~6.8 nm (shown in **Fig. 2.2(c)**) and the decorated Ag_2O NPs for TA2 have average diameter ~5.3 nm (shown in **Fig. 2.2(d)**). TEM images for TA1 and TA3 are also acquired and shown in **Fig. 2.2(e, f)**, respectively. In case of TA1, very small sized Ag2O NPs are formed with average diameter ~4.4 nm (shown as an inset in **Fig. 2.2(e)**), which may be due to the very low concentration of $AgNO_3$ during its growth. In contrast, comparatively large-sized Ag_2O NPs are formed for TA3 HS with average diameter ~18.2 nm (shown as an inset in **Fig. 2.2(f)**), due to the high concentration of precursor solution of Ag_2O during its growth. In both the cases of TA1 and TA3, most of the TiO_2 surface remains uncovered, while TA2 shows the maximum surface coverage by Ag_2O NPs with optimum size and number density. Due to the strong coupling,

decorated NPs are very stable on the porous surface of TiO_2 NRs and do not get detached even under ultrasonic vibration. **Fig. 2.2(g)** shows the HRTEM lattice fringe pattern of TA2 HS, which clearly reveals the simultaneous presence of crystalline Ag_2O and TiO_2(B) phases. Lattice spacing (d) of TiO_2(B) and Ag_2O has been calculated by measuring the intermediate distance between the lattice fringes.

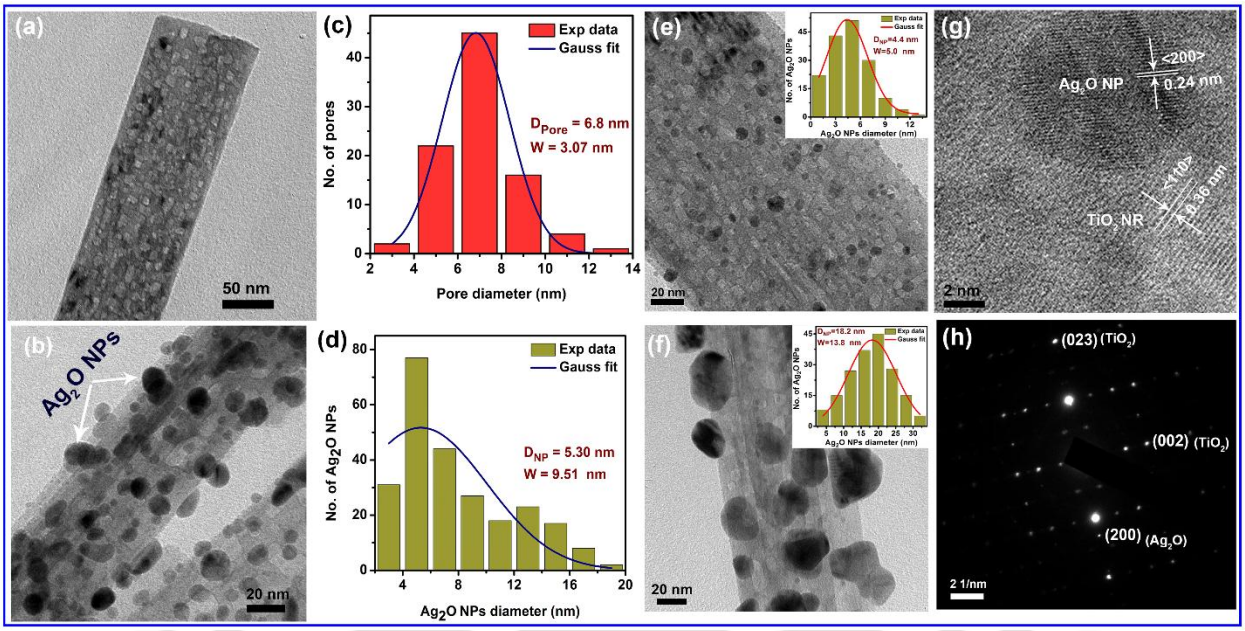

Fig. 2.2. TEM images of: (a) a single TiO_2(B) NR with nano-sized pores on it, (b) Ag_2O/TiO_2(B) NR HS in TA2. (c) The distribution of pore diameter on pristine TiO_2(B) NRs, and (d) the diameter distribution of Ag_2O NPs on TiO_2(B) NRs (in TA2) and their Gaussian fitting. (e, f) TEM images of TA1 and TA3 HSs, respectively. The inset shows the diameter distribution of Ag_2O NPs in each case. The average diameter (D) and width of the distribution (W) are also shown in respective cases. (g) The HRTEM lattice fringe pattern of TA2. The lattice spacing of Ag_2O and TiO_2(B) with orientation is also shown. (f) The SAED pattern of TA2 indicating the different planes of Ag_2O as well as TiO_2(B).

Pure B-phase TiO_2 with (110) crystal planes (d = 0.36 nm) and cubic Ag_2O with (200) crystal planes (d = 0.24 nm) are confirmed from the lattice fringe image. The SAED pattern of the corresponding HS is shown in **Fig. 2.2(h)**, which further confirms the crystalline nature of both Ag_2O and TiO_2(B). The (002) and (023) crystal planes of pure TiO_2(B) and (200) crystal plane of Ag_2O have been indexed in **Fig. 2.2(h)**.

2.3.2. Structural Analysis

2.3.2.1. XRD and XPS Analyses

Structure, phase and crystallinity of the as-grown TiO_2 NRs, Ag_2O NPs and their HS are studied by the XRD patterns, as shown in **Fig. 2.3**. Each diffraction peak of pristine TiO_2 NRs

corresponds to a pure TiO_2(B) phase[11] with a monoclinic structure, and that of Ag_2O NPs corresponds to the cubic structure.[6] The XRD peaks corresponding to the TiO_2(B) phase are marked by red diamonds, while those of the cubic Ag_2O are marked by black circles (filled). The relatively sharp diffraction peaks of Ag_2O NPs clearly imply its higher crystallinity compared to that of TiO_2(B). The phases of TiO_2(B) and Ag_2O co-exist in the Ag_2O/TiO_2(B) HS sample. Note that the XRD analysis on the HS sample does not show any measurable change in the crystal structure as well as the lattice parameter of the TiO_2(B) NRs.

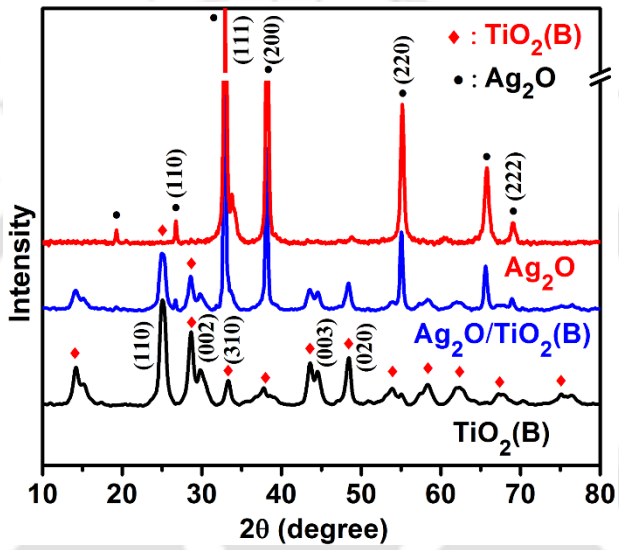

Fig. 2.3. XRD patterns of pristine TiO_2(B) NRs, Ag_2O NPs and TA2 HS. The curves are vertically shifted for clarity of presentation. The peaks corresponding to TiO_2(B) are indicated by red diamonds and the same for Ag_2O as black circles (filled).

To investigate the chemical environment, elemental composition and surface defects on the nanostructures, XPS studies were carried out on each of the catalysts. A comparison of the XPS core level O 1s spectra of pristine TiO_2(B) NRs and TA2 HS is shown in **Fig. 2.4(a)**, while that for Ti 2p spectra is shown in **Fig. 2.4(d)**. **Fig. 2.4(g)** shows a comparison of the Ag 3d core level spectra of pristine Ag_2O NPs and TA2 HS. O 1s spectrum of TA2 HS is observed to be slightly red shifted than the pristine TiO_2(B) NRs. Ti $2p_{3/2}$ peak for pristine TiO_2(B) NRs has been found at 458.6 eV, which is assigned to Ti^{4+} valence state, confirming the formation of TiO_2.[11] However, after the decoration of Ag_2O NPs on TiO_2(B) NRs, the Ti $2p_{3/2}$ peak is slightly red-shifted to a lower binding energy of 458.2 eV (as indicated by a vertical dashed line). This shift in the Ti $2p_{3/2}$ peak of TA2 HS may be due to the lattice distortion induced in TiO_2(B) due to the strong coupling of TiO_2(B) lattice with Ag_2O NPs.[12] This may partly be due to the band bending

at the TiO_2/Ag_2O interface. Both the samples shown in **Fig. 2.4(g)** exhibit a single valence state, Ag^+ in Ag_2O with Ag $3d_{5/2}$ peak at ~367.9 eV.[13]

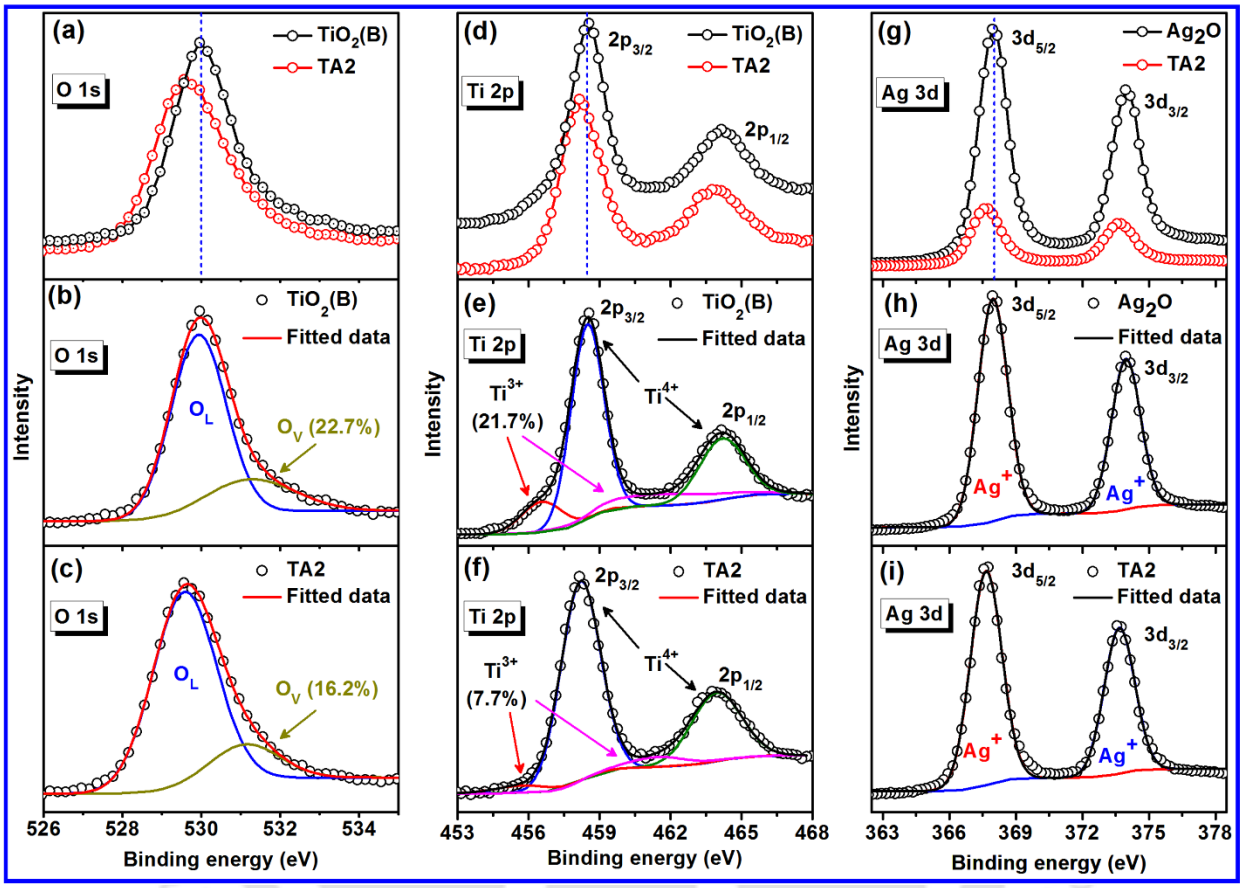

Fig. 2.4. A comparison of the core level XPS spectra of: (a) O 1s for pristine TiO_2(B) and TA2 HS, (d) Ti 2p for pristine TiO_2(B) and TA2 HS and (g) Ag 3d for Ag_2O NPs and TA2 HS. The vertical dashed lines drawn at 530.0 eV in (a), 458.6 eV in (d) and 367.9 eV in (g) indicate the red shift in the binding energy in the HS sample. (b, c) The Gaussian deconvolution of O 1s core level XPS spectra for pristine TiO_2(B) and TA2 HS, respectively. (e, f) The fitted Ti 2p XPS spectra for pristine TiO_2(B) and TA2 HS, respectively. (h, i) The fitted Ag 3d XPS spectra for Ag_2O and TA2, respectively. Each XPS spectrum is fitted with a Shirley baseline. The identity of each peak is denoted with the corresponding charge state in the respective cases.

Note that in TA2 HS, the Ag $3d_{5/2}$ peak is slightly shifted to the lower binding energy as compared to that in bare Ag_2O NPs, indicating the lattice distortion after HS formation. A vertical dashed line is drawn at 367.9 eV to discern the redshift. **Fig. 2.4(b, c)** show the O 1s core level XPS spectra of pristine TiO_2(B) and TA2 HS, respectively. In both cases, the O 1s spectra exhibit asymmetry in line shape with a shoulder at the higher binding energy side, indicating the presence of surface defect states. The O 1s spectrum can be deconvoluted into two symmetric Gaussian peaks. The intense peak at ~529.9 eV is attributed to the oxygen in the TiO_2 crystal

lattice (O_L), while the other lower intensity peak detected at ~531.2 eV can be assigned to the oxygen vacancy (O_{Ti}^{3+}). The result reveals that the oxygen vacancy (O_V) concentration decreases from 22.7% to 16.2% after the formation of HS with Ag_2O NPs. This may be due to the defect filling on the TiO_2(B) surface after the loading of oxide material (Ag_2O). **Fig. 2.4(e, f)** show the deconvolution of XPS Ti 2p spectra for pristine TiO_2(B) and TA2 HS with four symmetric Gaussian peaks in each case. For the pristine TiO_2(B), two major characteristic doublets for Ti $2p_{3/2}$ and $2p_{1/2}$, encompassing a set of two $2p_{3/2}$ peaks at 456.6 eV and 458.5 eV, are assigned to the 3+ and 4+ valence states of Ti, respectively. The result shows that the Ti^{4+} ions in the vicinity of O_V cavity accept an electron and transform to Ti^{3+} ions with an F^+ centre. In the case of TA2 HS, deconvolution of $2p_{3/2}$ peak shows two Gaussian peaks at 457.2 eV and 458.2 eV, assigned to the 3+ and 4+ valence states of Ti, respectively. It can be noticed that after the formation of HS, the Ti^{3+} concentration is reduced substantially (~2.8 fold) (shown in **Fig. 2.4(e, f)**) due to the defect filling, as confirmed from the O 1s spectrum. This is fully consistent with the PL analysis that shows lower vacancy concentration in TA2, as discussed later. Gaussian fittings of the Ag 3d XPS spectra for pristine Ag_2O NPs and TA2 HS with appropriate baseline (Shirley) are shown in **Fig. 2.4(h, i)**, respectively. In both the cases, each of the 3d peaks fits to a single peak corresponding to Ag^+ state. The Gaussian fitted Ag $3d_{5/2}$ peak for Ag_2O NPs is detected at 367.9 eV, which is shifted to the lower binding energy after the HS formation and detected at 367.7 eV. Thus, the redshift in XPS peak (Ti 2p and Ag 3d) after the HS formation could be resulting from the strong interaction of Ag_2O with TiO_2(B) NRs and may also result from the strain induced in the HS. Note that the atomic ratio of Ag to O found from XPS analysis is 2.1:1 indicating that no other phases of Ag oxides are present in the sample. Thus, XPS results show strong coupling between the Ag_2O NPs and TiO_2(B) NRs in HS samples, and this plays an important role in the enhanced photocatalytic efficiency.

2.3.2.2. Raman Analysis

For further endorsement of crystallinity and phase of TiO_2 NRs and its various HSs, Raman analysis has been performed for all the samples using a 633 nm laser excitation. **Fig. 2.5** shows a comparison of the Raman spectra for all the samples. The inset shows a magnified view of the prominent Raman modes in the region 250-1000 cm^{-1}. The peaks corresponding to the B-phase of TiO_2 are marked with '*' symbol, while those of the Ag_2O are marked with '♦' symbol.[11] The crystalline Ag_2O peaks at 323 and 489 cm^{-1} corresponds the Ag-O stretching/bending modes.[14]

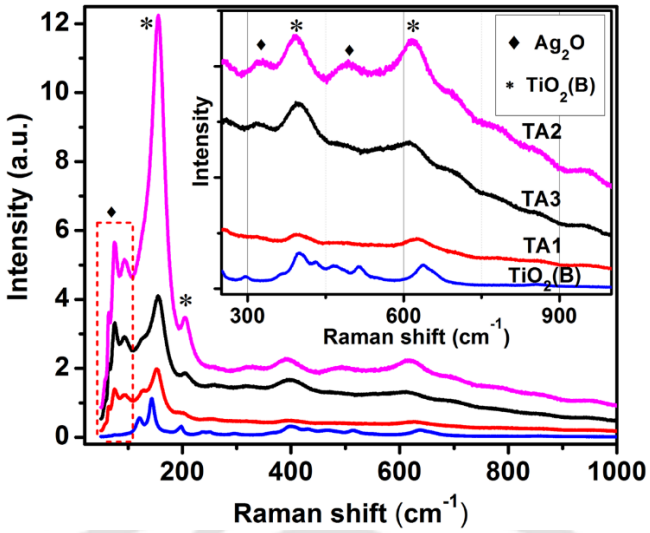

Fig. 2.5. Raman spectra of pristine $TiO_2(B)$ NRs and its HSs. The inset shows the magnified view of the spectra in the range 250-1000 cm^{-1}. Peaks related to Ag_2O and $TiO_2(B)$ are labelled with '♦' and '∗' symbols, respectively.

2.3.3. Brunauer–Emmett–Teller (BET) Surface Area Analysis

To evaluate the specific surface area of pristine $TiO_2(B)$ NRs, it's HS with Ag_2O and the coupling between the porous sites of the $TiO_2(B)$ NRs and Ag_2O NPs, the surface area of the samples has been measured by BET process. The N_2 adsorption-desorption isotherms of $TiO_2(B)$ NRs and TA2 HS are shown in **Fig. 2.6(a)**. The shape of the isotherms depends on the pore sizes in the nanostructure. The isotherms of the nanostructures with micropores (size ≥ 1 nm) exhibit an abrupt increase in the high-pressure region (> 0.8 P/P_0 value) that can be attributed to the capillary condensation and multilayer adsorption of N_2 in the micropores. Beside pores, the $TiO_2(B)$ nanostructures have rough surfaces. So, the isotherms before capillary condensation transition show a smooth behaviour without any inflections.[15] In this work, the specific surface area of pristine $TiO_2(B)$ NRs is measured as 51.09 m^2/gm, which is reduced considerably after the surface decoration with Ag_2O NPs (TA2 HS) and estimated to be 28.6 m^2/gm, as deduced from BET analysis. Note that some of the pores on the $TiO_2(B)$ surface act as the nucleation sites for the growth of Ag_2O NPs. Further, the BET provides the surface area of the material per unit mass (m^2/gm). Since the molar mass density of Ag_2O (7.14 gm/cm^3) is nearly double of the $TiO_2(B)$ (4.23 gm/cm^3), the surface area of the HS sample is reduced by nearly half, primarily due to the Ag_2O loading with nearly double molar mass density. Thus, the reduced surface area in the HS sample is mainly due to the higher mass loading effect, without any substantial reduction in average pore size.

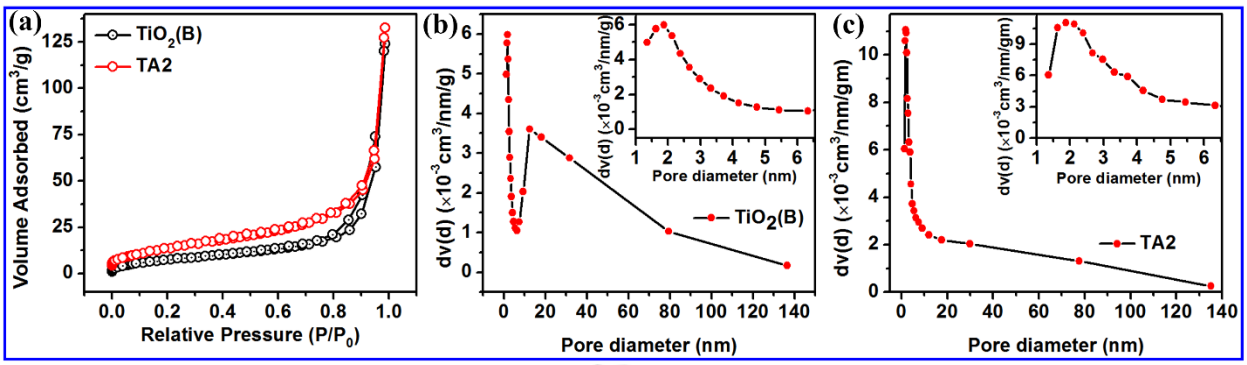

Fig. 2.6. (a) N_2 adsorption-desorption isotherms for pristine TiO_2(B) NRs and TA2 HS. Pore size distribution using BJH method for: (b) TiO_2(B) NRs and (c) TA2 HS.

It is apparent from the TEM analysis that the average size of the Ag_2O NPs is much larger than the pore sizes measured from the Barett–Joyner–Halenda (BJH) analysis. BJH pore size distribution profile for pristine TiO_2(B) and TA2 HS are shown in **Fig. 2.6(b, c)**. Average pore diameter is found to be ~1.9 nm for both the samples, as determined from the distribution profile. However, this size is much lower than the pore sizes obtained from the HRTEM analysis (6.8 nm), primarily due to the limitation of the TEM technique to probe the ultra-small size pores. In the case of HS sample, the bigger size pores are covered with Ag_2O NPs, while the smaller size pores with very high density are mostly uncovered, as evident from **Fig. 2.2(b)** and **Fig. 2.6(b, c)**. Though the average surface area is reduced in the HS sample, the presence of small pores and the suitable heterojunction are very important for the enhanced visible light photocatalytic activity.

2.3.4. Optical Analysis

2.3.4.1. UV-Vis Absorption Study

To measure the optical response of pristine TiO_2(B) NRs, Ag_2O NPs and their HSs, the UV-visible absorption spectra were studied from the measurement of the diffuse reflectance spectra (DRS) of the powdered samples. The absorbance of a material system is related to the diffuse reflectance (R) by the Kubelka-Munk (K-M) function, F(R), given by

$$F(R) = \frac{(100 - R)^2}{200R} = \frac{\alpha}{S} \qquad (2.1)$$

Where α and S represent the absorption and scattering coefficients, respectively and R is the percentage reflectance of the respective samples. **Fig. 2.7(a)** shows the plot of the K-M function

of different samples depicting their absorption spectra and **Fig. 2.7(b)** shows the $(F(R)h\nu)^{1/2}$ vs. $h\nu$ plot for the calculation of effective band gap (indirect) of the HSs. Extrapolation of the linear portion at $(F(R)h\nu)^{1/2} = 0$ gives the effective band gap of the nanostructures. As evident from the data, the pristine TiO_2(B) NRs exhibit a sharp absorption edge at ~400 nm and at higher wavelengths (visible region) the absorbance is negligibly low. However, the pristine Ag_2O NPs have strong absorption in the UV-visible-NIR range of 200-850 nm showing a broad absorption band centred at ~430 nm and the absorption tail extends to the NIR region.

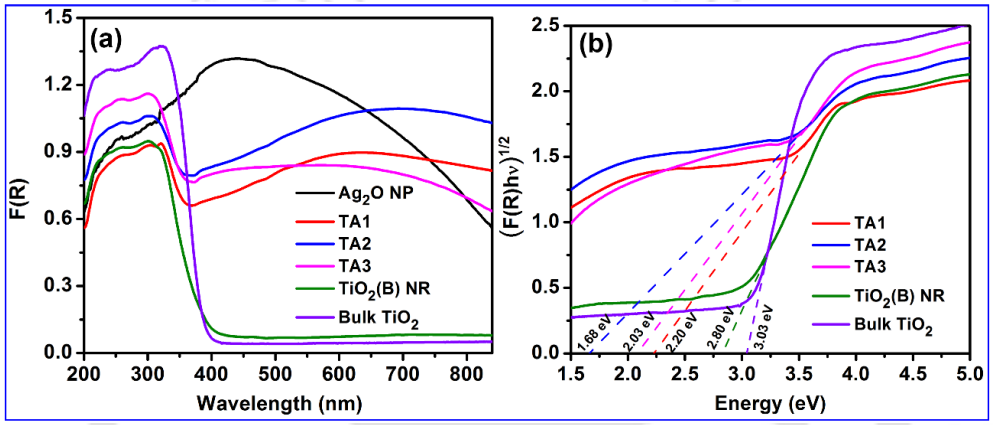

Fig. 2.7. (a) K-M function (F(R)) of different samples plotted against wavelength. (b) The corresponding Tauc plot considering the indirect bandgap nature of the TiO_2 samples. The effective band gaps of the respective samples are estimated from the intercept on the x-axis (extrapolated dashed lines).

The bandgap (direct) of Ag_2O NPs estimated from the corresponding Tauc plot is ~1.34 eV, which is consistent with the literature report[16]. The absorption spectra of Ag_2O/TiO_2(B) HSs illustrate that all HS systems have extremely high absorption in the entire UV-visible-NIR region of the optical spectrum. Among these, the TA2 HS shows the highest absorption in visible to NIR region, may be due to the optimum size and number density of the Ag_2O NPs decorated on the TiO_2(B) NRs, see **Fig. 2.2(b)**. For the visible light sensitization by Ag_2O NPs, the HSs are expected to have high photocatalytic activity under the visible as well as UV and NIR irradiation. Interestingly, the effective band gap of the TiO_2(B) NRs has been reduced considerably after loading with Ag_2O NPs. Considering the indirect nature of band gap in the pristine TiO_2(B) NRs as well as its HSs, the effective band gap of the respective samples has been estimated using Tauc plot, as shown in **Fig. 2.7(b)**.[11] The bulk anatase TiO_2 powder has a band gap 3.03 eV, which is reduced to 2.80 eV for pristine TiO_2(B) NRs due to the presence of O_V defects. This

reduction in the effective band gap helps the TiO_2(B) NRs to be active under the visible light and expected to have significant effect on the visible light photodegradation capability. Interestingly, after the decoration of the Ag_2O NPs, the effective band gap energy of TiO_2(B) NRs has been tuned in the range 2.20-1.68 eV, as shown in **Fig. 2.7(b)**. The detailed absorption range and the effective band gap of each catalyst are tabulated in **Table 2.1**. The modification of the band gap energy for the HS samples may be due to the efficient coupling between the Ag_2O NPs and TiO_2(B) NRs. The band structures of each of the nano-components are suitable enough to have proper band bending at the interface due to their close coupling. It is noteworthy that in case of TA2, the effective band gap is found to be lowest (1.68 eV), which implies that Ag_2O NPs and TiO_2(B) NRs HS has large band bending and may have high carrier concentration at room temperature. This turns out to be a very promising and an extremely beneficial approach for the efficient visible light photocatalysis by the HSs samples (discussed later).[17]

2.3.4.2. Photoluminescence Study

The advantage of the as-synthesized HSs in solar light-driven photocatalysis over the pristine TiO_2(B) NRs has been confirmed from the PL studies. The characteristic PL spectra clarify the mode of separation and recombination of the photogenerated e-h pairs. A comparison of the room temperature steady state PL spectra for pristine TiO_2(B) NRs, Ag_2O NPs and TA2 HS are shown in **Fig. 2.8(a)**. Interestingly, a significant decrease (by a factor of ~5.9) in PL intensity of the TiO_2(B) NRs has been observed after the decoration with Ag_2O NPs. However, the nature of the PL band remained unaltered. For a detailed understanding of the origin of the broad PL emission, each PL spectrum is deconvoluted with four symmetric Gaussian peaks, as shown in **Fig. 2.8(b, c)**. For both the samples, the well fitted individual bands are labelled as Peak 1, 2, 3, 4. For pristine TiO_2(B) NRs (**Fig. 2.8(b)**), Peak 1 (at 427.2 nm) is attributed to the self- trapped excitons located at TiO_6 octahedra.[11] Peak 2 (at 491.2 nm) is due to the charge transfer transition from Ti 3d orbital to O 2p orbital in TiO_6^{2-}octahedra[18], while Peak 3 (at 560.6 nm) is attributed to the shallow traps associated with the oxygen vacancies (V_O) in the TiO_2 structure.[19] Peak 4 (641.0 nm) is possibly due to the deep level emissions associated with V_O states.[20] Similarly, for TA2 HS (**Fig. 2.8(c)**), the four peaks are located at 434.9, 490.6, 561.0 and 648.6 nm, respectively, having the same identity. Note that the intensity ratio of the peaks in each sample is also almost the same in **Fig. 2.8(b)** and **2.8(c)**.

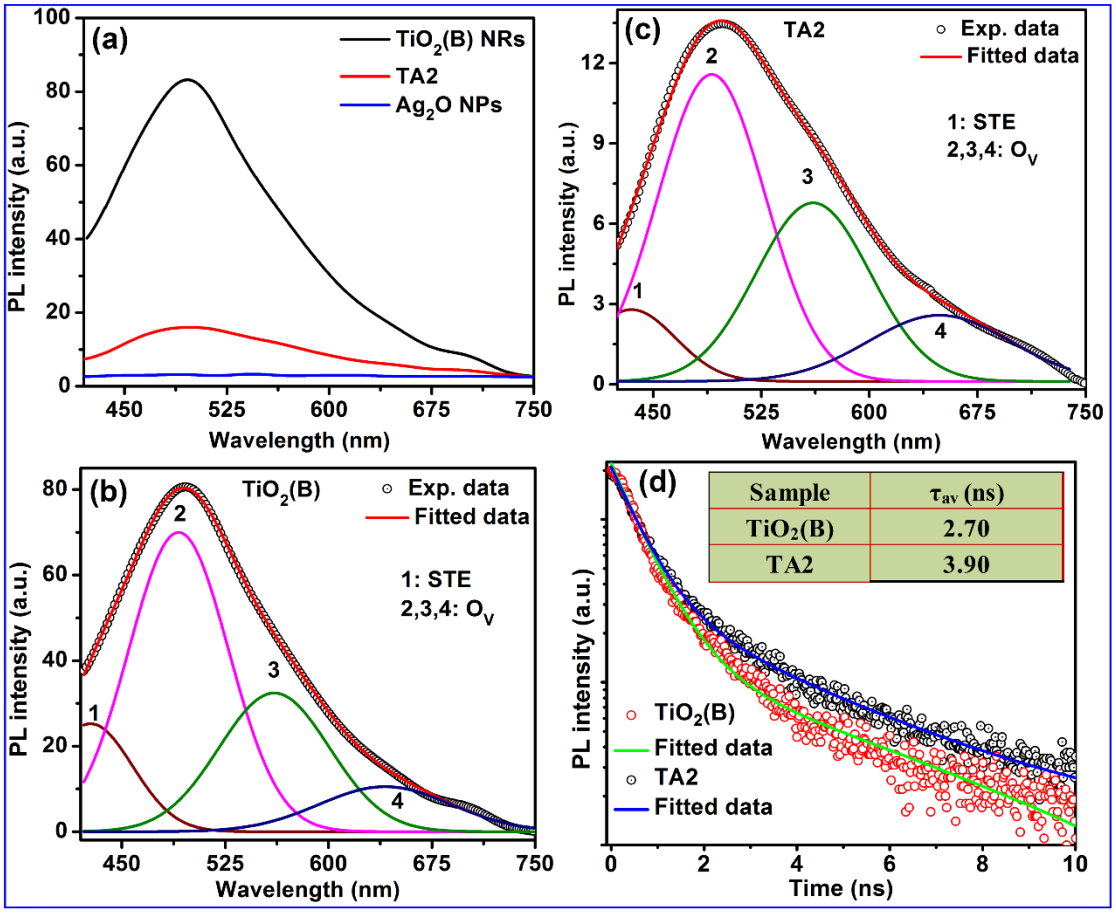

Fig. 2.8. (a) A comparison of the PL spectra for pristine TiO_2(B) NRs, Ag_2O NPs and TA2 HS excited with 405 nm laser. (b, c) Gaussian fitted PL spectra of TiO_2(B) NRs and TA2, respectively. (d) A comparison of the TRPL spectra for pristine TiO_2(B) NRs and TA2 HS monitored at 490 nm (emission) with a 405 nm laser excitation. The symbols represent the experimental data, and solid lines represent the corresponding tri-exponential fit. The inset shows the average time constant for different samples.

However, the intensity of each peak is substantially reduced in TA2 HS as compared to that in pristine TiO_2(B) NRs. The decrease in PL intensity after the decoration with Ag_2O NPs may be due to the following reasons: (i) the deposited Ag_2O NPs work as the trap centres of the photoexcited electrons and prevents their recombination;[6] (ii) due to band bending at the interface, the charge transfer process is very efficient in case of HSs and thus charge carriers (e, h) are separated enough reducing the recombination probability, lowering the PL intensity; (iii) Ag_2O NPs may partly passivate the luminescent centers on TiO_2(B) NRs. All these factors may contribute to reduce the PL intensity of the sample TA2 as compared to the pristine TiO_2(B) NRs. Thus, under visible light illumination, due to reduced recombination, plenty of excitons are

available near the interface of Ag_2O/TiO_2(B) HS, which may help in achieving high photocatalytic activity (discussed later).

2.3.4.3. Time-Resolved Photoluminescence Study

To investigate the recombination kinetics of photogenerated charge carriers, time-resolved photoluminescence (TRPL) measurement was performed on pristine TiO_2(B) NRs, and its HS with 405 nm laser excitation and the emission was monitored at 490 nm. The TRPL decay profiles are fitted using a tri-exponential decay function expressed as follows:

$$I(t) = \sum_{i=1}^{3} A_i e^{(-t/\tau_i)} \qquad (2.2)$$

Where τ_i is the lifetime of individual component, and A_i is the corresponding amplitude.

The average excited state lifetime can be calculated by using the following relation[21]:

$$\tau_{av} = \frac{\sum_{i=1}^{3} A_i \tau_i^2}{\sum_{i=1}^{3} A_i \tau_i} \qquad (2.3)$$

Fig. 2.8(d) shows a comparison of the TRPL decay curves for pristine TiO_2(B) NRs and TA2 HS with the average lifetime (τ_{av}) tabulated as the inset. Each TRPL spectral data can be fitted by a tri-exponential decay function, which implies that three different states contribute to the TRPL spectra in each sample, fully consistent with the steady-state PL spectra (**Fig. 2.8(b, c)**). It can be noted that the average lifetime is considerably increased from 2.70 ns to 3.90 ns after Ag_2O loading and consequently, the decay becomes slower in TA2. The increase in carrier lifetime seems to be playing a critical role in the enhanced visible light photocatalytic activity in the HS samples. The photogenerated charge carriers first migrate to the TiO_2/Ag_2O interface, which is thermodynamically favourable, since the valence and conduction band position of Ag_2O is above of that of TiO_2(B) NR.[16] After photoexcitation, electrons from the conduction band of Ag_2O NPs migrate to the conduction band of TiO_2(B) NRs and holes from the valence band of TiO_2(B) NRs migrate to that of Ag_2O NPs. Thus the interfacial charge transfer prolongs the lifetime of the photogenerated charge carriers, which clearly manifest as longer τ_{av} in the TRPL spectra. Surface decoration of TiO_2(B) NRs with the Ag_2O NPs reduces the probability of recombination facilitating higher density of carriers available near the surface of the HS, which promotes high visible light photocatalytic performance, as discussed below.

2.3.5. Visible Light Photodegradation Studies

The excitons generated within the HSs could be energetic enough to drive the photoelectrochemical reactions due to its broadband optical absorption and prolonged carrier lifetime. To investigate the photocatalytic efficiency of the as-synthesized catalysts, we examined the decomposition of aqueous MO (anionic dye) and MB (cationic dye) solution in presence of various catalysts.

2.3.5.1. Photodegradation and Reaction Kinetics of MO

Visible light photocatalytic studies of all the samples were carried out under identical conditions using an aqueous solution of MO as a reference dye. The normalized UV-visible absorption spectra of MO aqueous solution under visible light irradiation collected at a regular interval of time (10 min) are shown in **Fig. 2.9(a)** for pristine TiO_2(B) NRs, **Fig. 2.9(b)** for Ag_2O NPs, **Fig. 2.9(c)** for TA1, **Fig. 2.9(d)** for TA2 and **Fig. 2.9(f)** for TA3.

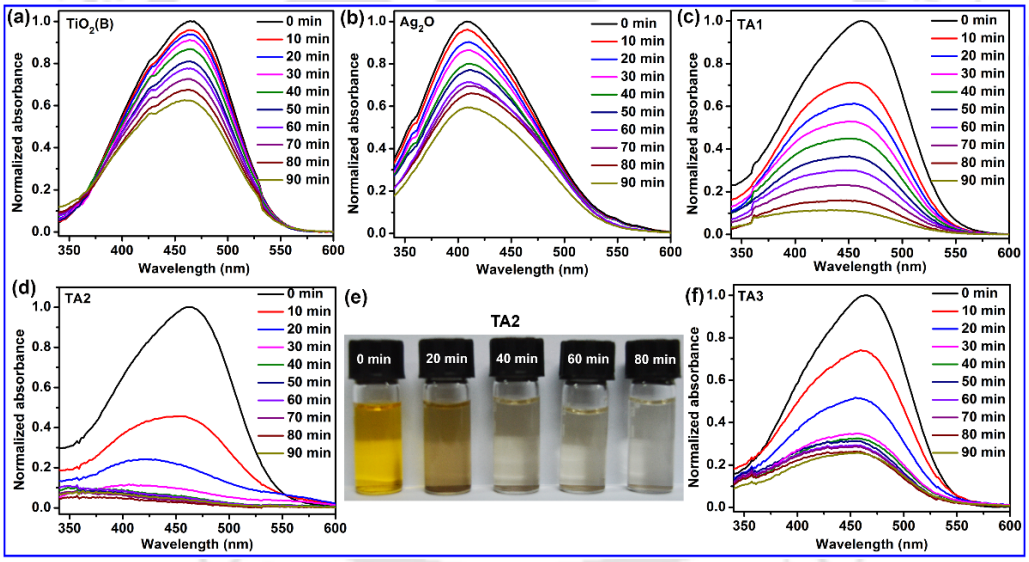

Fig. 2.9. Normalized absorption spectra of MO under visible light irradiation for 0-90 min at a regular interval of 10 min, catalyzed by (a) pristine TiO_2(B) NRs, (b) pristine Ag_2O NPs, (c) TA1, (d) TA2, (f) TA3. (e) Digital photograph of the degradation colour change of MO in the presence of TA2 after exposure to visible light for various times.

Though the absorbance peak intensity of MO (in the presence of a catalyst) is observed to be reduced systematically with the irradiation time, the reduction is most significant and prominent in case of TA2 HS. Digital photographs depicting the change in colour of MO solution due to the photodegradation at an interval 20 min in case of TA2 are shown in **Fig. 2.9(e)**. **Fig. 2.10(a)** shows a comparison of the photodegradation performance of pristine TiO_2(B) NRs, Ag_2O NPs,

TA1, TA2 and TA3 HSs in MO aqueous solution under visible light irradiation. To compare the efficiencies, the self-decomposition of the dye solution was also examined under identical illumination conditions.

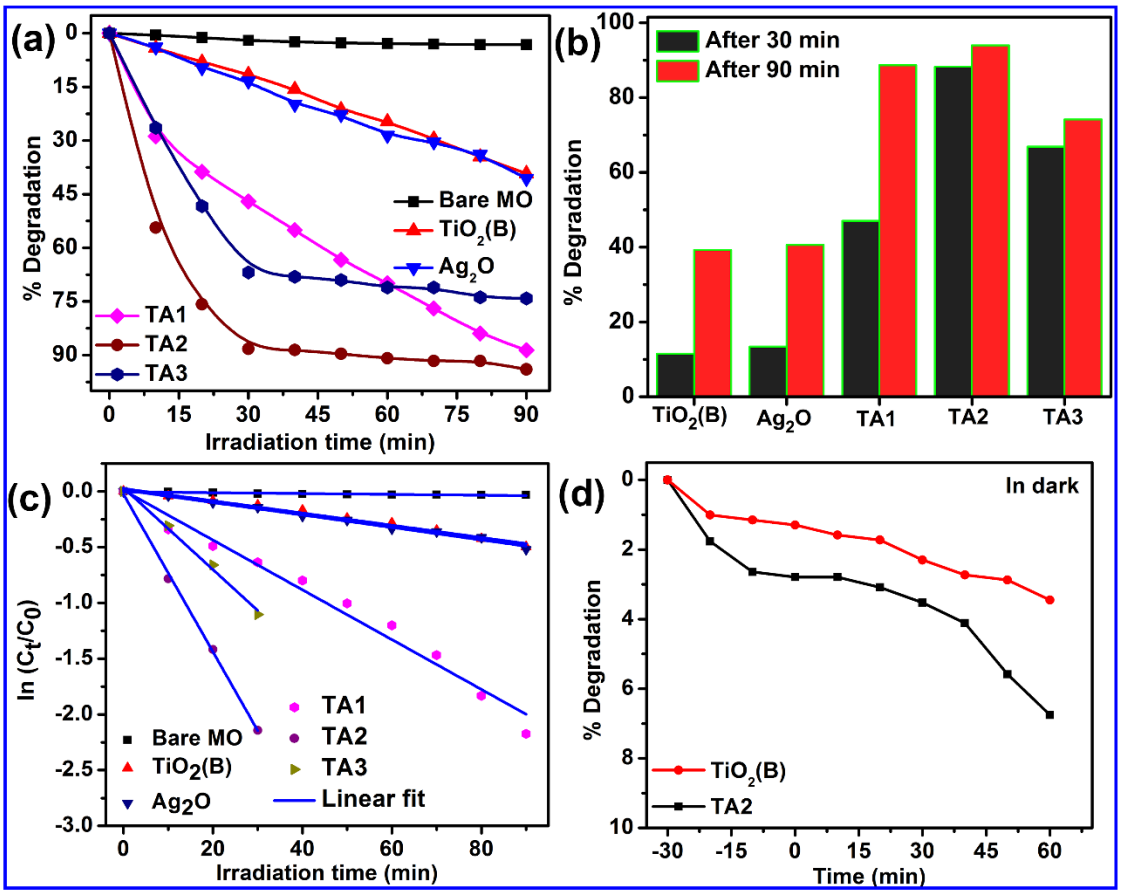

Fig. 2.10. (a) A comparison of the photocatalytic degradation profiles of MO with and without the presence of different catalyst samples under visible light irradiation. (b) A comparison of the degradation percentages of MO after 30 and 90 min of irradiation calculated for different samples. (c) A plot of $\ln(C_t/C_0)$ vs exposure time (t) for different samples and corresponding linear fitting. (d) A comparison of degradation of MO by pristine TiO_2(B) NRs and TA2 catalysts in the dark.

The HS samples show enhanced photodegradation efficiency as compared to the bare TiO_2 NRs as well as pristine Ag_2O NPs. Note that among all the HS samples, TA2 shows the highest photodegradation efficiency. **Fig. 2.10(b)** shows the comparison of the photodegradation efficiency of the samples after 30 min and 90 min light irradiation. The catalysts TA2 and TA3 degrade the dye very rapidly up to 30 min of irradiation, and then degradation rate becomes very slow (**Fig. 2.10(a)**), as expected for exponential decay kinetics. After 30 min of light irradiation, MO is decomposed by 88.2% and 66.9% for TA2 and TA3, respectively. The kinetics of the photodegradation of MO can be described by a pseudo-first order rate kinetics from Langmuir-

Hinshelwood expression: $\ln(C_t/C_0) = -kt$, where C_0 is the initial concentration of MO after reaching the adsorption-desorption equilibrium, C_t is the concentration of MO after irradiation time t and k is the rate constant (in min^{-1}). **Fig. 2.10(c)** shows a comparison of the values of $\ln(C_t/C_0)$ for all samples as a function of light irradiation time. The rate constant (k) is calculated by the corresponding linear fit, and the value of k is tabulated in **Table 2.2**. Interestingly, k (0.071 min^{-1}) is found to be the highest for the sample TA2 and it is ~13 fold stronger than that of the pristine TiO_2(B) NRs (0.0055 min^{-1}) as well as Ag_2O NPs (0.0056 min^{-1}). Considering the visible light irradiation, the obtained rate constant (0.071min^{-1}) is very significant for the HS sample. Most of the reported k-values are usually for UV-light irradiation, and reported rate constant for commercial photocatalyst (e.g., P25) is ~1×10^{-2} min^{-1} under UV light irradiation.[22] In the present case, even under visible light irradiation, the rate constant is about one order of magnitude higher than the reported values of TiO_2 under UV light irradiation.

Table 2.2: *Degradation performance of organic dyes (MO and MB) by various catalysts and the corresponding pseudo first-order rate constants.*

Catalyst name	***Degradation (%)***		***Rate constant (min^{-1}) $\times 10^{-2}$***	
	MO	**MB**	**MO**	**MB**
No catalyst	3.2	9.2	0.037	0.10
TiO_2(B) NRs	39.2	60.5	0.55	1.00
Ag_2O NPs	40.6	87.9	0.56	2.10
TA1 HS	88.6	93.5	2.20	3.30
TA2 HS	94.0	99.2	7.10	5.70
TA3 HS	74.2	97.5	3.70	4.60

To investigate the degradation efficiency of pristine TiO_2(B) NRs and its HSs in the dark, the experiments were performed under identical conditions in absence of light. The catalyst was mixed into aqueous solutions of MO under magnetic stirring in the dark and immediately 5 ml solution has been withdrawn. Then the process was continued for 90 min. It is assumed that within 30 min, the adsorption/desorption equilibrium condition has been reached. Beyond the equilibrium condition, degradation activity of TiO_2(B) NRs and the most efficient photocatalyst TA2 has been monitored up to 60 min further, and corresponding degradation results are shown in **Fig. 2.10(d)**. The concentration of the dye decreases very marginally with time because of the

adsorption of dye molecules on the porous sites of the catalyst surface. Since the degradation in the dark is very small (2% for TiO_2(B) NRs and 7% for TA2 after 90 min) than that under illumination, we have not considered the contribution of the adsorption in the calculation of rate constant.

2.3.5.2. Photodegradation and Reaction Kinetics for MB

To understand the enhanced visible light photocatalytic activity of Ag_2O/TiO_2(B) HSs, photodegradation has been monitored on a different ionic dye (cationic dye MB) under identical conditions as that of MO.

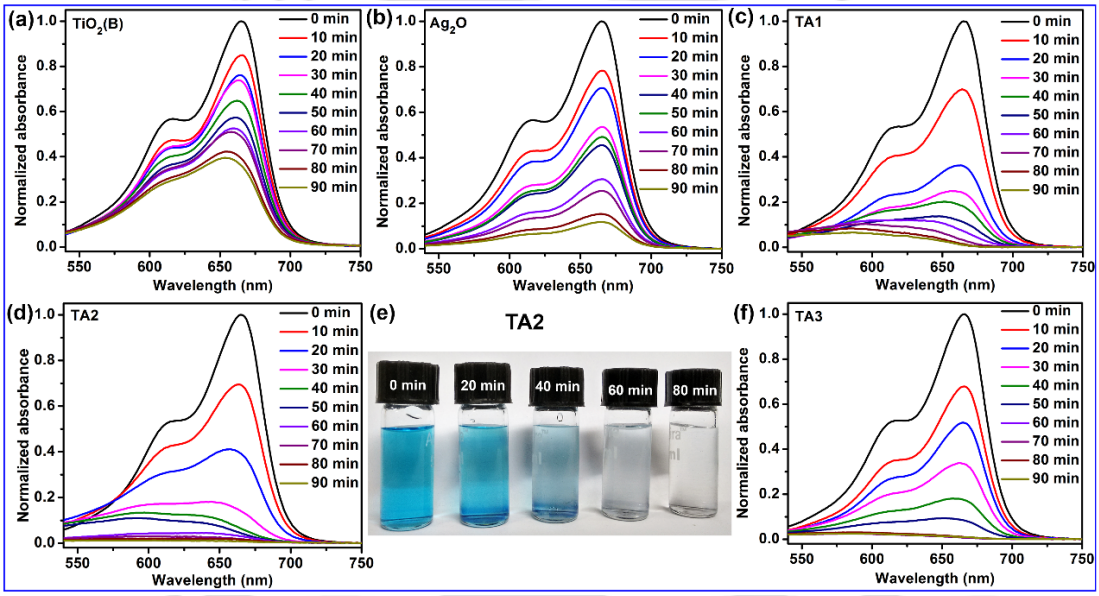

Fig. 2.11. Normalized absorption spectra of MB under visible light irradiation for 0-90 min at a regular interval of 10 min, catalyzed by (a) pristine TiO_2(B) NRs, (b) pristine Ag_2O NPs, (c) TA1, (d) TA2, (f) TA3. (e) Digital photograph of degradation colour change of MO in the presence of TA2 after exposure to visible light for various times.

The normalized UV-visible absorption spectra of aqueous MB solution under visible light irradiation collected at a regular interval of time (10 min) are shown in **Fig. 2.11(a)** for pristine TiO_2(B) NRs, **Fig. 2.11(b)** for Ag_2O NPs, **Fig. 2.11(c)** for TA1, **Fig. 2.11(d)** for TA2 and **Fig. 2.11(f)** for TA3. MB shows maximum absorbance at 665 nm and its degradation is estimated by monitoring the systematic decrease of its UV-visible absorption intensity with the light irradiation. Similar to the case of MO, TA2 shows the fastest degradation of MB under visible light (see **Fig. 2.11(d)**). **Fig. 2.11(e)** shows a digital photograph indicating the colour change of MB in the presence of TA2 at an interval of 20 min of visible light irradiation. **Fig. 2.12(a)**

shows a comparison of the photodegradation performance of pristine TiO_2(B) NRs, Ag_2O NPs, TA1, TA2 and TA3 HSs in MB aqueous solution under visible light irradiation. Here, again the HS samples show enhanced photodegradation efficiency as compared to the pristine TiO_2(B) NRs and Ag_2O NPs. As stated before, the sample TA2 shows highest photodegradation efficiency compared to the other samples. **Fig. 2.12(b)** shows a comparison of the photodegradation efficiency of all the samples after 30 min and 90 min of light irradiation. **Fig. 2.12(c)** shows a comparison of the value of $\ln(C_t/C_0)$ for the respective samples as a function of light irradiation time.

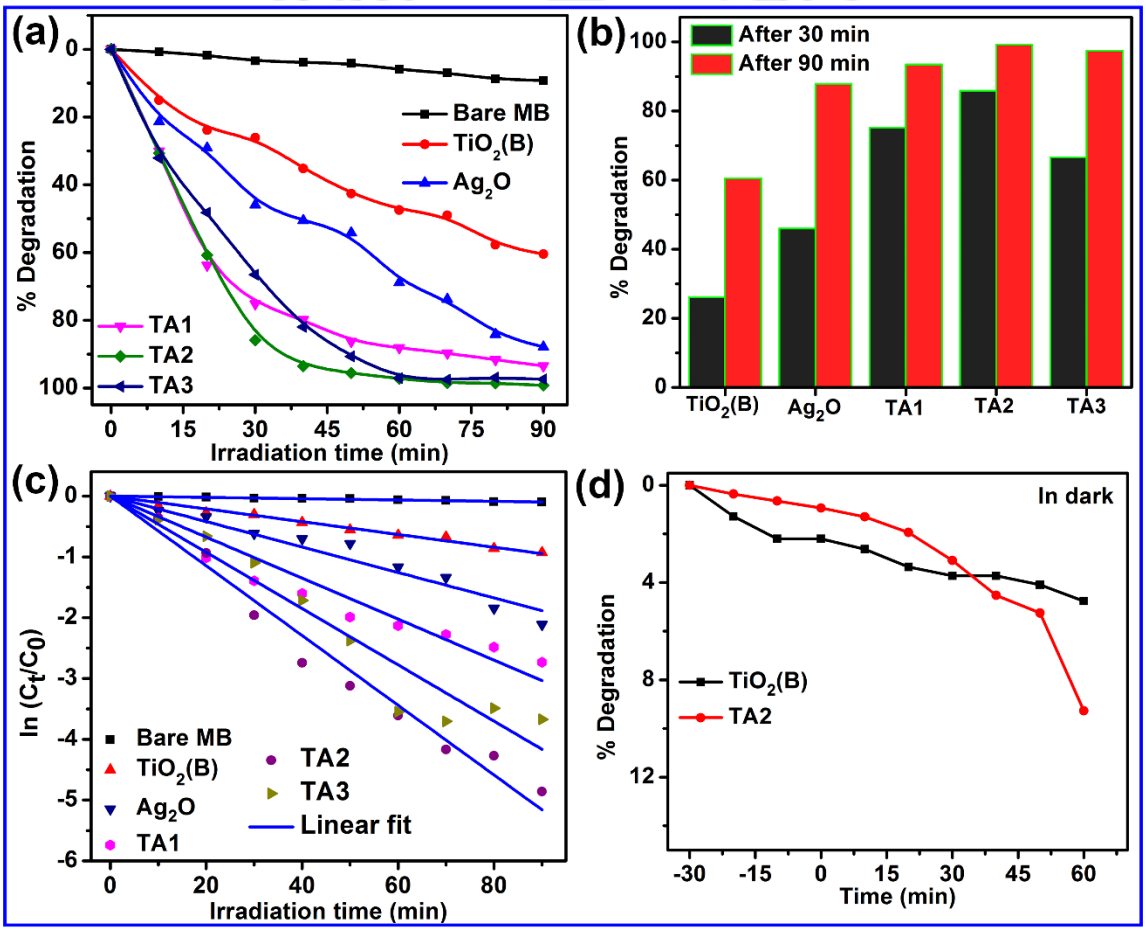

Fig. 2.12. (a) A comparison of the photocatalytic degradation profiles of MB with and without the presence of different catalyst samples under visible light irradiation. (b) A comparison of the degradation percentages of MB after 30 and 90 min of irradiation calculated for different samples. (c) A plot of $\ln(C_t/C_0)$ vs exposure time (t) for different samples and corresponding linear fitting. (d) A comparison of degradation of MB by pristine TiO_2(B) NRs and TA2 catalysts in the dark.

The degradation of MB solution by the pristine TiO_2(B) NRs and TA2 HS in the absence of light is depicted in **Fig. 2.12(d)**, showing marginal degradation. The rate constant in MB (as shown in

Fig. 2.12(c) and **Table 2.2**) for TA2 (0.057 min^{-1}) shows the highest value and it is ~6 times stronger than that of pristine TiO_2(B) NRs (0.01 min^{-1}). In this case, the enhancement factor (5.7) is lesser than that of the MO dye (12.9). However, strongly enhanced visible light photocatalytic activity is observed in both the dyes with different ionic nature and the detailed mechanism of the enhancement is discussed below.

2.3.5.3. Cyclic Stability

To investigate the cyclic stability of Ag_2O/TiO_2(B) HS as a visible light photocatalyst, the same sample has been repeatedly used for four cycles after separation by centrifugation followed by filtration. TA2 HS has been chosen as the model HS catalyst as it shows the highest photodegradation efficiency for both MO and MB, as shown in **Fig. 2.10(a)** and **Fig. 2.12(a)**, respectively. Interestingly, the TA2 photocatalyst exhibits highly stable photocatalytic activity under visible light irradiation for MO, as shown in **Fig. 2.13(a)** and there is no obvious reduction in the photodegradation efficiency after four cycles of use.

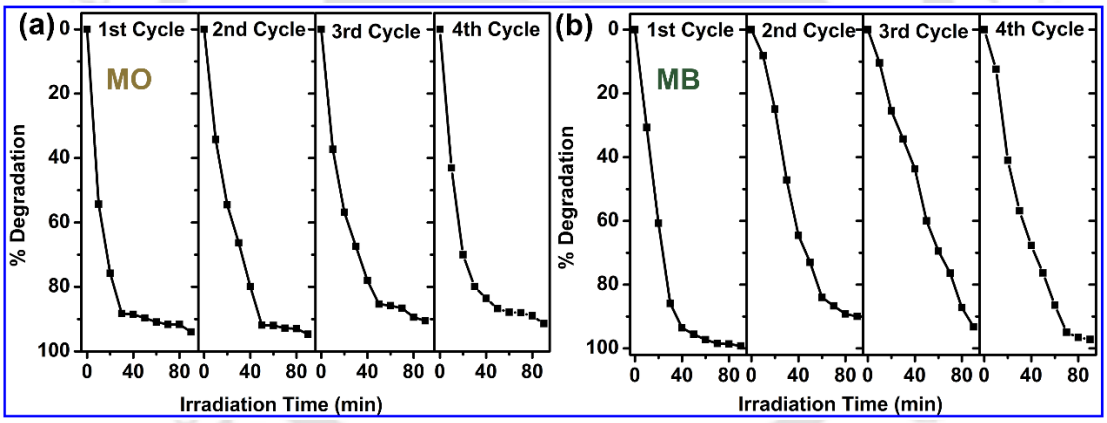

Fig. 2.13. The cyclic stability of TA2 HS as a visible light photocatalyst for four cycles: (a) in MO and (b) in MB.

In the case of MB, TA2 again shows very good stability under repeated cyclic process, though the degradation rate falls slightly at the higher cycle (**Fig. 2.13(b)**). Thus, the Ag_2O decorated TiO_2(B) NRs are found to be extremely stable photocatalyst with potential for real-life applications.

2.3.5.4. Mechanism of Enhanced Visible Light Photocatalytic Activity

TiO_2 is known to be a large band gap (~3.2 eV) semiconductor and is optically active mostly at the UV region (<400 nm). In this work, the band gap of pure TiO_2(B) NRs, as well as its HSs, is

tuned so that it can absorb broader window of the solar spectrum. In pure TiO_2(B) NRs, the range of photoactivity has been enhanced (band gap 2.8 eV) as compared to bulk TiO_2 and found to be capable for the light absorption up to ~440 nm. Thus, under visible light irradiation pristine TiO_2(B) NRs show reasonably high photodegradation efficiency (see **Table 2.2**). Pristine Ag_2O NPs also show high visible light photodegradation efficiency, as shown in **Table 2.2** due to the lower optical band gap. When Ag_2O NPs are decorated on pure B-phase TiO_2 NRs, a massive enhancement in the photodegradation efficiency has been observed. Here, the Ag_2O NPs might act as a visible light sensitizer leading to the enhanced visible light photocatalytic activity. There are several factors that may contribute to this enhancement, such as

i. Enhanced surface area
ii. Tunable band gap and enhanced optical absorption range
iii. High adsorption of dye and dye-catalyst interaction
iv. Efficient charge separation at the interface of the HS
v. Ionic condition of the dye as well the heterostructured material

High surface area is generally desirable to have enhanced photocatalytic activity of a semiconductor photocatalyst since higher surface area allows greater interfacial contact points with organic dyes leading to enhanced photodegradation efficiency. However, in our case, the specific surface area of the pristine TiO_2(B) NRs is reduced after the formation of HS with Ag_2O NPs, as confirmed from the BET analysis, although the photodegradation efficiency of the sample TA2 is much higher than the bare TiO_2(B) NRs, as shown in **Table 2.2**. Thus, it can be concluded that the surface area is not the primary factor for the enhanced photocatalytic activity observed here.

The rate of photocatalysis depends on the relative concentration of dye and the catalyst in the solution. In the present case, 100 mL dye solution (10 mg/L) was used with 20 mg catalyst. Thus, 1 mg dye was degraded up to 76% within 20 min by 20 mg of TA2 in the presence of visible light. Zhou et al. have reported ~77% degradation of MO in 20 min by Ag_2O and anatase TiO_2 HS with 1:1 weight ratio.[6] However, the authors have used only 0.4 mg MO in the aqueous solution, which is 2.5 times lower than the amount used in the present study. Thus, in the present case, the fabricated HS shows 2.5 times stronger photocatalysis than that reported earlier in the presence of visible light.

Enhancement of photocatalytic efficiency requires high absorption of light to create enough e-h pairs and easy separation of the photoexcited e-h pairs with minimum recombination. The band gap of the as-synthesized TiO_2(B) NRs and its HSs with Ag_2O NPs clearly falls in the visible region (in **Fig. 2.7(b)** and **Table 2.1**) and is likely to be effective for the generation of enough photoexcited carriers. The broadband optical absorption with high intensity for the HS samples allows generation of the high density of photoinduced carriers that can facilitate certain redox reactions to degrade the organic pollutants. The sample TA2 shows visible absorption with the highest intensity as compared to the other HS samples, and it is extended to the NIR region, which is possibly one of the important reasons behind its highest photocatalytic efficiency among all HS samples.

In a homogeneous semiconductor, fast recombination of the photoexcited e-h pairs is mostly observed in the form of PL, and their separation with minimum recombination is highly challenging. Efficient separation of photogenerated e-h pairs is essential for the generation of highly active superoxide and hydroxyl radicals to facilitate enough redox reaction for the degradation of the dye molecules. On the basis of the enhanced photodegradation by Ag_2O/TiO_2(B) HSs under visible light irradiation, the following mechanism can be proposed. A possible band diagram of the Ag_2O/TiO_2(B) HS at the interface and the carrier transfer mechanism are schematically illustrated in **Fig. 2.14**. In the HS, Ag_2O NPs are well coupled to the porous sites of TiO_2(B) NRs and energy bands of Ag_2O and TiO_2(B) are aligned suitably to facilitate charge transfer from Ag_2O to TiO_2 NRs. Previous reports suggest that in the Ag_2O/TiO_2(B) HSs, both the CB and VB of Ag_2O NPs lie above the corresponding bands of TiO_2(B).[16, 23] Therefore, the migration of the photogenerated charge carriers through the interface is thermodynamically favourable.[16] The decrease in the PL intensity of TiO_2(B) NRs and the slower decay rate in TRPL after Ag_2O NPs loading on to it strongly suggest that the efficient charge separation indeed takes place in the HS samples. Ag_2O NPs are fully visible light sensitive due to its narrow band gap (~1.34 eV). When the Ag_2O/TiO_2(B) HSs are exposed to the visible light, both the components produce electrons in the conduction band leaving behind holes in the valence band. Due to the band positions and their bending at the interface[24], photo-excited electrons from the CB of the Ag_2O migrate to that of TiO_2 and holes from VB of TiO_2 move to that of Ag_2O.

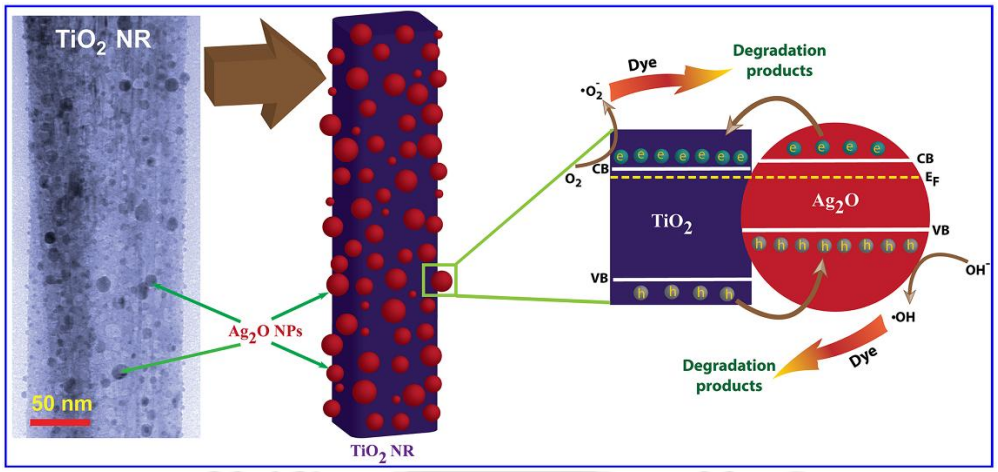

Fig. 2.14. A schematic representation of Ag_2O/TiO_2(B) NRs HS and the corresponding band alignment at the interface showing the charge separation and the corresponding photodegradation mechanism.

This charge transfer process promotes the charge carriers a longer lifetime reducing their recombination probability, which is consistent with the TRPL results. Adsorbed O_2 and H_2O molecules react with the photogenerated electrons at the interface of the HS to form superoxide radicals (strong reducing agent), and holes can be trapped by hydroxyl groups to form hydroxyl radicals (strong oxidizing agent). Thus a sufficient number of powerful superoxide and hydroxyl radicals are generated, and they decompose the adsorbed organic pollutants. The reaction mechanism goes as follows:[6]

1. $TiO_2(B) \xrightarrow{h\nu} e^- + h^+$
2. $Ag_2O \xrightarrow{h\nu} e^- + h^+$
3. O_2 (at interface) + $e^- \longrightarrow \bullet O_2^-$
4. $H_2O \longrightarrow H^+ + OH^-$
5. $OH^- + h^+ \longrightarrow \bullet OH$
6. Organic dye + $\bullet OH \longrightarrow$ degradation products
7. Organic dye + $\bullet O_2^- \longrightarrow$ degradation products

Under visible light illumination, the holes are accumulated on the Ag_2O surface by transferring electrons to the TiO_2(B) surface. Thus, the TiO_2(B) becomes anionic by gathering electrons, and Ag_2O becomes cationic in nature by accumulating holes. In the HS, Ag_2O NPs are uniformly coated on the TiO_2(B) surface, and thus the HS as a whole behaves cationic in nature from the

surface. As the dye MO is anionic in nature, in aqueous solution, the anionic dye radicals feel columbic attraction to the cations (h^+) on the HS surfaces. Thus, the anionic dye radicals get adsorbed very promptly to the HS surface and react with the hydroxyl radicals (step 6). As the hydroxyl radicals are mainly generated at the Ag_2O surface, the concentration of this radical is very high at the Ag_2O surfaces. Thus, the MO gets decomposed very rapidly with time under the visible light irradiation. Note that MB is slightly cationic in nature. So, in aqueous solution, there is columbic repulsion between the cationic MB radicals and cationic Ag_2O surface in the HS samples. Thus, the adsorption rate of MB dye radicals at the HS surface is slower than that of MO radicals, which results in the slower degradation rate of MB as shown in **Table 2.2**.[25] Nevertheless, the degradation rate is considerably high due to the high density of photoinduced carriers present in the HSs, resulting in the significant degradation of MB by the superoxide and hydroxyl radicals. Thus, the Ag_2O/TiO_2(B) HSs are highly efficient for the visible light photodegradation of dyes irrespective of their ionic nature.

2.4. Summary and Conclusions

In this chapter, we successfully demonstrated the solvothermal growth of porous TiO_2(B) NRs and its uniform surface coating with Ag_2O NPs at the porous sites by co-precipitation method. We extensively investigated the photophysical properties of the as-synthesized samples in order to achieve enhanced visible light photocatalytic efficiency. Important findings of this chapter are summarized below.

1. Ag_2O/TiO_2(B) HSs, especially TA2 shows strong visible light absorption extending to NIR region with relatively low PL intensity and the prolonged life time of the photogenerated charge carriers.
2. HS samples work as excellently visible light photocatalysts for both MO (anionic dye) and MB (cationic dye).
3. Though B-phase TiO_2 is not a very stable phase, we found an HS system with Ag_2O NPs which is rather stable under visible light photocatalysis up to 4^{th} cycle.
4. The degradation rate of MO (0.071 min^{-1}) is quite faster than that of MB (0.057 min^{-1}). A mechanism is proposed on the basis of thermodynamically favoured band structure (type-II) at the interface facilitating the easy separation of carriers. The coulombic interaction

between the catalyst surface and dye molecules explains the faster degradation of MO than MB.

References

1. H. Kazuhito, I. Hiroshi and F. Akira, *Jpn. J. Appl. Phys.*, 2005, **44**, 8269.
2. L. Chen, F. Chen, Y. Shi and J. Zhang, *J. Phys. Chem. C*, 2012, **116**, 8579.
3. Z. Xuming, C. Yu Lim, L. Ru-Shi and T. Din Ping, *Rep. Prog. Phys.*, 2013, **76**, 046401.
4. X. He, Y. Cai, H. Zhang and C. Liang, *J. Mater. Chem.*, 2011, **21**, 475.
5. A. Tanaka, A. Ogino, M. Iwaki, K. Hashimoto, A. Ohnuma, F. Amano, B. Ohtani and H. Kominami, *Langmuir*, 2012, **28**, 13105.
6. W. Zhou, H. Liu, J. Wang, D. Liu, G. Du and J. Cui, *ACS Appl. Mater. Interfaces*, 2010, **2**, 2385.
7. W. Choi, A. Termin and M. R. Hoffmann, *J. Phys. Chem.* , 1994, **98**, 13669.
8. M. Kong, Y. Li, X. Chen, T. Tian, P. Fang, F. Zheng and X. Zhao, *J. Am. Chem. Soc.*, 2011, **133**, 16414.
9. I. Blumberg, J. Starosvetsky, D. Bilanovic and R. Armon, *J Colloid Interface Sci*, 2009, **336**, 107.
10. R. Ghosh, K. Imakita, M. Fujii and P. K. Giri, *Phys. Chem. Chem. Phys.*, 2016, **18**, 7715.
11. B. Santara, P. K. Giri, K. Imakita and M. Fujii, *Nanoscale*, 2013, **5**, 5476.
12. B. Santara, P. K. Giri, K. Imakita and M. Fujii, *J. Phys. D: Appl. Phys.*, 2014, **47**, 215302.
13. B. J. Murray, Q. Li, J. T. Newberg, E. J. Menke, J. C. Hemminger and R. M. Penner, *Nano Lett.*, 2005, **5**, 2319.
14. G. I. N. Waterhouse, G. A. Bowmaker and J. B. Metson, *Phys. Chem. Chem. Phys.*, 2001, **3**, 3838.
15. A. V. Neimark, Y. Lin, P. I. Ravikovitch and M. Thommes, *Carbon*, 2009, **47**, 1617.
16. Y. Wang, L. Liu, L. Xu, X. Cao, X. Li, Y. Huang, C. Meng, Z. Wang and W. Zhu, *Nanoscale*, 2014, **6**, 6790.
17. R. Ramakrishnan, S. J. Devaki, A. Aashish, S. Thomas, M. R. Varma and N. Kpp, *J. Phys. Chem. C*, 2016, **120**, 4199.
18. B. Choudhury, S. Bayan, A. Choudhury and P. Chakraborty, *J Colloid Interface Sci*, 2016, **465**, 1.
19. M. Yang, W. Liu, J.-L. Sun and J.-L. Zhu, *Appl. Phys. Lett.*, 2012, **100**, 043106.
20. B. Choudhury, M. Dey and A. Choudhury, *Appl. Nanosci.*, 2013, **4**, 499.
21. M.-Z. Ge, C.-Y. Cao, S.-H. Li, Y.-X. Tang, L.-N. Wang, N. Qi, J.-Y. Huang, K.-Q. Zhang, S. S. Al-Deyab and Y.-K. Lai, *Nanoscale*, 2016, **8**, 5226-5234.
22. X. Shao, W. Lu, R. Zhang and F. Pan, *Sci. Rep.*, 2013, **3**, 3018.
23. G. B. Hoflund, Z. F. Hazos and G. N. Salaita, *Phys. Rev. B*, 2000, **62**, 11126-11133.
24. D. Sarkar, C. K. Ghosh, S. Mukherjee and K. K. Chattopadhyay, *ACS Appl. Mater. Interfaces*, 2013, **5**, 331.
25. I. K. Konstantinou and T. A. Albanis, *Appl. Catal. B Environ.*, 2004, **49**, 1.

Chapter 3

Role of Surface Plasmons and Hot Electrons on the Multi-Step Photocatalytic Decay by Defect Enriched Ag@TiO_2 Nanorods under Visible Light Illumination

This chapter presents a detailed investigation on the origin of the multi-step sequential degradation of an organic dye, Rhodamine-B (RhB), under visible light illumination by Ag NPs decorated anatase TiO_2 NRs grown by a two-step chemical route. Intrinsic surface defects and localized surface plasmon resonance (LSPR) in the optimized Ag@TiO_2 heterostructure (HS) facilitate strong optical absorption in the entire visible region. The generation of hot electrons and their fast migration away from the interface promoting the enhanced visible light photocatalysis are discussed in details based on the steady-state and time-resolved photoluminescence and photoconductivity studies. The dye degradation kinetics with HSs follows a sequential rate process with two distinct exponential decay functions, which give two different degradation rate constants. Simultaneous photoreduction induced enhanced plasmonic effect of Ag NPs and fast N-de-ethylation of RhB demonstrate the faster rate constant in the 2nd degradation zone than the 1st zone. This study offers new insights in understanding the mechanism of photocatalysis with multi-rate constants and thus designing the next generation photocatalysts.

3.1. Introduction

In the previous chapter, we have discussed the solvothermal growth of metastable TiO_2(B) porous nanorods (NRs) and successfully demonstrated its excellent stability as a visible light photocatalyst after the surface coating with Ag_2O nanoparticles (NPs). Narrow band gap Ag_2O was used as visible light sensitizer as pure TiO_2 is a wide band gap (~3.2 eV) material and thus the activation of its photocatalytic activity requires UV light that contributes less than 5% of the sunlight. Further, one of the most promising techniques to harvest the solar energy is to modify the surface morphology of TiO_2 and explore the localized surface plasmon resonance (LSPR) by plasmonic nanoparticles, e.g., Ag, Au, Pd and Pt[1-3]. Properly designed plasmonic nanostructures can drive coherent oscillation of confined free electrons on metal NPs with the identical frequency as the incident radiation known as LSPR, which in turn creates an intense, highly

localized electromagnetic field.[4] After the light absorption and LSPR excitation in the plasmonic nanostructures, a non-radiative electromagnetic decay takes place on a femtosecond timescale by transferring the energy to nearest hot electrons.[5] Among various plasmonic materials, Ag is regarded as the most significant and thus Ag based various nanostructures like Ag@AgCl[6], Ag/AgCl/TiO_2[7], Ag/TiO_2[8] and Ag_2O/TiO_2[9] have been studied extensively for the efficient visible light photocatalysis. Further, the hot electrons having energy (1-4 eV)[5] greater than the Schottky barrier can easily migrate from the metal to semiconductor surface, and the internal electric field developed at the space charge region accelerates the charge separation at the metal/semiconductor interface.[10] Thus, plasmonic nanostructures possess highly enhanced photocatalytic activity under visible light irradiation. Despite intense research on the TiO_2 based plasmonic nanostructures for photocatalysis, a proper understanding of the mechanism of catalytic enhancement and the degradation rate kinetics is still lacking. In this chapter, Ag@TiO_2 HS is studied systematically for the visible light photocatalysis with multi-step sequential degradation rate constants. Mechanism of multi-step degradation kinetics is elucidated.

3.2. Experimental Details

3.2.1. Sample Preparation

3.2.1.1. Preparation of TiO_2 NRs

TiO_2 nanostructures were synthesized by a typical solvothermal process as described in **Chapter 2, Section 2.2.1.1**. After the calcination at 700 °C for 5 h in air, pure anatase TiO_2 NRs are grown. To confirm the crystal structure and phase of the obtained product, XRD and micro-Raman analyses were performed.

3.2.1.2. Growth of Ag@TiO_2 NRs heterostructure

Ag NPs decorated TiO_2 NR HSs with various weight ratios (Ag:TiO_2) from 1:2 to 2:1 were synthesized by a photoreduction method. Typically, for 1:1 weight ratio, 0.05 g of TiO_2 NRs was dispersed in 25 ml of ethanol, and then 0.42 g of $AgNO_3$ (0.1 M) was dissolved into the above-suspended solution. The above mixture was then stirred magnetically for 1 h to reach adsorption equilibrium. Subsequently, the suspension was exposed to 250 W UV irradiation for 5 min under vigorous magnetic stirring to form the Ag NPs on the TiO_2 platform. The Ag@TiO_2 HS was obtained by washing with DI water several times, filtration and drying process. A summary of the samples studied with sample codes is provided in **Table 3.1**.

Table 3.1: *Sample specification and effective band gap of different samples, calculated from the respective Tauc plot.*

Sample composition		***Sample code***	***Effective band gap (eV)***
Weight ratio of			
Ag	**TiO_2**		
0	1	TiO_2	3.20
1	1	TA11	2.89
1	2	TA12	3.00
2	1	TA21	2.94
2	3	TA23	3.03
3	2	TA32	2.71

3.2.2. Photocatalytic Degradation under Visible Light

The photocatalytic activity of pure TiO_2 NRs and Ag@TiO_2 HSs has been evaluated considering the photodegradation of Rhodamine-B (RhB) as model dye under visible light irradiation. The details of the visible light source, experimental arrangements and photocatalysis methods were discussed in **Chapter 2, Section 2.2.2**. In this case, 50 ml aqueous suspension of RhB (10 mg/L) and 20 mg of catalyst powders have been placed in a 100 ml beaker. At chosen irradiation intervals, 3 ml of solution was collected and centrifuged to remove the catalyst particles to estimate the residual concentration of the dye solution.

3.2.3. Characterization Techniques

The details of the characterization techniques (XRD, XPS, Raman, FESEM, TEM, PL etc.) used to study the systems were described in **Chapter 2, Section 2.2.3**. In this case, a 355 nm diode laser excitation was used to record the room temperature steady-state photoluminescence (PL) spectra. Photoconductivity measurement was performed on the pristine TiO_2, and TA32 HS samples in the form of pellets (diameter 10 mm) using a microprobe station (ECOPIA EPS-500) connected to a source meter (Keithley 2400) to measure the dark- and photo-current under a constant bias voltage. A 250 W Xenon lamp (Newport, 10 USA) equipped with a 400 nm cut-off filter was used as a light source to excite the sample. This confirms the excitation of the sample only with the visible light. The setup is interfaced with a computer to collect the data using Lab Tracer 2.0 software.

3.3. Results and Discussion

3.3.1. Morphology and Composition Studies

The morphology and microstructural properties of pristine TiO_2 NRs and Ag@TiO_2 HSs were first characterized by FESEM. **Fig. 3.1(a)** shows the FESEM image of pure TiO_2 NRs with diameter ~40-120 nm and lengths up to a few μm, while **Fig. 3.1(b)** shows the FESEM image of Ag@TiO_2 HS (TA32, see **Table 3.1**). Though Ag NPs coated on the TiO_2 NRs have a sufficiently broad size distribution, particles only with size ≥ 30 nm were discernable due to the limitation of FESEM imaging. EDX analysis on as-grown TiO_2 NRs reveals that it is composed of only Ti and O elements (see **Fig. 3.1(c)**), while the **Fig. 3.1(d)** confirms that the HS consists of Ti, Ag and O elements.

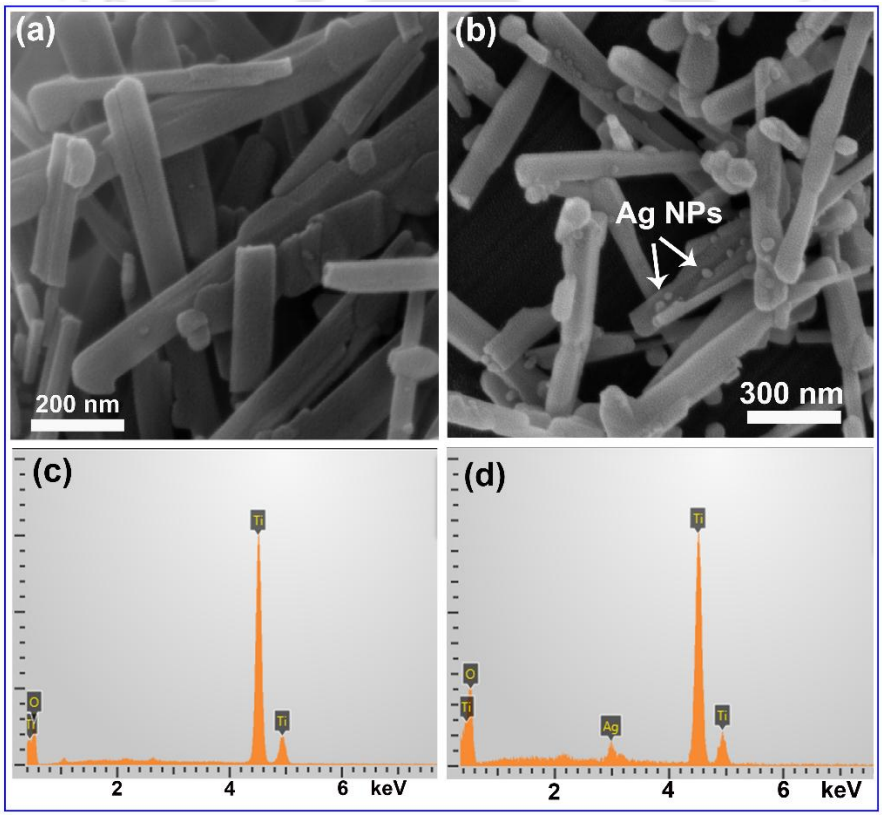

Fig. 3.1. FESEM images of (a) pristine TiO_2 NRs and (b) TA32 HS. (c, d) the corresponding EDX spectra, respectively.

To study the high-resolution surface morphology and structure of the pristine TiO_2 NRs and its HSs, TEM images are acquired for the respective samples. **Fig. 3.2(a)** shows the TEM image of a pristine TiO_2 NR, while Figs. 3.2(b, c and d) depict the typical TEM images of Ag@TiO_2 heterojunctions named as TA12, TA21 and TA32, respectively. Clearly, Ag NPs are

uniformly distributed over the TiO_2 NRs for all the HS samples. Interestingly, the distribution of Ag NPs is highly uniform in the TA32 sample in comparison to the other HS samples. **Fig. 3.2(e)** shows a magnified view of **Fig. 3.2(d)**, which proves further the spatial uniformity of Ag NPs with the uniformity in its size. For higher weight ratio of Ag (TA21 shown in **Fig. 3.2(c)**), the distribution is still uniform, but with some agglomeration, which may be due to the higher concentration of Ag.

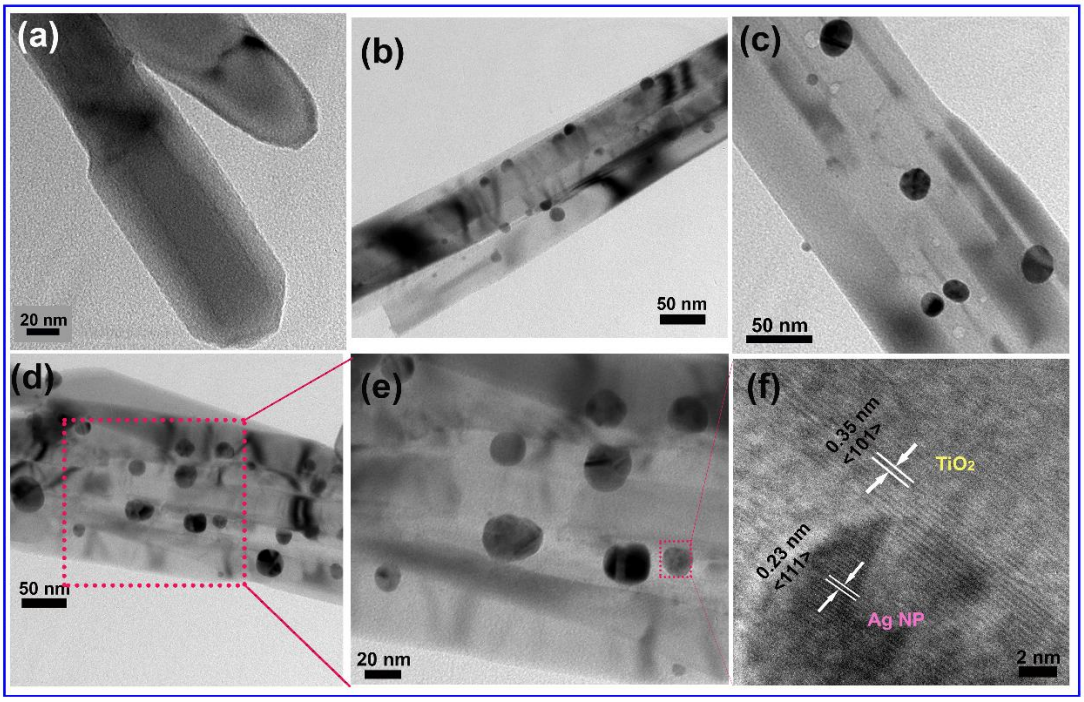

Fig. 3.2. (a) TEM image of faceted TiO_2 NRs, (b and c) TEM images of TA12 and TA21 HS, respectively. (d) TEM image of TA32 HS showing Ag NP decoration, (e) the enlarged view of image shown in (d), and (f) HRTEM lattice image of HS showing the lattice spacing of Ag and TiO_2 with respective crystal orientations.

Fig. 3.2(b) shows the TEM image of TA12, which reveals the uniform decoration of Ag NPs with nearly uniform size. In both the cases of extremely high (TA21) and low (TA12) concentration of Ag, we observe comparatively lower density of Ag NPs on the TiO_2 surface, which may be due to the aggregation in case of TA21 and lower concentration of precursor material for TA12. **Fig. 3.2(f)** shows the HRTEM lattice fringe pattern of TA32 HS, which clearly reveals the simultaneous presence of crystalline Ag and TiO_2. It is clear from **Fig. 3.2(d, e)** that the Ag NPs are decorated on the uneven TiO_2 surface, which enables close contact between them. Thus, the Ag NPs are tightly coupled with the TiO_2 surface so that an efficient charge transport can be expected at the interface of the HS. The lattice spacing of TiO_2 and Ag has been calculated by measuring the intermediate distance between the lattice fringes. Pure

anatase TiO_2 with (101) crystal planes (d = 0.35 nm) and cubic Ag with (111) crystal planes (d = 0.23 nm) are confirmed from the lattice fringe image. It is observed that the average size of decorated Ag NPs is increasing with increasing the Ag weight ratio. The average NP size is calculated as 17.64 nm for TA32 and 21.42 nm for TA21, respectively. Higher concentration of $AgNO_3$ may be leading to the fusion of Ag NPs into larger size ones.

3.3.2. Structural Analysis

3.3.2.1. XRD and Raman Analyses

To confirm the structure, phase and crystallinity of the as-synthesized TiO_2 NRs and Ag@TiO_2 HSs, XRD pattern of each sample has been recorded, and the results are shown in **Fig. 3.3(a)**. Each diffraction peak of TiO_2 NRs (labeled with '*' symbol) corresponds to pure anatase phase (JCPDS file # 841285) and the peaks corresponding to blue circles (filled) imply the presence of Ag NPs, which matches exactly with the JCPDS file # 040783. The diffraction peaks of TiO_2 are extremely sharp clearly implying its highly crystalline nature. The phases of anatase TiO_2 and Ag co-exist in the Ag@TiO_2 HS crystals. Note that the XRD data shows a marginal downshift in the TiO_2 peaks in the HS sample as compared to the pristine TiO_2 NRs. This may imply a tensile strain in the TiO_2 NRs in the HS due to strong coupling of the TiO_2 and Ag lattice, further discussed by Raman and XPS results.

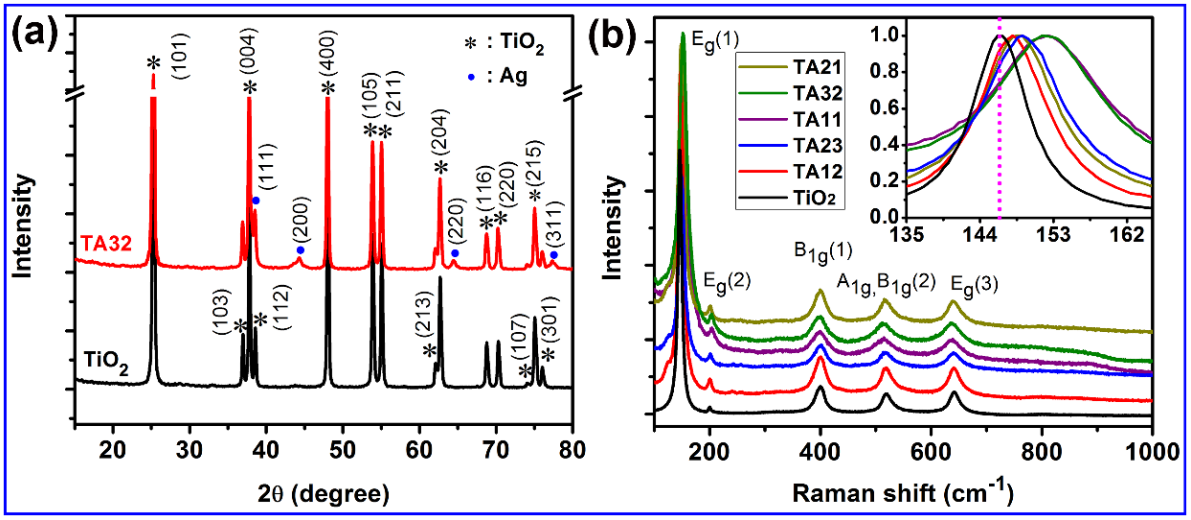

Fig. 3.3. (a) XRD patterns of pristine TiO_2 NRs and Ag@TiO_2 NR HS (TA32). The curves are vertically shifted for clarity of presentation. (b) Raman spectra of pristine TiO_2 NRs and various Ag@TiO_2 NR HSs. The curves are vertically shifted for clarity of presentation. All Raman peaks correspond to the anatase phase of TiO_2. The inset shows a magnified view of the Eg(1) peak for all samples. The dotted vertical line indicates the peak position of bare TiO_2 NRs, and it shows a clear shift of the Eg(1) mode after Ag NPs loading.

Fig. 3.3(b) demonstrates a comparison of the micro-Raman spectra for all samples. The Raman spectra of anatase TiO_2 phase has six active Raman modes: $E_g(1)$, $E_g(2)$, $B_{1g}(1)$, A_{1g}, $B_{1g}(2)$ and $E_g(3)$. The most prominent Raman mode, $E_g(1)$, appears to be at 144 cm^{-1}.[11] However, in the present case, the as-synthesized TiO_2 NR shows the $E_g(1)$ peak at 146.4 cm^{-1}, which may be due to the change in the oxygen stoichiometry in the TiO_2 crystal, as confirmed from the XPS analysis discussed later. With the loading of Ag NPs, the Raman peak gets broadened and shifts towards the higher frequency side, as tabulated in **Table 3.2**. In particular, the blue shift and full width at half maximum (FWHM) of the Raman peak are highest for TA11/ TA32. Comparison of the Raman shift and FWHM of band $E_g(1)$ is shown as an inset in **Fig. 3.3(b)**. As compared to the pristine TiO_2, TA11 and TA32 samples show nearly double FWHM with a blue shift of ~5.51 cm^{-1} and ~5.58 cm^{-1}, respectively. Such a large blue shift and high FWHM of $E_g(1)$ can be interpreted as non-stoichiometry in the TiO_2 lattice due to oxygen vacancies and strain induced by the vacancy related Ti relaxation and strong interaction between TiO_2 and Ag atoms.[12] It is observed that the oxygen vacancy/defect is increasing with the Ag loading amount and reaches an optimum value for the TA32 sample and then again it decreases. This may be due to the higher aggregation (for TA21), which leads to the formation of larger Ag NPs and consequently the interfacial contact and hence their interaction reduces. As the defects and disorders present in the TiO_2 lattice disturb the B_{1g} mode more intensely than the $E_g(1)$ mode,[13] we have studied the $B_{1g}(1)$ for all the samples. A large broadening of $B_{1g}(1)$ mode for TA32 (FWHM=35.22 cm^{-1}) and TA11 (34.00 cm^{-1}) samples have been observed as compared to that of the pristine TiO_2 (20.44 cm^{-1}). Thus, Raman studies revealed that the blue-shift and increase in FWHM in the specific Raman band is due to the nonstoichiometric oxygen defects in the Ag@TiO_2 HSs.

Table 3.2: *Summary of the changes in $E_g(1)$ Raman mode and relative area (%) under the Ti^{3+} and O_V peaks in the XPS spectra for different samples.*

Sample code	$E_g(1)$ mode		Ti^{3+}% in Ti 2p XPS spectrum	O_V% in O 1s XPS spectrum
	Frequency (cm^{-1})	FWHM (cm^{-1})		
TiO_2	146.44	8.16	17.4	13.2
TA11	151.95	17.23	-	-
TA12	147.95	10.11	-	-
TA21	148.70	11.27	-	-
TA23	149.26	12.47	-	-
TA32	152.02	16.27	18.6	26.3

3.3.2.2. XPS Analysis

In order to investigate the chemical valence state and surface defects of as-synthesized TiO_2 nanostructures, XPS studies were carried out. **Fig. 3.4(a, b)** show the Ti 2p core level XPS spectra of pristine TiO_2 NRs and Ag@TiO_2 HS (TA32). Each peak has been deconvoluted with two symmetric Gaussian peaks.

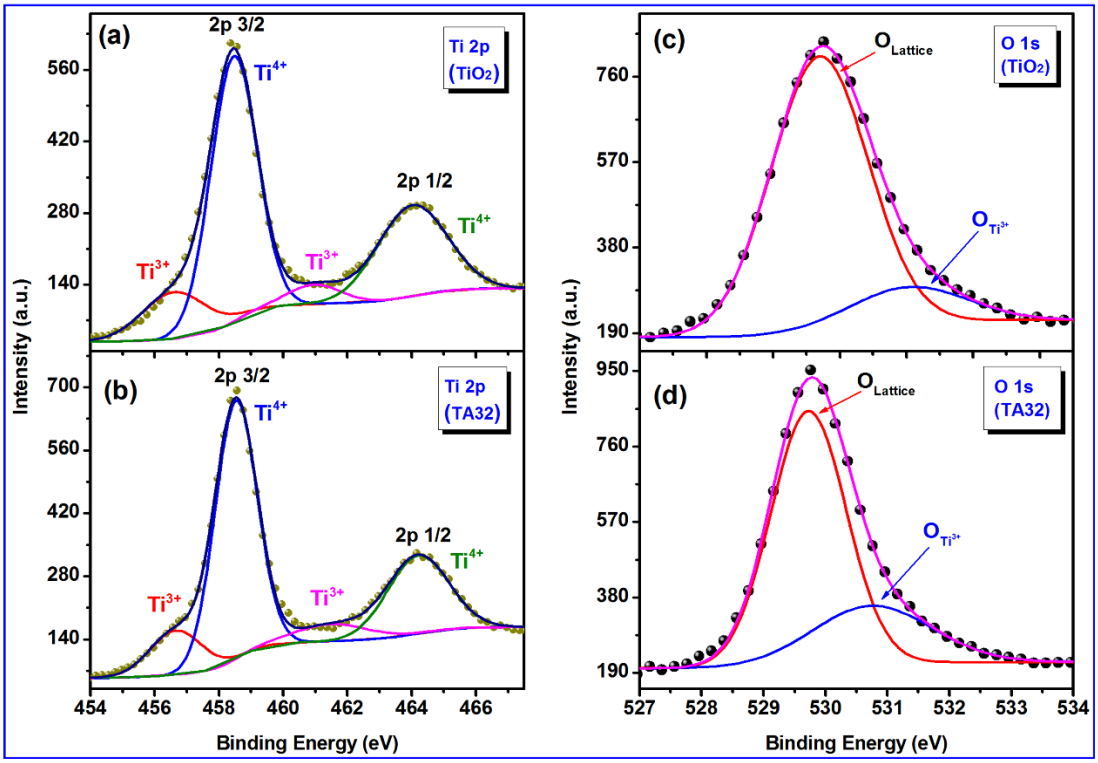

Fig. 3.4. (a, b) The Ti 2p core level XPS spectra for pristine TiO_2 NRs and TA32 HS, respectively. (c, d) The O 1s core level XPS spectra for pristine TiO_2 and TA32 HS, respectively. Each data is fitted with Shirley baseline. The symbols represent the experimental data, and the solid lines correspond to the Gaussian fits. The identity of each fitted peak is denoted with corresponding charge states in the respective cases.

The major Ti 2p doublet peaks for both pristine TiO_2 and TA32 HS exhibit a tail in the lower binding energy side, which indicates the presence of lower valence states of Ti. The main two peaks centered at around 458.5 eV and 464.2 eV are attributed to the +4 valence state for the Ti $2p_{3/2}$ and Ti $2p_{1/2}$, respectively, which further confirms the formation of TiO_2. Additionally, two Gaussian peaks centered at ~456.6 eV and ~461.5 eV were detected, which can be attributed to +3 valence state of Ti $2p_{3/2}$ and Ti $2p_{1/2}$, respectively, confirming the presence of oxygen vacancy defects in the system.[9] However, no measurable shift in binding energy has been detected in the Ti 2p spectra after HS formation. The relative Ti^{3+}% in the Ti 2p spectra was calculated as 17.4% for pristine TiO_2 NRs and 18.6% for TA32 HS, which again shows an indication of

enhancement of oxygen vacancy after HS formation. **Fig. 3.4(c, d)** display the O 1s spectra of pristine TiO_2 and TA32 HS, respectively. Each spectrum follows a long tail in the higher energy region making the spectrum asymmetric, and this tail implies the presence of defects in the sample. Each O 1s spectrum can be fitted with two symmetric Gaussian peaks, as reported in the literature.[9, 13] As discussed in **Chapter 2, Section 2.3.2.1**, the intense peak at ~529.7 eV is attributed to the TiO_2 crystal lattice, and the other peak at ~531.1 eV can be assigned to the Ti-O bond (O_{Ti}^{3+}). We have calculated the relative O_{Ti}^{3+}% in the O 1s spectra for both the samples and found it to be 13.16% for pure TiO_2, and 26.34% for TA32 HS, which further proves a substantial increase in the oxygen vacancy concentration in the heterostructured systems. These defect states may also serve as shallow donors and enhance charge transfer at the interface, which in turn improves the overall photocatalytic performance. A summary of the fitting parameters with relative vacancy percentage is shown in **Table 3.2**.

Fig. 3.5(a) shows a comparison of Ag 3d core-level XPS spectra of TA32 HS sample before and after photocatalysis. Before photocatalysis, the system exhibits an asymmetry in the higher binding energy region having Ag $3d_{5/2}$ peak at ~367.9 eV, which corresponds to the Ag^+ valence state and the asymmetry indicates the presence of different valence states of Ag in the HS sample.[14] This could happen due to the following two reasons: firstly, during the photoreduction process, all Ag^+ ions in the solution do not get reduced into metallic Ag^0, and the unsaturated Ag^+ ions are still present in the HS. Secondly, the reverse-spill over as the oxidation mechanism of deposited Ag^0 due to the oxygen ions in the atmosphere.[15]

$$4Ag^0 + O_2^- \longrightarrow 2Ag_2O + e^-$$

$$2Ag^0 + O^- \longrightarrow Ag_2O + e^-$$

Interestingly, after photocatalytic reaction, it is observed that the Ag 3d spectrum is relatively more symmetric and it shifts to the higher binding energy region having the Ag $3d_{5/2}$ peak at ~368.4 eV, which corresponds to the metallic Ag^0 valence state and the symmetry in the spectrum indicates that Ag is mostly in a particular valence state i.e.; in Ag^0 state and the Ag^+ state has been reduced.[14] Therefore, it can be concluded that during the photocatalysis the unsaturated Ag^+ ions get reduced into metallic Ag^0 state since the light source contains some UV photons (range of the source ~390-800 nm). For a better understanding, each peak of the Ag 3d spectra for TA32 sample has been deconvoluted into two symmetric Gaussian curves, as shown in **Fig. 3.5(b, c)**, before and after photocatalysis, respectively. It can be noted that the

deconvolution of Ag 3d asymmetric spectrum of TA32 sample before photocatalysis gives the relative percentage of Ag^{+} and Ag^{0} as 48.17% and 51.83%, respectively.

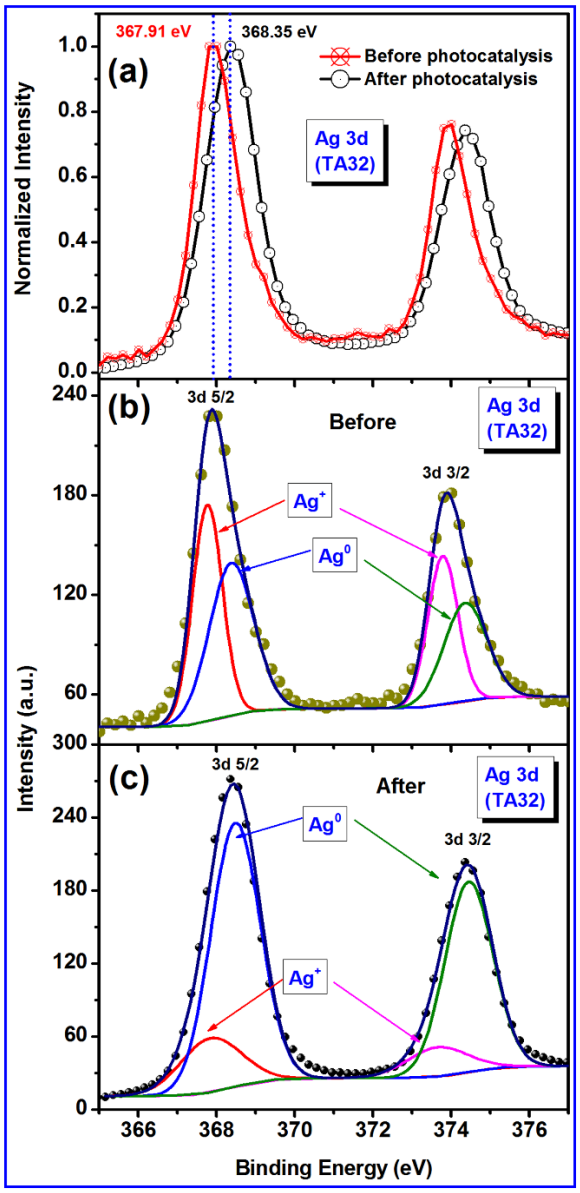

Fig. 3.5. (a) A comparison of Ag 3d core-level XPS spectra of sample TA32, before and after photocatalysis. The dotted vertical lines indicate the blue shift of the spectrum after photocatalysis. (b), (c) The Gaussian fit of each spectrum. Charge state associated with each peak is labeled.

On the other hand, deconvolution of the symmetric Ag 3d spectrum after photocatalysis provides the relative percentage of Ag^{+} and Ag^{0} as 18.35% and 81.65%, respectively. Thus, the concentration of Ag^{0} increases dramatically after photocatalysis. Further, the XPS analyses reveal the different oxidation states of Ti and Ag in the HS sample before and after photocatalysis clearly establishing the presence of defects induced in the system.

3.3.3. Optical Analysis

3.3.3.1. UV-Vis Absorption Study

Fig. 3.6(a) shows a plot of the K-M function of different samples depicting their absorption spectra and **Fig. 3.6(b)** shows the $(F(R)h\nu)^{1/2}$ vs. $h\nu$ plot for the calculation of effective band gap (indirect) of the HSs. In addition to the UV absorption band, Ag@TiO_2 heterojunctions exhibit a new absorption band in the visible-NIR region having a peak centered at 515-533 nm, as a consequence of the surface plasmon resonance (SPR) absorption of Ag NPs.[16]

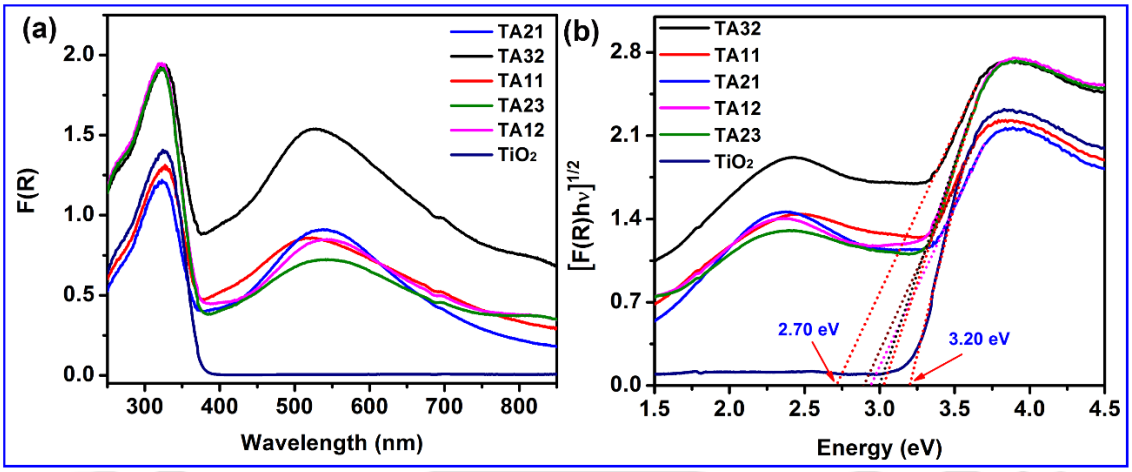

Fig. 3.6. (a) Kubelka–Munk plot, F(R), derived from the diffuse reflectance spectra of different samples. (b) Corresponding Tauc plot $[(F(R)h\nu]^{1/2}$ vs. hν plot) considering the indirect bandgap nature of the TiO_2 samples. Note that, all the HS samples show strong visible absorption band centered at ~2.3 eV.

It can be noted that the position and FWHM of the SPR peak vary with the loading amount of Ag NPs. The peak intensity, position and its broadening depend on the Ag NPs size, density, its distribution on the TiO_2 NRs and also the relative percentage of Ag^0 and Ag^+ in the HSs. As evident from the data, pristine TiO_2 NRs exhibit a sharp absorption edge ~380 nm and at a higher wavelength (visible region) the absorbance is negligibly low. However, when coupled with Ag NPs, Ag@TiO_2 HSs exhibit strong absorption in the UV-visible-NIR range of 200-850 nm showing a broad and intense visible absorption band with a tail extending to NIR region. Though each HS sample exhibits high visible absorption, the HS with Ag and TiO_2 in 3:2 weight ratio (TA32 HS) shows the highest absorption (~1.8 times stronger than other HS samples) in the visible to NIR region. This can be explained as follows. For the TA32 HS, the concentration of $AgNO_3$ in the solution and UV exposure time during the photoreduction synthesis reach the optimum value for the maximum reduction of Ag^+ ions into Ag^0 with uniform and dense

distribution on TiO_2 surfaces and comparatively less Ag^+ is present. Thus, the TA32 HS shows uniform size distribution and optimum density of Ag NPs on the TiO_2 surfaces. For the visible light sensitization by Ag NPs, the HSs are expected to have high solar light harvesting and hence enhanced visible light photocatalytic efficiency. Interestingly, the effective band gap of the TiO_2 NRs is reduced after loading with Ag NPs. Considering the indirect nature of the band gap in the TiO_2 NRs as well as its HSs, the effective band gap of the respective samples has been estimated using the Tauc plot, as shown in **Fig. 3.6(b)**.[17] After decorating with Ag NPs, the effective band gap energy of TiO_2 NRs has been tuned in the range 2.71-3.03 eV, while the pristine TiO_2 NRs exhibit a band gap of 3.2 eV. The effective band gap of each sample is tabulated in **Table 3.1**. The band gap energy modification for the HS samples may be due to the strong coupling between the Ag NPs and TiO_2 NRs. It is noteworthy that in case of TA32, the effective band gap is found to be the lowest (2.71 eV) among all samples, which implies that Ag NPs and TiO_2 NRs facilitate large band bending at the interface and may have high carrier concentration at room temperature. This turns out to be extremely beneficial for the efficient visible light photocatalysis by the HSs samples, as discussed later.

3.3.3.2. Photoluminescence study

Nature of defects, kinetics of charge recombination and the migration of the photogenerated charge carriers can be explored from the photoluminescence (PL) measurement. **Fig. 3.7(a)** shows a comparison of steady state PL spectra of pure TiO_2 NRs and the Ag@TiO_2 (TA32) HS with an excitation wavelength of 355 nm. It is observed that the introduction of Ag NPs on the surface of TiO_2 NRs greatly influences the PL intensity of TiO_2 NRs. The PL intensity of TiO_2 NRs is observed to be reduced by ~3 times after the decoration with Ag NPs, though the nature of the PL spectrum remains unaltered. In order to elucidate the origin of the broad visible PL from TiO_2 NRs before and after Ag NPs coating, each PL spectrum is deconvoluted with four Gaussian peaks. The deconvoluted PL spectra for pristine TiO_2 NRs and TA32 HS are shown in **Fig. 3.7(b)** and **Fig. 3.7(c)**, respectively. The deconvoluted four Gaussian peaks are centered at 433.6 (peak 1), 470.9 (peak 2), 510.3 (peak 3), 622.8 (peak 4) nm for TiO_2 NRs and at 434.1 (peak 1), 475.7 (peak 2), 529.4 (peak 3), 603.6 (peak 4) nm for TA32, respectively. It can be noted that the center of the peaks of the individual bands of sample TA32 and TiO_2 NRs are almost the same. The identity of each of the Gaussian fitted PL emission matches with the emission peaks explained in **Chapter 2, Section 2.3.4.2**.[9]

Though the HS samples are found to be more defect enriched than the pristine TiO_2 NRs (confirmed from Raman and XPS), the intensity of each Gaussian fitted PL peak is strongly reduced after the surface coating with Ag NPs.

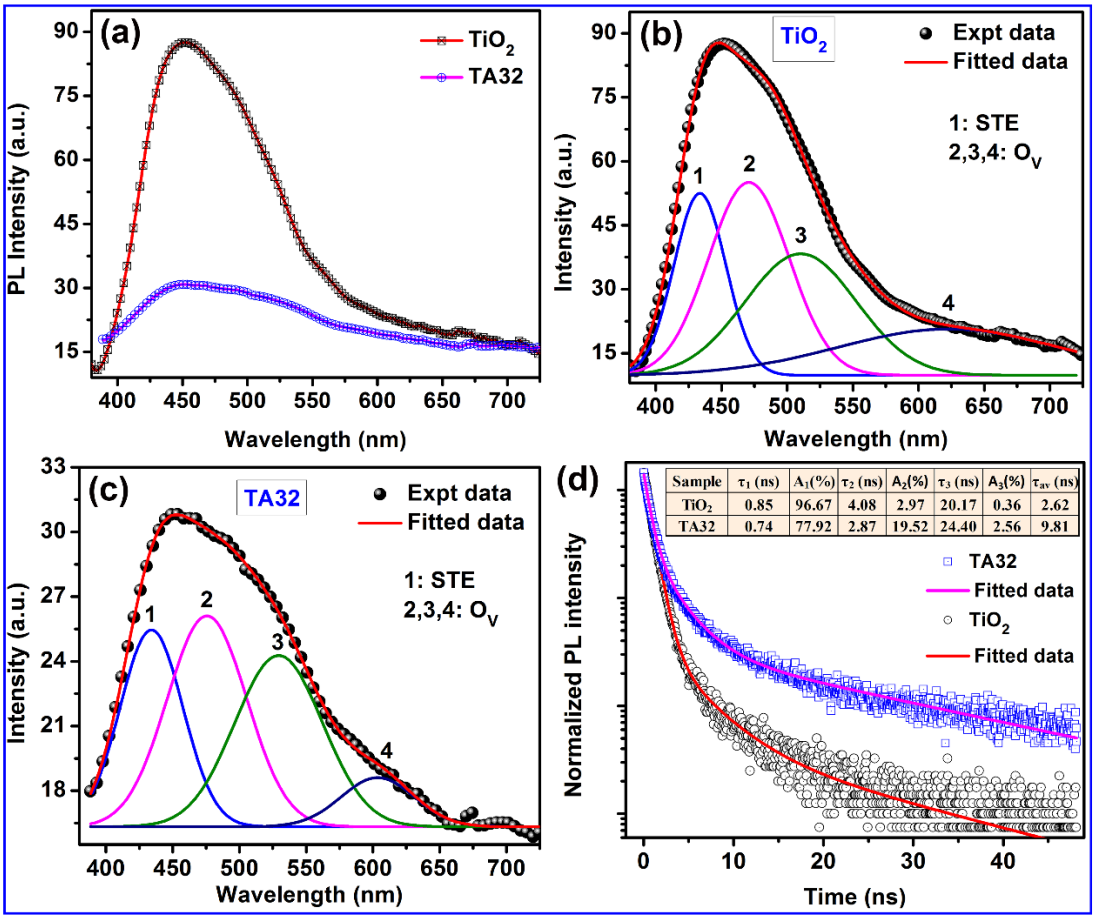

Fig. 3.7. (a) A comparison of the PL spectra of pristine TiO_2 NRs and Ag@TiO_2 HS (TA32) excited with 355 nm laser. (b, c) Gaussian fitted PL spectra of pristine TiO_2 NRs and TA32, respectively. (d) A comparison of TRPL spectra of pristine TiO_2 NRs and TA32 monitored at 471 nm (emission) with 375 nm excitation. The symbols represent the experimental data, and solid lines represent the corresponding tri-exponential fit. The inset shows the details of the lifetime of carriers in different samples.

The lower PL intensity signifies the strong coupling between the Ag and TiO_2, facilitating the efficient charge transfer resulting to the lower recombination probability. Another possible way is the formation of Schottky junction at the Ag/TiO_2 interface and the buildup of internal electric field directed from TiO_2 to Ag that facilitates the forced as well as fast lane charge transfer from Ag to TiO_2 surface[10].

3.3.3.3. Time-Resolved Photoluminescence Study

Time-resolved photoluminescence (TRPL) measurement was performed on pristine TiO_2 NRs, and Ag@TiO_2 NR HS (TA32) with 375 nm laser excitation and the emission was monitored at 471 nm. The details of the time constants (τ) of pristine TiO_2 NRs and TA32 HS are tabulated in the inset of Fig 3.7(d). The tri-exponential fit suggests that three different states contribute to the TRPL spectra in each sample, consistent with the steady-state PL spectra. It can be noted that the average lifetime (τ_{av}) is considerably increased after Ag loading from 2.62 ns to 9.81 ns, resulting in the slower decay in TA32. A longer decay lifetime clearly indicates lower recombination and greater separation efficiency of photogenerated e–h pairs. The efficient charge migration at the interface prolongs the lifetime of the photogenerated excitons, and thus, a higher concentration of charge carriers are available near the interface of the HS, enhancing the visible light photocatalytic performance[9], as discussed below.

3.3.3.4. Photoconductivity Study

To investigate the generation of LSPR induced hot electrons in the Ag NPs anchored TiO_2 HSs and their role in the enhanced visible light photocatalysis, visible light photoresponse measurements at a fixed bias voltage (5V) were carried out on the pristine TiO_2 NRs and TA32 HS. In dark condition, the current for TA32 is measured as ~35 nA, which is ~4 times higher than that of pristine TiO_2 NRs (9 nA). This may be attributed to the higher carrier density in the HS samples than the pristine one, confirmed from the PL, Raman and XPS analyses. Under visible light illumination, the current of TA32 and pristine TiO_2 NRs are measured to be 5080 nA and 990 nA, respectively.

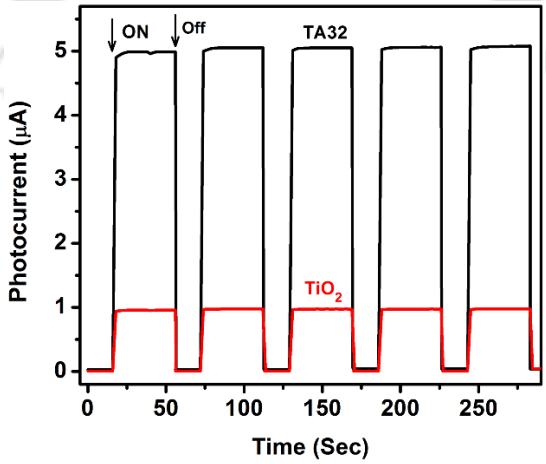

Fig. 3.8. Dark and photocurrent response of pristine TiO_2 and TA32 under visible light irradiation ON-Off process, at a fixed bias voltage 5V.

Thus, the photocurrent gain of pristine TiO_2 NRs is ~110 with respect to the dark current, while it is ~150 for the TA32 HS, as shown in **Fig. 3.8**. The enhancement in the photocurrent in pure TiO_2 NRs may be due to the generation of electrons in the conduction band of TiO_2, which is likely due to the sub-bandgap defects in TiO_2. However, the enormous enhancement in the photocurrent for TA32 HS is contributed by sub-bandgap defects as well as the generation and easy interfacial transfer of LSPR induced hot electrons from the Ag side to the TiO_2. These photogenerated carriers contribute significantly to the enhanced photocatalytic performance of the HS sample.

3.3.4. Visible Light Photodegradation Studies

3.3.4.1. Photodegradation of RhB

RhB was chosen as reference dye for the evaluation of visible light photocatalytic activity of pristine TiO_2 NRs and its heterojunctions with Ag NPs (details shown in **Table 3.3**). **Fig. 3.9(a)** shows a comparison of the photodegradation performance of various samples including pristine TiO_2 NRs and commercial P25 catalyst under visible light irradiation. In order to compare the efficiencies, self-decomposition of the dye solution was also examined under identical conditions. The HS samples show enhanced photodegradation efficiency as compared to the pristine TiO_2 NRs; details are tabulated in **Table 3.3**.

Table 3.3: Two-stage *degradation of RhB by various catalysts under visible light and the corresponding pseudo-first-order rate constants.*

Catalyst name	***Maximum degradation (%)***		***Total degradation after 100 min (%)***	***Rate constant (min^{-1}) $\times 10^{-3}$***	
	1st stage	***2nd stage***		***1st stage***	***2nd stage***
Without catalyst	12.2	-	12.2	1	-
TiO_2 NRs	65.9	-	65.9	8	-
TA11	77.9	20.0	97.9	23	60
TA12	47.6	28.3	75.9	9	19
TA21	54.5	25.0	79.5	12	20
TA23	47.8	13.8	61.6	9	12
TA32	82.9	17.1	100	33	83
P 25	50.4	-	50.4	7	-

Note that among all the HS samples, TA32 shows highest photodegradation efficiency. **Fig. 3.9(b)** shows a digital photograph demonstrating the systematic change in colour of RhB solution due to the visible light induced photodegradation of RhB by TA32 at an interval of 10 min. Before the illumination of visible light, the catalysts were well dispersed in the dye solution and magnetically stirred for 45 min in the dark. This established the equilibrium between dye molecules and the catalyst surfaces. After reaching the adsorption/desorption equilibrium (at 0 min of irradiation) we have observed that ~85% and ~92% of dye still present in the solution of pristine TiO_2 and HSs, respectively. Thus, it can be noted that after the decoration of Ag NPs, the dye adsorption by TiO_2 NRs has been decreased from 15% to 8%. This may be due to the presence of pores on the TiO_2 surface into which the dye molecules get adsorbed. However, after the formation of HSs, some of these pores have been filled by the Ag NPs leading to the lower adsorption efficiency.

3.3.4.2. Degradation Rate Kinetics of RhB

Photodegradation kinetics of several common organic dyes (methyl orange, methylene blue, RhB, etc.) is usually described by a pseudo-first order rate kinetics from Langmuir-Hinshelwood expression.[9, 18] **Fig. 3.9(c)** shows a comparison of the plots of $\ln\left(\frac{C_t}{C_0}\right)$ vs. irradiation time (t) for different samples. The degradation characteristics could be elucidated by the corresponding linear fit, and the value of its slope (k-value) is a measure of the rate constant. Note that our data cannot be fitted by a single or bi-exponential decay behaviour. It is clear from the figure that each $\ln\left(\frac{C_t}{C_0}\right)$ vs. time curve of HS samples can be divided into two decay zones/steps with two distinct linear fits and thus two different k values, whereas the pristine TiO_2 NRs and P25 follow a single decay zone with a single k value 0.008 min^{-1} and 0.007 min^{-1}, respectively. **Fig. 3.9(d)** shows the percentage degradation of dye as a function of irradiation time fitted with exponential functions. Note that, the data for HSs can be well fitted by two distinct exponential functions, while the degradation kinetics for the pristine TiO_2 NRs and P25 follow a single step decay with a perfect single exponential fit. Interestingly, for TA32, k-value (0.083 min^{-1}) is found to be extremely high in the second zone, an order of magnitude higher than that of the commercial P25 and about 2.5 fold stronger than that in the first zone (0.033 min^{-1}) (see **Fig. 3.9(c)**). Further, in comparison to pristine TiO_2 NRs, this k-value is about 10 times stronger in the second zone and 4 times stronger in the first zone.

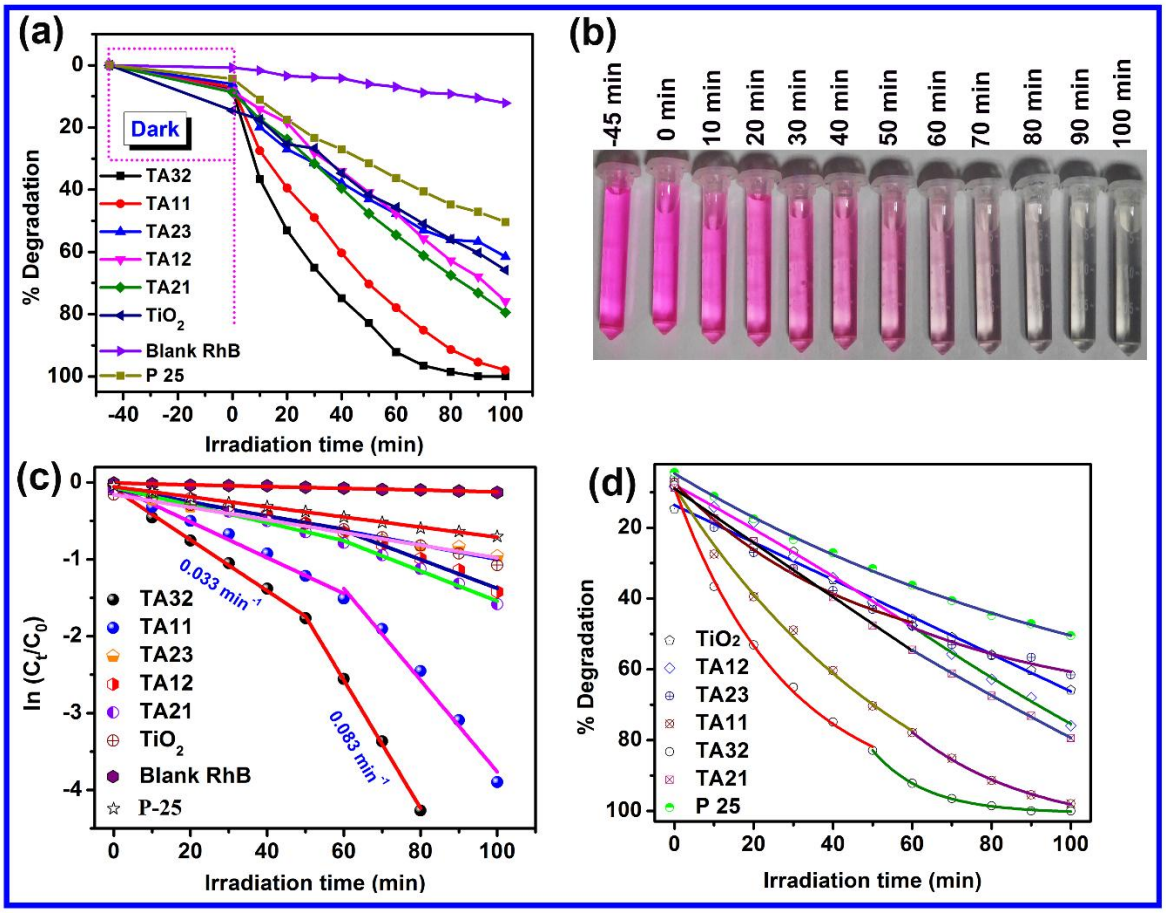

Fig. 3.9. (a) Comparison of the photocatalytic degradation profiles of RhB with and without the presence of different catalyst samples under visible light irradiation. (b) Digital photograph of the degradation induced colour change of RhB in the presence of TA32 after exposure to visible light for various time durations. (c) A plot of $\ln\left(\frac{C_t}{C_0}\right)$ vs. time for different samples and corresponding linear fitting. (d) Comparison of degradation plots showing exponential decay in two different compartments.

Considering the visible light irradiation, the high rate constant of 0.083 min^{-1} of the HS sample is very significant. Note that, most of the reported k-values under visible light irradiation are about one order of magnitude lower than our result.[19] It is observed that a large fraction of total dye is decomposed in the first zone of degradation and a lower fraction in the second zone (see **Fig. 3.10(a)**). It is noteworthy that in the case of HSs, the degradation rate constant is much higher in the 2nd zone as compared to that of the 1st zone (see **Fig. 3.10(b)**). In both, the zones, TA11 and TA32 show the maximum overall photodegradation efficiency.

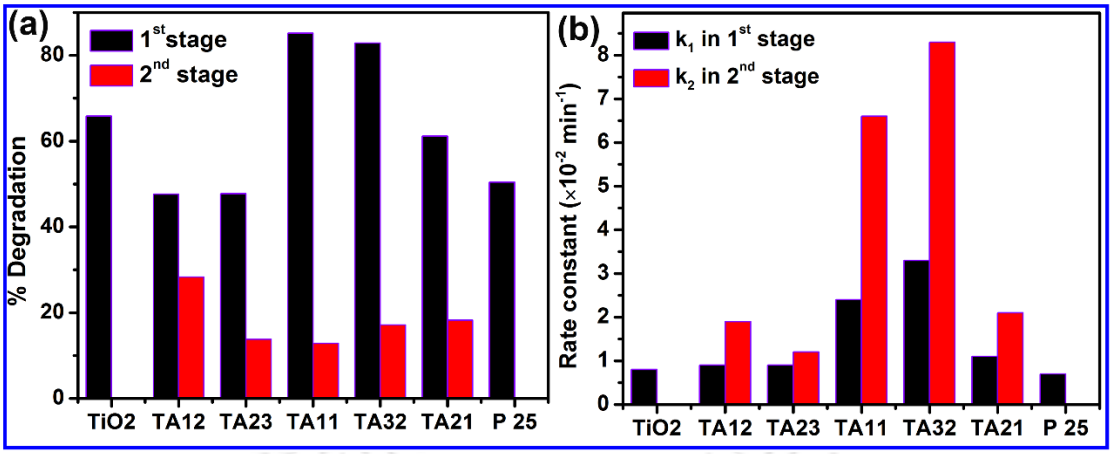

Fig. 3.10. (a) A comparison of the photodegradation percentages of RhB in the first and second compartment of degradation calculated for different samples, (b) the associated rate constants.

3.3.4.3. Modelling of Degradation Kinetics

Scherr et al.[20] studied the degradation kinetics of bio compound Estrone-3-sulfate (E1-3S), formed in the kidneys of pregnant cattle, with 'single first-order exponential decay model' and 'two-compartment first-order bi-exponential decay model', assuming no back conversion, no influence of sorption on the degradation and no altering due to microbial growth. These models can be described mathematically as follows:

Single first-order (SFO): $C_t = C_0 e^{-k_1 t}$

Double first-order in parallel (DFOP): $C_t = C_0[ge^{-k_1 t} + (1-g)e^{-k_2 t}]$

Where t is time of irradiation, k_1 and k_2 are the degradation rate constants (min^{-1}) in 1st compartment and 2nd compartment, respectively, C_0 is the initial concentration of parent compound, C_t is the total concentration of parent compound at time t and g is the fraction of C_0 applied to compartment 1 of the DFOP model. We noticed that the single first-order exponential decay model is not valid in our case, as we have observed two different degradation zone with two distinct rate constants. According to the DFOP model, degradation takes place in two compartments: rapid degradation in the first compartment as the microorganisms have easy access to the compound, whereas in the second compartment, degradation is rather slow and the compound is expected to be adsorbed to soil particles or to be located in micropores within the soil matrix. The speed at which the parent compound is transformed is expressed as degradation rate constant (k_1, in the first compartment, and k_2, in the second compartment) and usually k_1 >

k_2. However, our data could not be fitted either with the SFO or the DFOP model (see **Fig. 3.14(a, b)**).

Interestingly, in the present case, the degradation process of all HS samples follows a sequential decay model in contrast to the parallel decay model of DFOP. This sequential decay process can be modelled as:

$$C_t = C_0 e^{-k_1 t} \quad \ldots\ldots \text{ up to } 0 \leq t \leq t_1 \tag{3.1}$$

$$C'_t = C_{t_1} e^{-k_2(t-t_1)} = C_0 e^{-k_1 t_1} e^{-k_2(t-t_1)} \quad \ldots\ldots\ldots \quad t > t_1 \tag{3.2}$$

Where C_0 is the concentration of parent dye before the light irradiation, C_t & C'_t are the concentration of the dye after t time of irradiation in stage 1 and stage 2, respectively. k_1 and k_2 are the degradation rate constants (in min^{-1}) in 1st and 2nd stage, respectively. t_1 is the irradiation time up to which 1st compartment of degradation extends (eqn. 3.1) and beyond which 2nd compartment of degradation starts (eqn. 3.2). Herein, the whole degradation process occurs in two different compartments/stages separately, where the 1st compartment runs in the irradiation time range $0 \leq t \leq t_1$ and afterwards ($t > t_1$) 2nd compartment extends. The limiting time t_1 is found to be ~60 min for all the HS samples except the optimized HS, TA32 (50 min). It can also be noted that a higher fraction of dye is being decomposed in the 1st zone and lesser fraction in the 2nd zone (**Fig. 3.10(a)**), though the degradation rate is higher in the 2nd compartment (**Fig. 3.10(b)**). Note that this is in contrast to the DFOP model where the 2nd stage rate constant is always lower than the 1st stage rate constant. More details of the physical mechanism behind the sequential decay model are discussed later.

3.3.4.4. Cyclic Stability of Photocatalyst

For the cyclic stability study, TA32 has been chosen as the model HS catalyst as it has the best photodegradation capability, as shown in **Fig. 3.9(a)**. TA32 photocatalyst exhibits very stable photocatalytic activity under visible light irradiation, as shown in **Fig. 3.11** and there is no obvious change in the photodegradation efficiency after four cycles of use. After the 1st cycle of photocatalysis, the reduced Ag^+ ions may get again oxidized by the reverse spillover effect[15] and additionally after the migration of hot electrons through the interface of Ag and TiO_2, the Ag NPs get positively charged and thus have higher tendency to be oxidized in ambient condition. However, the Ag decorated TiO_2 NRs are found to be extremely stable photocatalyst with

potential for commercial applications. Our results demonstrate the superiority of the Ag@TiO_2 HS over the bare TiO_2 NRs for its advanced application in environmental cleaning.

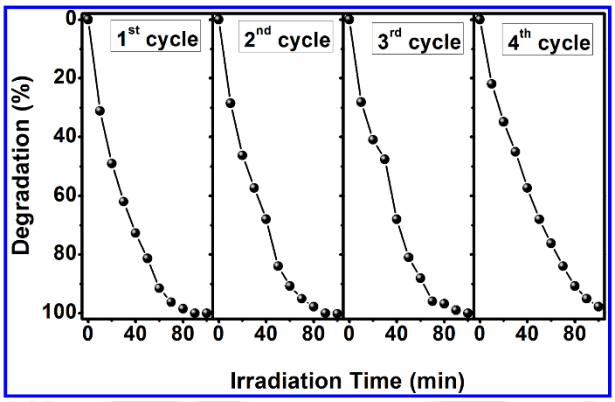

Fig. 3.11. Cyclic stability of TA32 as a visible light photocatalyst for four cycles considering RhB as a model dye.

3.3.4.5. Mechanism of Enhanced Visible Light Photocatalytic Activity

In the present work, band gap, as well as the absorption range of TiO_2 NRs, is tuned with the decoration of Ag NPs so that it can sense an extended spectrum of solar light. In case of HS samples, the Ag NPs are strongly coupled with TiO_2 lattice, and due to the synergetic effect and band bending, the HS shows strong absorption of visible-NIR light and efficient charge transfer at the interface.[9] As a result, the visible light photocatalytic activity of TiO_2 NRs HS has been found to be enhanced enormously. Possible mechanisms including additional boosting factors behind the enhanced visible light photocatalysis are discussed below.

3.3.4.5.1. Generation and Interfacial Migration of Hot Electrons

Fig. 3.12(a) shows a schematic of the vacancy rich n-type TiO_2 NR coupled with an Ag NP, while **Fig. 3.12(b)** depicts a schematic illustration of the energy band diagram of Ag@TiO_2 HS. The presence of Ag NP on TiO_2 results in a Schottky barrier with a space charge region in the TiO_2 side, which builds up an internal electric field E pointing from the TiO_2 to the Ag.[10] Such an internal field forces the electron-hole pairs generated in the space charge region (TiO_2 side) to move in opposite direction separating electrons and holes and suppressing their easy recombination in TiO_2. A noteworthy feature of plasmonic photocatalysis is that the Ag NP can absorb visible light and drives coherent collective oscillation of electrons, which in turn generates electrons with high kinetic energy in the range 1-3 eV.[5]

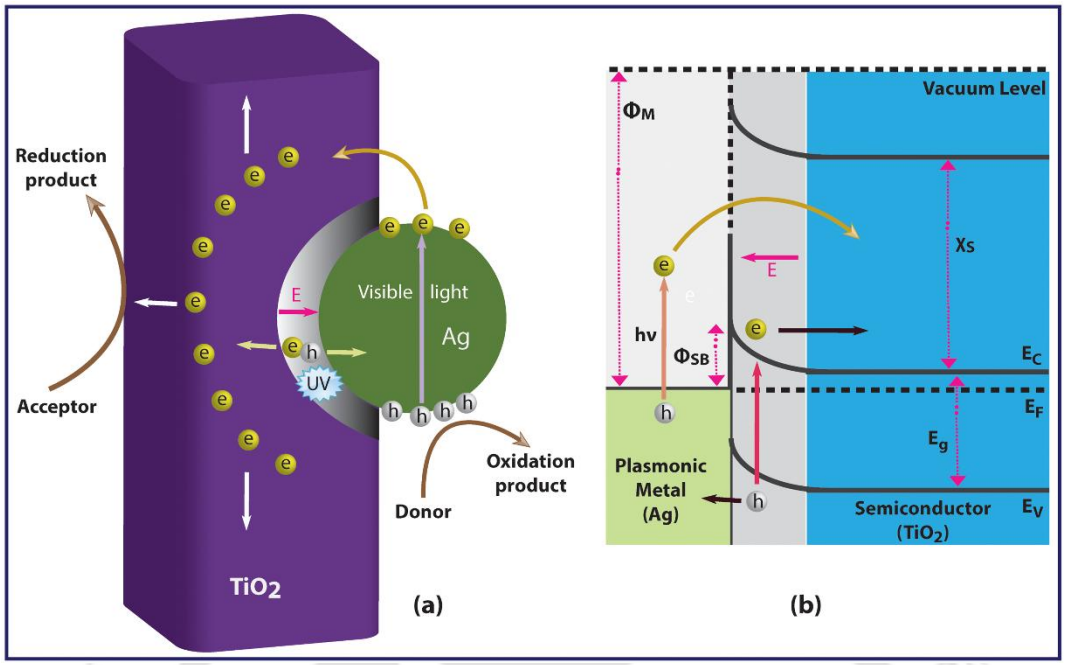

Fig. 3.12. (a) Schematic representation of Ag@TiO_2 NRs HS showing the generation of hot electrons, their separation and participation in the photocatalysis. (b) A schematic illustration of energy band diagram of TiO_2 in the presence of Ag NP, where a Schottky barrier is formed between the two. The vacuum level is the vacuum energy level, Φ_M is the work function of the Ag NP, Φ_{SB} is the Schottky barrier height, and χ_S is the electron affinity of TiO_2. In the proposed mechanism, the decaying SPR excites "hot" electrons in the Ag nanoparticles that possess enough energy to overcome the Schottky barrier, and inject into the TiO_2.

With the visible light illumination, the Ag NP on the surface of TiO_2 NR absorbs light, and consequently, the LSPR occurs. The excited plasmons can decay in the femtosecond time scale through two different processes: radiatively via re-emitting the photons and non-radiatively via transferring the gathered energy to electrons in the conduction band of the material. Thus, the non-radiative energy transfer produces highly energetic electrons, also known as 'hot electrons' at the Ag surface. Generally, the energy of these hot electrons is greater than the Schottky barrier height ($h\nu > \varphi_{SB}$) and can escape easily from the Ag surface and are collected by the TiO_2, since TiO_2 is a good electron-accepting metal-oxide because of the high density of states in its conduction band.[5] Further, the internal electric field (E) assists their separation forcing the electron to move to the TiO_2 region and the hole to the Ag region and thus prevents the recombination. After separation of photoinduced charge carriers, the TiO_2 surface near the Ag NPs is crowded by the electrons. Having a 1D structure, TiO_2 NR possesses a low axial resistance, and thus the electrons can diffuse slowly through their length making their lifetime further lengthened, as confirmed by PL and TRPL analyses (see **Fig. 3.12(a)**). Thus, the electrons and holes available at the surface of Ag@TiO_2 HS shown in the illustrated figure react

with the adsorbed O_2 and H_2O molecules and eventually form highly active superoxide and hydroxyl radicals, which are strong reducing and oxidizing agents, respectively. These radicals are primarily responsible for the efficient degradation of dye under visible light irradiation.[9, 21]

Further, our results showed that after incorporation of Ag NPs on the TiO_2 NRs, the concentration of oxygen vacancy defects was increased, as concluded from the Raman and XPS analyses. The TA32 HS showed the maximum blue shift in the Raman spectra, indicating the optimum value of oxygen vacancy defects. The defects are known to increase the free carrier density in the TiO_2 surface, which increases the probability of superoxide radical formation at the surface and hence the improved photocatalytic efficiency. It also serves as a shallow trap and improves charge transfer at the interface between the Ag and TiO_2. The UV light generated electrons (in TiO_2) migrate to shallow traps and reduce the Ti^{4+} species into Ti^{3+} states through the following pathway:[22]

$$TiO_2 \xrightarrow{h\nu\ (UV)} e^-_{CB} + h^+_{VB}$$

$$e^-_{CB} + Ti^{4+} \longrightarrow Ti^{3+}\ (\text{trapped electron})$$

For the visible light irradiation, the TiO_2 does not get excited directly, but the hot electrons generated at the Ag surface can excite it.[22]

$$Ag\ NP \xrightarrow{h\nu\ (Vis)} e^-(hot)$$

$$e^-(hot) \xrightarrow{\text{after migration}} e^-_{CB} + Ti^{4+} \longrightarrow Ti^{3+}\ (\text{trapped electron})$$

Thus, the defect-assisted charge separation plays an important role as one of the boosting factors for the enhanced photocatalytic efficiency by suppressing the charge recombination process.

3.3.4.5.2. N-de-ethylation Process

Interestingly, with light irradiation time, not only the absorption peak intensity of RhB centered at ~554 nm (the most intense peak) is decreased, but also there is a blue shift of the peak position (see **Fig. 3.13**). This shift is quite small for pristine TiO_2 for the entire irradiation period (only ~6 nm after 80 min of irradiation, see **Fig. 3.13(a)**) and it is significantly large (~32 nm) for the TA32 HS (**Fig. 3.13(b)**).

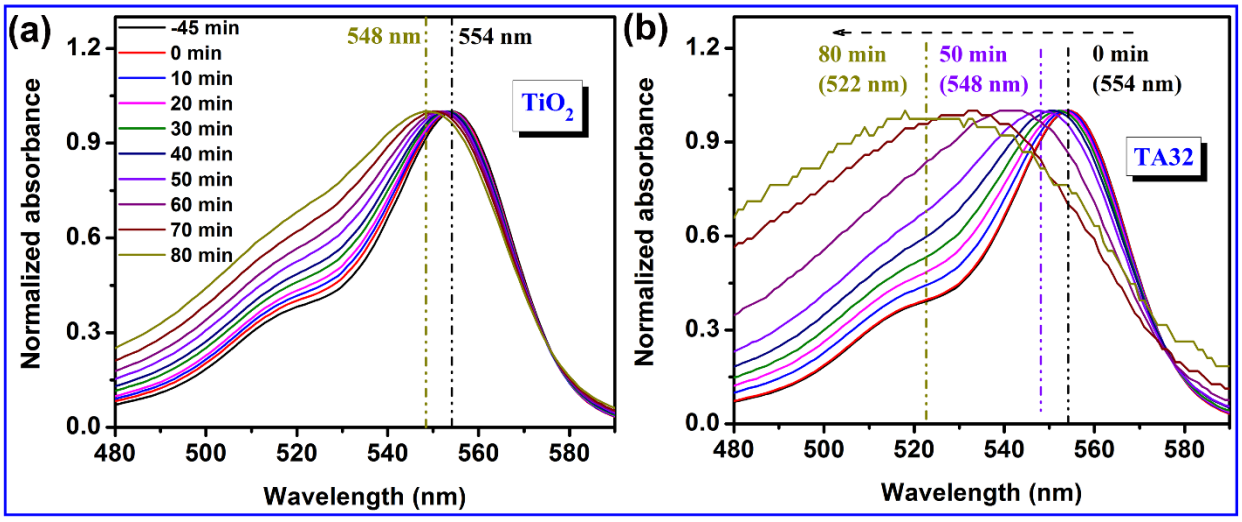

Fig. 3.13. Normalized absorbance of RhB under various visible light illumination time in the presence of (a) pristine TiO_2 and (b) TA32 catalyst showing the shift in absorbance peak with the illumination of visible light.

It is noteworthy that in the 1st compartment of degradation the blue shift is relatively small, while it changed dramatically in the 2nd compartment of degradation and is measured to be very large as shown in **Fig. 3.14(c, d)**. The blue shift of absorption peak is generally caused by de-ethylation of RhB (N, N, N′, N′ tetraethylated rhodamine) because of the attack by the active oxygen species on the N-ethyl group. The N-de-ethylation is a process of stepwise removal of ethyl group (C_2H_5) attached to the nitrogen atom of RhB molecule during irradiation. Detailed studies by Li et al.[23] and Sridharan et al.[24] showed the stepwise de-ethylation of RhB under the visible light irradiation and formation of rhodamine as the final product. The N-de-ethylation process could be initiated both by valence band hole and conduction band electron in the HSs. The reaction steps are given below:

$$HS + RhB \longrightarrow RhB_{Adsorbed}$$

$$RhB_{Adsorbed} \xrightarrow{h\nu} RhB^{*}_{Adsorbed}$$

$$RhB^{*}_{Adsorbed} + HS \longrightarrow RhB^{+}_{Adsorbed} + HS(e^{-})$$

$$HS(e^{-}) + O_2 \longrightarrow HS + \bullet O_2^{-}$$

$$HS \xrightarrow{h\nu} h^{+} + e^{-}$$

$$RhB_{Adsorbed} + HS(h^{+}) \longrightarrow RhB^{+} + HS$$

$$RhB^{+} \xrightarrow{N-de-ethylation} de-ethylated\ intermediates \longrightarrow degraded\ product$$

In the present case, the small shift of the absorption peak (554 nm) for the bare TiO_2 with irradiation in the whole illumination period indicates a negligibly slow N-de-ethylation process and relatively dominant chromophore structure degradation.

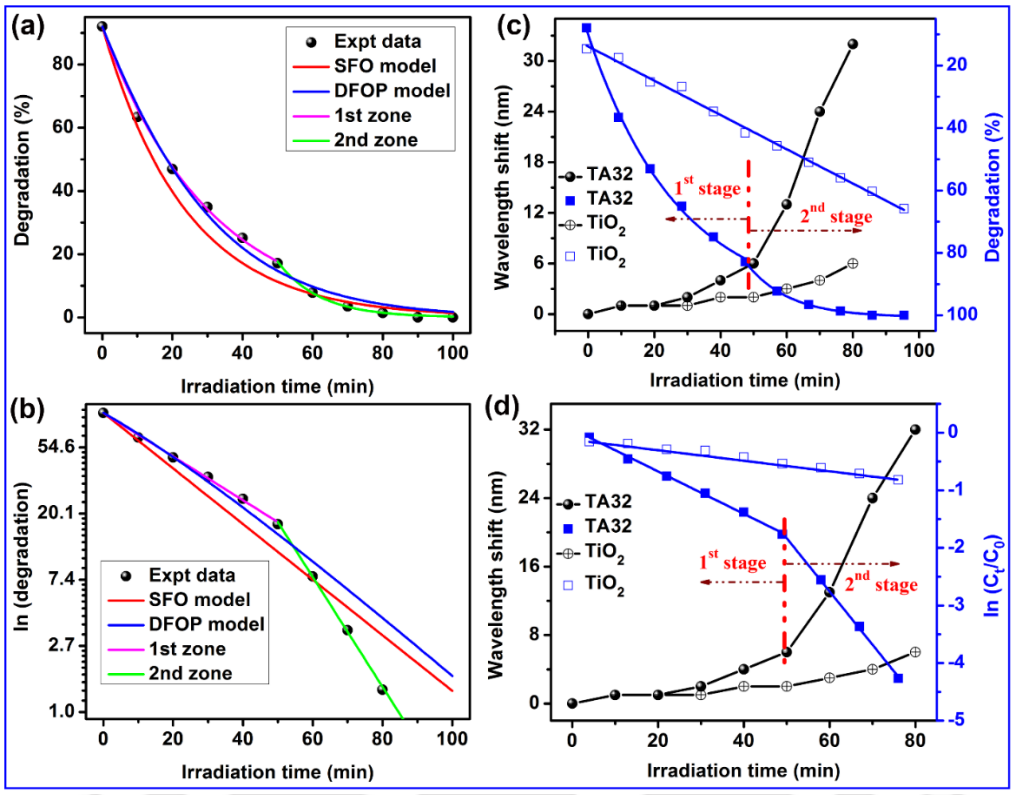

Fig. 3.14. Percentage degradation of RhB under visible light illumination (a) and a plot of ln(degradation) vs. irradiation time (b), fitted with SFO, DFOP and sequential model. (c) A plot of degradation (%) vs. irradiation time (min) for TiO_2 and TA32 samples (blue Y-axis) and corresponding wavelength shifts in the absorbance band of RhB (black Y-axis). The degradation vs. irradiation time curves has been fitted with exponential to identify the distinct stages of degradation (d) A plot of $\ln\left(\frac{C_t}{C_0}\right)$ vs. irradiation time (min) for TiO_2 and TA32 samples (blue Y-axis) and corresponding wavelength shifts in the absorbance band of RhB (black Y-axis). The $\ln\left(\frac{C_t}{C_0}\right)$ vs. irradiation time curves have been fitted with linear equations to identify the distinct stages of degradation.

In case of HSs, up to the certain time of irradiation, a very small blue shift in the absorption peak of RhB shows that the degradation occurs mainly due to the adsorption and chromophore ring structure destruction, but not due to the N-de-ethylation. However, after a certain time of irradiation (50 min for TA32), the N-de-ethylation process dominates over the other degradation processes and occurs very quickly with the irradiation, as shown in **Fig. 3.14(c, d)**. After 60 min, the absorption peak of RhB detected at ~539 nm can be assigned to N, N, N′ triethylated

rhodamine[24] and after 80 min at ~522 nm for N, N′ diethylated rhodamine[24]. **Fig. 3.14(c)** shows a plot of degradation (%) vs. irradiation time (min) for TiO_2 and TA32 samples (see RHS Y-axis) and corresponding wavelength shifts in the absorbance band of RhB (see LHS Y-axis). The degradation curves have been fitted with exponential decay function to identify the distinct stages of degradation. **Fig. 3.14(d)** depicts a plot of $\ln\left(\frac{C_t}{C_0}\right)$ vs. irradiation time (min) for TiO_2 and TA32 samples (see RHS Y-axis) and corresponding wavelength shifts in the absorbance band of RhB (see LHS Y-axis). The $\ln\left(\frac{C_t}{C_0}\right)$ vs. irradiation time curves have been fitted with straight lines to identify the distinct stages of degradation. It is clear from **Fig. 3.14** that up to 50 min of irradiation (for TA32), the degradation curve follows a pseudo 1st order decay, beyond which the N-de-ethylation process dominates and the shift of the resultant absorption peak of RhB becomes very large and significant. This results in a separate degradation rate starting after 50 min and thus the two separate degradation rate constants, which are sequential in nature.

3.3.4.5.3. Simultaneous Photoreduction Process

Another important mechanism that may contribute to the two distinct compartments of photodegradation and the enhanced photocatalysis in the 2nd stage of degradation is the reduction process of Ag^+ ions into metallic Ag^0 NPs during photocatalysis. At the initial stage of photocatalysis, the concentration of Ag^+ ions in the solution may be high enough and the UV irradiation time during the photoreduction process is insufficient so that some fraction of the Ag^+ ions do not get reduced into metallic Ag NPs. XPS analysis before photocatalysis showed that 48.17% of the Ag is present in the Ag^+ ion form. Thus, the plasmonic effect during the photocatalysis is expected only from the remaining 51.83% of Ag NPs, and the 48.17% of Ag^+ ions do not contribute to the plasmonic effect. During the photocatalysis process, the light irradiation transforms the Ag^+ ions into Ag^0 NPs with a very slow rate as the irradiation spectrum contains a small portion of UV light (>390 nm). After certain irradiation time, the amount of Ag^0 NPs in the solution increases (81.65% Ag^0 NPs after photocatalysis) and consequently the plasmonic effect enhances. Thus, due to the combined effects of photoreduction of Ag and rapid rate of N-de-ethylation process, the degradation rate was enhanced enormously after a certain time of irradiation and thus the calculated rate constant. Thus, two distinct degradation rate constants were observed in two different irradiation time zone. Note that, our data could not be fitted with the SFO & DFOP models as shown in **Fig. 3.14(a, b)**. However, it fits very well to the

sequential model represented by eqn. 3.1 and 3.2 (see **Fig. 3.14(a, b)**), as simulated by Mathematica.

Additionally, it has been reported that the photodegradation rate depends on the relative concentration of dye and catalyst present in the solution. For example, a lower dye to catalyst ratio gives the higher degradation rate. In the 1st stage of degradation, the full amount of dye (0.5 mg) takes part, which represents a higher ratio of dye to catalyst. Next, in the 2nd stage of degradation, the remaining amount of dye was involved, and as the maximum fraction of total dye is being degraded in the 1st zone, the dye to catalyst ratio is reduced in the 2nd zone of degradation. For example, in the case of the TA32 sample, the dye to catalyst ratio is 0.025 in the 1st compartment and 0.0035 in the 2nd compartment. Thus, in the 1st compartment, the dye to catalyst ratio is more than seven times that of the 2nd compartment. In the 1st compartment, 20 mg catalyst was applied to entire RhB in the solution, but in the 2nd compartment almost the same amount of catalyst takes part in the reaction with a less amount of dye (~15% for TA32). Thus the lower dye to catalyst ratio assists the faster degradation in the 2nd compartment of degradation. Thus, in the present case, a two-stage degradation process is very appropriate. Interestingly, photocatalytic degradation studies reported by Cheng et al.[25], Chen et al.[26], Wang et al.[27] and Cui et al.[28] using Ag, Ag_2O and AgBr incorporated TiO_2 nanostructures assumed the pseudo-first-order rate kinetics with a single rate constant. However, the presented data is not consistent with the single exponential decay model, and the data could be fitted better with a sequential rate process, as discussed above.

3.4. Summary and Conclusions

In this chapter, uniformly designed Ag NPs on TiO_2 NRs grown by a low-temperature solvothermal technique has been investigated thoroughly to elucidate the effects of NPs on the stoichiometry, band structure and optical absorbance of TiO_2 and thus the enhanced visible light photocatalysis. Important findings of this chapter are summarized below. These results are very significant, and it may provide valuable insights into design and understanding of the advanced photocatalytic material with noble metal NPs and enhanced photocatalytic activity with multi-rate constants.

1. Ag@TiO_2 HSs exhibit LSPR induced strong visible light absorption with relatively low PL intensity, prolonged carrier lifetime and high photoconductivity owing to the photogenerated charge carriers.
2. HS samples demonstrate the superior photocatalytic activity (~10 fold) as compared to the commercial P25 catalyst.
3. Photocatalytic degradation of dyes by the HS samples possesses two distinct decay compartments in time and thus two separate degradation rate constants. In the 2nd compartment, the decay rate constant is about three times higher than that of the 1st compartment for TA2 HS.
4. We have proposed a sequential decay model to fit the degradation data. The higher value of k_2 than k_1 has been explained on the basis of ultra-fast N-de-ethylation of RhB, enhanced plasmonic effect on Ag NPs with the irradiation and hence the more hot electron generation and their easy injection into the TiO_2 surface.
5. Ag@TiO_2 HS shows excellent stability under repeated visible light photocatalysis up to 4th cycle.

References

1. Z. Bian, T. Tachikawa, P. Zhang, M. Fujitsuka and T. Majima, *J. Am. Chem. Soc.*, 2014, **136**, 458-465.
2. H. Lee, Y. K. Lee, E. Hwang and J. Y. Park, *J. Phys. Chem. C*, 2014, **118**, 5650-5656.
3. Z. Zhang, Z. Wang, S.-W. Cao and C. Xue, *J. Phys. Chem. C*, 2013, **117**, 25939-25947.
4. H.-N. Barad, A. Ginsburg, H. Cohen, K. J. Rietwyk, D. A. Keller, S. Tirosh, Y. Bouhadana, A. Y. Anderson and A. Zaban, *Adv. Mater. Interfaces.*, 2016, **3**, 1500789-n/a.
5. C. Clavero, *Nat Photon*, 2014, **8**, 95-103.
6. P. Wang, B. Huang, X. Qin, X. Zhang, Y. Dai, J. Wei and M.-H. Whangbo, *Angew. Chem. Int. Ed. Engl.*, 2008, **47**, 7931-7933.
7. J. Yu, G. Dai and B. Huang, *J. Phys. Chem. C*, 2009, **113**, 16394-16401.
8. K. Awazu, M. Fujimaki, C. Rockstuhl, J. Tominaga, H. Murakami, Y. Ohki, N. Yoshida and T. Watanabe, *J. Am. Chem. Soc.*, 2008, **130**, 1676-1680.
9. K. K. Paul, R. Ghosh and P. K. Giri, *Nanotechnology*, 2016, **27**, 315703.
10. Z. Xuming, C. Yu Lim, L. Ru-Shi and T. Din Ping, *Rep. Prog. Phys.*, 2013, **76**, 046401.
11. H. C. Choi, Y. M. Jung and S. B. Kim, *Vib. Spectrosc*, 2005, **37**, 33-38.
12. S. Balaji, Y. Djaoued and J. Robichaud, *J. Raman Spectrosc.*, 2006, **37**, 1416-1422.
13. B. Santara, P. K. Giri, K. Imakita and M. Fujii, *Nanoscale*, 2013, **5**, 5476.
14. B. J. Murray, Q. Li, J. T. Newberg, E. J. Menke, J. C. Hemminger and R. M. Penner, *Nano Lett.*, 2005, **5**, 2319.
15. E. Albiter, M. A. Valenzuela, S. Alfaro, G. Valverde-Aguilar and F. M. Martínez-Pallares, *J. Saudi. Chem. Soc.*, 2015, **19**, 563-573.

16. R. Sellappan, M. G. Nielsen, F. González-Posada, P. C. K. Vesborg, I. Chorkendorff and D. Chakarov, *J. Catal.*, 2013, **307**, 214-221.
17. B. Choudhury, S. Bayan, A. Choudhury and P. Chakraborty, *J. Colloid Interface Sci.*, 2016, **465**, 1-10.
18. X. Li, G. Chen, L. Yang, Z. Jin and J. Liu, *Adv. Funct. Mater.*, 2010, **20**, 2815-2824.
19. S. A. Ansari and M. H. Cho, *Sci. Rep*, 2016, **6**, 25405.
20. F. F. Scherr, A. K. Sarmah, H. J. Di and K. C. Cameron, *Environ. Sci. Technol.*, 2008, **42**, 8388-8394.
21. W. Zhou, H. Liu, J. Wang, D. Liu, G. Du and J. Cui, *ACS Appl. Mater. Interfaces*, 2010, **2**, 2385.
22. Z. Lin, X. Wang, J. Liu, Z. Tian, L. Dai, B. He, C. Han, Y. Wu, Z. Zeng and Z. Hu, *Nanoscale*, 2015, **7**, 4114-4123.
23. X. Li and J. Ye, *J. Phys. Chem. C*, 2007, **111**, 13109-13116.
24. K. Sridharan and T. J. Park, *Appl. Catal. B Environ.*, 2013, **134–135**, 174-184.
25. B. Cheng, Y. Le and J. Yu, *J. Hazard. Mater.*, 2010, **177**, 971-977.
26. L. Chen, S. Yang, B. Hao, J. Ruan and P.-C. Ma, *Appl. Catal. B Environ.*, 2015, **166–167**, 287-294.
27. Y. Wang, L. Liu, L. Xu, C. Meng and W. Zhu, *J. Appl. Phys.*, 2013, **113**, 174311.
28. Y. Cui, Q. Ma, X. Deng, Q. Meng, X. Cheng, M. Xie, X. Li, Q. Cheng and H. Liu, *Appl. Catal. B Environ.*, 2017, **206**, 136-145.

Chapter 4

Trap State Mediated Plasmonic Hot Electron Injection and Efficient Charge Separation in Ag-TiO_2(B) and Au-TiO_2(B) Nanorods decorated over g-C_3N_4 Nanosheets with Superior Visible Light Photocatalytic Performance

In this chapter, ternary hybrids consisting of Ag-TiO_2(B) and Au-TiO_2(B) nanostructures decorated on graphitic carbon nitride nanosheets are synthesized by an in-situ chemical method. Visible light driven photocatalytic degradation of rhodamine-B and phenol is systematically investigated by the hybrid catalysts and >98% degradation is achieved after 100 min of irradiation. Close inter-particle separation of plasmonic NPs in the HSs possess numerous plasmonic hot spots for the generation of hot electrons that are excited to the conduction band of TiO_2 followed by an interfacial migration to 2D-C_3N_4 (CN) network, supported by steady-state PL and TRPL studies. The monochromatic photoexcitation at wavelengths corresponding to the plasmonic absorption peaks possesses highly enhanced photocurrent due to hot electron injection from plasmonic NPs to TiO_2-CN integrated network facilitating enhanced photocatalysis.

4.1. Introduction

Enhancement of photocatalytic activity by various metal oxides decorated with plasmonic nanoparticles (NPs) occurs via different processes[1-3]. These include: (i) hot electron generation and injection into semiconductor either by an indirect way in which the hot electron is transferred to TiO_2 surpassing the Schottky barrier at the interface of metal-semiconductor, or by direct excitation of the hot electrons into the semiconductor, (ii) localized electromagnetic field enhancement in the near surface region of the semiconductor followed by electron-hole generation, (iii) plasmon resonance energy transfer from metal to semiconductor through dipole-dipole interaction. In the previous chapter, we have demonstrated the enhanced visible light photocatalysis by a binary plasmonic Ag@TiO_2 nanoheterostructure, driven by the enhanced visible light absorption and interfacial transfer of hot electrons. In the present chapter, we choose three-component plasmonic photocatalysts consisting of Ag-TiO_2(B)-g-C_3N_4 and Au-TiO_2(B)-g-C_3N_4 for the degradation of rhodamine-B (RhB) and phenol under the illumination of visible light. There are very few reports on the photocatalytic activity of Ag-TiO_2-CN and Au-TiO_2-CN

for H_2 production, CO_2 reduction and water purification under visible light.[4-7] The reported studies have considered anatase or rutile forms of TiO_2 for photocatalysis. Herein, we have considered mesoporous monoclinic TiO_2(B) nanorods (NRs) as the platform to decorate the plasmonic metal NPs (Au, Ag). The results of photocatalysis are supported by photoresponse study which clearly demonstrates the hot electron injection and interfacial charge transfer mediated photocatalysis in the system.

4.2. Experimental Details

4.2.1. Sample Preparation

4.2.1.1. Synthesis of TiO_2(B) NRs

TiO_2(B) NRs were synthesized by a typical solvothermal process at a fixed temperature of 180 ºC under autogenous pressure and constant magnetic stirring at 500 rpm for 16h, as described in **Chapter 2, Section 2.2.1.1**.

4.2.1.2. Preparation of g-C_3N_4 Nanosheets

Urea was taken as the precursor material and dried by heating. Afterwards, the white powder was calcined at 550 °C for 3 h at a heating rate of 3 °C/min. The resultant yellowish powder was labeled as g-C_3N_4 nanosheets.

4.2.1.3. Preparation of Au and Ag NPs

Au and Ag NPs were synthesized by a citrate reduction method [8, 9]. For Ag NPs, 0.5 mM $AgNO_3$ solution was prepared in 100 ml milli-Q water and heated to boiling. 10 ml of 30 mM aqueous trisodium citrate dihydrate solution was added dropwise to the above solution while continuing stirring at the boiling temperature. A light greenish-yellow colour solution was obtained at the end of the reaction. The solution was then allowed to cool down to room temperature. A similar procedure was adopted for the synthesis of Au NPs, starting with the 300 ml aqueous 0.5 mM precursor $HAuCl_4.3H_2O$, and heating to the boiling point. 30 ml of 30 mM trisodium citrate dihydrate solution was added dropwise to the boiling gold chloride solution with vigorous magnetic stirring. The reaction was stopped when the solution became purple-red colour and then it was cooled down to room temperature.

4.2.1.4. Preparation of Ag-TiO_2, Au-TiO_2, and Its Decoration over g-C_3N_4 Nanosheets

We have adopted an in-situ method for the decoration of Au and Ag NPs over TiO_2(B) NRs. In a typical synthesis, the in-situ decoration was achieved by a citrate reduction process of silver

nitrate/gold chloride solution as discussed above, simultaneously dispersed with TiO_2(B) NRs. After the reaction, the solution was allowed to cool down to room temperature and centrifuged three times with DI water to remove the additional salts and unreacted precursors from the system followed by a drying process at 60 °C to get Ag-TiO_2 or Au-TiO_2 NRs HS. In order to decorate Ag-TiO_2 or Au-TiO_2 NRs HS over the g-C_3N_4 nanosheets, 80 mg Ag-TiO_2 or Au-TiO_2 was dispersed in a 20 ml 2-propanol and 40 mg g-C_3N_4 was mixed with 20 ml 2-propanol in a bath sonicator for 30 min. Then, the Ag-TiO_2 or Au-TiO_2 dispersion was added dropwise into the g-C_3N_4 solution under vigorous magnetic stirring to form Ag-TiO_2-CN or Au-TiO_2-CN NRs HS, and finally it was dried at 60 °C.

4.2.2. Characterization Techniques

The details of XRD, Raman, XPS, TEM, BET, UV-Vis absorption and TRPL measurements are discussed in **Chapter 2, Section 2.2.3**. In addition, Fourier transform infrared (FTIR) spectroscopy measurements were performed in Perkin Elmer, Spectrum BX spectrophotometer. Room temperature steady state PL spectra of the catalysts were recorded with the help of a spectrometer (focal length: 15 cm; blaze wavelength: 500 nm; groove density: 150g mm^{-1}) equipped with a cooled charge-coupled device (Princeton Instruments, PIXIS 100B) detector using a 405 nm diode laser (Coherent, Cube) excitation. The PL measurement was done in Kobe University, Japan.

4.2.3. Photocatalytic Measurements

4.2.3.1. Photodegradation of RhB and Phenol

The photocatalytic activity of pristine TiO_2 NRs, CN nanosheets and their plasmonic HSs with Ag and Au NPs has been estimated considering the photodegradation of RhB (visible light-sensitive dye) and phenol (UV light-sensitive dye). The details of the light source, arrangements and process of photocatalysis are similar to that discussed in **Chapter 3, Section 3.2.2**.

4.2.3.2. Scavenging Test

In order to confirm the involvement of various radical species participating in the photocatalysis, typical photodegradation process was repeated under some sacrificial agents, which can trap active radicals selectively in the aqueous dye solution. In this experiment, Ammonium oxalate (AO), tert-butanol (t-BA) and p-benzoquinone (BQ) were used as a hole (h^+), hydroxyl radical (•OH) and superoxide radical ($O_2^{\bullet-}$) scavengers, respectively. For each scavenging test, 1 mM of

scavenger was added to the 50 mL RhB aqueous solution (10 mg/L) containing 20 mg Ag-TiO_2-CN. The mixed dispersion was then exposed to visible light for different irradiation time, and the decrease in the concentration of RhB was analyzed to confirm the active radicals driving the photocatalysis.

4.2.3.3. Hydroxyl Radical Test

In a typical experiment, a solution with 2 mM NaOH and 5 mM terephthalic acid (TA) was prepared in 50 mL DI water. After a few min of magnetic stirring, 20 mg catalyst (Ag-TiO_2-CN) was added to the solution and irradiated. The solution was collected after 10 min interval and the PL spectra were measured with the excitation of 312 nm.

4.2.3.4. Superoxide Radical Test

Nitro blue tetrazolium chloride (NBT) of 1×10^{-5} M was dissolved into 50 mL of DI water. Then 20 mg of catalyst (Ag-TiO_2-CN) was added and stirred for 45 min under dark prior to the irradiation. The irradiation time and sample collection interval were similar to that of hydroxyl radical test. UV-vis absorption spectra were measured after the collection.

4.2.4. Photoresponse Study

Pristine TiO_2, CN and their HSs with Ag and Au NPs were spin coated on a glass substrate in order to form a homogeneous film of catalysts. Afterwards, Al layer of thickness ~100 nm was deposited on the sample with proper masking by the thermal evaporation method (base pressure of $\sim1\times10^{-6}$ torr) which serves as the electrodes for the photoconductivity measurement. The details of the photoresponse measurement were discussed in **Chapter 3, Section 3.2.3**. In this case, the excitation wavelength was varied using a monochromator (Oriel Instruments, USA) and the continuous visible-NIR spectrum was generated using a 400 nm cut-off filter attached to the lamp.

4.3. Results and Discussion

4.3.1. Morphology Studies

The morphology and microstructural properties of Ag-TiO_2, Au-TiO_2 and their HSs with CN nanosheets are shown in **Fig. 4.1**. **Fig. 4.1(a)** shows the TEM image of TiO_2 NR uniformly coated with Ag NPs and the **Fig. 4.1(b)** depicts its enlarged view. The co-existence of TiO_2 NRs, CN nanosheets and Ag NPs are observed in **Fig. 4.1(c)**, while their interfaces are shown

magnified in **Fig. 4.1(d)**. **Fig. 4.1(e)** shows the TEM image of TiO_2 NRs decorated with Au NPs with sizes larger than those of Ag NPs. **Fig. 4.1(f)** shows a TEM image of three component HS with Au, TiO_2 and CN. It is observed from **Fig. 4.2(a, b)** that the Ag, Au NPs are uniformly dispersed on the TiO_2 NRs with a size distribution of 7.2 nm and 12.3 nm, respectively, while over the TiO_2-CN composite the Ag, Au NPs possess a larger size distribution of 14.9 nm and 16.8 nm, respectively (**Fig. 4.2(d, e)**).

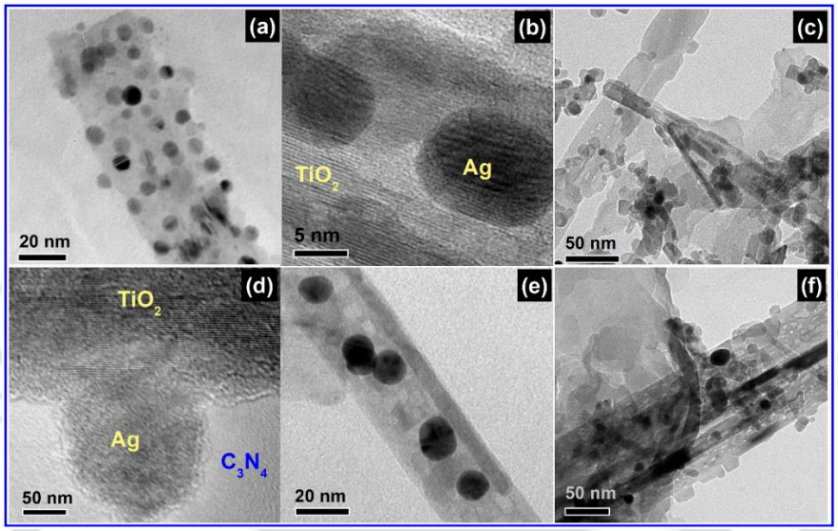

Fig. 4.1. (a) TEM image of Ag-TiO_2 HS, (b) magnified view of Ag NP over TiO_2 NR. (c) TEM image of Ag-TiO_2-CN HS and (d) enlarged view of Ag NP and TiO_2 NR over CN nanosheet. (e) TEM image of Au-TiO_2, (f) TEM image of Au-TiO_2-CN HS.

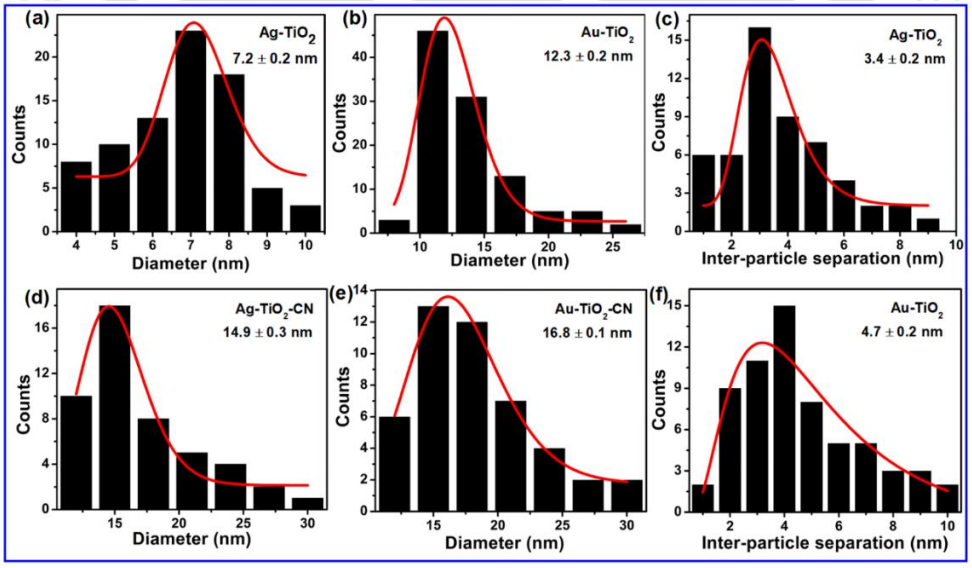

Fig. 4.2. Size distribution of (a, d) Ag NPs in Ag-TiO_2 and Ag-TiO_2-CN, respectively, (b, e) Au NPs in Au-TiO_2 and Au-TiO_2-CN, respectively. (c, f) Distribution of interparticle separation between the closely spaced Ag/Au NPs in Ag-TiO_2/Au-TiO_2, respectively. Each distribution is fitted with the log-normal function to calculate the average value.

It may be due to the special surface feature of pristine TiO_2, which is porous in nature, and it may act as the nucleation site for the growth of Ag/Au NPs. In the TiO_2-CN composite, the pores on the TiO_2 may be blocked due to the presence of CN causing agglomeration of NPs and a larger size.

4.3.2. Structural Analysis

4.3.2.1. XRD Analysis

XRD patterns of TiO_2, CN, Ag-TiO_2, Au-TiO_2, Ag-TiO_2-CN and Au-TiO_2-CN are shown in **Fig. 4.3(a)**. The cubic Au NPs exhibit major diffraction peaks at 38.21, 44.41, 64.61 and 77.61° assigned to Au (111), (200), (220) and (311) planes, respectively.[8] Ag NPs having diffraction peaks at 38.2, 44.4, 64.5 and 77° can be attributed to the planes similar to that of Au due to its identical cubic crystal structure.[10] In the hybrid systems, the diffraction peaks corresponding to Au NPs are observed to be stronger than that of Ag NPs. A single intense peak at $2\theta = 27.8°$ is observed in the diffraction pattern of CN corresponding to the (002) planes.[11] All the diffraction peaks detected for TiO_2 correspond to the monoclinic phase of TiO_2(B) (JCPDS 74-1940).[12]

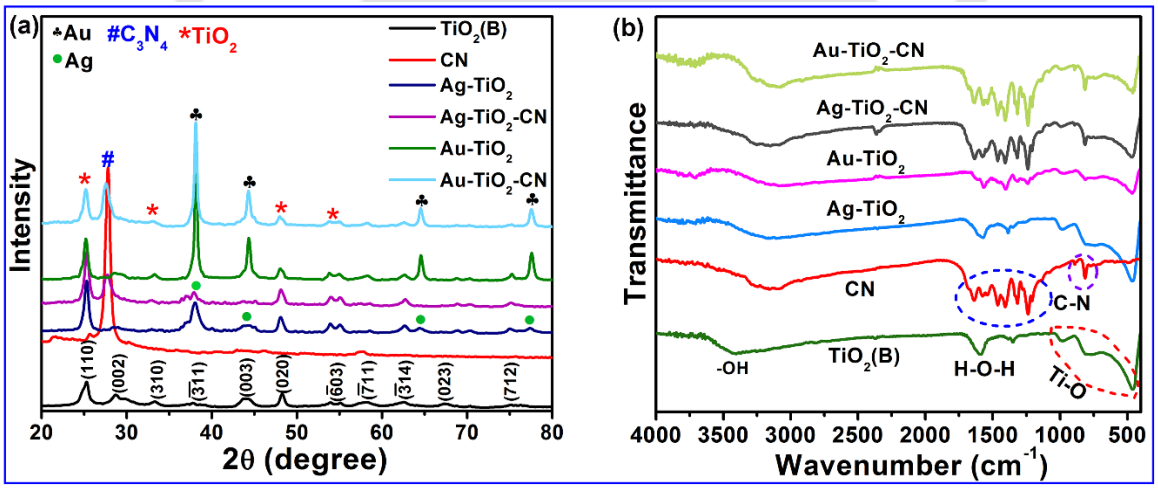

Fig. 4.3. (a) XRD patterns of pristine TiO_2(B), Ag-TiO_2, Au-TiO_2 and their HS with CN. (b) FTIR spectra of all catalysts.

4.3.2.2. FTIR Analysis

The presence of surface adsorbed functional groups is inferred from the FTIR spectra, as shown in **Fig. 4.3(b)**. Stretching (-OH) and bending (H-O-H) vibration modes of surface adsorbed water over TiO_2(B) surface can be seen at 3431 cm^{-1} and 1592 cm^{-1}, respectively.[13] The stretching vibrational mode of –OH is blue-shifted in other samples, may be due to the adsorption of –OH

on different sites over the surface of those catalysts. Along with Ti-O stretching vibrational mode at 454.8 cm^{-1}, there are other modes detected at 805.9 cm^{-1} and 990 cm^{-1}. Presence of trititanate phase and linking up of Na^+/H^+ ions with the nonbridging oxygen atom of TiO_2 may have resulted in these modes[13]. The fingerprint region of CN lies in between 1750-700 cm^{-1}. The absorption band at 806 cm^{-1} is the breathing mode of the C-N aromatic ring.[11] The multiple absorption bands in between 1750-1100 cm^{-1} are the vibration modes corresponding to CN_3 heterocycle.[11] Ag-TiO_2 and Au-TiO_2 display similar spectra as pristine TiO_2. Similarly, the FTIR spectra corresponding to Ag-TiO_2-CN and Au-TiO_2-CN can be identified with the absorption bands corresponding to TiO_2 and C_3N_4.

4.3.2.3. XPS Analysis

Fig. 4.4 shows the core level XPS spectra of different elements present in Ag-TiO_2-CN and Au-TiO_2-CN. The core level Ti 2p XPS spectrum of each HS can be identified with two doublets located at ~458.7 eV (Ti $2p_{3/2}$) and ~464.3 eV (Ti $2p_{1/2}$), respectively. A similar feature is also observed for Ag-TiO_2 and Au-TiO_2 samples. The splitting of 5.6 eV is an indication of normal Ti^{4+} state in TiO_2(B).[14] In addition to the major doublets, each Ti 2p XPS spectrum of the HS samples contains two shoulder peaks at ~457 eV (Ti $2p_{3/2}$) and ~461.3 eV (Ti$2p_{1/2}$). These minor shoulder peaks are attributable to Ti^{3+} states.[13] The core level O 1s XPS spectra of Ag-TiO_2-CN and Au-TiO_2-CN (**Fig. 4.4(b, e)**) are deconvoluted with four Gaussian peaks.

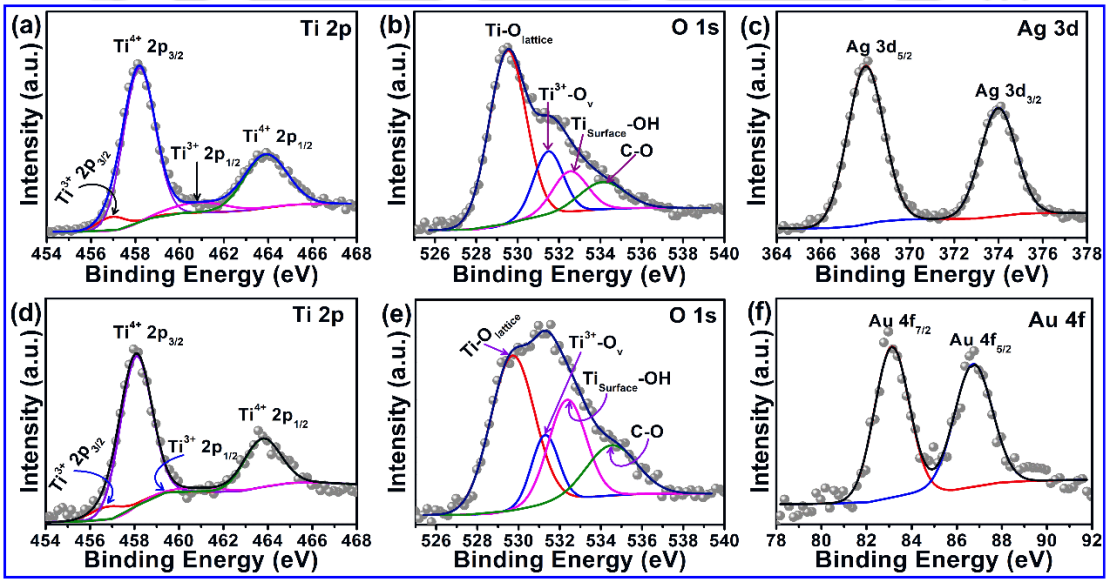

Fig. 4.4. Core level XPS spectra of Ag-TiO_2-CN and Au-TiO_2-CN with (a, d) Ti 2p, (b, e) O 1s, (c) Ag 3d and (f) Au 4f, respectively.

The first three peaks at 530.0 eV, 531.2 eV and 532.7 eV are attributed to the lattice oxygen ($TiO_{lattice}$), oxygen vacancy (Ov)-Ti^{3+} surface states and –OH group attached to the surface of TiO_2, respectively. The higher energy peak at ~534.8 eV is associated with C-O bonding, most likely associated with the adsorbed CO_2 on the surface of TiO_2, CN or the bonding between the surface oxygen on TiO_2 with unsaturated carbon of CN.[15] The O 1s XPS spectra for Ag-TiO_2 and Au-TiO_2 exhibit similar peaks. As shown in **Fig. 4.5(a, c)**, three common peaks are detected at ~284.8 eV, ~286.1 eV and ~287.9 eV, assigned as C-C, $(C)_3$-N and C-N-C groups for Ag-TiO_2-CN and Au-TiO_2-CN, respectively, which is similar to pristine CN. The N 1s XPS spectrum of each CN and CN based HS shows three major peaks, which are attributed to C-N=C (398.4 eV), N-$(C)_3$ (399.8 eV) and C-N-H (401.0 eV), see **Fig. 4.5(b, d)**.[5] The Ag 3d XPS spectrum of Ag-TiO_2-CN is identified with two characteristic doublets at 368.0 eV ($3d_{5/2}$) and 374.0 eV ($3d_{3/2}$) with an energy separation of 6 eV corresponding to metallic Ag (0), see **Fig. 4.4(c)**.[16] The peak position of deposited Ag NPs in the HS is shifted to lower binding energy by an amount of 0.3 eV in comparison to that of bare Ag (368.3 eV and 374.3 eV) [17]. The XPS spectrum of Au is identified with doublets at 83.0 eV ($4f_{7/2}$) and 86.6 eV ($4f_{5/2}$) characteristic of metallic Au(0), as shown in **Fig. 4.4(f)** for Au-TiO_2-CN. In comparison to the peak positions reported in unsupported Au (84.0 eV and 87.7 eV) [17], we encountered a negative shifting of 1.0 eV. This shifting signifies strong interaction between deposited Ag and Au NPs with the TiO_2 and CN.

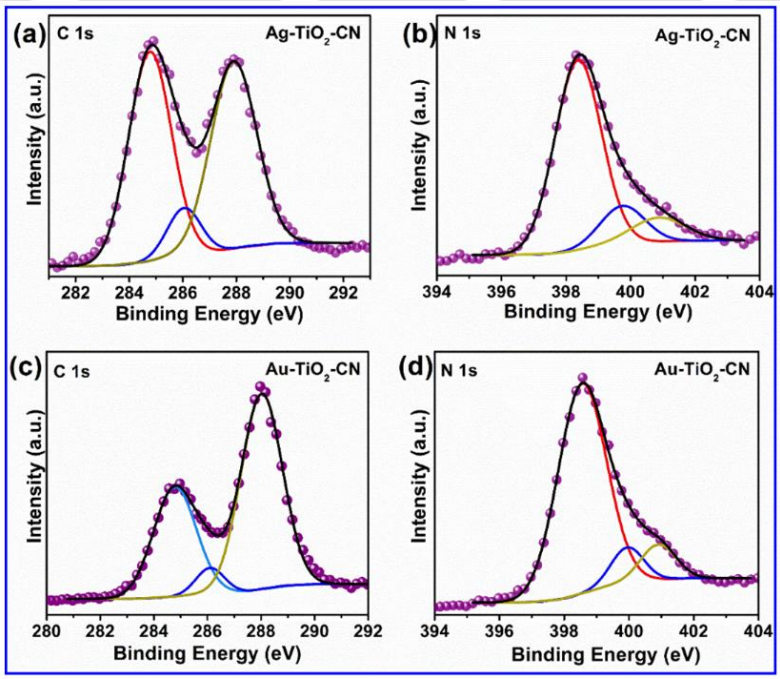

Fig. 4.5. Core level XPS spectra of Ag-TiO_2-CN and Au-TiO_2-CN with (a, c) C 1s and (b, d) N 1s, respectively.

4.3.3. BET Surface Area Analysis

Fig. 4.6(a) depicts the N_2 adsorption-desorption isotherms for all the catalysts. The type of the curves is characteristic of type IV isotherms with a type H_3 hysteresis loop at high relative pressure (p/p_0) of 0.9-1.0.[18] This H_3 hysteresis loop is a characteristic of the presence of asymmetric, interconnected slit-shaped pores.[18] Nitrogen uptake is quite increased above a relative pressure of 0.9. BET surface area, mean pore diameter and pore volume for different samples are given in **Table 4.1**.

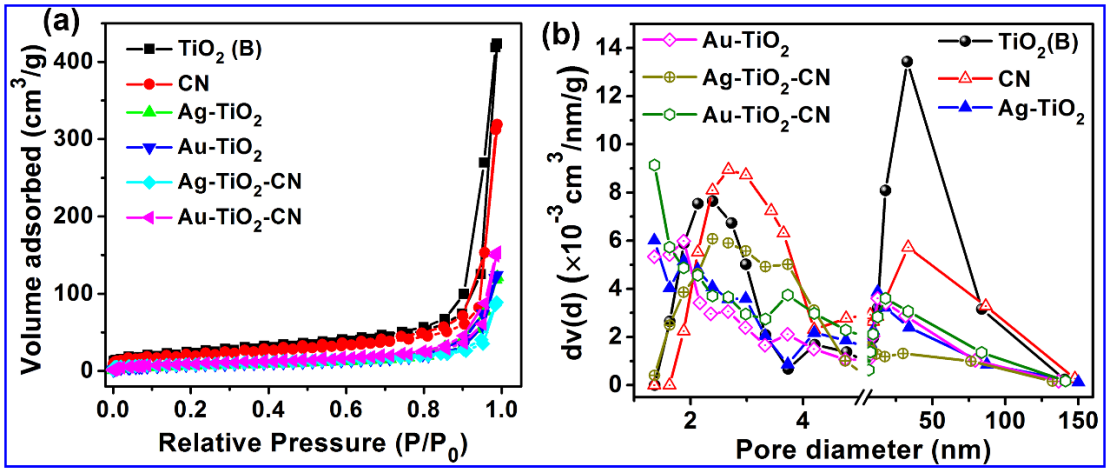

Fig. 4.6. (a) N_2 adsorption-desorption isotherms of pristine TiO_2, CN and their plasmonic HSs with Ag and Au NPs. (b) Shows the respective pore size distribution using the BJH method.

The pore size distribution is determined from desorption data using the BJH model, as shown in **Fig. 4.6(b)**. The surface area, as well as the pore size of pristine TiO_2, is observed to be higher than that of CN nanosheets, while the binary and ternary composites of these materials with Ag and Au NPs have smaller pore size as well as surface area. Lowering in the BET surface area and average pore size in Au-TiO_2 and Ag-TiO_2 is possibly due to partial filling up of pores, pore blocking and shrinking with deposited plasmonic nanoparticles, which is consistent with the TEM analysis [19].

Table 4.1. *Summary of results from N_2 adsorption-desorption study.*

Sample	BET surface area (m^2/g)	Mean pore diameter (nm)	Pore volume (cc/g)
TiO_2 (B)	83.2	32.86	0.65
C_3N_4	69.5	3.72	0.49
Ag-TiO_2	26.4	1.35	0.19
Au-TiO_2	28.6	1.87	0.20
Ag-TiO_2-CN	30.0	2.38	0.14
Au-TiO_2-CN	34.0	1.36	0.24

4.3.4. Optical Analysis

4.3.4.1. UV-Vis Absorption Study

Note that the bare TiO_2 NR has no absorption in the visible region (see **Fig. 4.7**). After Au NPs decoration over TiO_2, a strong absorption band appears at ~550 nm, which can be described as the SPR band of Au NPs, as shown in **Fig. 4.7**. The SPR band of Ag NPs in Ag-TiO_2 appears as a broad peak with its center at ~514 nm. CN contains two prominent absorption bands at ~370 nm and ~390 nm, due to n→π* electronic transition involving non bonded N 2p orbital and conduction band C 2p orbital.[11] In the Au-TiO_2-CN hybrid structure, the intensity of SPR band of Au NPs diminishes with no alteration in the position or intensity of UV band of pristine CN. In the case of Ag-TiO_2-CN, there is a marginal reduction in the intensity of UV and visible absorption corresponding to TiO_2/CN and SPR band.

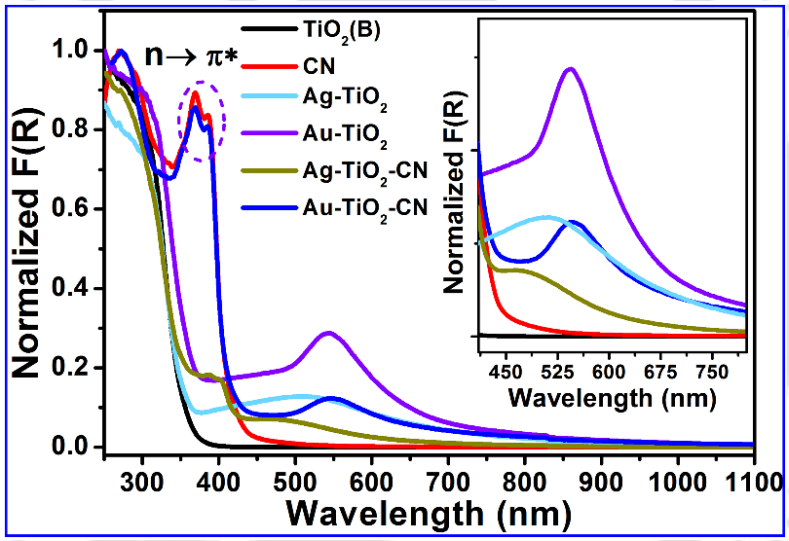

Fig. 4.7. Kubelka−Munk plot, F(R), derived from the diffuse reflectance spectra of different samples. The inset shows the magnified view in the range 350-780 nm.

In comparison to the SPR band (peak at ~527 nm) of colloidal Au NPs in aqueous solution, Au NPs on TiO_2 shows a red-shift of ~25 nm. There is, however, no further shift in the SPR band in Au-TiO_2-CN. Pure colloidal Ag NPs show SPR absorption at ~468 nm, which is observed to be redshifted to ~514 nm and ~480 nm in Ag-TiO_2 and Ag-TiO_2-CN, respectively. The plasmon resonance frequency shows dependence on the surrounding material having different dielectric constant [20]. This can be described with the equation:

$\omega_{LSPR} = \frac{\omega_p}{\sqrt{1+2\varepsilon_m}}$, where ω_p is plasma frequency of bulk metal and ε_m is the dielectric constant of the surrounding medium. The expression for $\omega_p = \sqrt{\frac{n_e e^2}{\varepsilon_0 m}}$, where n_e is number density of electrons, e is the electronic charge, m is the effective mass of the electron. Therefore, the red-shift in the absorption is due to the changes in the dielectric constant of the surrounding medium (ε_m) of Au and Ag NPs from water ($\varepsilon_m \approx 1.77$) to TiO_2 ($\varepsilon_m \approx 4.8$) and CN ($\varepsilon_m \approx 7.2$) and the magnitude of the shift is a measure of the interfacial electronic coupling between plasmon and surrounding media [21-23].

4.3.4.2. Photoluminescence Study

Fig. 4.8 shows the PL spectra of pristine TiO_2, CN and its plasmonic hybrids under the excitation wavelength of 405 nm. The broad PL spectrum of TiO_2 is identified with an oxygen vacancy-related defect emission peak at ~540 nm.[13] The intensity of this emission quenches after loading with Au and Ag NPs. Note that the reduction in intensity is more profound in the case of Au-TiO_2, as shown in the inset of **Fig. 4.8(a)**. It is likely that the surface defects in TiO_2 are passivated after Au and Ag NPs decoration. The photogenerated electrons on the oxygen defect sites are captured by Au and Ag NPs and thereby quench the defect emission in TiO_2.[24] The quenching results from the electron transfer from conduction band or shallow defect states in TiO_2 to Ag (or Au) under the laser excitation. We have noticed changes in the PL features when Ag-TiO_2 and Au-TiO_2 are decorated over CN nanosheets to form the ternary hybrid systems. Note that CN possesses intense excitonic blue emission[25]. However, after the loading Ag-TiO_2 and Au-TiO_2 over CN nanosheets, the strong emission of the latter is diminished. In comparison to the PL peak of Ag-TiO_2, the emission peak position in Ag-TiO_2-CN is red-shifted to 580 nm, whereas there is a spectral blue shift to 500 nm in case of Au-TiO_2-CN from the peak position of Au-TiO_2 detected at 520 nm. The suppression of excitonic emission in CN could be resulted from the possible exciton-plasmon interaction, exciton dissociation with the subsequent enhancement of charge transfer interaction between Au-TiO_2 and CN nanosheets.[26, 27] Blue or red spectral shift is also associated with exciton-plasmon interaction and near-field plasmon coupling of Au/Ag NPs in Au-TiO_2-CN or Ag-TiO_2-CN.

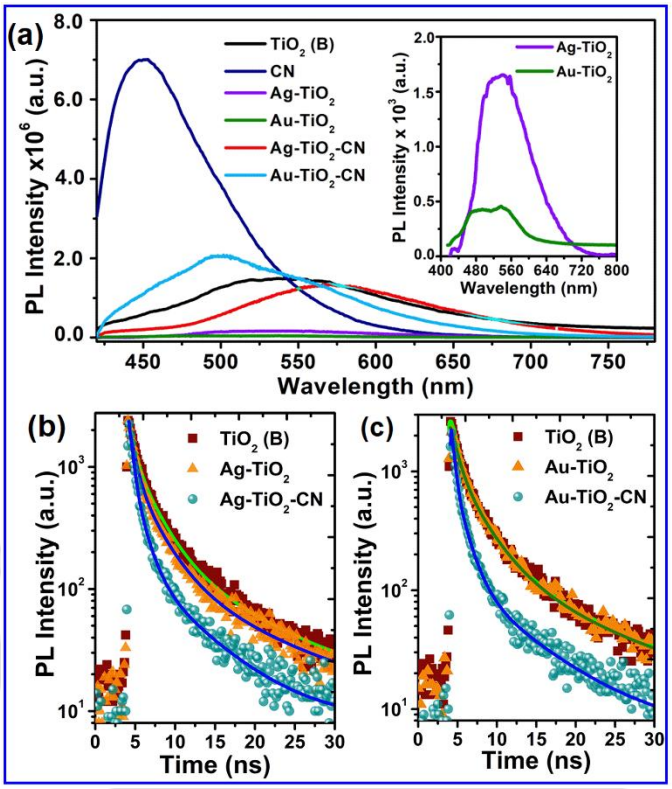

Fig. 4.8. (a) Steady-state PL spectra of pristine TiO_2, CN and their plasmonic systems. TRPL spectra of (b) TiO_2 and CN composites with Ag NPs, and (c) TiO_2 and CN composites with Au NPs.

4.3.4.3. Time-Resolved PL Study

The lifetime of the photoexcited charge carriers is estimated with time-resolved PL spectroscopy. **Fig. 4.8(b, c)** compares the time-resolved PL decay profiles of various samples at an excitation of 375 nm and monitored at the emission maximum of respective samples. The PL decay can be best described by fitting with a tri-exponential decay function. The measured carrier lifetime components and amplitude for different samples are shown in **Table 4.2**. The decoration of Ag and Au NPs on TiO_2 not only reduces the average lifetime of carriers in TiO_2 but also influences the individual lifetime components related to STE (self-trapped exciton) emission as well as defect emission. Thus, the PL quenching and reduction in average lifetime of TiO_2 can be linked with the electron transfer from TiO_2 to metal NPs. The charge transfer time (τ_{CT}) is calculated from the relation: $\tau_{CT} = \frac{\tau_{Semi}\,\tau_{Hybrid}}{\tau_{Semi} - \tau_{Hybrid}}$. The efficiency of charge transfer (η) is measured as $\eta\,\% = \frac{\tau_{Hybrid}}{\tau_{CT}}$ 28.

Table 4.2. *Summary of the fitting parameters for the TRPL data: average carrier lifetime (τ_{av}), charge transfer time (τ_{CT}) and charge transfer efficiency (η).*

Sample	Lifetime (ns)			τ_{av} (ns)	τ_{CT} (ns)	η
	τ_1 (a_1)	τ_2 (a_2)	τ_3 (a_3)			
TiO_2	0.9 (0.23)	3.0 (0.46)	11.2 (0.31)	8.6	-	-
Ag-TiO_2	0.6 (0.17)	2.5 (0.48)	10.0 (0.35)	7.8	84.0	9.3 %
Ag-Ti-CN	0.4 (0.28)	1.3 (0.40)	6.4 (0.32)	5.2	13.1	39.5 %
Au-TiO_2	0.7 (0.32)	2.7 (0.41)	10.8 (0.27)	8.1	140.0	5.7 %
Au-TiO_2-CN	0.3 (0.28)	1.4 (0.41)	7.5 (0.31)	6.1	22.2	28.0 %

The calculated results for τ_{CT} and η are shown in **Table 4.2**. The charge transfer time decreases from 84.0 ns in Ag-TiO_2 to 13.1 ns in case of Ag-Ti-CN. Similarly, Au-TiO_2-CN exhibits a much-reduced charge transfer lifetime (22.2 ns) than Au-TiO_2 (140 ns). As shown in **Table 4.2**, there is more than 4 times increment in the photoinduced charge transfer efficiency in Ag-TiO_2-CN and Au-TiO_2-CN in comparison to Ag-TiO_2 or Au-TiO_2, respectively. Samples displaying higher photoinduced charge transfer efficiency can be expected to exhibit higher photocatalytic efficiency.

4.3.5. Photocatalytic Studies

Fig. 4.9(a) shows the temporal changes in absorption intensity of RhB under visible light irradiation in the presence of Ag-TiO_2-CN. The blank RhB shows maximum absorption at 550 nm. This peak falls in intensity with an increase in light irradiation time and on reaching 100 min this peak completely disappears. **Fig. 4.9(b)** shows the efficiency of different catalysts for the degradation of RhB in an aqueous solution. Measurement of the photocatalytic activity under dark reveals that Ag-TiO_2-CN is quite effective in removing 20% of RhB. On exposure to light, about 90% of RhB degradation has been achieved for an irradiation time of 60 min. Moreover, the determination of first-order rate kinetics reveals that RhB degradation is very fast in the presence of Ag-TiO_2-CN (**Fig. 4.9(c)**). The results of RhB degradation and rate constant (k, min^{-1}) are summarized in the form of a histogram in **Fig. 4.9(d)**. It is observed that the pristine TiO_2(B) NR shows ~44% degradation efficiency with a first order rate constant of 6.5×10^{-3} min^{-1}. On decorating the NRs with Ag NPs, the % degradation and rate constant are dramatically increased to ~92% and 2.0×10^{-2} min^{-1}, respectively. Similarly, Au-TiO_2 shows 84% degradation of RhB with a first order rate constant of 1.7×10^{-2} min^{-1}. There is a synergetic increase in photodegradation % and rate constant in case of Ag-TiO_2-CN and Au-TiO_2-CN. RhB

degradation increases to ~98% with a rate constant of 4.1×10^{-2} min^{-1} in case of Ag-TiO_2-CN. In case of Au-TiO_2-CN, the degradation is ~95% with a rate constant of 2.6×10^{-2} min^{-1}. Thus, it is evident that the three component plasmonic photocatalysts Ag-TiO_2-CN and Au-TiO_2-CN exhibit much improved photocatalytic efficiency as compared to the binary plasmonic systems of Ag-TiO_2 and Au-TiO_2.

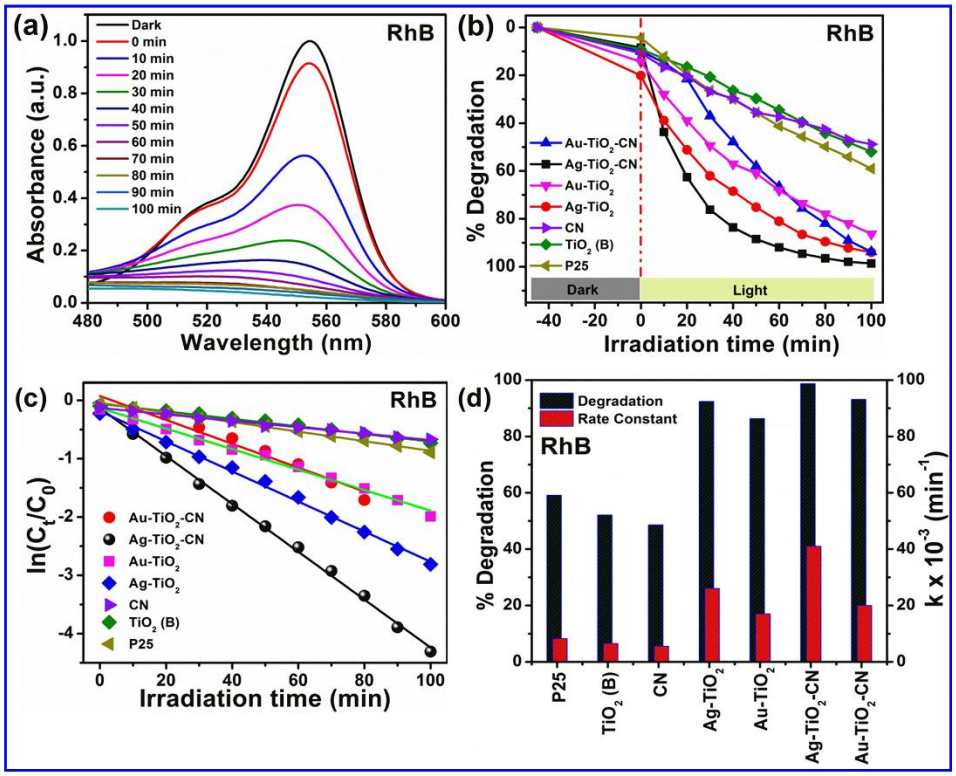

Fig. 4.9. (a) Photodegradation of RhB in the presence of Ag-TiO_2-CN under the illumination of visible light. (b) Comparison of the photocatalytic activity of different catalysts in the degradation of RhB under dark and light condition. (c) First order rate constant determination from the linear fitting of $\ln(C_t/C_0)$ vs t plot. (d) Comparison of the reaction rate constant and % degradation in the photocatalytic reaction by different samples.

Next, we have tested the reusability of Ag-TiO_2-CN for 6 consecutive photocatalytic reaction cycles. The degradation is monitored through absorption measurement after each run, and after the 6th cycle, we have recorded ~95% photodegradation of RhB (**Fig. 4.10(a)**). This implies that the catalyst retains its efficiency in RhB removal at least up to the 6th cycle of reaction. In order to determine the quality and stability of the catalyst after 6th cyclic run, we have recorded FTIR and XRD pattern of used Ag-TiO_2-CN. The FTIR spectra of Ag-TiO_2-CN before and after the photocatalysis are shown in **Fig. 4.10(b)**. No notable change is detected in the vibrational modes of the catalyst after the 6th cycle of photodegradation, revealing its stability and the identical bonding interaction between each component of the HS.

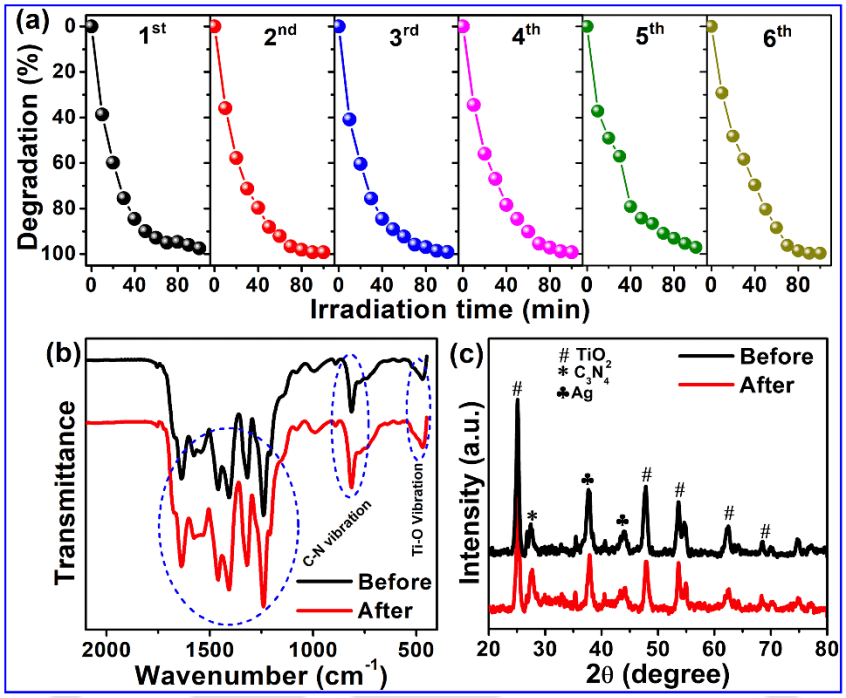

Fig. 4.10. (a) Cyclic test of Ag-TiO_2-CN up to six consecutive reactions, (b) FTIR spectra and (c) XRD pattern of Ag-TiO_2-CN before and after the light irradiation (6 cycles).

Fig. 4.10(c) shows the XRD pattern of Ag-TiO_2-CN before and after light irradiation. There is no loss in crystallinity of the catalyst after the 6th cyclic run. These results clearly demonstrate the superior stability of the photocatalyst under the irradiation of full visible light spectrum.

In order to understand the type of radical that is triggering the photocatalytic process in the systems, few radical scavenging tests have been performed. The result of the test is shown in **Fig. 4.11(a)**. AO, t-BA, and p-BQ are the active scavengers for h^+, •OH, and $O_2^{\bullet-}$ radicals, respectively. As shown in the bar diagram of **Fig. 4.11(b)**, degradation of RhB decreases from ~98% (without any scavenger) to ~60% and ~50% on addition of h^+ scavenger (AO) and •OH scavenger, respectively.[29] Interestingly, only ~10% of RhB degradation is achieved when p-BQ is added to the solution containing RhB and Ag-TiO_2-CN. The scavenging test clearly reveals that the RhB degradation is suppressed predominantly due to the absence of superoxide radicals ($O_2^{\bullet-}$). Furthermore, terephthalic acid (TA) and NBT test can further support the result of scavenging tests.[30] In the presence of OH, TA is converted to 2-hydroxy terephthalic acid in the aqueous solution and shows strong fluorescence at 445 nm, as shown in **Fig. 4.11(c)**.

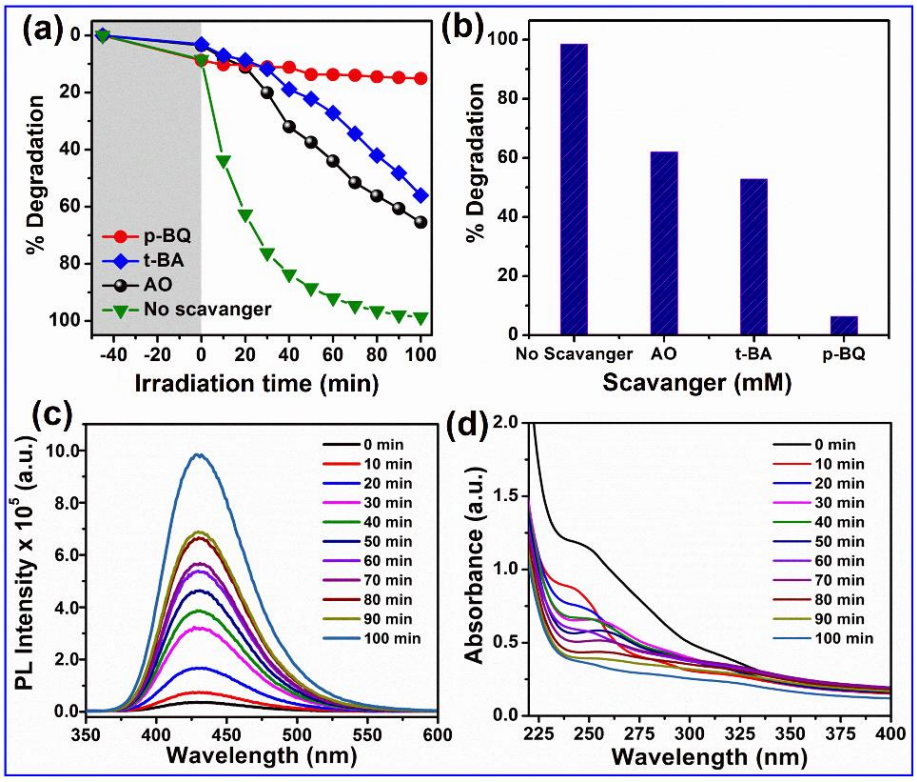

Fig. 4.11. (a) Degradation of RhB in the presence of various radical scavengers, (b) a comparison of degradation with various radical scavengers after 60 min of irradiation. Photodegradation of Ag-TiO_2-CN without any scavengers is also shown for the better comparison of performance. (c) Fluorescence spectra in TA and (d) absorbance spectra in NBT, of Ag-TiO_2-CN suspension at different irradiation times.

The intensity of the fluorescence measures the number of OH radicals available in the solution. In solution, OH radicals could also be formed from O_2 by following the reaction: $O_2+3e^-+2H^+ \rightarrow$ •OH + -OH. Thus, the presence of superoxide radicals in solution may also form OH radicals indirectly. We performed the NBT test to identify the presence of O_2^{2-} radicals, as shown in **Fig. 4.11(d)**. The absorption peak at 255 nm corresponding to NBT diminishes its intensity monotonously with the increase in irradiation time. As irradiation time progresses, a higher concentration of superoxide ions interact with NBT and transforms it into blue formazon with a reduction in absorption peak intensity. The results of TA and NBT test are in agreement with the results obtained from radical scavenging test, confirming the major role of O^{2-} radicals in driving the enhanced photodegradation.

Table 4.3. *Summary of results for k/S_{BET} from the BET surface area and the 1st order rate kinetics of photodegradation of each catalyst.*

Sample	*BET surface area (m^2/g)*	*Rate constant (k, min^{-1})×10^{-3}*		*k/S_{BET} ($min^{-1}m^{-2}g$)*	
		RhB	**Phenol**	**RhB**	**Phenol**
TiO_2	83.2	6.5	7.7	7.8×10^{-5}	9.2×10^{-5}
CN	69.5	5.5	5.1	7.9×10^{-5}	7.3×10^{-5}
Ag-TiO_2	26.4	20	23	7.5×10^{-4}	8.7×10^{-4}
Au-TiO_2	28.6	17	19	5.9×10^{-4}	6.4×10^{-4}
Ag-TiO_2-CN	30.0	41	48	1.3×10^{-3}	1.5×10^{-3}
Au-TiO_2-CN	34.0	26	32	7.6×10^{-4}	9.4×10^{-4}

The parameters that govern the efficiency of a visible-light-photocatalyst are its surface area, strong absorption in the visible region and available free charge carriers. The influence of the surface area on the kinetics of the photocatalytic reaction can be determined by comparing the kinetic rate constant per unit surface area (k/S_{BET}) for different samples.[31] The results of k/S_{BET} for RhB degradation are displayed in **Table 4.3**. Although the binary (Ag-TiO_2, Au-TiO_2) and ternary (Ag-TiO_2-CN, Au-TiO_2-CN) plasmonic composites possess lower surface area than pristine TiO_2, the k/S_{BET} is higher in the hybrid samples. These results clearly indicate that surface area plays a less significant role in the overall enhancement of the photocatalytic activity of the hybrid structure, as discussed in Chapter 2. Based on this observation, we believe that SPR absorption, interfacial charge carrier separation, and charge transfer are the main driving forces for the enhanced photocatalytic activity in the hybrid plasmonic systems.

We have tested the photocatalytic performance of the samples with another toxic organic compound, phenol. Of note, Ag-TiO_2-CN shows excellent photodegradation of phenol in 40 min of irradiation time. **Fig. 4.12(a)** shows the changes in absorption intensity of phenol in presence of Ag-TiO_2-CN under the visible light illumination. **Fig. 4.12(b)** shows a comparison of the efficiency of different catalysts in order to degrade the phenol, while **Fig. 4.12(c)** depicts the 1st order degradation rate kinetics of each catalyst. From **Fig. 4.12(d)**, it is clear that Ag-TiO_2-CN exhibits the highest percentage of photodegradation with the highest rate constant. It can also be noted that the phenol degrades at a faster rate (4.8×10^{-2} min^{-1}) than RhB (4.1×10^{-2} min^{-1}) in the presence of Ag-TiO_2-CN. Thus, fairly consistent photocatalysis is observed by Ag-TiO_2-CN in RhB as well as phenol degradation.

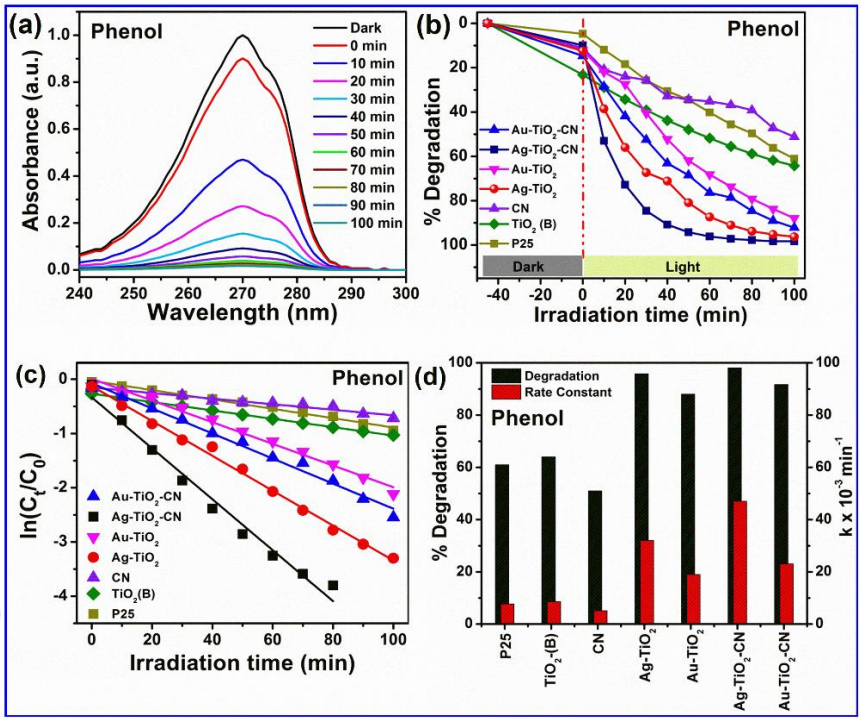

Fig. 4.12. (a) Photodegradation of phenol in the presence of Ag-TiO_2-CN under the illumination of visible light. (b) Comparison of the photocatalytic activity of different catalysts in the degradation of phenol under dark and light condition. (c) First order rate constant determination from the linear fitting of $\ln(C_t/C_0)$ vs t plot. (d) Comparison of the reaction rate constant and % degradation in the photocatalytic reaction by different samples.

4.3.6. Photoresponse Study

Fig. 4.13(a) shows a schematic representation of the photoconductivity measurement for the various photocatalysts under light irradiation. **Fig. 4.13(b)** represents the steady state dark- and photo-current as a function of voltage for the Ag-TiO_2-CN, with the excitation of broadband light (>400 nm). I–V characteristics are observed to be nonlinear with a drastic enhancement in current after the light illumination, showing more than one order of magnitude enhancement at 5 V. The higher value of current is primarily due to the increase in free carrier concentration in the system due to the light illumination, confirming the generation of photoexcited charge carriers and their easy separation. Photocurrent evolution versus time (I-t) measurement is performed under broadband light source using a UV cut-off filter, and under monochromatic irradiation at 470 nm, 510 nm and 545 nm, respectively. When light is on, the current sharply rises to reach its maximum value, clearly indicating the photocurrent enhancement under illumination.

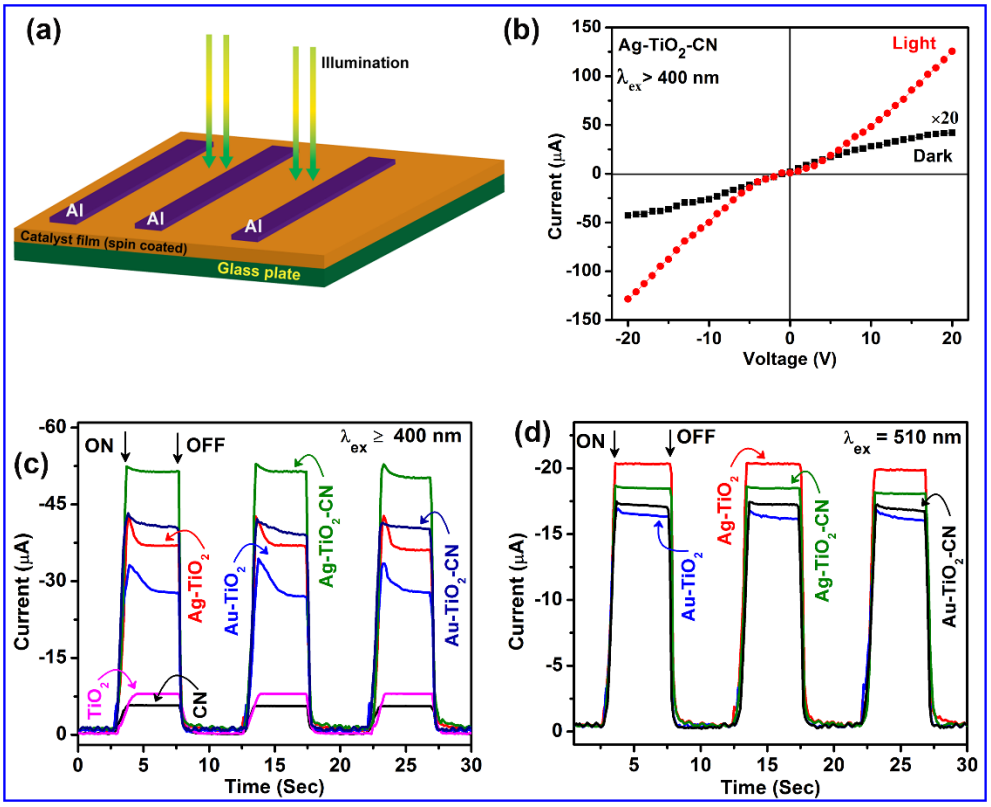

Fig. 4.13. (a) Schematic of the photoconductivity measurement. (b) Current vs voltage curve for Ag-TiO_2-CN under dark and visible light illumination (λ>400 nm). Photocurrent response of binary (Ag-TiO_2, Au-TiO_2) and ternary (Ag-TiO_2-CN, Au-TiO_2-CN) plasmonic photocatalysts with respect to pristine TiO_2 and CN under the illumination of (c) full visible solar spectrum irradiation (λ ≥ 400 nm) and under monochromatic irradiation at (d) 510 nm.

When the light is OFF, the current swiftly reduces to zero. Alternating ON-OFF light illumination is considered for 3 cycles, indicating repeatable photocurrent generation in the system. There is no noticeable change in the maximum photocurrent in each cycle. Under white light illumination (λ>400 nm) on pristine TiO_2 and C_3N_4, we have recorded a low magnitude of photocurrent (**Fig. 4.13(c)**). The low photocurrent is possibly due to the large band gap of TiO_2 (~3.2 eV). Even though C_3N_4 shows band gap absorption in the visible region, the photocurrent response is very small, may be due to its low thickness and higher recombination of carriers in the 2D layered nanosheets [11]. In Au-TiO_2, the photocurrent enhances by 4-times, while it is ~5.5-times in Ag-TiO_2 and Au-TiO_2-CN. Highest photocurrent value is recorded for Ag-TiO_2-CN which is 7-times higher than that of TiO_2 and 9-times higher than CN, see **Fig. 4.13(c)**. Next, the photocurrent is measured at 510 nm which is close to the plasmonic absorption peak of Ag in Ag-TiO_2. The measured photocurrent magnitude under 510 nm excitation can be arranged as Au-TiO_2<Au-TiO_2-CN<Ag-TiO_2-CN<Ag-TiO_2 (**Fig. 4.13(d)**). This shows that the plasmon

excitation of Ag generates a sufficient number of hot electrons which contribute to the photocurrent enhancement.

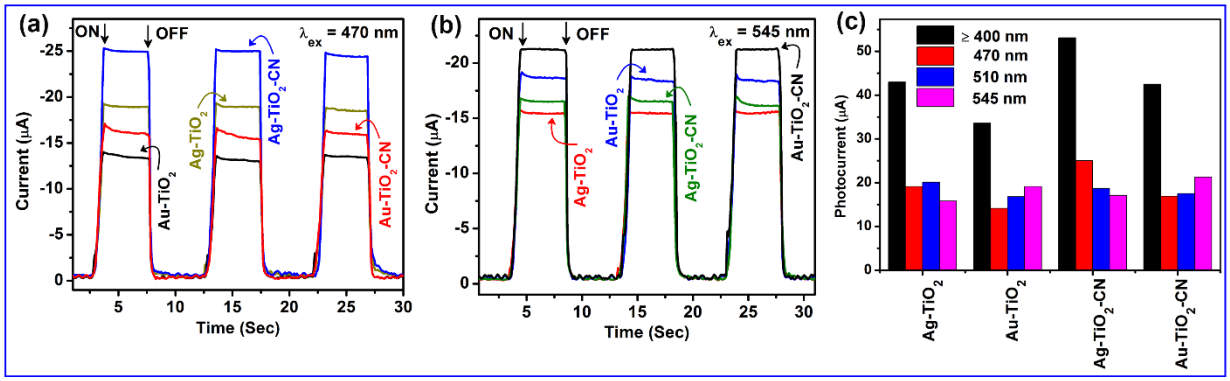

Fig. 4.14. Photocurrent response of the pristine and plasmonic HSs under λ_{ex} of (a) 470 nm and (b) 545 nm. (c) Maximum photocurrent recorded for various samples under different illumination wavelength.

Next, the photocurrent of each catalyst was measured under monochromatic wavelengths 470 nm and 545 nm. These wavelengths are close to the plasmonic absorption peak of Ag in Ag-TiO_2-CN (~470 nm), and Au in Au-TiO_2 (~540 nm) and Au-TiO_2-CN (~545 nm). Under 470 nm excitation, the photocurrent magnitude follows a trend Au-TiO_2<Au-TiO_2-CN<Ag-TiO_2<Ag-TiO_2-CN, as shown in **Fig. 4.14(a)**. The measured photocurrent under 545 nm irradiation can be arranged as Ag-TiO_2<Ag-TiO_2-CN<Au-TiO_2<Au-TiO_2-CN (see **Fig. 4.14(b)**). **Fig. 4.14(c)** shows the highest photocurrent displayed by various samples under different excitation wavelength. Thus, the photoresponse measurement clearly demonstrates the generation of high photocurrent when the catalyst is illuminated at or near their respective plasmonic absorption peaks.[32]

We have, however, observed the highest photocurrent response when the white light excitation is used. Illumination under broadband light source (400-900 nm) can photoexcite electrons and holes in both TiO_2 and C_3N_4, promoting charge transfer from TiO_2 to C_3N_4, and when the excitation wavelength matches with the plasmonic frequency, there is a promotion of hot electron injection from Ag (or Au) to TiO_2. Thus, the photocurrent at each wavelength add up to contribute to the strong photocurrent generation in the system. Photoexcitation at 470 nm, which is near the Ag plasmonic peak in Ag-TiO_2-CN, enhances photocurrent evolution in the system. This is achieved because of hot electron injection from Ag to TiO_2 followed by interfacial charge transfer from TiO_2 to C_3N_4. Photoexcitation at 510 nm, near the SPR band of Ag-TiO_2, promotes

hot electron injection mediated photocurrent enhancement. Au-TiO_2 and Au-TiO_2-CN exhibit photocurrent enhancement with the photoexcitation at 540 nm and 545 nm, respectively near their plasmonic absorption peaks. These results clearly demonstrate that sharp photocurrent response involves hot electron generation, migration to the interface and transfer to the attached semiconductors. The photoresponse study supports the fact that photocatalysis in binary and ternary plasmonic systems is regulated by hot electron generation and interfacial charge transfer.

4.3.7. Mechanism for Enhanced Photocatalysis

On the basis of the results discussed above, the photocatalytic enhancement in the plasmonic HSs is believed to result from SPR absorption of metal NPs, interfacial charge separation, and their transfer through the multiple interfaces of the HS. In order to discuss these phenomena, we have determined the conduction and valence band-edge potential energy of a semiconductor by Mulliken electronegative theory.

$$E_{CB} = \chi - E^{C} - 0.5E_{g}$$

$$E_{VB} = E_{CB} - E_{g}$$

Where E_{CB} is conduction band-edge potential, E_{VB} is valence-band potential, χ is absolute electronegativity of a semiconductor, which is the geometric mean of the absolute electronegativity of the constituent atoms. Absolute electronegativity of the constituent atoms is expressed as the arithmetic mean of the first ionization energy and the electron affinity. E^{C} is the energy of the free electron on the hydrogen scale, which is ~4.5 eV, and E_g is the band-gap of the semiconductor. For TiO_2 and CN nanosheets, the χ values are 5.81 eV and 6.9 eV, respectively. The measured values of bandgap for TiO_2 and CN are 3.31 eV and 2.92 eV, respectively. Therefore, E_{CB} and E_{VB} band edge potentials for TiO_2 are estimated to be -0.345 eV and 2.965 eV, respectively. The calculated values of E_{CB} and E_{VB} for CN are determined to be 0.94 eV and 3.86 eV, respectively. The band edge in electrochemical scale and absolute vacuum scale (AVS) are inter-convertible by following the relation: $E_{AVS}(eV) = -E_{NHE} - 4.5$ (V).[33] Therefore, the energies of VB and CB edges for TiO_2 are -7.465 eV and -4.155 eV, while these positions for CN are at -8.36 eV and -5.44 eV, respectively. Based on the VB and CB edge positions, we might predict effective interfacial charge separation in the HSs of CN and TiO_2.

The work function of Au NPs and Ag NPs are reported to be at -5.1 eV and -4.7 eV, respectively.[34]

We speculate that there are two synergetic plasmonic effects which might regulate the photocatalytic activity in Ag-TiO_2 and Au-TiO_2 HS: (i) localized electromagnetic field enhancement in the vicinity of the metal-semiconductor interface. This radiative coupling between metal-semiconductor requires a field energy equivalent to or higher than the band gap of the semiconductor and depends on the inter-particle gap as well as the distance of metal from the semiconductor. (ii) Hot electron injection or LSPR (localized surface plasmon resonance) sensitization effect. In this process, the energetic hot electrons transfer to the semiconductor following direct or indirect electron injection pathways.[35] We will now attempt to explain the plasmonic mediated photocatalytic enhancement based on these two controlling effects.

Ag-TiO_2 and Au-TiO_2 exhibit the maximum plasmonic absorption band at ~500 nm and ~520 nm, respectively. Under visible light, the plasmonic excitation is activated, which results in strong electromagnetic field intensity enhancement at the metal-semiconductor interface. The enhancement factor again depends on the separation between the metal NPs. Yang et al. reported maximum field enhancement when the separation between particles is between ~5-10 nm.[36] Harutyunyan et al. suggested that the strong coupling of metal NPs near the semiconductor interface increases the generation of hot-electron at those confined hot-spot regions.[37] Increase in the separation weakens the inter-particle coupling contributing to less hot electron generation.[38] From our TEM analysis, the average inter-particle separation between the nearest Ag and Au NPs are estimated to be ~3.4 nm and ~4.7 nm for Ag-TiO_2 and Au-TiO_2, respectively, as shown in **Fig. 4.2(c, f)**. Therefore, in agreement with the observation by Yang et al.[36], we presume that this interparticle distance could be the regions of plasmonic hot spots formation in the present system. The total rate of generation of hot electrons on a nanosphere is expressed by the equation:

$$\text{Rate} = \frac{2}{\pi^2}\frac{e^2 E_F^2}{\hbar}\frac{(\hbar\omega - \Delta E_b)}{(\hbar\omega)^4}\frac{4\pi}{3}R_0^2\left|\frac{3\varepsilon_0}{2\varepsilon_0 + \varepsilon_{metal}}\right|\cdot E_0^2 \qquad (4.1)$$

Where E_F is the Fermi energy, R_0 is the radius of the nanosphere, $\frac{3\varepsilon_0}{2\varepsilon_0 + \varepsilon_{metal}}E_0$ is the electric field inside the nanosphere and E_0 is the external field of light.[39] The high energy hot electrons

(E) are distributed in the range $E_F + \Delta E_b < E < E_F + \hbar\omega$, and the low energy hot electrons are distributed in the range $E < E_F + \Delta E_b$, where ΔE_b is the Schottky energy barrier.[40]

The equation (1) shows that the rate of hot electron energy generation on the nanosphere has a dependence on the size of the plasmonic NPs. In larger nanocrystals, the hot electron energy dissipates quickly due to large electron-electron (e-e) scattering. In the present study, following equation (1) we can predict that the rate of hot electron generation is higher in Au NPs (R_0 ~12.3 nm, from TEM) than that in Ag NPs (~7.2 nm). However, because of the large size of the Au NPs, the hot electron energy dissipates quickly while moving to the surface. The other factors which influence the high energy hot electron generation are its mean free path for the plasmonic metals and the field enhancement factor at the interparticle gap (hotspot). The electric field enhancement factor increases with a decrease in the interparticle separation. From TEM analysis, we find that the interparticle separation is smaller in Ag case (3.4 nm) than the Au case (4.7 nm). Thus, the hot spot regions in Ag-TiO_2 could generate more high energy electrons than in Au. Furthermore, the electron in Ag have longer mean free path than that in Au[39], and thus the electron-electron scattering is expected to be less in Ag than in Au. Hence, high density of hot electron energy will be generated at the hot spots. The hot electrons have lifetime within fs–ps time scale. The attached semiconductor must extract these hot electrons within this time-scale.

The extraction of hot electrons by a semiconductor follows either an indirect or a direct pathway (see **Fig. 4.15(a, b)**). As mentioned, the low energy hot electrons are distributed near the Fermi surface, and the high energy hot electrons are distributed in the range $E_F + \Delta E_b < E < E_F + \hbar\omega$. In the indirect process of charge extraction, the high energy electrons migrate to the metal-semiconductor interface and cross the Schottky energy barrier ΔE_b, which for metal-semiconductor is ~1 eV (equation 1, **Fig. 4.15(a)**). Reports show that the charge extraction efficiency by this process is < 1%.[41] In a direct charge extraction process, the low energy hot electrons can be directly excited to the semiconductor without the need to cross ΔE_b (**Fig. 4.15(b)**). This can happen either through quantum tunnelling of low energy hot electrons through the interfacial barrier or via the coupling of the hot electrons with the interfacial defect states. The direct process is known to have a charge extraction efficiency of >20 %.[41] The

possibility of quantum tunnelling depends on the width of the depletion layer at the metal-semiconductor interface.

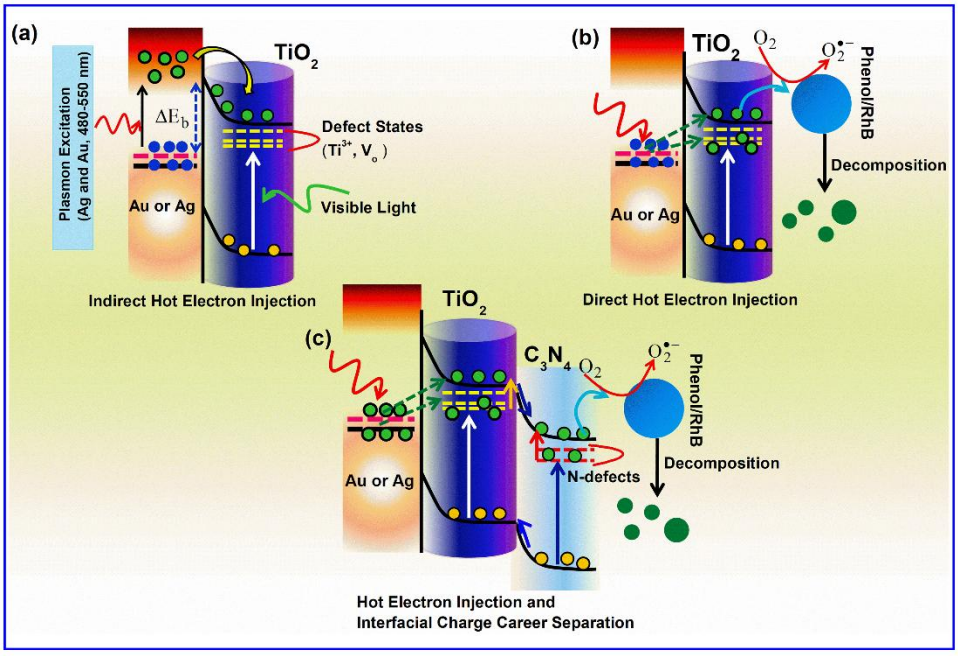

Fig. 4.15. Schematic representation of hot electron generation and its injection to the semiconductor by (a) indirect process, (b) direct process and (c) the direct injection of hot electrons and their migration through the multiple interfaces of the HS.

The depletion layer width increases if there is a large collection of electrons from semiconductor to metal in which the metal is negatively charged at the interface. However, if the interface contains cationic trap states such as Ti^{3+}, the negative charge on metal gets neutralized by the balancing of cationic states at the interface. Thus, the depletion layer width narrows at higher cationic dopants such as Ti^{3+}. This might facilitate quantum tunnelling of hot electrons directly to the conduction band of TiO_2 (**Fig. 4.15(b)**).

Recently, Tan et al. proposed that the hot electrons couple with intermediate trap states at the metal-TiO_2 interface and thereby, the carriers undergo photoexcitation to the semiconductor.[42] Similar type of studies have shown that the Ti^{3+} present in the system (TiO_2) could act as mediator for the plasmonic energy transfer from metal NPs to the semiconductor.[43] Our XPS results have shown that the samples contain Ti^{3+} with an associated oxygen vacancy defects in the system. The Ti^{3+} states and oxygen vacancy states in TiO_2 can be distributed in the range 0.8-1 eV below the conduction band edge.[44] Those hot electrons which have sufficient energy to surpass the Schottky energy barrier can move to the conduction band of TiO_2, shown

in **Fig. 4.15(a)**. However, the low energy hot electrons migrate to the interface, couple with the interfacial Ti^{3+} states and transfer the hot energy to trigger excitation of the electrons to the conduction band of TiO_2. The electrons collected at the conduction band migrate to the surface, interact with the adsorbed RhB or phenol molecule and decompose it (**Fig. 4.15(b)**). It is observed that Ag-TiO_2 shows better photocatalytic activity than Au-TiO_2. As mentioned, Ag has a longer mean free path than Au with less interparticle gap separation. Therefore, hot electron generation, accumulation at the hot spot region and their migration through the interface is expected to be more efficient in Ag-TiO_2 than in Au-TiO_2. Therefore, from the results, we might speculate that hot electron injection via the intermediate defect states could be partly responsible for the enhanced photocatalytic efficiency in Ag-TiO_2 and Au-TiO_2.

Next, we discuss the mechanism of superior photocatalytic activity displayed by Ag-TiO_2-CN and Au-TiO_2-CN. Along with hot electron generation and injection, the interfacial charge transfer is an additive for the superior photocatalytic activity in the three component plasmonic photocatalyst. Visible light excitation in CN could transfer electrons from VB to CB or the nitrogenated defect states. Initially, hot electrons are excited to the conduction band of TiO_2 via the intermediate defect states. The electrons from CB of TiO_2 then transfer to the CB of CN, which possesses an extended 2D network of C, N bondings, as depicted in **Fig. 4.15(c)**. Thus, once transferred to CN the electrons could easily transport to a distant position over the 2D surface away from the interface, thus reducing the carrier recombination probability. The electrons on the surface of CN generate superoxide radicals, interact with RhB and phenol and results in their decomposition.

4.4. Summary and Conclusions

1. An in-situ chemical method was adopted to prepare binary and ternary plasmonic hybrids of Au and Ag with porous TiO_2(B) NRs and g-C_3N_4 nanosheets.
2. Lower inter-particle gap of Ag NPs facilitates numerous plasmonic hot spots, electromagnetic field enhancement and hot electron generation at the Ag-based binary and ternary HSs.
3. Ag-TiO_2-C_3N_4 HS with optimum charge transfer time (13.1 ns) and charge transfer efficiency (39.5%) is found to be the most promising visible light photocatalyst studied here.

4. We have achieved >98% degradation of RhB and phenol after 100 min of visible light irradiation.
5. Photoresponse study with monochromatic photoexcitation near the plasmonic absorption peak confirms the hot electron injection from plasmonic NPs to TiO_2-CN.
6. Trap state mediated direct hot electron injection from Ag NP to TiO_2(B), and efficient interfacial separation is shown to yield the high visible light photocatalysis.

References

1. M. Kim, M. Lin, J. Son, H. Xu and J. M. Nam, *Adv. Opt. Mater*, 2017, **5**, 1700004.
2. T. G. U. Ghobadi, A. Ghobadi, E. Ozbay and F. Karadas, *ChemPhotoChem*, 2018, **2**, 161-182.
3. K. K. Paul and P. K. Giri, *J. Phys. Chem. C*, 2017, **121**, 20016-20030.
4. X. Wei, C. Shao, X. Li, N. Lu, K. Wang, Z. Zhang and Y. Liu, *Nanoscale*, 2016, **8**, 11034-11043.
5. Y. Chen, W. Huang, D. He, Y. Situ and H. Huang, *ACS Appl. Mater. Interfaces*, 2014, **6**, 14405-14414.
6. Z. Yajun, S. Jian-Wen, M. Dandan, F. Zhaoyang, N. Chunming and W. Lianzhou, *ChemCatChem*, 2017, **9**, 3752-3761.
7. M. Zang, L. Shi, L. Liang, D. Li and J. Sun, *RSC Adv.*, 2015, **5**, 56136-56144.
8. M.-J. Lee, S.-H. Lim, J.-M. Ha and S.-M. Choi, *Langmuir*, 2016, **32**, 5937-5945.
9. P. C. Lee and D. Meisel, *J. Phys. Chem.*, 1982, **86**, 3391-3395.
10. K. Dongjo, J. Sunho and M. Jooho, *Nanotechnology*, 2006, **17**, 4019.
11. B. Choudhury and P. K. Giri, *RSC Adv.*, 2016, **6**, 24976-24984.
12. Y. Zhang, Z. Xing, X. Liu, Z. Li, X. Wu, J. Jiang, M. Li, Q. Zhu and W. Zhou, *ACS Appl. Mater. Interfaces*, 2016, **8**, 26851-26859.
13. B. Santara, P. K. Giri, K. Imakita and M. Fujii, *Nanoscale*, 2013, **5**, 5476.
14. M. Wang, J. Han, H. Xiong, R. Guo and Y. Yin, *ACS Appl. Mater. Interfaces*, 2015, **7**, 6909-6918.
15. J. Zhang, A. Byeon and J. W. Lee, *ChemComm*, 2014, **50**, 6349-6352.
16. S. Ma, S. Zhan, Y. Jia, Q. Shi and Q. Zhou, *Appl. Catal. B Environ.*, 2016, **186**, 77-87.
17. G. M. National Institute of Standards and Technology, *NIST Standard Reference Database Number 20*, 2000, DOI: doi:10.18434/T4T88K.
18. X. Pan, M.-Q. Yang, Z.-R. Tang and Y.-J. Xu, *J. Phys. Chem. C*, 2014, **118**, 27325-27335.
19. A. Zielińska-Jurek, E. Kowalska, J. W. Sobczak, W. Lisowski, B. Ohtani and A. Zaleska, *Appl. Catal. B Environ.*, 2011, **101**, 504-514.
20. P. Zhang, T. Wang and J. Gong, *Adv. Mater.*, 2015, **27**, 5328-5342.
21. Y. Horiguchi, T. Kanda, K. Torigoe, H. Sakai and M. Abe, *Langmuir*, 2014, **30**, 922-928.
22. S. Melissen, T. Le Bahers, S. N. Steinmann and P. Sautet, *J. Phys. Chem. C*, 2015, **119**, 25188-25196.
23. L. Xiang, X. Zhao, C. Shang and J. Yin, *J Colloid Interface Sci*, 2013, **403**, 22-28.
24. A. Stevanovic, S. Ma and J. T. Yates, *J. Phys. Chem. C*, 2014, **118**, 21275-21280.
25. B. Choudhury, K. K. Paul, D. Sanyal, A. Hazarika and P. K. Giri, *J. Phys. Chem. C*, 2018, **122**, 9209-9219.
26. K. Wu, Q. Li, Y. Du, Z. Chen and T. Lian, *Chem. Sci.*, 2015, **6**, 1049-1054.
27. M. D. L. Ruiz Peralta, U. Pal and R. S. Zeferino, *ACS Appl. Mater. Interfaces*, 2012, **4**, 4807-4816.

28. N. T. Khoa, S. W. Kim, D.-H. Yoo, S. Cho, E. J. Kim and S. H. Hahn, *ACS Appl. Mater. Interfaces*, 2015, **7**, 3524-3531.
29. B. Choudhury and P. K. Giri, *RSC Adv.*, 2016, **6**, 24976-24984.
30. R. Gone, C. Biswajit and P. K. Giri, *Nanotechnology*, 2017, **28**, 395703.
31. C. G. Silva, M. J. Sampaio, S. A. C. Carabineiro, J. W. L. Oliveira, D. L. Baptista, R. Bacsa, B. F. Machado, P. Serp, J. L. Figueiredo, A. M. T. Silva and J. L. Faria, *J. Catal.*, 2014, **316**, 182-190.
32. L. J. Brennan, F. Purcell-Milton, A. S. Salmeron, H. Zhang, A. O. Govorov, A. V. Fedorov and Y. K. Gun'ko, *Nanoscale Res. Lett*, 2015, **10**, 38.
33. Z. Xiong, L. L. Zhang, J. Ma and X. S. Zhao, *Chem. Commun.*, 2010, **46**, 6099-6101.
34. L.-L. Tan, W.-J. Ong, S.-P. Chai and A. R. Mohamed, *Appl. Catal., B*, 2015, **166-167**, 251-259.
35. M. Kim, M. Lin, J. Son, H. Xu and J.-M. Nam, *Adv. Opt. Mater*, 2017, **5**, 1700004.
36. T.-H. Yang, Y.-W. Harn, M.-Y. Pan, L.-D. Huang, M.-C. Chen, B.-Y. Li, P.-H. Liu, P.-Y. Chen, C.-C. Lin, P.-K. Wei, L.-J. Chen and J.-M. Wu, *Appl. Catal., B*, 2016, **181**, 612-624.
37. H. Harutyunyan, A. B. F. Martinson, D. Rosenmann, L. K. Khorashad, L. V. Besteiro, A. O. Govorov and G. P. Wiederrecht, *Nat. Nanotechnol.*, 2015, **10**, 770.
38. D. C. Ratchford, A. D. Dunkelberger, I. Vurgaftman, J. C. Owrutsky and P. E. Pehrsson, *Nano Letters*, 2017, **17**, 6047-6055.
39. X.-T. Kong, Z. Wang and A. O. Govorov, *Adv. Opt. Mater.*, 2016, **5**.
40. X.-T. Kong, Z. Wang and A. O. Govorov, *Adv. Opt. Mater*, 2017, **5**.
41. S. K. Cushing, *Nat. Photonics*, 2017, **11**, 748-749.
42. S. Tan, A. Argondizzo, J. Ren, L. Liu, J. Zhao and H. Petek, *Nat. Photonics*, 2017, **11**, 806-812.
43. A. Naldoni, F. Fabbri, M. Altomare, M. Marelli, R. Psaro, E. Selli, G. Salviati and V. Dal Santo, *Phys. Chem. Chem. Phys.*, 2015, **17**, 4864-4869.
44. A. Naldoni, M. Allieta, S. Santangelo, M. Marelli, F. Fabbri, S. Cappelli, C. L. Bianchi, R. Psaro and V. Dal Santo, *J. Am. Chem. Soc.*, 2012, **134**, 7600.

Chapter 5

Strongly Enhanced Visible Light Photoelectrocatalytic Hydrogen Evolution Reaction in n-doped MoS_2/TiO_2(B) Heterojunction by Selective Decoration of Platinum Nanoparticles at the MoS_2 Edge Sites

In this chapter, we demonstrate strongly enhanced visible light photoelectrocatalytic hydrogen evolution reaction (HER) in few-layer MoS_2 grown on a mesoporous TiO_2(B) nanobelt (NB) by selective decoration of platinum (Pt) nanoparticles (NPs) with extremely low concentration on the edge/defect sites of the MoS_2 layer. Three catalytically active components are anchored together to increase the photoelectrocatalytic HER activity synergistically, beyond that of commercial Pt/C electrode. During the heterojunction formation, S is doped in the TiO_2 layer causing the high density of electrons in TiO_2 that migrate to the MoS_2 layer inducing n-type doping in it and thus TiO_2 acts as an efficient photocathode in the photoelectrocatalysis. The marginal Pt loaded ternary system exhibits an extremely low charge transfer resistance and low overpotential as well as Tafel slope, boosting the overall HER performance with high stability under the visible light. The results show that the marginally-loaded Pt NPs activate the inert basal plane, edge sites of MoS_2 and porous sites of TiO_2, making an integrated network where the photogenerated electrons can easily be injected from the TiO_2 to MoS_2 and then to Pt NPs, presenting a feasible approach to boost the HER activity under visible light.

5.1. Introduction

The fast-rising energy crisis and environmental pollution are driving the development of new, sustainable, pollution-free sources that can be used on an industrial scale. Hydrogen is believed to be one of the most promising alternatives to fossil fuels and a source of renewable green energy due to its high energy density and carbon-free combustion emission. Solar-light-driven electrocatalysis using semiconductor heterostructures (HSs) is one of the most promising sustainable technologies for the generation of hydrogen by water splitting.[1, 2] Though platinum (Pt) group noble metals are the most efficient conventional electrocatalysts, their extremely high cost and scarcity in nature hinder their industrial-scale usage.[3] Two-dimensional (2D) transition metal dichalcogenide nanosheets, especially MoS_2 has now been recognized as an efficient co-

catalyst incorporated with TiO_2 nanostructures due to its structural anisotropy, chemical inertness, good electroconductivity, and efficient catalytic properties.[4-6] Theoretical and experimental studies found that the HER ability of MoS_2 mainly derives from the edge sites of its 2D layers, whereas the basal planes are catalytically inert, limiting its overall performance.[7] Thus, tuning the architecture of MoS_2 to preferentially edge-exposed sites, semiconducting (2H) to metallic (1T) phase transformation, the introduction of vacancies and incorporation with metal NPs are the synergistic strategies for the enhancement of HER activity.[8-11] Recently, edge-site-activated ultra-thin MoS_2 nanostructures with optimum defect density, especially S-vacancies, have been identified as tunable active sites to stimulate the originally inert basal plane for the HER.[12, 13] Xu et al.[14] demonstrated a smart strategy of utilizing the inert basal plane by loading Pt NP (2.45 wt%) on the porous MoS_2 nanostructures anchored vertically with the carbon fiber cloths, which in turn reduces Pt consumption without compromising the HER activity. It may be noted that though there are several reports on the catalytic activity of binary MoS_2/Pt and TiO_2/Pt system, there is hardly any report on the TiO_2/MoS_2/Pt composite system.[14-17] Very recently, photocatalytic and electrocatalytic H_2 generation in TiO_2/Pt/MoS_2 composite system was reported by Li et al.[18]. However, the system was not well characterized and the performance of the composite system was comparable or inferior to that of binary systems. Herein, a solvothermally grown porous TiO_2(B) NBs are considered as a novel platform for the decoration of edge site exposed few-layer MoS_2. Subsequently, marginal Pt NPs are preferentially decorated at the edge sites of MoS_2 and porous sites of TiO_2(B) to exploit its application in next-generation photoelectrocatalysis.

5.2. Experimental Details

5.2.1. Sample Preparation

5.2.1.1. Synthesis of TiO_2(B) NBs

TiO_2 NBs were synthesized by a typical solvothermal process described in **Chapter 2, Section 2.2.1.1**. with a modified solvothermal reaction temperature at 220 °C. The morphology, crystal structure and phase of the sample were characterized by FESEM, TEM, XRD and micro-Raman analyses.

5.2.1.2. Growth of MoS_2/TiO_2 NBs HSs

Typically, 20 mg of TiO_2(B) NBs powder was homogeneously dispersed into 40 ml of Milli-Q (MQ) water in a bath sonication for 30 min. Next, 60 mg sodium molybdate ($Na_2MoO_4 \cdot 2H_2O$) and 120 mg thioacetamide (C_2H_5NS) as a source of Mo and S, respectively were dissolved in the above dispersion. The mixture was then treated in a Teflon-lined stainless steel autoclave at 240 °C for 24 h with a constant magnetic stirring at 250 rpm. The resultant black precipitate was washed thoroughly with DI water to eliminate the additional salts and impurities followed by a centrifugation. A uniform decoration of few-layer MoS_2 on the TiO_2 NBs platform with 1:1 weight ratio of MoS_2 and TiO_2 was obtained after a drying process at 50 °C for 12 h. For comparison, pure few-layer MoS_2 were synthesized under identical conditions but in the absence of TiO_2 NB platform.

5.2.1.3. Decoration of Pt NP on the TiO_2 NBs, MoS_2 Nanosheets and MoS_2/TiO_2 NBs

50 mg of MoS_2/TiO_2 powder was dispersed into 100 ml of MQ water in an ultrasonic bath for 30 min. 52 mg H_2PtCl_6 was dissolved into 100 ml of MQ water and added dropwise into the MoS_2/TiO_2 dispersion under magnetic stirring. Then, 50 ml of 0.01 M aqueous $NaBH_4$ solution was added slowly into the above mixture to deposit Pt NP uniformly over the MoS_2/TiO_2 HSs. Similar process was adopted to decorate Pt NPs on the pristine TiO_2(B) NBs as well as MoS_2 nanosheets. A summary of the samples studied with sample codes is provided in **Table 5.1**.

Table 5.1: *Summary of the samples, the relative percentage of oxygen vacancy (O_V), hydroxyl group (O_H), lower and higher binding energy (BE) sulfur (S) present in the samples.*

Sample code	***Sample***	***Various species from deconvoluted XPS spectra (in %)***			
		O_V	O_H	Lower BE S (terminal and unsaturated)	Higher BE S (bridging and apical)
TB	TiO_2(B)	22.2	18.4	-	-
MS	MoS_2	-	-	60.9	39.1
MSTB	MoS_2/TiO_2	46.1	32.7	45.6	54.4
PMS	Pt@MoS_2	-	-	-	-
PTB	Pt@TiO_2	15.5	23.1	-	-
PMSTB	Pt@MoS_2/TiO_2	31.4	47.3	27.8	72.2

5.2.2. Photoelectrocatalysis Measurements under Visible Light

Photoelectrochemical measurements were performed systematically in a conventional three-electrode electrochemical cell: a commercial Ag/AgCl (saturated KCl) (CH instruments) as reference electrode, Pt wire or graphite rod as counter electrode and the as-grown catalysts supported on a glassy carbon substrates were used as working electrodes, as schematically shown in **Fig. 5.1**. All the PEC measurements were performed in Tata Institute of Fundamental Research-Hyderabad, India. Prior to catalyst loading, the surface of the glassy carbon substrate is polished with 50 μm alumina powders on a polishing cloth and washed with DI water. A 4 mg catalyst was dissolved in 1 mL DI water and the dispersion was sonicated for 1 h. A 6 μL of as-prepared sample was drop cast on the glassy carbon electrode (diameter = 3 mm) and dried in the inert atmosphere. The net loading of each catalyst is ~0.34 mg/cm^2. Electrochemical surface area (ECSA) of each catalyst was measured using Randel-Sevick equation:

$$I_p = (2.69 \times 105)n^{3/2}AD^{1/2}v^{1/2}C\ ,$$

Where I_p is anodic peak current (amps), υ is the scan rate of potential, n is the number of electrons involved in the reaction, A is the active surface area (cm^2), C (moles/cm^3) is the concentration of electroactive species, D is diffusion coefficient (cm^2/s). Thus, the active surface area 'A' of the electrode is calculated from the cyclic voltammetry (CV) response of 5 mM $[Fe(CN)_6]^{3-/4-}$ in 0.1 M KCl at different scan rates. The calculated ECSA for the TB, MS, PMS, PTB, MSTB and PMSTB are 0.038, 0.042, 0.048, 0.050, 0.052 and 0.045 cm^2, respectively.

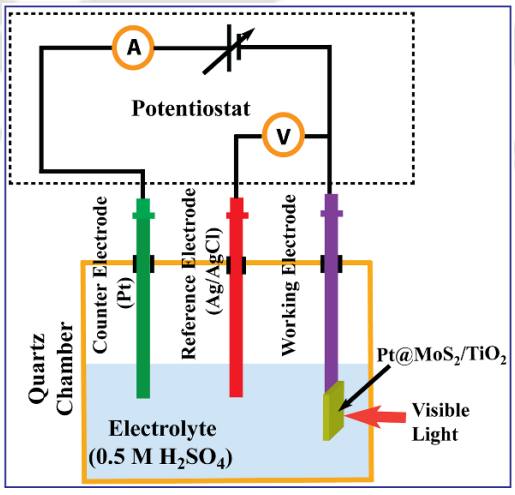

Fig. 5.1. Schematic illustration of the experimental setup for the photoelectrochemical (PEC) measurements and hydrogen evolution reaction (HER). Bias is applied between the working electrode (as-grown catalyst) and counter electrode (Pt).

The photoelectrocatalytic studies were performed using a Bio-Logic SP-300 electrochemical workstation. A 250 W Xenon lamp (Lelesil Innovative Systems, India) was used as the visible light source with the wavelength range of ~370–730 nm during the photoelectrochemical measurements. A 0.5M H_2SO_4 solution was used as an electrolyte, deaerated by N_2 purging until saturation prior to any electrochemical experiment. Linear sweep voltammetry (LSV) was conducted at a scan rate of 5 mV/s. Electrochemical impedance spectroscopy (EIS) was also performed in 0.5M H_2SO_4 under dark and light at HER onset potential of each catalyst over the frequency range 7 MHz–100 Hz with an input sine wave having 10 mV amplitude.

5.2.3. Characterization Techniques

The details of the FESEM, EDS, XRD, Raman, TEM and XPS were described in **Chapter 2, Section 2.2.3**. Additionally, edge sites of MoS_2 layers and the selective decoration of Pt NPs were identified using bright field scanning transmission electron microscopy (STEM) mode using an aberration-corrected STEM (JEM 2100F, 200 kV), performed in University of Birmingham, UK. UV-Vis diffuse reflectance spectroscopy (DRS) measurements were recorded using a commercial spectrophotometer (SHIMADZU 2600). The details of the room temperature (RT) steady-state PL measurement were discussed in **Chapter 4, Section 4.2.2**.

5.3. Results and Discussion

5.3.1. Morphology and Composition Studies

Fig. 5.2(a) shows a FESEM image of the pristine TiO_2 NBs with diameter ~30-100 nm and length ~ a few μm, while **Fig. 5.2(b)** shows a uniform decoration of Pt NPs over the TiO_2 NBs. **Fig. 5.2(c, d)** exhibit the FESEM image of MoS_2 nanosheets before and after the Pt NP decoration, respectively. During the 2nd stage hydrothermal treatment, self-assembly of few-layer MoS_2 nanosheets on the porous TiO_2 NB template transforms it into discrete MoS_2 nanoflowers (NFs) decorated on the TiO_2 NBs with the size distribution 130-350 nm, as shown in **Fig. 5.2(e)**. **Fig. 5.2(f)** shows the FESEM micrograph of Pt NP-decorated MSTB HSs. Large Pt NPs observed on the TiO_2 and MoS_2 surface may be due to the aggregation. Note that, the deposited Pt NPs on the edge-exposed MoS_2 NFs have appreciably small size and a narrow size distribution (discussed later), and hence the NPs were not discernable here due to the resolution limit of the FESEM.

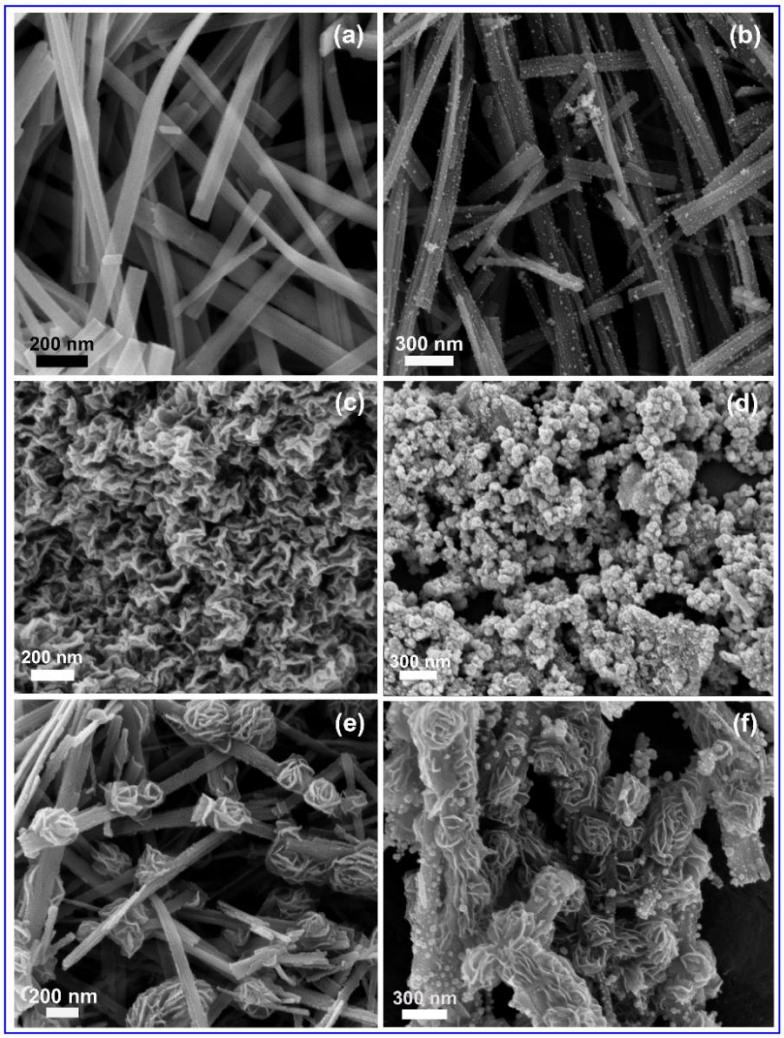

Fig. 5.2. FESEM images of (a) pristine TiO_2 NBs, (b) Pt NP decorated TiO_2 NBs, (c) pristine MoS_2 nanosheets, (d) Pt NP decorated MoS_2 nanosheets, (e) MoS_2 NF decorated on TiO_2 NBs, and (f) Pt NP decorated MoS_2/TiO_2 HSs.

Fig. 5.3(a, b) exhibit TEM micrographs of Pt NPs decorated on TiO_2 NBs (PTB HS) at two different magnifications, demonstrating an overall uniform decoration of Pt NPs, and the **Fig. 5.3(c)** shows an HRTEM lattice fringe pattern of well-crystalline Pt NPs and TiO_2 NBs in PTB. The calculated lattice spacing of 0.22 nm corresponds to the (111) plane of Pt NP, and 0.29 nm and 0.32 nm correspond to the (111) and (002) crystal planes of TiO_2(B), respectively, in the PTB HSs. TEM images in **Fig. 5.3(d, e)** reveal the in-situ growth of MoS_2 layers on the porous TiO_2 NBs platform with a broad size distribution of 100-380 nm, which is in good agreement with the FESEM analysis. As evident from the image, the pure MoS_2 crystals with maximally exposed edge active sites appear to be layered wavy petals, and they gather together to form distinct nanorose-like structures on the porous TiO_2 NBs platform due to the high autogenous

pressure (~45 bar) inside the autoclave. Insets in Fig 2(d, e) depict the hexagonal diffraction spots and a honeycomb atom arrangement in a 2H-MoS_2, respectively, grown over TB. The HRTEM lattice fringe pattern of MSTB HS shown in **Fig. 5.3(f)** clearly reveals the co-existence of few-layer MoS_2 with the TiO_2 lattice. **Fig. 5.3(f)** shows a typically layered nanosheet having ~6 sandwiched S–Mo–S layers with interlayer spacing ~0.67 nm. Additional ordered domains with a lattice spacing of 0.28 nm can be assigned to the (100) plane at the basal surface of 2H-MoS_2. The lattice spacing of 0.37 nm, 0.39 nm, and 0.64 nm corresponds to the (110), (201) and (001) crystal planes, respectively for pure B-phase TiO_2.

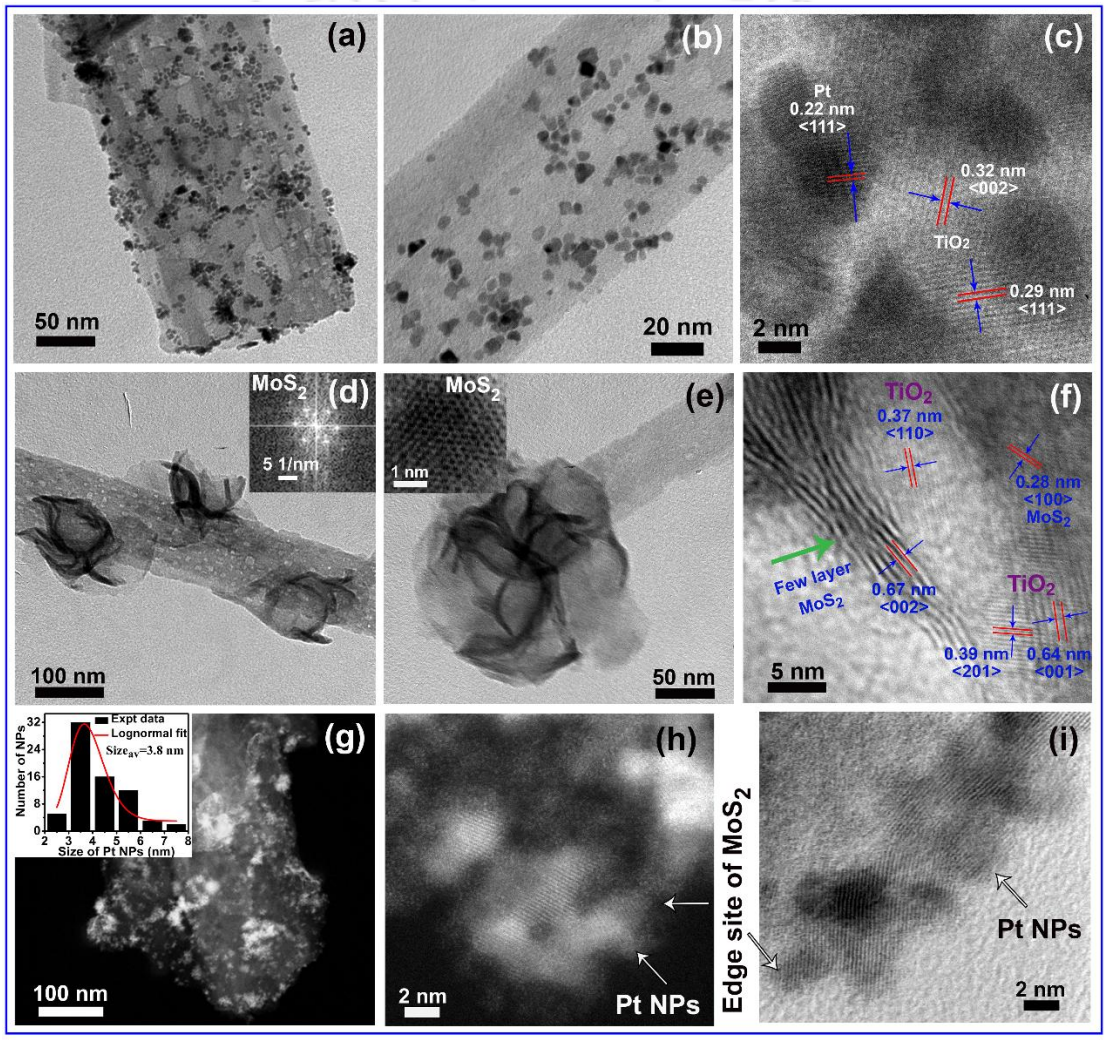

Fig. 5.3. (a, b) Pt NP decorated porous TiO_2 NBs at different magnifications, (c) HRTEM lattice fringe pattern showing the simultaneous presence of Pt and TiO_2. (d) TEM image of MoS_2 NF decorated nanoporous TiO_2 NB; inset shows the hexagonal diffraction spots on the NF site. (e) TEM image of TiO_2 NB coated with MoS_2 NF; the inset shows the BF-STEM image corresponding to the MoS_2 layer. (f) HRTEM lattice fringe pattern of MoS_2/TiO_2 HSs, (g) HAADF image of Pt NP decorated on MoS_2/TiO_2 HSs. Inset shows the size distribution of Pt NPs decorated on MoS_2/TiO_2 HSs. (h, i) High-resolution dark field and bright field STEM images of crystalline Pt NPs selectively decorated on edge-sites of MoS_2 NF, respectively.

It can be observed from the DF-STEM image of PMSTB shown in **Fig. 5.3(g)** that the Pt NPs are selectively decorated at the exposed edge sites of MoS_2 over the MSTB HS, and the inset shows the size distribution of Pt NPs over the MSTB HSs. It shows a very narrow size distribution (distribution width ~0.19 nm) with an average size of 3.8 nm. **Fig. 5.3(h, i)** depict the dark field, and bright field STEM images of Pt NPs anchored selectively on edge/defect sites of MoS_2 layer supported on the TiO_2 NBs, respectively.

In order to estimate the individual contribution of Pt NP and MoS_2 on HER, we performed STEM-EDS elemental mappings on the PMSTB HSs. **Fig. 5.4(a)** shows a STEM image of PMSTB on which elemental mapping was performed. The EDS elemental mapping reveals that the core of the HS is composed of Ti and O elements, as shown in **Fig. 5.4(b, c)**, which further confirms the uniform growth of TiO_2. **Fig. 5.4(d, e)** exhibit the elemental mapping for Mo and S, respectively, which supports our argument that the discrete MoS_2 NF grows on the TiO_2 platform as an outer layer. The Pt NPs are observed to be dispersed with overall uniformity over the MoS_2 NFs, as confirmed by the elemental map of Pt shown in **Fig. 5.4(f**). Similar results of the elemental distribution of Ti, O as the core layer and Mo, S as an outer layer were observed in case of MSTB. However, in the case of PTB, most of the Pt NPs are preferentially attached to the porous sites of TiO_2 nanostructures.

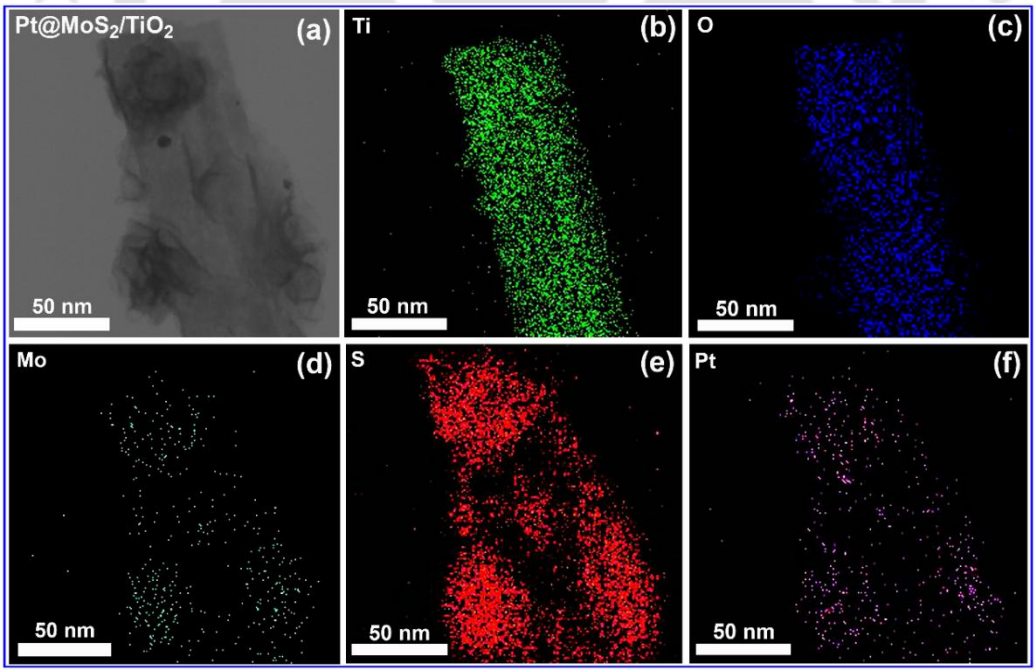

Fig. 5.4. STEM elemental mappings of PMSTB HS: (a) a raw image of the HS, (b-f) elemental maps of Ti, O, Mo, S and Pt, respectively.

5.3.2. Structural Analysis

5.3.2.1. XRD Analysis

Fig. 5.5 depicts the XRD pattern of the as-grown catalysts. The diffraction peaks for pristine MoS_2 (marked with "*") in **Fig. 5.5(a)** detected at 2θ ≈ 14.5°, 32.9° and 56.5° can be attributed to the (002), (100) and (106) crystal planes, respectively (JCPDS card no. 37-1492). XRD peaks corresponding to pristine TiO_2 NBs (labeled with "♦" mark) match with the standard values of the TiO_2 monoclinic structure.[19] **Fig. 5.5(c)** shows the diffraction pattern of few-layer MoS_2 designed on porous TiO_2 NBs (MSTB).

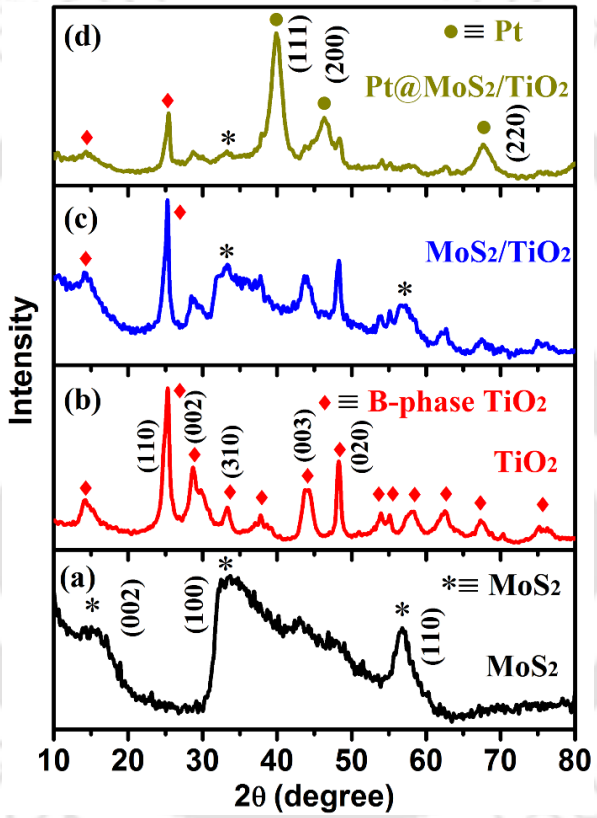

Fig. 5.5. (a) XRD patterns of (a) few-layer MoS_2 NFs, (b) TB, (c) MSTB, and (d) PMSTB.

It can be noted that the diffraction peak of pristine MoS_2 at ~14.5° corresponding to the c-plane was not detected in the case of MSTB. Thus, the absence of this peak confirms the coating of TiO_2 NBs with extremely thin few-layer MoS_2 nanosheets, which may prevent the crystal growth along the c–axis. **Fig. 5.5(d)** shows the XRD pattern of PMSTB, which clearly confirms the co-existence of Pt, MoS_2, and TiO_2(B) crystals. In the figure, the Pt has been labeled as circles (filled). The diffraction peaks of Pt are relatively sharp, clearly implying its highly crystalline nature.

5.3.2.2. Raman Analysis

To investigate the crystallinity, phase and layer numbers in as-grown catalysts, micro-Raman analysis has been performed, as shown in **Fig. 5.6**. Each of the phonon modes of TiO_2 NBs correspond to the monoclinic structure of B-phase TiO_2, see **Fig. 5.6(a)**. The pristine MoS_2 exhibits two active Raman modes attributed to E_{2g}^1 and A_{1g} having separation of 25.1 cm^{-1}, as shown in **Fig. 5.6(a)**. However, MSTB exhibits a combination of B-phase TiO_2 and MoS_2. In MSTB, these Raman modes are observed with a reduced separation of 22.3 cm^{-1}, as clarified by the vertical dotted lines. After loading the Pt NPs on MSTB, the intensity of the characteristic MoS_2 peaks is significantly reduced, while that of TiO_2 is not affected much. This may be due to the screening effect of Pt NPs decorated over the edge-rich MoS_2 NFs.

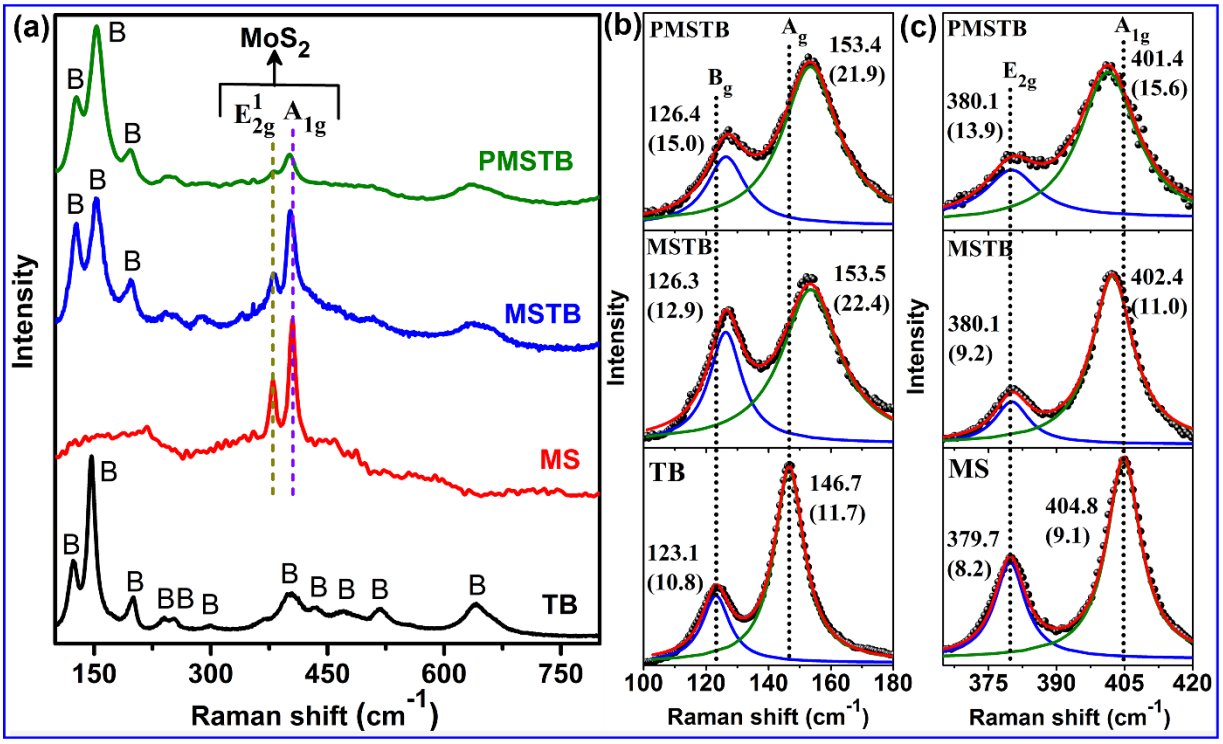

Fig. 5.6. (a) Raman spectra of pristine TiO_2(B) NBs, bare MoS_2 NFs, few-layer MoS_2 NFs decorated TiO_2(B) NBs and Pt loaded MoS_2/TiO_2 HSs. (b) Lorentzian fittings of Raman spectra for TB, MSTB and PMSTB in the range of 100-180 cm^{-1}. (c) Lorentzian fittings of active Raman modes of MoS_2 corresponding to the bare MoS_2, MSTB and PMSTB (360-420 cm^{-1}). The vertical dotted lines indicate the position of standard Raman mode of pristine MoS_2 and TiO_2(B).

Fig. 5.6(b) exhibits the B_g and A_g Raman modes for B-phase TiO_2 in the pristine TB, MSTB, and PMSTB, and their corresponding Lorentz fittings. It is evident that the intensity of TiO_2 Raman modes decreases after the decoration of MoS_2, which may be due to the bonding of MoS_2 at the porous site of TiO_2 NBs. The B_g and A_g Raman modes of TiO_2 NBs at 123.1 cm^{-1} and 146.7

cm^{-1}, respectively, are broadened, and blueshifted after the MoS_2 growth, as indicated by the vertical dotted lines in **Fig. 5.6(b)**. The MSTB shows a blue shift of 3.2 cm^{-1} in B_g mode with broadening in FWHM from 10.8 cm^{-1} to 12.9 cm^{-1}. Similarly, for A_g mode, the MSTB HS exhibits a huge blue shift of 6.8 cm^{-1} with an increment in the FWHM from 11.7 cm^{-1} to 22.4 cm^{-1}. Such a large blue shift and broadening are mostly due to a surface strain (compressive type) induced by the MoS_2 nanosheets covered on the TiO_2 surface originating from the non-stoichiometric oxygen vacancy (O_v) defects resulting possibly from the S-doping at the O-site in the TiO_2 lattice.[20] After the loading of Pt NPs over MSTB, no further increase of defect concentration in the TiO_2 lattice is observed. **Fig. 5.6(c)** exhibits the E_{2g} and A_{1g} Raman modes for MoS_2 in the pristine MS, MSTB, and PMSTB, and the corresponding Lorentz fittings are also shown as solid lines. The pristine MoS_2 exhibits two active Raman modes centered at 379.7 cm^{-1} and 404.8 cm^{-1}, which are attributed to $E_{2g}{}^1$ and A_{1g} modes, respectively, as shown in **Fig. 5.6(c)**. However, in MSTB, these Raman modes are observed at 380.1 cm^{-1} and 402.4 cm^{-1}, respectively.[4, 21] The former peak ($E_{2g}{}^1$) is attributed to the in-plane vibrations and the later one (A_{1g}) to the vertical-plane vibrations in the Mo-S bond of MoS_2 and the separation between these two peaks is mainly determined by the layer number in MoS_2 nanosheets.[22] The estimated frequency differences between these two modes are $\Delta\nu \approx 25.1$ cm^{-1} and 22.3 cm^{-1} for pristine MS and MSTB, respectively. Thus, the growth of few-layer pristine MoS_2 is confirmed and the reduction in $\Delta\nu$ for MSTB may be interpreted as follows: first, the overall growth of layered MoS_2 on the TiO_2 platform leads to a reduced number of layers (bilayer/few-layer): this is due to the presence of numerous porous nucleation sites in TiO_2 NBs, which not only act as the nucleation sites for the growth of layered MoS_2 but also constrain their aggregation to yield bilayer/few-layered structures. In contrast, the bare MoS_2 NFs aggregate during the hydrothermal growth due to the absence of any anchoring support, resulting in multilayered MoS_2. Second, in MSTB, the only A_{1g} peak is observed to be redshifted (by ~2.4 cm^{-1}), whereas the E_{2g} peak remained unchanged. This may be due to the softening of A_{1g} vibrations at high electron concentrations, which indicates the n-type doping of MoS_2 grown over the S-doped and O_V enriched TiO_2.[23, 24] In PMSTB, A_{1g} mode exhibits a further redshift of 1 cm^{-1} with a larger FWHM, indicating the n-doping effect in MoS_2 lattice. This can be understood from the band bending at the interfaces of MoS_2 and TiO_2, facilitating the electron transfer from the TiO_2 to MoS_2 side, which will be discussed later.

5.3.2.3. XPS Analysis

The chemical valence state, stoichiometric ratio of the systems and the surface defects present in pristine catalysts and their HS were investigated by the XPS analysis. The Ti 2p core level XPS spectra of pristine TB were deconvoluted by Gaussian fitting to determine the double peak features of Ti $2p_{3/2}$ and Ti $2p_{1/2}$, as shown in **Fig. 5.7(a)**. The fitted peaks corresponding to the binding energies of 458.8 and 464.5 eV can be attributed to the Ti^{4+} cation. Two additional Gaussian peaks centered at 456.7 eV and 461.0 eV related to Ti^{+3} valence states were detected with relative percentage of 4.9% for TB, which reveals the presence of nonstoichiometric O_v defects in the system.[19] **Fig. 5.7(b)** depicts the Mo 3d core-level XPS spectra of MSTB. The strongest Mo 3d doublet peaks for MSTB detected at 229.2 eV ($3d_{5/2}$), and 232.5 eV ($3d_{3/2}$) correspond to the 4+ oxidation state of Mo, confirming the formation of MoS_2. The shoulder peaks detected at 226.4 eV and 235.7 eV can be attributed to the S 2s state and Mo 6+ oxidation state, respectively, probably due to the formation of MoO_3 during the hydrothermal growth and post-synthesis exposure to air. After the Pt NP decoration on MSTB, the major Mo 3d doublet peaks corresponding to 4+ valence state are also detected at similar binding energy values. **Fig. 5.7(c)** shows the Pt 4f core level XPS spectrum for the PMSTB, which can be deconvoluted into four symmetric Gaussian peaks, corresponding to the two different valence states of Pt. The Pt $4f_{7/2}$ and Pt $4f_{5/2}$ peaks detected at 71.5 eV and 74.8 eV, respectively, originate from the metallic Pt^0, while the other pair at 72.7 and 76.4 eV correspond to Pt $4f_{7/2}$ and Pt $4f_{5/2}$ of Pt^{2+}, respectively.[25, 26] The area under each peak reveals the relative atomic percentage of Pt^0 and Pt^{2+} as 75.8% and 24.2%, respectively, in PMSTB, signifying that the Pt is mainly in the metallic state. The additional Pt^{2+} in the HS sample may form Pt–O bond due to the chemisorption of oxygen and hydroxyl group on the surface of the Pt NP and MoS_2 layer. Additionally, a marginal amount Pt NPs (~1.4 wt%) is observed to be present on each of the samples, as confirmed from the XPS analysis.

To characterize the nature of S atoms present in the catalysts, which are responsible for the HER activity, the core level XPS spectra of different samples were recorded, and results are shown in **Fig. 5.7(d-f)** and the corresponding area percentage is shown in **Table 5.1**. The pristine MoS_2 layers contain S atoms with electron binding energies at ~161.9/163.1 eV and ~163.4/164.6 eV, respectively (two sets of doublets), as shown in **Fig. 5.7(d)**.

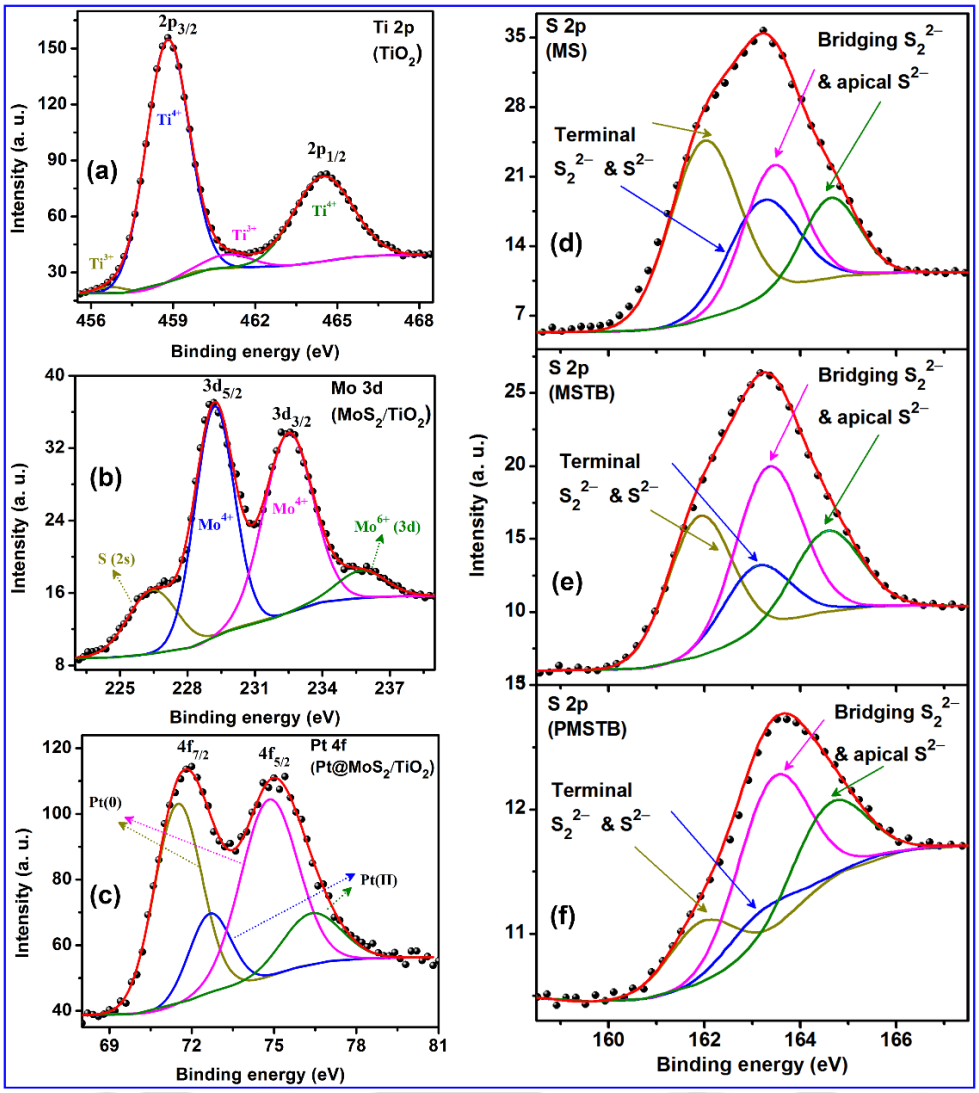

Fig. 5.7. XPS core level spectra for (a) Ti 2p in TB, (b) Mo 3d in MSTB, and (c) Pt 4f in PMSTB, fitted with the Shirley baseline. S 2p core level XPS spectra for (d) MS, (e) MSTB and (f) PMSTB, fitted with the Shirley baseline. The symbols represent the experimental data, and the solid lines correspond to the Gaussian fits. The identity of each fitted peak is denoted with corresponding charge states in the respective cases.

The lower binding energy doublets are assigned to unsaturated S^{2-} and terminal S_2^{2-}, while the higher binding energy doublets are assigned to bridging S_2^{2-} and apical S^{2-}.[27] In addition to the formation of MoS_2, presence of S^{2-} in the HS sample perhaps indicate the Ti–S bond formation during the substitution of O-atoms by S-atoms in the TiO_2 crystal lattice, resulting in S-doped TiO_2, which is consistent with the large blue shift in TiO_2 Raman spectra and enhancement of O_V concentration in TiO_2 lattice after the in-situ growth of MoS_2 over TiO_2 (discussed later).[28] Ting et al.[27] demonstrated that the catalytic reactivity, as well as the turnover frequency of hydrogen production, increases almost linearly with increasing the amount of bridging S_2^{2-}/apical S^{2-} in

the catalysts. In the present case, pristine MS exhibits S atoms with bridging S_2^{2-}/apical S^{2-} as 39.1%, which is found to be increased to 54.4%, after its growth on porous TB, as shown in **Fig. 5.7(d, e)**. Therefore, the TB NBs not only facilitate the few-layer growth of MoS_2 with edge-exposed sites but also serve as an effective platform for mediating the evolution of MoS_2 with more bridging S_2^{2-}/apical S^{2-} to promote the enhanced HER activity. It is noteworthy that after Pt NP decoration on MSTB, the bridging S_2^{2-}/apical S^{2-} increases dramatically to 72.2%, as shown in **Fig. 5.7(f)**. Thus, it is clear that the Pt NP plays a crucial role to increase the bridging S_2^{2-}/apical S^{2-} amount in the HS and eventually in the superior HER performance.[27]

Fig. 5.8(a-d) displays the O 1s XPS spectra of TB, MSTB, PTB and PMSTB, respectively. The spectra corresponding to pristine TB and PTB possess a long tail towards the higher-energy region making the spectra asymmetric in nature. In addition, MSTB and PMSTB exhibit exceptionally-broad O 1s spectra implying the presence of defects or impurity on its surface. Each O 1s spectra can be fitted with three symmetric Gaussian peaks, similar to that reported in the literature.[29]

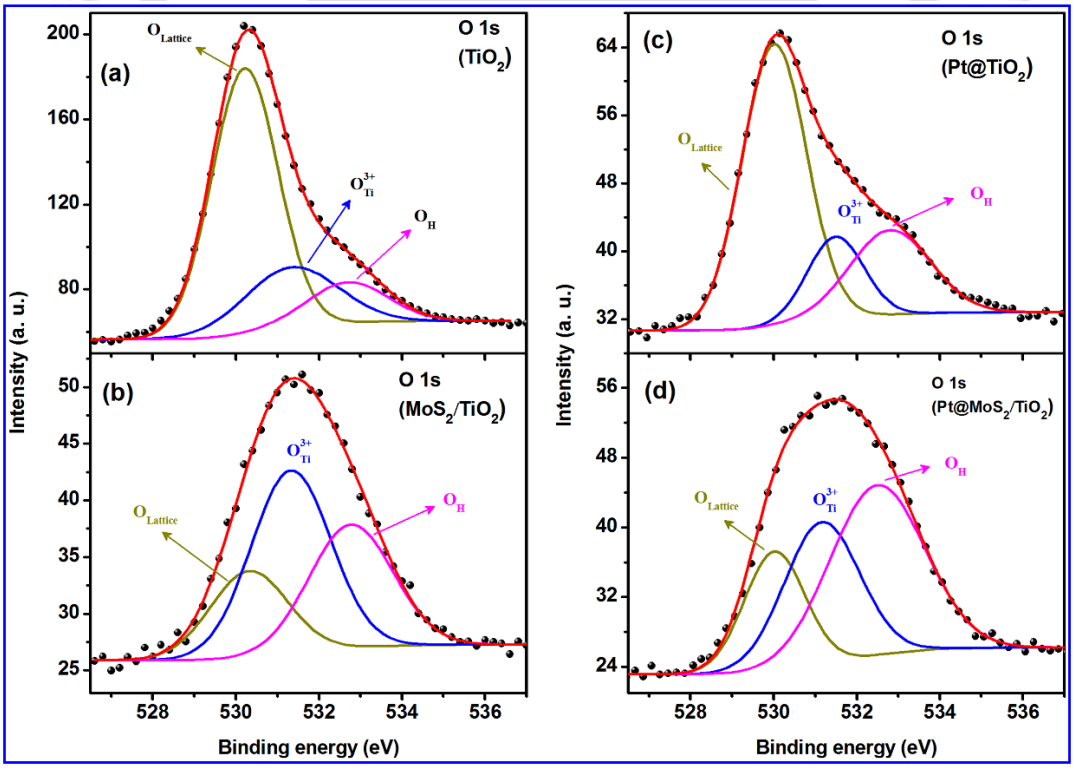

Fig. 5.8. O 1s core level XPS spectra of (a) TB, (b) MSTB, (c) PTB and (d) PMSTB with Gaussian fit of each spectrum with Shirley baseline. Symbols represent the experimental data and solid lines the Gaussian fits. Charge states associated with each peak is labeled in the spectrum.

The first peak at ~530.1 eV is attributed to the lattice O in the TiO_2 crystal lattice, and its relative percentages are calculated to be 66.6%, 61.4%, 21.2% and 21.3% for TB, PTB, MSTB, and PMSTB, respectively. Thus, it is clear that the relative percentage of lattice oxygen in TiO_2 decreases marginally after the Pt decoration (PTB), but it decreases dramatically after the decoration of MoS_2. The second peak at ~531.2 eV can be assigned to the Ti-O bond ($O_{Ti^{3+}}$) and the relative $O_{Ti^{3+}}$% calculated from the O 1s XPS spectra is tabulated in **Table 5.1**. After the decoration of MoS_2, the O_v concentration in the TiO_2 lattice is observed to be more than doubled from 21.1% to 46.1%, which may be due to the substitution of O-atoms in TiO_2 with the S-atoms during the in-situ growth of MoS_2 over TiO_2 platform. This is consistent with the large blue shift in the Raman spectrum, discussed in **Section 5.3.2.2**. Loading of Pt NPs on TB or MSTB results in the decrease in O_v concentration from its initial value, perhaps due to the presence of Pt^{2+} species, which reduce the vacancy concentration. The third peak at ~532.7 eV is attributed to the hydroxyl group adsorbed on the HS surfaces, and its relative percentages are shown in **Table 5.1**. Thus, it is observed that introduction of Pt NP in the nanostructures enhances the relative percentage of the adsorbed hydroxyl group from 12.3% to 23.1% for pristine TB and from 32.7% to 47.3% for MSTB. Thus, it can be concluded that the Pt NP introduces the hygroscopic nature in the nanostructure and also increases the adsorption capability in the system. These exceptionally high defect states may serve as shallow donors and enhance the charge transfer at the multiple interfaces, which in turn improves the overall photoelectrocatalytic water splitting under solar light, as discussed later.

5.3.3. UV-Vis Absorption and Photoluminescence Study

To investigate the solar energy harvesting efficiency, the pristine TiO_2 and the HS catalysts were analyzed by UV-visible diffuse reflectance spectroscopy (DRS). **Fig. 5.9(a)** shows the Kubelka-Munk (K-M) function, F(R), for each of the samples corresponding to their DRS spectra. The pure TiO_2(B) NBs exhibit a sharp rise in absorption edge at ~360 nm (indirect bandgap estimated from Tauc plot is ~3.25 eV), which is attributed to its intrinsic band gap absorption. Pristine few-layer MoS_2 NFs exhibit a broad absorption band having a peak at ~670 nm (direct bandgap estimated from Tauc plot ~1.63 eV) showing a large blue shift compared to its bulk counterpart. This may be attributed to the strong quantum confinement effect of the thin and layered MoS_2 nanosheets, which makes the MoS_2 a promising candidate for the visible light photocatalysis.[30] Incorporation of few-layer MoS_2 on TiO_2 NBs enhances the absorption intensity significantly

over the wide range of UV-visible-NIR spectrum, as shown in **Fig. 5.9(a)**. Introduction of Pt NPs on the TiO_2 NBs further enhances the visible light absorption efficiency, with a new absorption band centered at ~415 nm, besides its enhanced UV and visible-NIR absorption. Cueto et al.[31] have shown that the Pt NPs with size 5-35 nm exhibit a plasmonic absorption covering a narrow band in the range 200−320 nm, and a broader band with a tail extending up to the NIR region. However, in the case of large Pt NPs, the absorption band becomes intense and broad enough as a consequence of stronger plasmonic excitation due to the formation of numerous hotspots between two or more Pt NPs close to each other. In the present work, the Pt NPs decorated over the MoS_2 NFs are closely spaced, which enables high plasmonic excitation generated in the numerous hotspots, and results in high absorption. Interestingly, the absorption edge of the TiO_2 NBs is observed to be red-shifted after the decoration of MoS_2 NFs as well as Pt NPs. With Pt NPs, the absorption edge of the TiO_2 is red-shifted from ~360 nm to ~380 nm. In the case of MSTB, it is further red-shifted to ~402 nm, which implies an efficient band bending at the interface arising from the strong coupling between the porous TiO_2 and wrapped MoS_2 layers. S-doping in TiO_2 lattice may also be attributed to this red shift.[32] However, maximum redshift is observed in PMSTB (~471 nm), which may be attributed to the strong coupling between each pair of the components MoS_2-Pt, MoS_2-TiO_2, and Pt-TiO_2. Thus, the HSs are expected to be extremely sensitive to the visible-NIR light and would be beneficial for the efficient visible light photoelectrocatalytic hydrogen evolution.

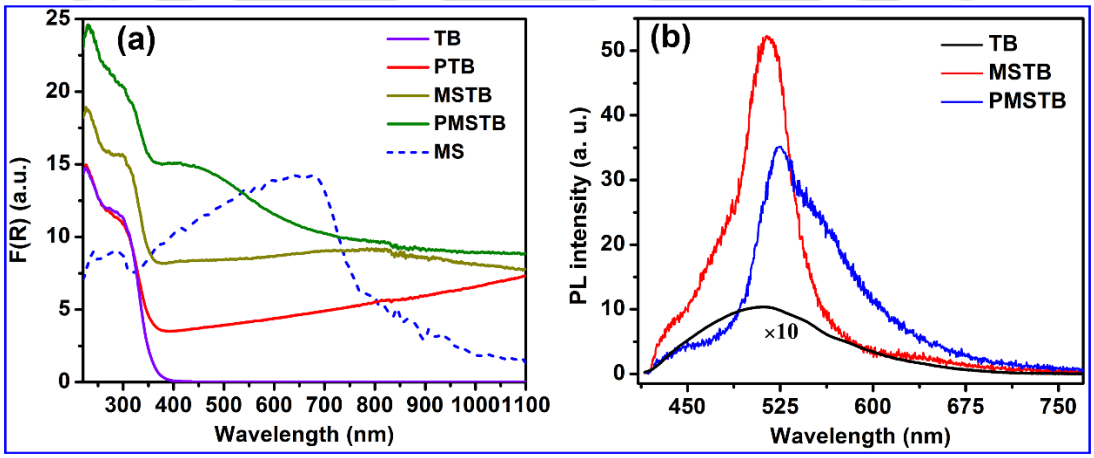

Fig. 5.9. (a) Kubelka–Munk plot, F(R), for different samples derived from the diffuse reflectance spectra. (b) PL spectra of TiO_2 and its HSs measured with 405 nm laser excitation. The PL spectrum of TB is shown in magnified scale to enable comparison.

Fig. 5.9(b) shows a comparison of room temperature PL spectra of TB, MSTB, and PMSTB. Pristine TiO_2 NBs exhibit very weak and broad PL emission having an emission peak at ~515 nm, which is attributed to the single electron trapped oxygen vacancy (O_V) defects (F^+ center), mentioned in **Chapter 3, Section 3.3.3.2**. After the growth of the MoS_2 layer on TiO_2 NB, the PL intensity corresponding to the F^+ center increases strongly, indicating an increase in the concentration of O_V defects. During the in-situ hydrothermal growth of MoS_2 on TiO_2, S-atoms may diffuse and substitute the O-atoms in TiO_2 lattice, causing S-doping in TiO_2. This causes an increase in the O_V concentration and an eventual increase in electron density in TiO_2. Due to the high optical absorption and O_V defects in MSTB HS, the PL intensity corresponding to the F^+ center increases substantially. After loading of Pt NPs over MSTB, the PL intensity reduces, which is due to the fast interfacial electron transfer from TiO_2 to Pt NPs via MoS_2. Additionally, PMSTB shows a relatively broader PL spectrum indicating the contribution from the hydroxyl group attached to the TiO_2 surface, which is consistent with the XPS analysis, discussed in **Section 5.3.2.3**.

5.3.4. Hydrogen Evolution Reaction (HER) Study

The visible light HER performance of various catalysts, such as TB, MS, MSTB, PMS, PTB and PMSTB as working electrodes made on glassy carbon disk was investigated in an N_2-saturated 0.5M H_2SO_4 solution at a scan rate of 5 mV/s using a typical three-electrode linear sweep voltammetry (LSV) method. For a better comparison, each measurement has been repeated under dark conditions as well. The electrochemical HER activities (LSVs) of various catalysts under dark and light (wavelength range 370-730 nm) are shown in **Fig. 5.10(a, b)** and the corresponding Tafel slopes are shown in **Fig. 5.10(c, d)**, respectively. As shown in **Fig. 5.10(a)**, the HER for pristine TiO_2 NBs starts at a potential of –623 mV and –616 mV (versus RHE) under dark and light, respectively, above which the current increases dramatically. In spite of very low overall current density, TB exhibits HER overpotential (to attain –10 mA/cm^2 current density) of –796 mV under the light, which is positively shifted by 87 mV as compared to that under dark. The pristine few-layer MoS_2 exhibits much higher current density with low onset potential of –246 mV, which reduces to –193 mV after light illumination. The overpotential is observed to be –425 mV and –395 mV under dark and light, respectively (see **Table 5.2**). Interestingly, in MSTB the uniform decoration of edge-exposed few-layer MoS_2 on the porous sites of TiO_2 NBs decreases the onset potential to –215 mV in the dark, which further reduces to

–178 mV after irradiation with visible light. In MSTB, the overpotentials are calculated to be –336 mV and –305 mV under dark and light conditions, respectively. Thus, it can be concluded that more carriers are being generated in MSTB with light irradiation, which augments the reduction process of electroadsorbed protons. The introduction of merely ~1.4 wt% Pt NP on the TB, MS, and MSTB results in a dramatic reduction in the onset potential towards HER reaction.

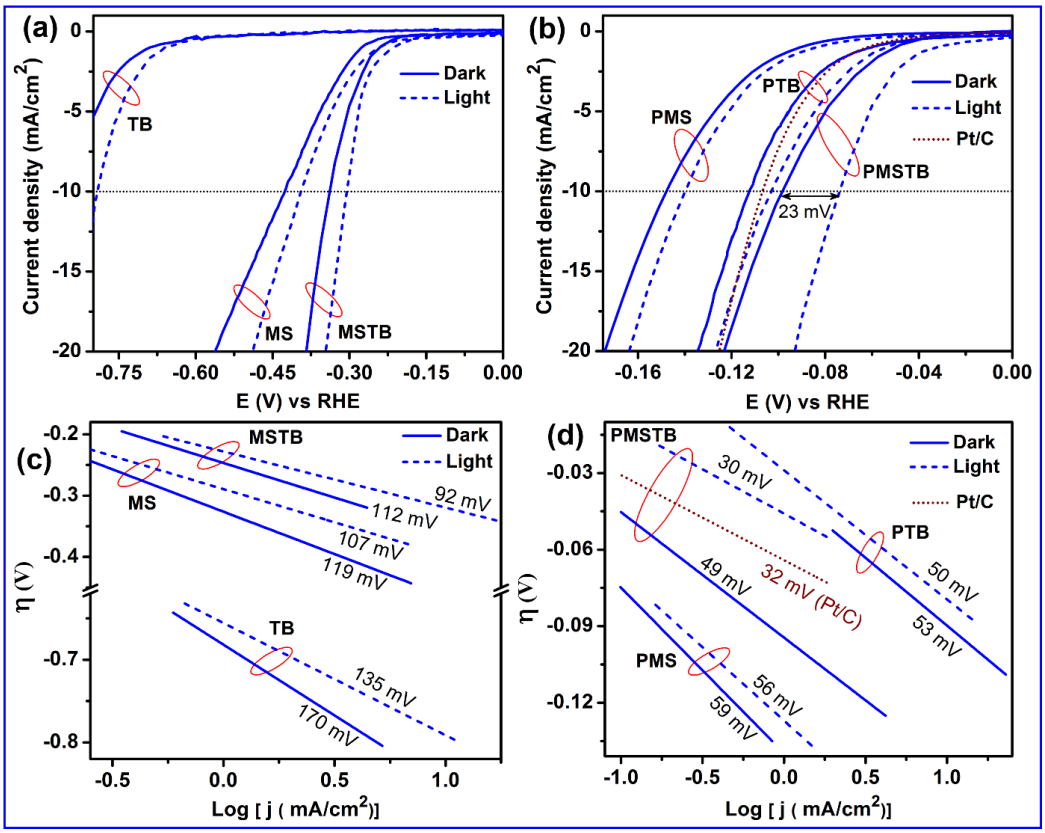

Fig. 5.10. Polarization curves of the hydrogen evolution reaction (HER) in dark and light conditions in (a) pristine TiO_2(B), MoS_2 and MoS_2/TiO_2(B) HS, (b) Pt@MoS_2, Pt@TiO_2 and Pt@MoS_2/TiO_2 HSs. (c, d) Tafel plots of different working electrodes derived from their LSV curves shown in (a, b), respectively. Polarization curve and the corresponding Tafel plot for Pt/C electrode are also shown in (b, d), respectively.

For PMS, it is measured to be –76 mV and –66 mV, while for PTB it is observed at –45 mV and –41 mV, under dark and light, respectively. In case of PMSTB, onset potential under dark is measured to be –40 mV, which is dramatically reduced to –9 mV after light irradiation, which essentially outperforms the commercial Pt/C electrode (–48 mV) that contains much higher amount of Pt (~20 wt%). The summary of the performance of various catalysts is presented in **Table 5.2**. As evident from the table, the PMSTB exhibits exceptionally low overpotential under the light, –74 mV, which is much lower (by 23 mV) than the value measured in the dark (–97 mV) and this is further lower than the commercial Pt/C electrode (–106 mV). Thus, a dramatic

enhancement in the photogenerated charge carriers, as well as reduced charge transfer resistance, is expected in the systems after the Pt NP decoration, which serves as favorable nodes with large electron-accepting and buffering properties to facilitate electron transport, which in turn improve the overall conductivity.[14]

Tafel slopes of all the samples in both dark and light (in mV $decade^{-1}$), estimated from the linear fit of overpotential and logarithmic function of current density (log|j|), are shown in **Fig. 5.10(c, d)** and tabulated in **Table 5.2**. Lower Tafel slopes not only reveal about the rate-determining step of the hydrogen evolution electrocatalysis mechanism but are also desirable to minimize the energy input required to achieve a targeted HER current density. From **Fig. 5.10(c, d)**, it is evident that in each catalyst the Tafel slope decreases after the illumination of light compared to their respective dark values, which eventually confirms the acceleration of the electron transfer kinetics upon irradiation. In the dark, a much lower Tafel slope is estimated for pristine MS (119 mV dec^{-1}) than for pristine TB (170 mV dec^{-1}), which further decreases in their composite system (MSTB) to 112 mV dec^{-1}. Under visible light illumination, their corresponding values are calculated to be 135 mV dec^{-1} (TB), 107 mV dec^{-1} (MS) and 92 mV dec^{-1} (MSTB), as shown in **Table 5.2**. After Pt NP loading on MS, TB, and MSTB, the Tafel slope is observed to be decreased drastically, as demonstrated in **Fig. 5.10(d)**. Tafel slopes for PMS and PTB are 59 and 53 mV dec^{-1} under dark, and 56 and 50 mV dec^{-1} under the light, respectively. PMSTB exhibits exceptionally low Tafel slope (30 mV dec^{-1}) under the light, which is much lower (19 mV dec^{-1}) than the value measured under dark (49 mV dec^{-1}) and our values are comparable/ better than that of a commercial Pt/C electrode (32 mV dec^{-1}).

Two main reaction pathways are widely accepted in HER electrocatalysis, commencing with a primary discharge step (i.e., Volmer reaction: $H_3O^+ + e^- \rightarrow H_{adsorbed}$), followed by either the electrochemical desorption step (i.e., Heyrovsky reaction: $H_3O^+ + e^- + H_{adsorbed} \rightarrow H_2$) or the monoatomic hydrogen recombination step (i.e., Tafel reaction: $H_{adsorbed} + H_{adsorbed} \rightarrow H_2$). As broadly reported in the literature, Tafel slopes of ~120 mV dec^{-1}, ~40 mV dec^{-1}, and ~30 mV dec^{-1} are allocated to Volmer, Heyrovsky and Tafel reactions being the HER rate-determining step, respectively.[33] In our case, the Tafel slopes of all the HSs photoelectrocatalysts (MSTB, PMS, PTB, and PMSTB) fall between the Volmer mechanism and the Tafel mechanism indicating that the Volmer−Tafel mechanism plays the predominant role in

the catalysts' HER kinetics.[34] The lowest Tafel slope (i.e. best HER kinetics) found for PMSTB under visible light illumination consequently supports its high HER performance.

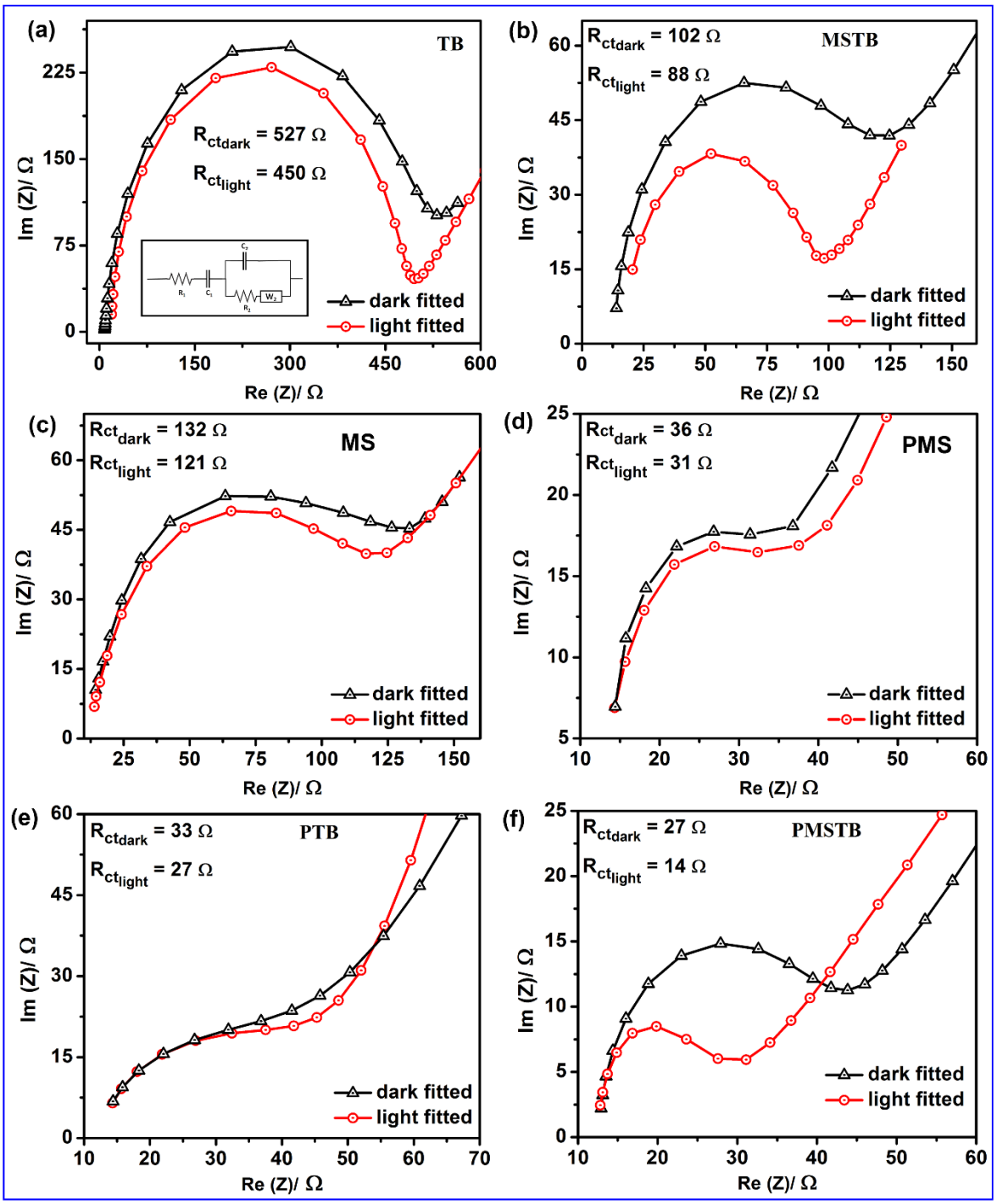

Fig. 5.11. Nyquist plots of (a) pristine TiO_2(B), (b) MoS_2/TiO_2, (c) pristine MoS_2, (d) Pt@MoS_2, (e) Pt@TiO_2 and (f) Pt@MoS_2/TiO_2 HSs, under dark and light conditions. Note that the points represent experimental data, while the solid lines are simulation using the Randle's circuit to estimate the characteristic charge-transfer resistance (R_{ct}).

Electrochemical impedance spectroscopy is a powerful tool to characterize interface reactions and heterogeneous electron transfer process in HER.[35] **Fig. 5.11(a-f)** show the Nyquist plots of all the samples corresponding to their EIS response. The charge transfer resistance (R_{ct}) values have been calculated for all the samples estimated from the Randles circuit (see inset of **Fig. 5.11(a)**) under dark and light condition. In dark, the R_{ct} is calculated to be lower for MSTB (102 Ω) as compared to the pristine TB (527 Ω) as well as MS (132 Ω). Interestingly, after the Pt NP decoration, the R_{ct} dramatically reduces to 36 Ω, 33 Ω and 27 Ω for PMS, PTB, and PMSTB, respectively, under dark. The R_{ct} values of all catalysts are decreased even further upon illumination, indicating the presence of photogenerated carriers in these electrodes, as shown in **Table 5.2** and **Fig. 5.12(a)**. Under illumination, R_{ct} for PMSTB decreases to the minimum value of 14 Ω indicating the augmented charge transfer process in the presence of light. The n-type doping in the catalytically-active edge-exposed MoS_2 NFs (as demonstrated from Raman analysis, see **Fig. 5.6(c)**) provides a fast electron transfer from TiO_2 side to the MoS_2 side and results in a superior HER kinetics, which is dramatically enhanced after the introduction of metallic and highly-active catalyst Pt NP into the MSTB system.

Table 5.2: *Comparison of various catalytic parameters of different photoelectrocatalysts under dark and light.*

Catalyst code	***Onset potential (at -0.5 mA/cm^2) [(mV) V RHE]***		***Overpotential at -10 mA/cm^2 [(mV) V RHE]***		***Tafel slope (mV dec^{-1})***		***Charge transfer resistance, R_{ct} (Ω)***		***Exchange current density, j_0 (mA/cm^2)***	
	dark	light	dark	light	dark	light	dark	light	dark	light
TB	-623	-616	-883	-796	170	135	527	450	0.001	0.002
MS	-246	-193	-425	-395	119	107	132	121	0.008	0.013
MSTB	-215	-178	-336	-305	112	92	102	88	0.012	0.019
PMS	-76	-66	-147	-140	59	56	36	31	0.164	0.193
PTB	-45	-41	-113	-105	53	50	33	27	0.175	0.209
PMSTB	-40	-9	-97	-74	49	30	27	14	0.182	0.296
Pt/C	-48	-	-106	-	32	-	6	-	0.305	-

Further insight into the HER electrocatalysts intrinsic activity can be obtained by comparison of exchange current density (j_0) values, which is determined by the ability to exchange electrons from the working electrode to the counter electrode through the electrolyte

solution at null potential. **Fig. 5.12(b)** shows a comparison of the exchange current density, j_0, values obtained under dark and light conditions for all studied samples. It is noteworthy that a dramatic enhancement (~10-fold) in j_0 value is observed in TB after the decoration with MoS_2 layers. Furthermore, for all samples tested, there is a significant increase in j_0 values after visible light illumination, consistent with the lower R_{ct} and Tafel slope values found after light irradiation.

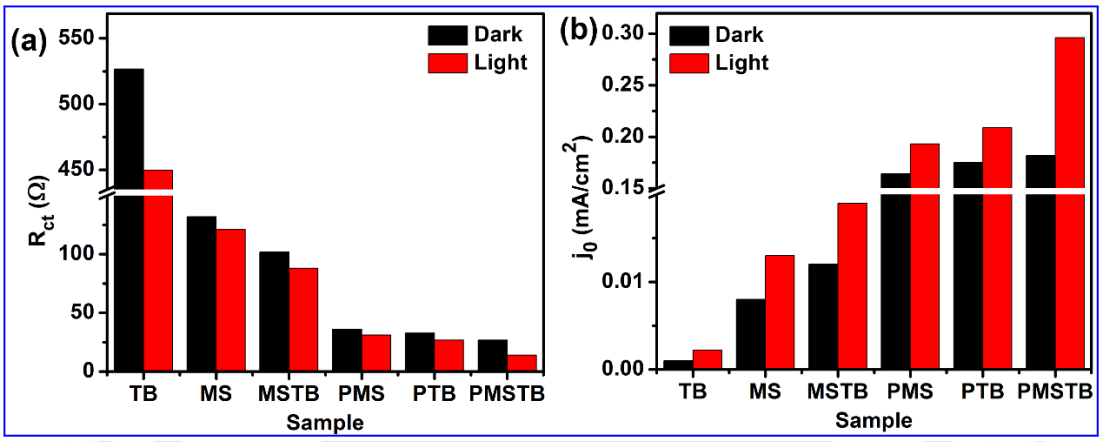

Fig. 5.12. (a) The characteristic charge-transfer resistance (R_{ct}) and (b) exchange current density (j_0) values of various electrodes in dark and light conditions.

Among the various electrodes studied here, PMSTB showed the highest j_0 (~0.182 mA/cm^2 under dark and 0.296 mA/cm^2 under visible light), which are more than two orders of magnitude higher than the pristine TiO_2 NBs. Thus, the aforementioned enhanced HER performance of MSTB is a result of the efficient charge transport and favorable HER kinetics at the interface of the HS components, which is further enhanced after the decoration with Pt NPs, widely regarded as the best performing noble metal catalyst for the HER.

To evaluate the durability of as-prepared catalyst, the cyclic durability, as well as long-term stability, was investigated, and the results are presented in **Fig. 5.13**. Long-term cycling experiment (up to 22 hours) was performed for PMSTB by recording 10,000 cycles from 0 V to -0.2 V vs RHE. As shown in **Fig. 5.13(a)**, the polarization curve shows no loss in current density after 10,000 CV cycles, though the performance marginally improves with time, which may be due to the improved interfacial contact and possible Pt dissolution/ redeposition at the PMSTB surface, which may yield an increase in the HER active sites. The long-term stability test was performed by chronopotentiometry measurements to evaluate the catalyst capability of sustaining a 10 mA/cm^2 cathodic current over a 12 h period (see inset of **Fig. 5.13(a)**).

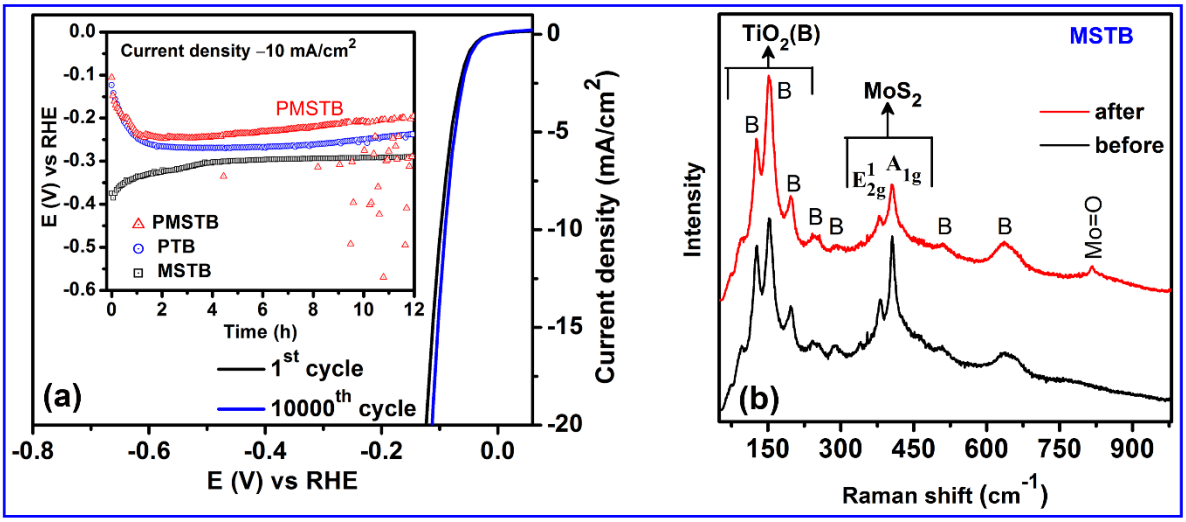

Fig. 5.13. (a) Polarization curves recorded for PMSTB before and after 10,000 CV cycles. Inset shows the chronopotentiometry showing the stability of the catalysts for 12 h at a sustained current density of -10 mA/cm^2. (b) Raman spectra of MSTB before and after the PEC reaction, showing the high structural stability of the catalyst.

The catalyst PTB shows the initial decay of HER performance up to 3 h of operation (-0.270 V @ 3 h vs -0.123 V @ 0 h), indicating the stabilization of the anchoring effect of MoS_2 with respect to the decorated Pt NPs. Beyond 3 h, PTB performance marginally improves up with time up to 12 h (-0.238 V @ 3 h). PMSTB shows a similar trend with an initial decay of HER performance with time up to 3 h, as shown in the inset of **Fig. 5.13(a)**. Eventually, it reaches HER performance of -0.195 V @ 12 h, which is better than PTB. Note that after 12 h of continuous galvanostatic operation at 10 mA/cm^2, the HER performance of PMSTB decays by ~90 mV. Additionally, some intermittent fluctuation in the potential values is observed for PMSTB beyond ~4 h of continuous operation, which may be due to the mild oxidation of the MoS_2 sites accelerated by the anchored Pt NPs and the H_2 bubble movement. Interestingly, the performance of MSTB initially improves with time and then reaches a saturation value. Possible coarsening of the MoS_2 layer along with electrochemical activation of the high binding energy S_2^{2-} sites upon irreversible HER cathodic cleaving may explain the observed enhancement.[27] To evaluate the structural stability of the catalyst, the Raman spectra of MSTB were recorded before and after the PEC reaction. The crystallinity and stability of both TiO_2(B) and MoS_2 components are observed to be retained under the PEC reaction, as evident from **Fig. 5.13(b)**. However, the relative intensity of MoS_2 characteristic peaks slightly decreases after the reaction, which may be due to oxidation and associated introduction of defects in the MoS_2 layers. One additional Raman peak is detected at ~820 cm^{-1} after the PEC reaction, which may be assigned to the M=O bond[36]

resulting from the marginal oxidation of MoS_2 in the acidic media. However, chronopotentiometric measurement shows that the MSTB catalyst exhibits excellent stability towards HER activity up to 12 h, confirming the non-photocorrosive nature of our catalyst.

5.3.5. Mechanism of enhanced HER activity

Though MoS_2 is known as a catalytically active material, poor charge transport in the basal plane is often responsible for it inferior HER performance. Fabrication of edge-exposed MoS_2 and activation of the inert basal plane through Pt doping or extrinsic S vacancy generation have proven to be successful strategies to trigger superior HER electrocatalytic activities.[37, 38] In this study, few-layer MoS_2 with a high density of catalytically-active edge-exposed sites are tightly coupled with the porous surface of S-doped TiO_2 NBs. Structural analysis by HRTEM and STEM imaging of the as-grown MoS_2 layers on the TiO_2 NBs confirms their edge-rich nature and presence of surface defects. This defect-rich structure leads to a higher exposure of unsaturated sulfur edge sites, which are widely regarded as the active sites responsible for the overall HER activity.[27] Additionally, the MoS_2 layers grown onto the TiO_2 NBs surface present an n-type doping of MoS_2, contributing to maximize its HER activities after MoS_2 basal plane activation.

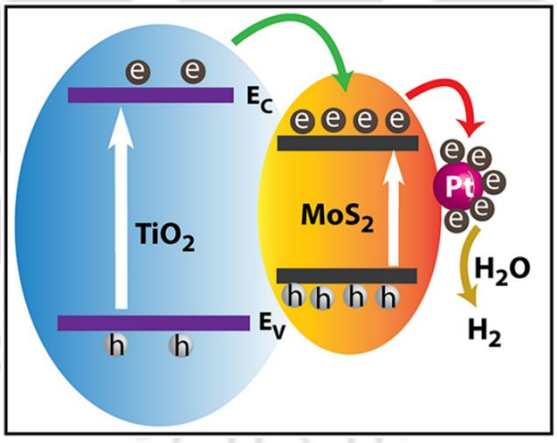

Fig. 5.14. Schematic illustration of charge transfer at the multiple interfaces of PMSTB and the mechanism of enhanced visible light PEC activity of Pt NP decorated on MoS_2/TiO_2.

Upon illumination with visible light, electrons in TiO_2, as well as MoS_2 in the HSs, may be excited, as confirmed by the UV-visible absorption analysis and photoconductivity measurement (data not shown). Due to the appropriate band alignment at the interface, the photogenerated electrons at the TiO_2 NBs can easily be transferred to the MoS_2 layer, avoiding possible

recombination loss of carriers and it induces n-doping of the MoS_2 layer, as depicted in **Fig. 5.14**. Consequently, this efficient charge transfer occurring at the heterojunction (MSTB) greatly reduces the charge transfer resistance under visible light (88 Ω) and accounts for the enhanced exchange current density (j_0) under illumination, which is measured to be 0.019 mA/cm^2. A marginal amount of Pt NP (1.4 wt.%) loading on the MSTB is found to decorate the catalytically-active edge sites of MoS_2 as well as porous sites of TiO_2 with Pt NPs. The enhanced HER activities obtained after Pt decoration onto porous MoS_2 NFs/TiO_2 NBs indicate an even higher density of proton-accepting sites compared to MoS_2 NFs/TiO_2 NBs, which presumably arises from further activation of initially electrocatalytically-inert MoS_2 basal planes and S-edge sites. In addition, the presence of Pt NPs can also serve as advantageous metallic current collector nodes to facilitate lower resistance transport pathways of photo-excited electrons from TiO_2 domains to Pt NPs through MoS_2 (see **Fig. 5.14**), improving the overall conductivity.[14] Hence, significantly enhanced HER activity was observed by PMSTB with a minimum charge transfer resistance of 14 Ω and a maximum exchange current density of 0.296 mA/cm^2. Additionally, the work function of TiO_2 decreases by the modification with H_2SO_4, which changes its conduction band offset.[39] A schematic illustration of the excitation of electrons and their separation through two interfaces under the light irradiation is shown in **Fig. 5.14** and this results in the superior HER performance of the composite system. The structural defects and porous S-doped TiO_2 surface also promotes a closer interaction between MoS_2 and TiO_2 during hydrothermal synthesis (i.e. higher availability of nucleation sites), which may be responsible for the catalytically active n-type doped structure of MoS_2 NFs.

On a separate note, the adsorbed hydroxyl group in TiO_2 lattice increases greatly after the decoration of MoS_2 layers (32.7%), which further enhances to 47.3% after the loading of Pt NPs on MSTB, as confirmed from XPS analysis. As the Volmer-Tafel HER mechanism is governing the HER performance in our HS catalysts, the higher presence of hydroxyl groups at the PMSTB electrode, known to facilitate electroadsorbed hydrogen desorption, may promote the rate-limiting electrochemical desorption step involving hydrogen gas formation.

5.4. Summary and Conclusions

In this chapter, we have demonstrated two-step hydrothermal growth of few-layer MoS_2 decorated porous TiO_2(B) NBs, followed by an in-situ decoration of Pt NPs onto it. We

extensively investigated the structural, optical and electronic properties of the as-synthesized heterostructured samples systematically to achieve strongly enhanced visible light photoelectrocatalytic activity. Important findings of this chapter are summarized below.

1. Edge-site exposed few-layer MoS_2 NFs are successfully grown on porous TiO_2(B) NBs. Marginal Pt NPs (1.4 wt.%) are selectively decorated on the edge-sites/defect-sites of MoS_2 and porous sites of TiO_2 NBs.
2. In addition to the formation of well-coupled heterojunction, S-doping in TiO_2 and n-type doping in MoS_2 enable the HS samples to be highly active in UV-Vis-NIR region with accelerated charge transfer rate from TiO_2 to MoS_2 side.
3. Catalytically active bridging S_2^{2-}/apical S^{2-} increases in HS samples and reaches to ~72% in PMSTB, primarily responsible for high HER activity.
4. PMSTB (with 1.4 wt.% Pt) outperforms the as-grown binary HSs as well as the commercial Pt/C electrode (with 20 wt.% Pt) both under dark and irradiation condition and shows high stability up to 10,000 CV cycles.
5. PMSTB shows the lowest charge transfer resistance (14Ω), the lowest onset potential (–9 mV) and the lowest Tafel slope (30 mV dec^{-1}) with exceptionally high exchange current density (0.296 mA/cm^2) under light irradiation. Appropriate band alignment at different interfaces enables easy transfer of charge carriers.
6. The Pt NPs activate the inert basal plane, edge sites of MoS_2 and porous sites of TiO_2 and thus offer an integrated network facilitating an easy injection of photogenerated electrons from the TiO_2 to Pt NPs via MoS_2 layer, which presents a feasible approach to boost the HER activity of multicomponent catalyst under visible light.

References

1. C. G. Morales-Guio, L.-A. Stern and X. Hu, *Chem. Soc. Rev.*, 2014, **43**, 6555-6569.
2. H. Li, Y. Zhou, W. Tu, J. Ye and Z. Zou, *Adv. Funct. Mater.*, 2015, **25**, 998-1013.
3. J. Greeley, T. F. Jaramillo, J. Bonde, I. Chorkendorff and J. K. Nørskov, *Nat. Mater.*, 2006, **5**, 909.
4. H. Li, Y. Wang, G. Chen, Y. Sang, H. Jiang, J. He, X. Li and H. Liu, *Nanoscale*, 2016, **8**, 6101-6109.
5. Y. Li, Y.-L. Li, C. M. Araujo, W. Luo and R. Ahuja, *Catal. Sci. Technol.*, 2013, **3**, 2214-2220.
6. D. Wang, Z. Wang, C. Wang, P. Zhou, Z. Wu and Z. Liu, *Electrochem commun.*, 2013, **34**, 219-222.
7. H. Li, K. Yu, C. Li, Z. Tang, B. Guo, X. Lei, H. Fu and Z. Zhu, *Sci. Rep.*, 2015, **5**, 18730.
8. D. Voiry, M. Salehi, R. Silva, T. Fujita, M. Chen, T. Asefa, V. B. Shenoy, G. Eda and M. Chhowalla, *Nano Lett.*, 2013, **13**, 6222-6227.

9. M. A. Lukowski, A. S. Daniel, F. Meng, A. Forticaux, L. Li and S. Jin, *J. Am. Chem. Soc.*, 2013, **135**, 10274-10277.
10. J. Xie, H. Zhang, S. Li, R. Wang, X. Sun, M. Zhou, J. Zhou, X. W. Lou and Y. Xie, *Adv. Mater.*, 2013, **25**, 5807-5813.
11. D. Escalera-López, Y. Niu, J. Yin, K. Cooke, N. V. Rees and R. E. Palmer, *ACS Catal.*, 2016, **6**, 6008-6017.
12. H. Li, C. Tsai, A. L. Koh, L. Cai, A. W. Contryman, A. H. Fragapane, J. Zhao, H. S. Han, H. C. Manoharan, F. Abild-Pedersen, J. K. Nørskov and X. Zheng, *Nat. Mater.*, 2015, **15**, 48.
13. J. Xie, H. Zhang, S. Li, R. Wang, X. Sun, M. Zhou, J. Zhou, X. W. Lou and Y. Xie, *Adv. Mater.*, 2013, **25**, 5807-5813.
14. X. Y. Xu, X. F. Dong, Z. J. Bao, R. Wang, J. G. Hu and H. B. Zeng, *J. Mater. Chem. A*, 2017, **5**, 22654-22661.
15. X. Chia, N. A. A. Sutrisnoh and M. Pumera, *ACS Appl. Mater. Interfaces*, 2018, **10**, 8702-8711.
16. C. E. Blackmore, N. V. Rees and R. E. Palmer, *Phys. Chem. Chem. Phys.*, 2015, **17**, 28005-28009.
17. E. Kemppainen, A. Bodin, B. Sebok, T. Pedersen, B. Seger, B. Mei, D. Bae, P. C. K. Vesborg, J. Halme, O. Hansen, P. D. Lund and I. Chorkendorff, *Energy Environ. Sci.*, 2015, **8**, 2991-2999.
18. S. Li, T. Pu, J. Wang, X. Fang, Y. Liu, S. Kang and L. Cui, *Int. J. Hydrog. Energy*, 2018, **43**, 16534-16542.
19. K. K. Paul, R. Ghosh and P. K. Giri, *Nanotechnology*, 2016, **27**, 315703.
20. S.-H. Nam, T. K. Kim and J.-H. Boo, *Catalysis Today*, 2012, **185**, 259-262.
21. Z. Yin, Z. Zeng, J. Liu, Q. He, P. Chen and H. Zhang, *Small*, 2013, **9**, 727-731.
22. K. C. J. Lee, Y.-H. Chen, H.-Y. Lin, C.-C. Cheng, P.-Y. Chen, T.-Y. Wu, M.-H. Shih, K.-H. Wei, L.-J. Li and C.-W. Chang, *Sci. Rep.*, 2015, **5**, 16374.
23. D. Kiriya, M. Tosun, P. Zhao, J. S. Kang and A. Javey, *J. Am. Chem. Soc.*, 2014, **136**, 7853-7856.
24. A. Shaista, S. Arun Kumar and E. Jonghwa, *Sci. Technol. Adv. Mater*, 2015, **16**, 035009.
25. B. Yue, Y. Ma, H. Tao, L. Yu, G. Jian, X. Wang, X. Wang, Y. Lu and Z. Hu, *J. Mater. Chem.*, 2008, **18**, 1747-1750.
26. K. Yang, J. Li, Y. Peng and J. Lin, *Phys. Chem. Chem. Phys.*, 2017, **19**, 251-257.
27. L. R. L. Ting, Y. Deng, L. Ma, Y.-J. Zhang, A. A. Peterson and B. S. Yeo, *ACS Catal.*, 2016, **6**, 861-867.
28. N. Li, X. Zhang, W. Zhou, Z. Liu, G. Xie, Y. Wang and Y. Du, *Inorg. Chem. front.*, 2014, **1**, 521-525.
29. B. Santara, P. K. Giri, K. Imakita and M. Fujii, *Nanoscale*, 2013, **5**, 5476.
30. W. Ho, J. C. Yu, J. Lin, J. Yu and P. Li, *Langmuir*, 2004, **20**, 5865-5869.
31. M. Cueto, M. Piedrahita, C. Caro, B. Martínez-Haya, M. Sanz, M. Oujja and M. Castillejo, *J. Phys. Chem. C*, 2014, **118**, 11432-11439.
32. N. Li, X. Zhang, W. Zhou, Z. Liu, G. Xie, Y. Wang and Y. Du, *Inorganic Chemistry Frontiers*, 2014, **1**, 521-525.
33. D. Hou, W. Zhou, X. Liu, K. Zhou, J. Xie, G. Li and S. Chen, *Electrochim. Acta*, 2015, **166**, 26-31.
34. B. Ma, P.-Y. Guan, Q.-Y. Li, M. Zhang and S.-Q. Zang, *ACS Appl. Mater. Interfaces*, 2016, **8**, 26794-26800.
35. L. Liao, J. Zhu, X. Bian, L. Zhu, M. D. Scanlon, H. H. Girault and B. Liu, *Adv. Funct. Mater.*, 2013, **23**, 5326-5333.
36. H. Nan, Z. Wang, W. Wang, Z. Liang, Y. Lu, Q. Chen, D. He, P. Tan, F. Miao, X. Wang, J. Wang and Z. Ni, *ACS Nano*, 2014, **8**, 5738-5745.
37. J. Deng, H. Li, J. Xiao, Y. Tu, D. Deng, H. Yang, H. Tian, J. Li, P. Ren and X. Bao, *Energy Environ. Sci.*, 2015, **8**, 1594-1601.
38. H. Li, C. Tsai, A. L. Koh, L. Cai, A. W. Contryman, A. H. Fragapane, J. Zhao, H. S. Han, H. C. Manoharan, F. Abild-Pedersen, J. K. Nørskov and X. Zheng, *Nat. Mater.*, 2015, **15**, 48.

39. S. Xiaolin, C. Guifeng, G. Lixiu, Z. Hui and T. Junguang, *Appl. Phys. Express*, 2016, **9**, 095801.

Chapter 6

Tunable and High Photoluminescence Quantum Yield from Self-Grown TiO_2 Quantum Dots on Fluorine doped Mesoporous TiO_2 Nanoflowers by Rapid Thermal Annealing

In this chapter, we demonstrate a color tunable and high photoluminescence quantum yield (PL QY) from the self-grown spherical TiO_2 quantum dots (QDs) on fluorine-doped mesoporous TiO_2 (F-TiO_2) nanoflowers (NFs), synthesized by a simple hydrothermal process followed by a post-growth rapid thermal annealing (RTA) under vacuum. The strong PL emission from F-TiO_2 QDs is associated with shallow and deep traps, and a record high PL QY of ~5.76% is achieved at room temperature even with its indirect bandgap. Size distribution and doping of F-TiO_2 nanocrystals (NCs) are successfully tuned by simply varying the HF concentration during synthesis. Optimized post-growth RTA under vacuum transforms the arbitrary shaped F-TiO_2 NCs into spherical QDs with smaller sizes and with optimum defect concentration to yield a dramatic enhancement (~163 times) in the PL intensity.

6.1. Introduction

Among different morphological features, three-dimensional (3D) hierarchical architectures have opened up a wide research window in the past few years for their high aspect ratio (surface-to-volume ratio), and distinctive physicochemical properties compared to the conventional nanostructures. Under equilibrium, {001} facet dominated TiO_2 nanostructure is rarely observed as it has very high surface energy than that of {101} facet.[1] However, several reports[1-3] have been published on the controlled growth of TiO_2 single crystals with exposed {001} facet after the breakthrough work by Yang et al.[4] that demonstrated the hydrothermal synthesis of anatase TiO_2 single crystals with 47% exposed {001} facet. Following this work, {001} facet dominated TiO_2 microcrystals are being extensively investigated with various dopings for photocatalytic applications. Recently, mesoporous TiO_2 single crystals delivering enhanced mobility and optoelectronic device performance were reported by Crossland et al.[5] Ding et al. reported on mesoporous hollow TiO_2 microspheres with enhanced photoluminescence (PL).[6] Cleary et al.[7] reported on the highly luminescent TiO_2 nanoparticles (NPs) with a PL QY up to ~3.5%. However, the reported PL yields were measured mostly in colloidal solution or using a

mesoporous template. To the best of our knowledge, there is no report on fluorine doping of mesoporous TiO_2 nanostructure and the extremely high PL quantum yield (QY) of self-grown anatase fluorine doped TiO_2 (F-TiO_2) nanocrystals (NCs) on mesoporous F-TiO_2 nanoflowers (NFs). Thus, a detailed study on structural and optical properties of mesoporous F-TiO_2 nanostructures is warranted to explore its various optoelectronic properties including high PL QY. TiO_2 NCs with high PL QY could be useful for sensing and bioimaging, considering its good biocompatibility.

6.2. Experimental Details

6.2.1. Sample Preparation

6.2.1.1. Preparation of F-TiO_2 NFs

Commercially procured Titanium foil (Sigma Aldrich, purity 99.7%) was first degreased using acetone, 2-propanol and then washed with de-ionized (DI) water. Afterwards, the foil was cleaned by ~18% aqueous HCl solution at 90 °C for 20 min to remove the oxide layer and impurities on its surface followed by DI water washing and finally dried in the inert gas atmosphere. A 50 mL aqueous HF solution with various molar concentrations (10 mM - 80 mM) was prepared and transferred to a Teflon-lined autoclave (Berghof, BR-100) along with the cleaned Ti foil. The sealed autoclave was heated and maintained at 150 °C for pre-selected times (2 - 16 h). After the hydrothermal treatment, the autoclave was allowed to cool down naturally. Then the foil was gently washed with DI water and dried in an oven at 80 °C.

6.2.1.2. Growth of F-TiO_2 QDs on F-TiO_2 NFs

The as-grown F-TiO_2 NF sample was cut into pieces and subjected to rapid thermal annealing (RTA) (Mila 3000P, ULVAC) at 600 °C for 3 min. During the RTA process, the heating and cooling rates were kept at 20 °C/sec and 10 °C/sec, respectively. RTA treatment was performed in three different ambients: ambient air, vacuum (~ $1.5x10^{-2}$ mbar) and hydrogen atmosphere.

Additionally, for comparison, some of the TiO_2 NF samples were annealed at 600 °C for 60 min in a conventional tube furnace with heating and cooling rates at 5 °C/min. The furnace heat treatment was performed under ambient air and in vacuum (~$1.5x10^{-2}$ mbar). A summary of the samples studied under different growth and processing conditions is provided in **Table 6.1**, with respective sample codes. The first part of the sample code refers to the HF concentration during growth and the second part refers to the post-treatment condition.

Table 6.1. *Details of the sample preparation conditions, post-synthesis treatment, crystal structure and surface morphology of the F-TiO_2 NFs.*

Sample code	*HF conc. (mM)*	*Reaction duration (h)*	*Post-growth treatment at 600 °C*	*Crystal structure*	*Surface feature of F-TiO_2 NFs*
T10	10	8	Nil	TiO_2(B), anatase, brookite	Incomplete flower formation
T20	20				Small NCs
T40	40				Excessive selective etching on (001) facet
T60	60				NCs
T80	80				NCs
T20-4h	20	4			Incomplete flower formation
T20-6h		6			Moderate flower growth
T20-12h		12			Overgrowth observed
T20-16h		16			Excessive growth and fusion of nano-cube
T20VR	20	8	Vacuum RTA	Anatase	QDs
T60VR	60				NPs
T80VR	80				NPs
T20AR	20		Air RTA		NPs
T80AR	80				
T20HR	20		Hydrogen RTA		QDs
T20VA	20		Vacuum annealing		NCs
T80VA	80				
T20AA	20		Air annealing		NCs
T80AA	80				
Pure TiO_2 QDs	Sol-gel		Vacuum RTA	Anatase	Pure TiO_2 QDs

6.2.2. Characterization Techniques

The details of XRD, Raman, FESEM, EDS, TEM, UV-Vis absorption and TRPL measurements were discussed in **Chapter 2, Section 2.2.3**. XPS measurement was carried out with a photoelectron spectrometer (AXIS Supra, Kratos Analytical, UK) using Al Kα X-ray beam (1486.6 eV). The XPS measurement was done in IIT Bombay, India. The room temperature steady state PL spectra are recorded using a 355 nm DPSS (Diode-Pumped Solid State) laser excitation with the help of a fluorimeter (Fluoromax-4, Horiba Scientific) equipped with a PMT detector. The PL QY is measured using an integrating sphere (Horiba FM-sphere) incorporated in the Fluoromax-4 system. Fluorescence confocal microscopy is carried out using a laser scanning confocal microscope (LSM 880 microscope (Carl Zeiss)) with a laser excitation at 355 nm. Low temperature (80–300 K) PL measurements are carried out using a liquid nitrogen

cooled optical cryostat (Optistat DNV, Oxford Instruments). XPS measurements are carried out with a photoelectron spectrometer (AXIS Supra, Kratos Analytical, UK) using Al Kα X-ray beam (1486.6 eV). ESR measurements are performed with a JEOL (JES-FA200) instrument operating in the X band.

6.3. Results and Discussion

6.3.1. FESEM and EDS Analyses

The morphology and microstructural properties of the as-synthesized F-TiO_2 NFs were first studied by FESEM. **Fig. 6.1** depicts the FESEM images of the systematic growth of TiO_2 NCs on the TiO_2 NF surface with the variation of HF concentration from 20 mM to 80 mM, keeping the reaction duration fixed at 8 h.

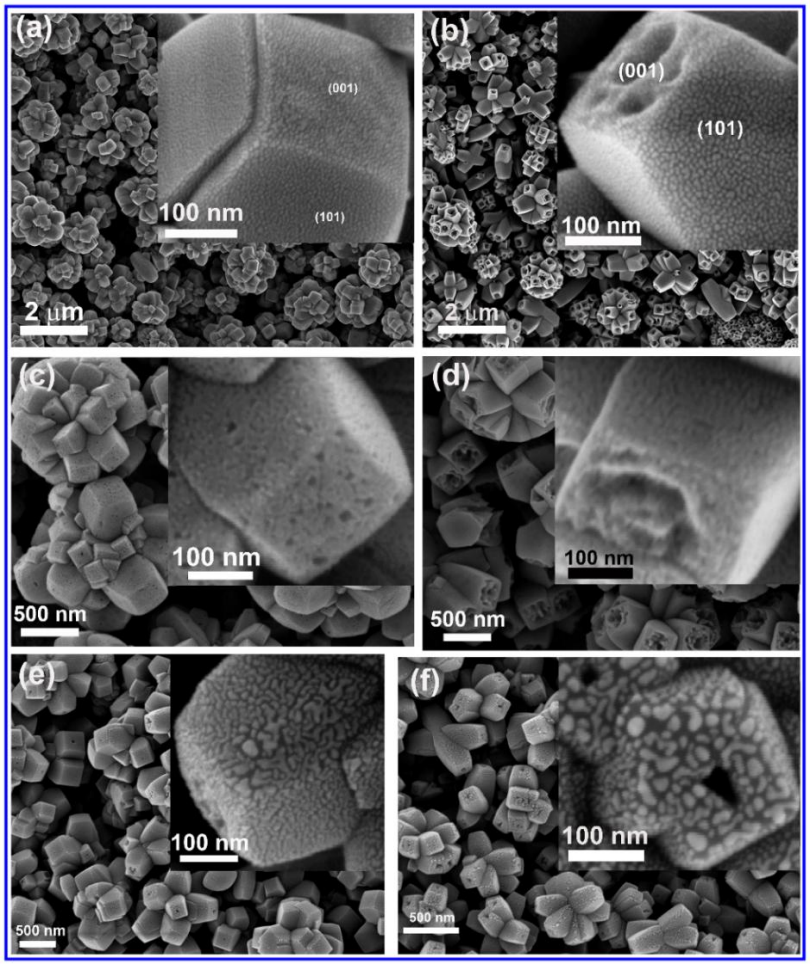

Fig. 6.1. FESEM images of F-TiO_2 NFs: (a) T20, (b) T40; the inset in each case shows the enlarged view of the exposed facets of F-TiO_2 NF decorated with self-grown F-TiO_2 NCs. (c, d) FESEM images of T20VR and T40VR, respectively. The inset in each case shows the magnified image revealing the mesoporous nature of the TiO_2 NF. (e, f) FESEM images of F-TiO_2 NFs in T60 and T80, respectively. The inset in each case shows the magnified view of the mesoporous F-TiO_2 NFs decorated with self-grown F-TiO_2 NCs.

It is clear from **Fig. 6.1(a)** that for the sample T20, the growth of symmetric TiO_2 NFs is complete and the surface of each NF petal/component (truncated tetragonal pyramidal TiO_2 nanocrystal[1]) is covered with uniform self-grown TiO_2 NCs due to the irregular surface etching by HF. Here due to selective etching, small sized NCs separated by nanosized pores are created on each surface. When the HF concentration increases from 20 mM to 40 mM, the exposed highly reactive {001} surface gets etched selectively creating cavities on each {001} surface (see **Fig. 6.1(b)**), while the {101} surface remains relatively smooth covered with TiO_2 NCs due to the less reactivity. After the post-growth heat treatment (RTA or furnace annealing) under vacuum, a major change in the surface feature of the TiO_2 NFs has been observed from FESEM. After vacuum RTA, the surface of T20 is transformed into a mesoporous structure with very tiny NCs in between the pores, as shown in **Fig. 6.1(c)**. The FESEM image of T40VR shown in **Fig. 6.1(d)** depicts the cavity formation in {001} facet and overall mesoporous surface. When the HF concentration is further increased (> 40 mM), the cavity on the {001} facet becomes smaller, and all the surfaces of the TiO_2 NFs get etched nearly uniformly irrespective of the nature of the facets, and larger NCs are formed. Theoretical and experimental studies on anatase TiO_2 have shown that surface energy (g) of {001} facet is greater than the {101} facet ($g_{\{001\}}$ (0.90 J m^{-2}) > $g_{\{101\}}$ (0.44 J m^{-2})). Thus, {001} facet is more chemically active than {101}, and it reacts with the HF faster, which creates the cavities on the {001} faceted TiO_2 surface. This results in the formation of TiO_2 NCs of arbitrary shape and size. It is observed that the size of the TiO_2 NCs becomes larger with increasing the HF molar concentration (from 60 mM to 80 mM) (see **Fig. 6.1(e, f)**).

We have also monitored the growth of TiO_2 NFs with the variation of reaction duration from 4 h to 16 h using 20 mM HF solution as solvent (see **Fig. 6.2**). An incomplete growth of TiO_2 NFs is observed for 4 h reaction (see **Fig. 6.2(a)**), where the NF like structures start evolving. After 6 h of reaction, it is observed that the NFs are developed with truncated tetragonal pyramidal TiO_2 NCs, and the NF size becomes larger, as shown in **Fig. 6.2(b)**. After 8 h of reaction, the growth of NFs is completed as shown in **Fig. 6.1(a)**, where a uniform growth of the NF components in all directions with almost identical size is observed. Further increase in reaction duration leads to the over-growth of the NFs. For 12 h of reaction, the number of truncated tetragonal pyramidal TiO_2 NFs growth increases and it starts fusing with each other (see **Fig. 6.2(c)**).

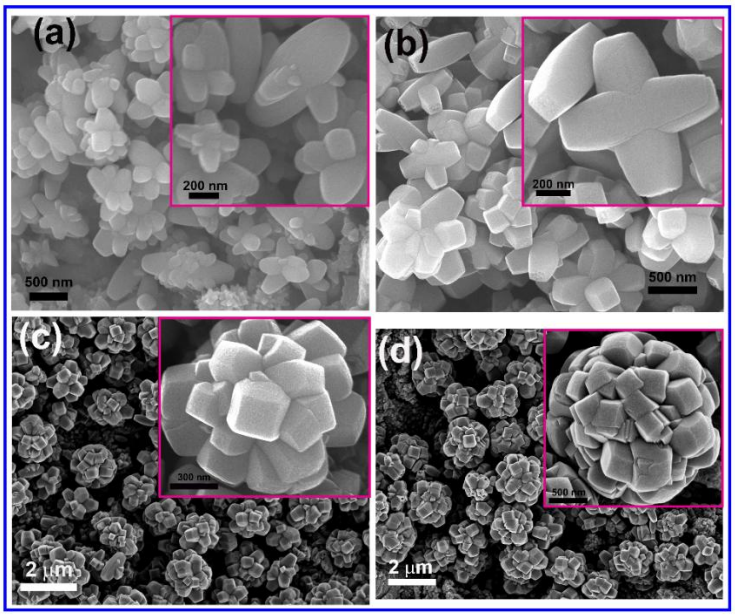

Fig. 6.2. FESEM images of F-TiO_2 NFs: (a) T20-4h, (b) T20-6h, (c) T20-12h and (d) T20-16h. The inset in each case shows the enlarged view of the F-TiO_2 NF.

After 16 h of reaction, excessive growth is observed, and thus the TiO_2 NFs are fused with each other compactly giving it a nearly spherical shape, see **Fig. 6.2(d)**. Similar to T20VR and T40VR, T60VR and T80VR also exhibit a similar type of porous surface feature, as shown in **Fig. 6.3(a, b)**, respectively. However, the sample T20VR shows the optimal mesoporous nature with very tiny NCs uniformly distributed over the surface.

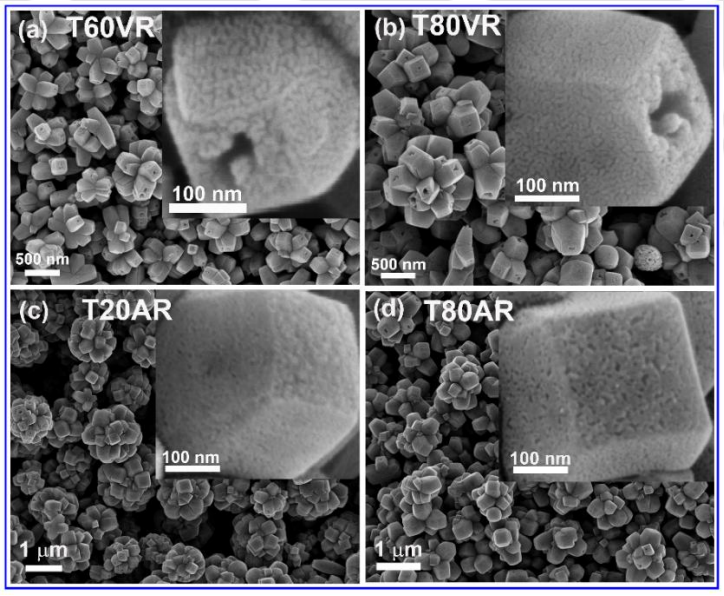

Fig. 6.3. FESEM images of differently annealed F-TiO_2 NFs prepared with various HF concentrations: (a) T60VR, (b) T80VR, (c) T20AR and (d) T80AR. The inset in each case shows the enlarged view of the exposed facets of F-TiO_2 NF.

After air RTA, T20 and T80 exhibit comparatively less mesoporous nature, which may be due to the lower density of O_V defects (See **Fig. 6.3(c, d)**). During vacuum RTA, oxygen atoms may leave the bulk of the crystals, and as a result, Ov defects are created in high density, which may eventually form Ov clusters/voids inside the TiO_2 crystal.[8] These voids may be responsible for the evolution of the mesoporous structure in TiO_2.[9] Particularly, in case of vacuum RTA, the rapid change in thermal environment promotes coalescence of O_v defects and creation of voids as compared to the case of conventional annealing with slow heating/cooling rate. In the case of air RTA, due to the high oxygen partial pressure, the creation of void is not favorable and hence it gives rise to a less mesoporous structure.

To confirm the elemental composition and the doping of TiO_2, EDX spectra of the as-grown, as well as the differently treated samples, were recorded and the corresponding atomic percentage of the constituent elements are tabulated in **Table 6.2**. The EDX spectra of various as-grown TiO_2 NFs confirm the presence of Ti, O and F in the nanostructures. In case of T10, TiO_2 is formed with a low density of oxygen vacancy (O_V) and with 3.5 at% of F. When the HF concentration is increased to 20 mM, the concentration of F reaches to ~7.5 at% with a higher density of O_V. Further increase in HF concentration and reaction duration leads to the increase in O_V concentration, though the concentration of F in the samples remains almost unaltered (see **Table 6.2**), which implies that the doping and surface adsorption of F ions reaches to its optimum level beyond the 20 mM HF concentration and 8 h of reaction duration.

Table 6.2. *Details of the atomic percentage (at%) of constituent elements in the various samples analyzed from their respective EDX spectra.*

Sample code	*O (at%)*	*Ti (at%)*	*F (at%)*
T10	62.3	34.2	3.5
T20	59.2	33.3	7.5
T20-12h	57.2	34.9	7.9
T40	57.0	35.1	7.9
T20VR	53.8	45.3	0.9
T20AR	58.5	39.3	2.2
T20VA	57.9	40.6	1.5
T20AA	60.5	36.7	2.8

It is observed that after the vacuum annealing (RTA and furnace), the O_V density increases further, but the density of F ions decreases dramatically (see **Table 6.2**). The heat treatment at high temperature (600 °C) removes the F adsorbed on the surface of the TiO_2 NFs. In the case of

sample T20, after vacuum RTA the O_V density increases dramatically and reaches the highest value among all the samples. This effect is found to be less in the sample T20AR (air RTA, oxygen-rich environment). In the case of furnace annealing, the O_V density increases from that of the untreated sample, but not as high as in RTA treated sample. Thus, it is clear that the RTA treatment is superior over the normal furnace annealing to create controlled defects in the TiO_2 system.

6.3.2. FETEM Analysis

To study the surface morphology and structure of F-TiO_2 NFs/NCs, FETEM images are acquired. Higher magnification FETEM image of T20 is shown in **Fig. 6.4(a)**. During the hydrothermal growth, TiO_2 NCs of average size ~5.0 nm (**Fig. 6.5(a)**) are observed to be grown by irregular etching on the TiO_2 NFs surface. **Fig. 6.4(b)** shows the HRTEM lattice fringe pattern confirming the co-existence of TiO_2 NCs and (001) facet of TiO_2 NF. The corresponding SAED pattern shows a signature of mixed phase TiO_2 as shown in **Fig. 6.4(c)**. In case of T20VR, TiO_2 NFs uniformly decorated with spherical TiO_2 QDs having an average size ~4.2 nm are found (see **Fig. 6.4(d)**) and the corresponding size distribution is depicted in **Fig. 6.5(b)**. HRTEM lattice fringe pattern of a crystalline TiO_2 QD in T20VR is shown in **Fig. 6.4(e)**. Due to its ultra-small size and spherical shape, these are termed as QDs. SAED pattern of the TiO_2 QD showing its single crystal nature is shown in **Fig. 6.4(f)**. At higher HF concentration, the size of the TiO_2 NCs grows bigger due to the intense surface etching effect. For 60 mM HF, the average NCs size was measured to be 8.4 nm, while for 80 mM HF it increases to 11.4 nm, as shown in **Fig. 6.5**. **Fig. 6.4(g)** shows a typical FETEM image of T80, showing the self-grown TiO_2 NCs while **Fig. 6.4(h)** depicts a magnified view of the NCs showing its arbitrary shape on the surface of TiO_2 NF. **Fig. 6.4(i)** shows the HRTEM lattice fringe pattern of T80 showing the simultaneous presence of highly crystalline TiO_2 NCs and TiO_2 NFs. It can be noted that the lattice spacing for the TiO_2 NCs are calculated to be 0.33 nm, which corresponds to the (101) planes, while that of the truncated tetragonal pyramidal TiO_2 facet is 0.55 nm, which corresponds to the (001) planes. **Fig. 6.4(j)** shows the FETEM image of T80VR and **Fig. 6.4(k)** shows its enlarged view. It is clear that the truncated tetragonal pyramidal TiO_2 NFs are uniformly decorated with TiO_2 NPs having average size ~12.8 nm (see **Fig. 6.5(f)**). **Fig. 6.4(l)** shows the high-resolution lattice-fringe pattern involving highly crystalline TiO_2 NP oriented along (004) planes grown on (101) facet of TiO_2 NF.

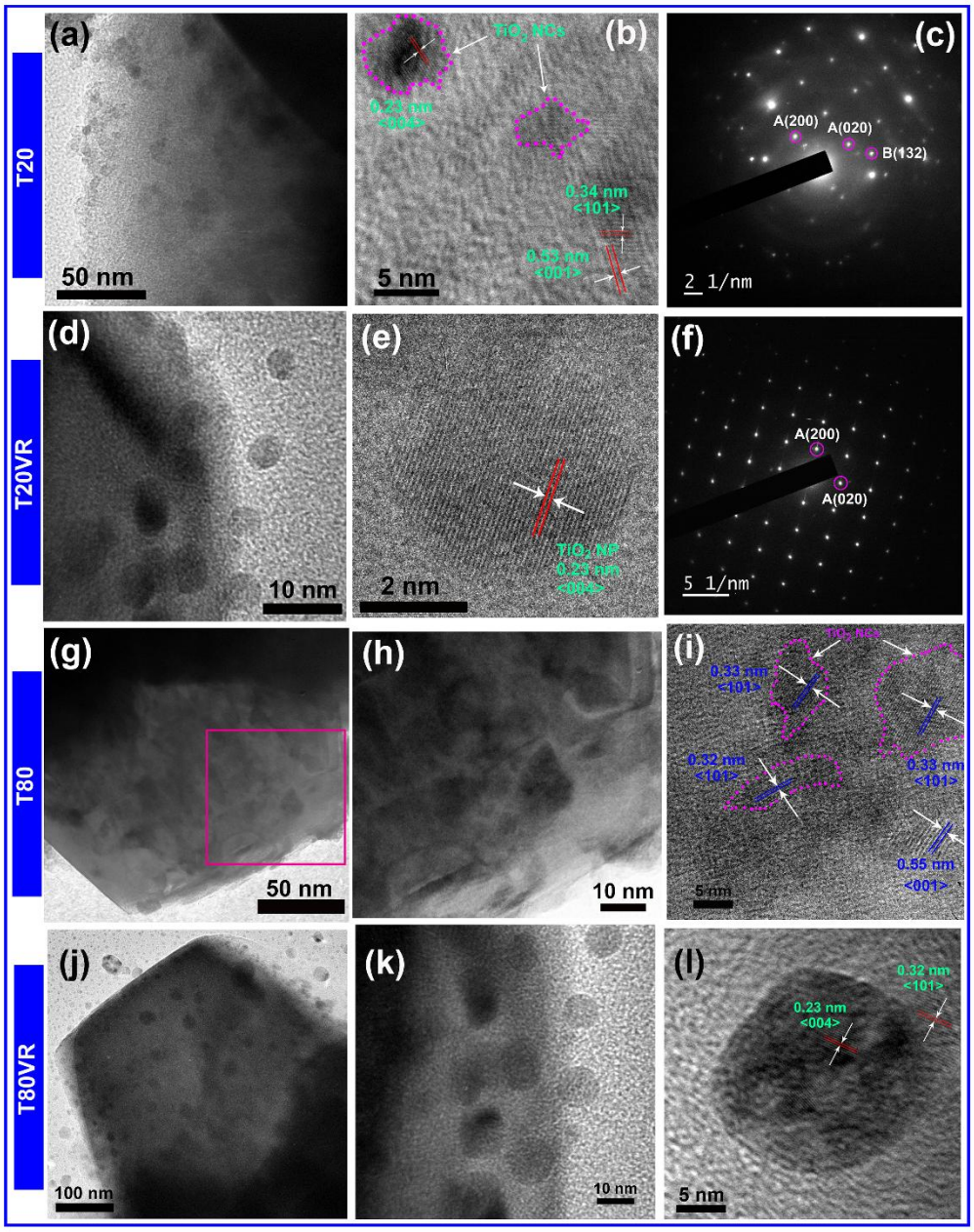

Fig. 6.4. (a) FETEM image of T20 showing a clearer view of the self-grown NCs on TiO_2 NF. (b) HRTEM lattice fringe pattern of TiO_2 NCs on TiO_2 NF. The arbitrary shape of the NCs is shown with dotted boundary lines. (c) SAED pattern of the self-grown NCs on the TiO_2 NFs showing single crystal pattern. (d) FETEM images of T20VR showing the presence of spherical TiO_2 QDs on the TiO_2 NF. (e) HRTEM lattice fringe pattern of a crystalline TiO_2 QD in T20VR. (f) SAED pattern of the TiO_2 QD. (g) FETEM image of self-grown NCs in T80, (h) a magnified view of the NCs showing the arbitrary shape of the NCs on the surface of TiO_2 NF. (i) HRTEM lattice image of TiO_2 NCs. (j, k) FETEM images of T80VR at lower and higher magnification showing TiO_2 NPs on the TiO_2 NF, and (l) HRTEM lattice fringe pattern of TiO_2 NPs.

The lattice d-spacing calculated here for all the cases is smaller than the standard value, which indicates a compressive strain in the TiO_2 lattice, and this is consistent with the Raman and XPS analyses discussed later.

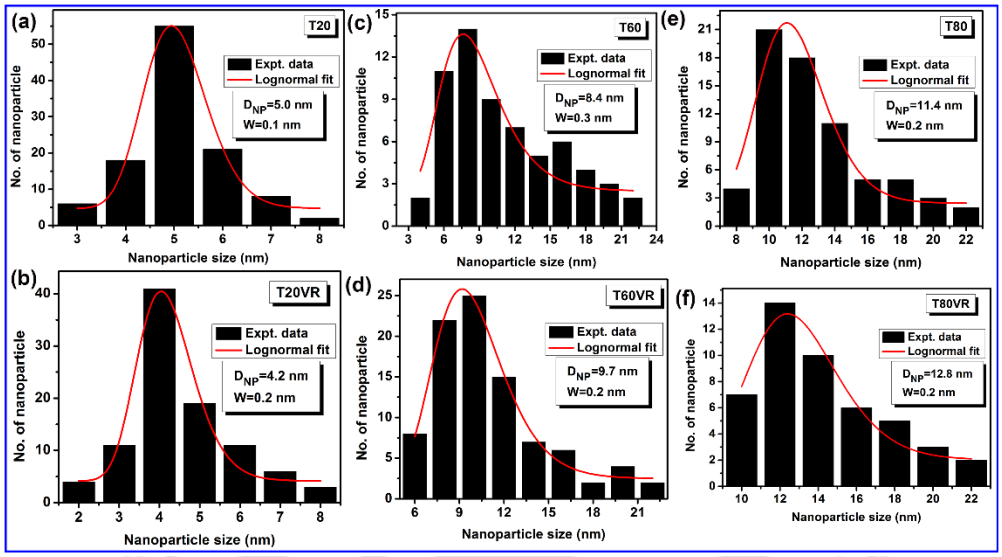

Fig. 6.5. The size distribution of F-TiO_2 NCs grown on (a) T20, (c) T60 and (e) T80. (b, d, f) The respective size distribution after vacuum RTA treatment. The average diameter (D) with lognormal fitting and width of the distribution (W) are shown as an inset.

Spherical TiO_2 QDs are formed here from the arbitrary shaped TiO_2 NCs by the TRA treatment, which involves an extremely fast change in the thermal environment (20 °C/sec) of the sample. During the RTA treatment under vacuum, TiO_2 NCs with average size 5.0 nm (for T20) are observed to be transformed into spherical QDs with average diameter 4.2 nm, which falls in the weak quantum confinement regime[10], and thus these ultrasmall spherical NPs are referred as QDs. For T60 and T80, the NCs with average size are 8.4 nm and 11.4 nm, respectively, and these are transformed into spherical NPs with sizes 9.7 nm and 12.8 nm, respectively after vacuum RTA, see **Fig. 6.5**. STEM elemental mapping analysis of T20 and T20VR also confirms the presence of Ti, O and F in the system, as shown in **Fig. 6.6**. After RTA treatment, the concentration of F reduces greatly, though it does not vanish completely, which may be due to the elimination of surface adsorbed F but not the F doped in the TiO_2 crystal lattice. It appears that F doped in the TiO_2 lattice has high thermal stability.

Now we attempt to explain the shape evolution of TiO_2 NCs from arbitrary shape into spherical NPs/QDs during the RTA treatment. In the classical nucleation theory[11, 12], interface/boundary of the NCs plays an important role in the evolution of the NCs to a critical size. Classical nucleation theory predicts that to reduce the total free energy, the size of the NCs may reduce/increase to arrive at the critical radius and spherical shape assumes a minimal surface area. Due to the thermal stress during the RTA process, the interfacial contact angle for

the attached NCs increases when the shape evolves to spherical type, and this helps in achieving the minimum free energy.

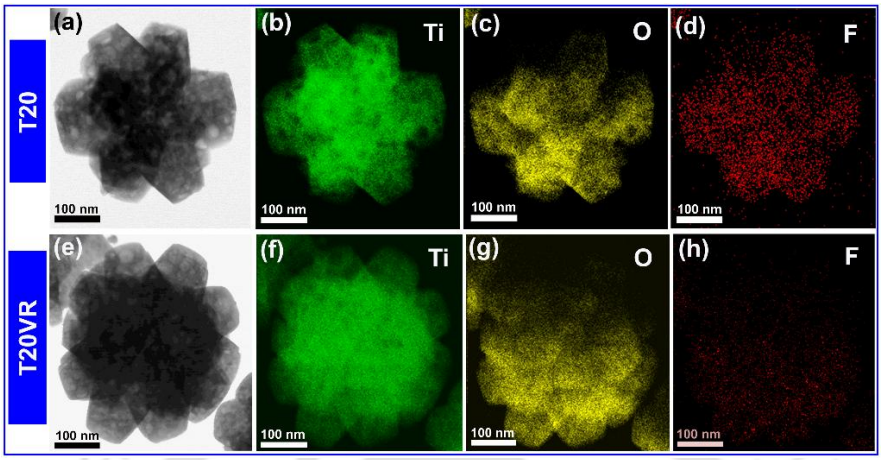

Fig. 6.6. STEM images of mesoporous TiO_2 NFs and its elemental mapping in T20: (a-d) as-grown, and (e-h) after vacuum RTA.

In the present case, after 3 min vacuum RTA, we observe a remarkable shape evolution of self-grown TiO_2 NCs to perfect spherical shape in each case. This may be explained as follows. As compared to its bulk form, the melting point of the TiO_2 NCs reduces substantially due to the formation of very small NCs. With the thrust of the thermal energy during RTA, the NCs tend to make a higher contact angle with the TiO_2 NFs interface to reduce the surface energy. Thus, the arbitrary shaped TiO_2 NCs transform into the spherical QDs having higher contact angle. Additionally, during the vacuum RTA, the concentration of O_V defects in the sample enhances dramatically, which induces compressive strain in the lattice that in turn squeeze the crystallite size of the TiO_2 QDs. Note that in case of normal furnace annealing, such a shape evolution to spherical QDs was not observed, implying the critical role of thermal stress during the RTA process in achieving the spherical NPs/QDs along with high defect density. Further, it has been reported that fluorine has an important role in controlling the faceted growth of TiO_2 nanostructures. Yang et al.[13] reported that in the absence of fluorine, no crystal facet control was observed for TiO_2 and only spherical polycrystalline anatase particles were formed. In this case, we noticed that after RTA, surface adsorbed fluorine is completely removed from the TiO_2 NCs, as revealed from XPS results (see **Section 6.3.3.3**) and this helps partly in achieving the growth of spherical TiO_2 NPs/QDs after annealing.

6.3.3. Structural Analysis

6.3.3.1. XRD Analysis

In order to confirm the crystal structure and phase of the F-TiO_2 NFs, XRD pattern of each sample has been recorded, and the results are shown in **Fig. 6.7**. All the diffraction peaks are very sharp clearly implying that the as-grown TiO_2 NFs are highly crystalline in nature. With increasing HF concentration or reaction duration, the intensity of Ti peaks is reduced due to the higher density of NF growth, as shown in **Fig. 6.7(a, b)**, respectively. Most of the crystal planes of TiO_2 NFs correspond to pure anatase phase (JCPDS file # 782486) (marked as "A" in the figure). Besides the anatase phase, an additional monoclinic B-phase TiO_2 is detected at $2\theta \approx 44.59°$ corresponding to (60-1) plane in all the samples. Another diffraction peak is detected at $2\theta \approx 47.94°$, which can be assigned to either the A(200) TiO_2 (JCPDS file # 782486) or B(321) metastable brookite TiO_2 (JCPDS file # 761936). To investigate the effect of post-growth annealing, all the samples were treated at 600 °C under vacuum and air ambient. It is observed that after the annealing, the later peak is almost vanished (see **Fig. 6.7(c)**.

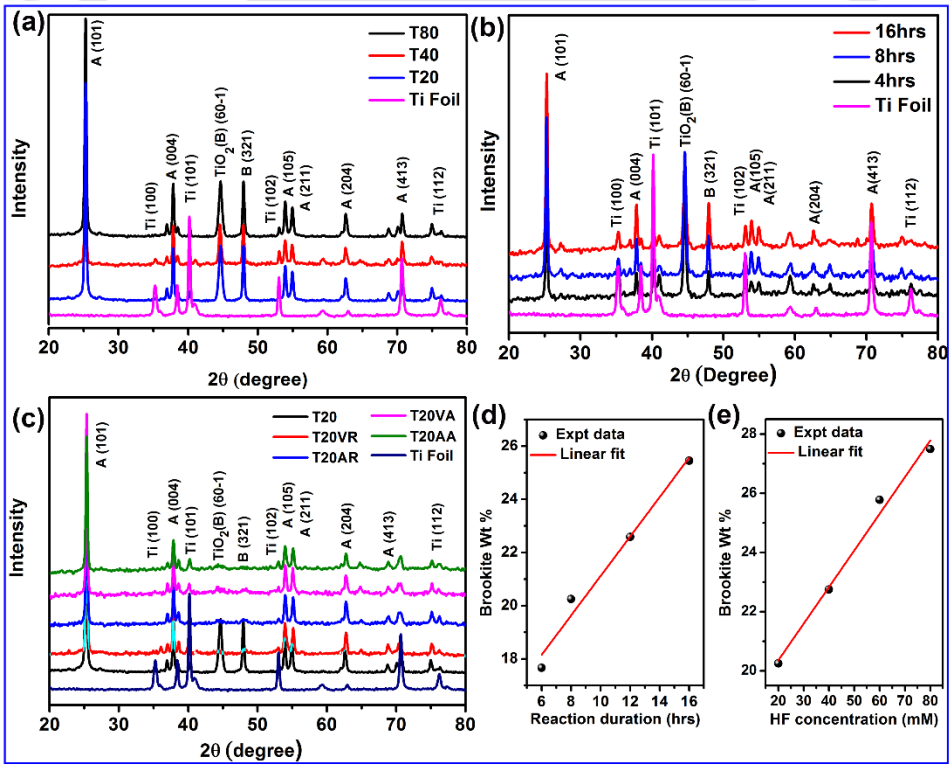

Fig. 6.7. XRD patterns of as-grown F-TiO_2 NFs grown at (a) various HF molar concentration (20 mM - 80 mM) and (b) hydrothermal reaction duration (4-16 h). (c) T20 sample after various annealing. The weight percentage of brookite TiO_2 phase as a function of the (d) reaction duration and (e) HF concentration, respectively, calculated from XRD analysis.

This implies that the corresponding brookite phase is not thermally stable. The XRD peak intensity corresponding to the brookite phase increases with increasing HF molar concentration as well as the reaction duration. It is observed that the percentage of brookite phase increases almost linearly in both cases (see **Fig. 6.7(d, e)**). After the heat treatment (RTA and annealing), the most intense anatase (101) peak shows an upshift in Bragg angle ($\Delta 2\theta \approx 0.06°$) along with a decrease in the FWHM. The upshift may be a signature of compressive strain in the lattice structure due to the defects in the lattice. After RTA treatment, the FWHM decreases, which implies an increase in the crystallite size of the respective sample.

6.3.3.2. Raman Analysis

Fig. 6.8(a) displays the Raman spectra of F-TiO_2 NCs/NFs grown at various HF concentrations. The inset shows a magnified view of the spectra along with that of the bulk TiO_2, which clearly reveals the peak shift and asymmetry in the Raman line shape. For the bulk TiO_2, the $E_g(1)$ Raman mode is detected at ~142 cm^{-1} and observed to be symmetric in nature.[14]

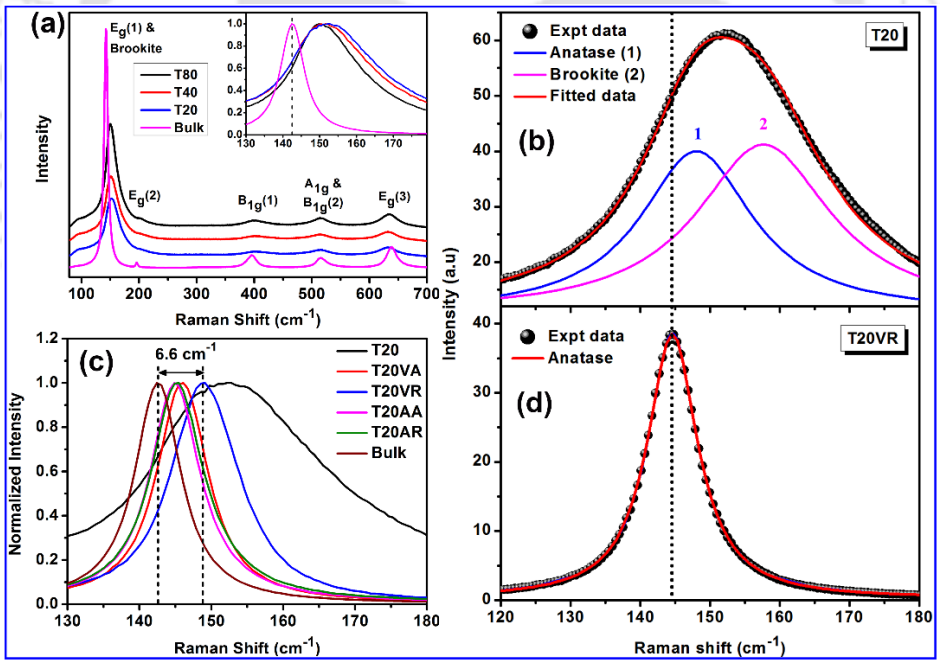

Fig. 6.8. (a) Raman spectra of F-TiO_2 NFs grown at various HF concentrations. The inset shows the normalized Raman spectra indicating large blue shift of $E_g(1)$ peak from that of the bulk TiO_2. (b) Comparison of the normalized $E_g(1)$ peak for T20 before and after RTA/furnace annealing under different ambient. (c, d) Lorentzian fit to the $E_g(1)$ peak in T20 before and after vacuum RTA, respectively. The vertical dotted line shows the peak shift and elimination of peak 2 after RTA.

It can be observed that for the sample T20 (**Fig. 6.8(a)**), the most intense Raman peak is detected at ~151.7 cm^{-1}, which is ~9.7 cm^{-1} blue shifted along with an asymmetry in higher wavenumber

compared to bulk TiO_2. As this large blue shift is unlikely to originate from a single source, phonon confinement[15] and nonstoichiometric defects[14] and presence of brookite phase[16] may contribute substantially to the observed blue shift. For a clear understanding of the origin of asymmetry and large shift of the Raman peak, it is deconvoluted into two Lorentzian peaks; one centered at 147 cm^{-1} denoted as anatase E_{1g} and other centered at 156 cm^{-1} denoted as brookite[17] (T20), as shown in **Fig. 6.8(b)**. Thus, the presence of brookite phase probably contributes to the large blue shift as compared to its bulk counterpart. Note that both the anatase and brookite peaks are blue shifted, partly because of the compressive strain induced in the lattice due to the oxygen vacancy, as evidenced from XRD, PL, ESR and XPS analyses (discussed later). Note that TiO_2 NFs are covered with self-grown TiO_2 NCs of very small size (~5.0 nm), which may results in the phonon confinement effect and asymmetry in the Raman line shape. It is further observed that with increasing HF concentration, the Raman band exhibits red shift with little asymmetry (see inset of **Fig. 6.8(a)**) due to the formation of larger TiO_2 NCs (as confirmed from FESEM & FETEM). The decrease in FWHM implies the improvement in the crystallinity with increasing molar concentration of HF.

Interestingly, after the controlled heat treatment, the blue shift in the $E_g(1)$ peak is reduced and becomes symmetric in nature, which is due to the elimination of brookite phase and presence of only anatase phase (see **Fig. 6.8(c, d)**), as evident from the XRD analysis. The reduced blue shift may partly be due to the reduction of lattice strain in the crystal. However, the $E_g(1)$ peak is still blue shifted with respect to that of the bulk, indicating the contribution of phonon confinement in the observed blueshift. In case of T20, after vacuum RTA the blue shift is highest (6.6 cm^{-1}) among differently processed samples (as shown by a pair of dashed line in **Fig. 6.8(c)**) and it might be contributed by phonon confinement and the oxygen vacancy defects in TiO_2 lattice. Note that after vacuum RTA of T20, the size of the self-grown TiO_2 NCs reduces and the arbitrary shape is transformed to spherical QDs with an average diameter ~4.2 nm. Even though this size for TiO_2 falls in the weak confinement region for the electron, we observe phonon confinement induced blue shift from these NPs/QDs.

6.3.3.3. XPS and ESR Analyses

Fig. 6.9 shows the XPS survey spectrum of various F-TiO_2 NFs before and after different thermal treatments at 600 °C. XPS spectra show that the F-TiO_2 contains only Ti, O, and F elements and a trace amount of carbon.

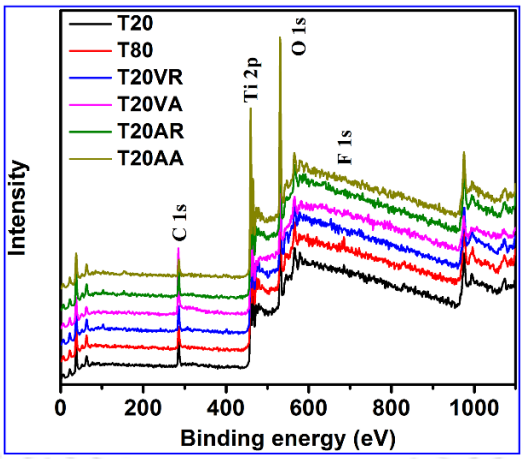

Fig. 6.9. Survey scan XPS spectra of various F-TiO_2 NFs before and after annealing.

Each of the as-grown and annealed samples shows four symmetric Gaussian peaks in the Ti 2p XPS spectrum. **Fig. 6.10(a)** shows the Ti 2p core level spectra of T20. The main two peaks at 458.8 eV (Ti $2p_{3/2}$) and 464.5 eV (Ti $2p_{1/2}$) are associated with the Ti^{4+} valence state, confirming the formation of TiO_2. The other two shoulder peaks at 457.3 eV (Ti $2p_{3/2}$) and 460.2 eV (Ti $2p_{1/2}$) are due to Ti^{3+} valence state, which is a signature of oxygen vacancy (O_V) defects in the system.[18] The relative concentration of Ti^{3+} in the Ti 2p spectra was calculated as ~9.2% for both T20 and T80. Thus, it can be concluded that Ti^{3+}% remains almost unaltered with the variation of HF molar concentration. However, after vacuum RTA, Ti^{3+}% marginally increases to 9.5%, as shown in **Table 6.3**. **Fig. 6.10(b)** shows the normalized Ti $2p_{3/2}$ core level spectra of T20 sample before and after vacuum RTA. It can be noted that the peak at 458.8 eV corresponding to Ti^{4+} valence state, marked with a vertical dotted line, shifts to a lower binding energy, 458.7 eV after vacuum RTA. The shift to lower binding energy may be attributed to the lattice contraction.[19] After the vacuum RTA treatment, decoration of self-grown TiO_2 NPs/QD on the surface of the TiO_2 NFs was observed. Li et al.[20] showed that the lattice contraction with decreasing particle size is thermodynamically favorable due to the higher surface curvature. One of the dominant phenomena governing the contraction in lattice volume with the reduction in particle size is the surface stress due to the excess oxygen vacancy, which can create a positive pressure that in turn produces a lattice contraction. To ascertain the doping of fluorine (F) in the TiO_2, high-resolution F 1s XPS spectrum of each sample was acquired, and the results are presented in **Fig. 6.10(c, d)**. Each of the F 1s spectra of the as-grown samples is composed of two peaks, as shown in **Fig. 6.10(c)**.

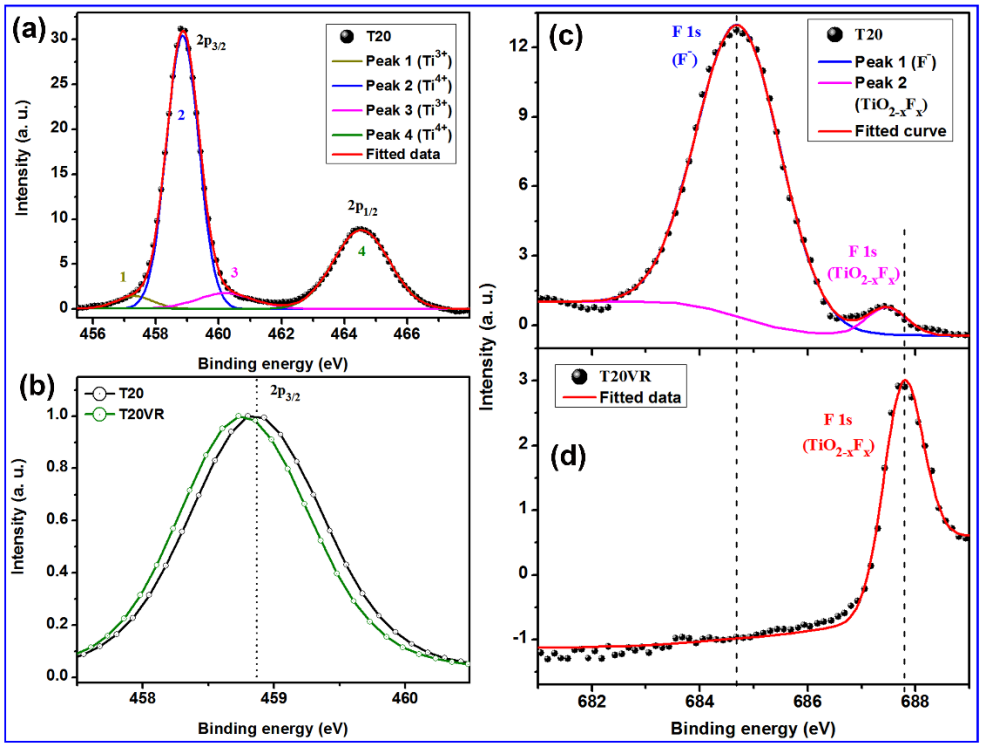

Fig. 6.10. (a) Ti 2p core level XPS spectrum of T20 with Gaussian fitting and Shirley baseline. (b) Normalized Ti $2p_{3/2}$ XPS spectra of T20 and T20VR for comparison. The vertical dotted line is shown to visualize the peak shift after RTA. (c) F 1s XPS spectrum and its Gaussian fittings for T20, with Shirley baseline. (d) The F 1s XPS spectrum of T20VR fitted with a Gaussian peak, showing the absence of lower energy F^- peak. The vertical dashed lines are shown to visualize the adsorbed and doped F positions before and after RTA.

The major peak located at ~684.7 eV can be attributed to the F ions physically adsorbed on the surface of the TiO_2 NFs, while the other small peak located at 687.6 eV can be attributed to the substitutional F atoms in the TiO_2 lattice.[21] The second peak originates from the F atoms doped into the TiO_2 crystal lattice during the hydrothermal process. Quantitative analysis shows that the relative percentage of doped fluorine increases from 4.3% to 7.2% when the HF molar concentration increases from 20 mM to 80 mM, see **Table 6.3**. Thus, it can be concluded that the doping concentration increases with increasing the molar HF concentration and with reaction duration as well. **Fig. 6.10(d)** shows the high-resolution F 1s XPS spectrum of T20VR. It is clear that the intense peak at ~684.7 eV associated with the physically adsorbed F disappears completely after RTA, which signifies the complete removal of surface fluorine by thermal treatment. Interestingly, the only peak detected at 687.6 eV for T20VR is fully consistent with the doped F content in solid solution $TiO_{2-x}F_x$. The substitution of F^- for O^{2-} in the TiO_2 lattice is not too surprising as the atomic radii of F^- and O^{2-} ions are almost identical. Interestingly, despite

high-temperature annealing, the doped F atoms remains inside the TiO_2 lattice, and it strongly influences the optical properties of the NCs.

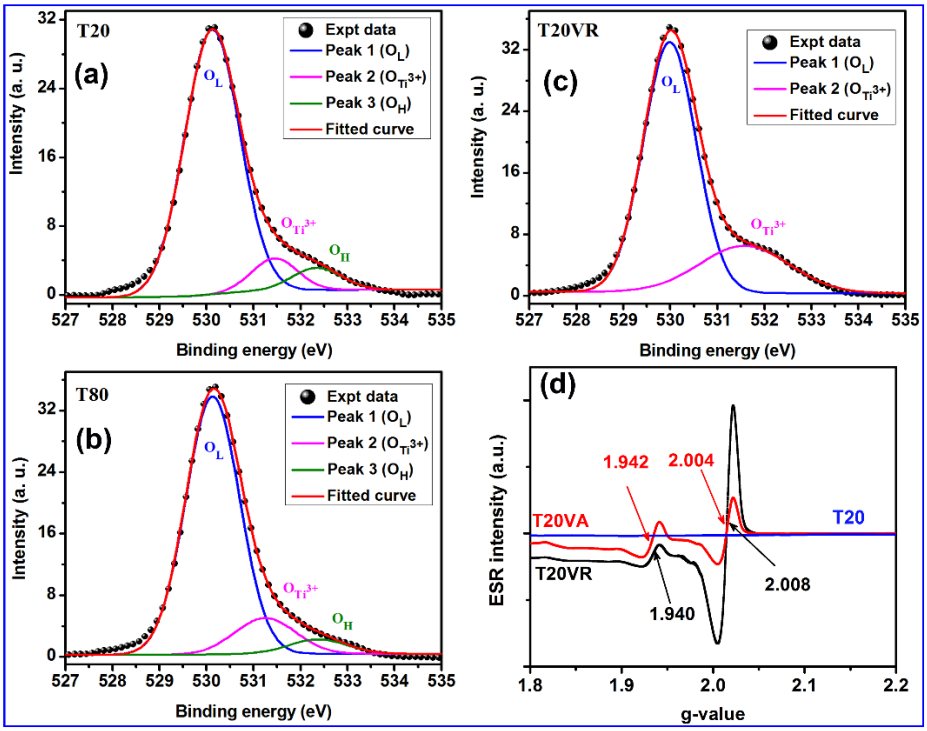

Fig. 6.11. XPS O 1s spectra and its Gaussian fittings for (a) T20, (b) T80, with Shirley baseline. (c) The XPS O 1s spectra with fitting for T20VR. (d) Comparison of the room temperature ESR spectra for T20, T20VR and T20VA. The respective g-values are indicated in each case.

Fig. 6.11(a, b) display the O 1s spectra of F-TiO_2 synthesized with 20 mM and 80 mM aqueous HF solvent, respectively. Each spectrum contains a long tail in the higher binding energy region making the spectrum asymmetric in nature, and this tail implies the presence of impurities/defects in the sample. Each spectrum can be fitted with three symmetric Gaussian peaks. In addition to the lattice oxygen (O_L), O_{Ti}^{3+} and adsorbed hydroxyl group, one minor peak at ~528.5 eV is also seen for all the samples (see **Fig. 6.11(a-c)**), which may be due to the subsurface oxygen atom adsorbed on the TiO_2 lattice.[22] It is consistent with the fact that after vacuum RTA, this peak contribution is reduced (see **Fig. 6.11(c)**), due to the annealing in oxygen deficient environment. The relative concentration of O_{Ti}^{3+} for the samples T20 and T80 is calculated to be 8.5% and 12.9%, respectively (see **Table 6.3**). Thus, an enhancement in the concentration of O_V defects in the systems synthesized with higher HF concentration as well as reaction duration is confirmed, which is fully consistent with the PL results (discussed in **Section 6.3.4.2**). The O 1s spectrum of T20VR with two symmetric Gaussian deconvoluted peaks is

shown in **Fig. 6.11(c)**. It can be noted that the adsorbed hydroxyl group disappears from the sample due to the thermal treatment at high temperature (600 °C). The vacuum annealing enhances the concentration of oxygen vacancy defects greatly in the system. For the sample T20, the relative concentration of O_{Ti}^{3+} is calculated to be 22.4% and 24.3% after vacuum annealing and vacuum RTA, respectively. Though, both the RTA and furnace annealing were carried out under identical vacuum level (1.5×10^{-2} mbar), RTA creates more oxygen vacancy defects in the system. It may be due to the thermal stress caused by the rapid change in the thermal environment during RTA, which creates more surface defects in a reduced atmosphere. A summary of the relative concentration of Ti^{3+}, O_V and surface adsorbed F in various pre- and post-treated samples is shown in **Table 6.3**.

Table 6.3. *Summary of the relative percentage of Ti^{3+}, O_V, surface adsorbed F and doped F in various samples obtained from Ti 2p, O 1s, and F 1s XPS spectra, respectively.*

Sample code	*Ti^{3+} %*	*O_V %*	*Adsorbed F (%)*	*Doped F (%)*
T20	9.2	8.5	95.7	4.3
T80	9.2	12.9	92.8	7.2
T20VA	11.5	22.4	0.0	0.4
T20VR	9.5	24.3	0.0	0.4
T20AA	9.3	18.2	0.0	0.3
T20AR	9.4	18.9	0.0	0.3

ESR is a powerful tool to detect the spin-polarized charge states in the defective TiO_2 nanostructure. ESR spectra of different samples are shown in **Fig. 6.11(d)**. The samples T20VR and T20VA exhibit strong ESR signal at g = 1.940 and 1.942, respectively, which confirms the presence of Ti^{3+} interstitial in the samples. Additionally, the ESR signals at g values of 2.008 and 2.004 are attributed to the singly ionized oxygen vacancy F^+ center for T20VR and T20VA, respectively.[23] From the figure, it can be noted that in case of T20VR, the singly ionized oxygen vacancy defect (F^+ center) density is much higher than the Ti^{3+} and the F^+ species of other samples, which is fully consistent with the PL analysis. As compared to the post-annealed samples, the as-grown samples show negligibly low ESR signal as it contains a very low density of defects. For the comparison, the ESR signal of T20 was also recorded, and the result is shown in **Fig. 6.11(d)**, showing negligible defects.

6.3.4. Optical Analysis

6.3.4.1. UV-Vis Absorption Study

Fig. 6.12(a) shows a plot of the K-M function of the pre- and post-treated samples corresponding to their diffused reflectance spectra and **Fig. 6.12(b)** shows the $(F(R)h\nu)^{1/2}$ vs hν plot for the calculation of effective band gap (indirect) of the F-TiO_2 NFs. It is observed that the commercial bulk TiO_2 powder shows a band-edge absorption at ~375 nm, which changes to ~380 nm for the F-TiO_2 NCs/NFs. A marginally improved absorption is observed in the visible region for the as-grown sample. After vacuum RTA or furnace annealing, the surface adsorbed F disappears. However, the lattice doped F along with the enhanced nonstoichiometric surface defects leads to the higher absorption in the visible region.

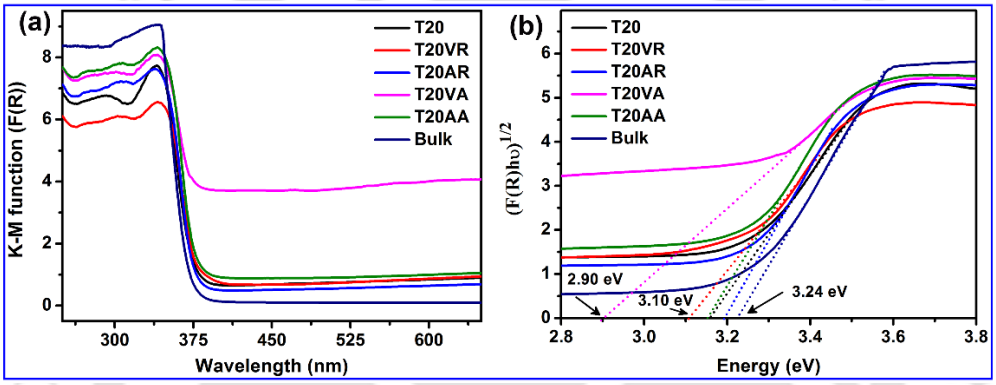

Fig. 6.12. (a) Kubelka–Munk plot, F(R), derived from the diffuse reflectance spectra of T20 before and after annealing in different environments. The spectrum for the bulk TiO_2 is shown for comparison. (b) Corresponding Tauc plot $[(F(R)h\nu]^{1/2}$ vs hν plot) considering the indirect bandgap nature of the F-TiO_2 NFs. The effective band gap of different TiO_2 NFs is estimated from the intercept on the x-axis (extrapolated dashed lines).

On the other hand, after vacuum annealing (conventional), a dramatic enhancement in the absorption intensity in the visible region is noticed, which may be due to the high density of O_V defects, both on the NF and NC surface. The effective band gap for the corresponding sample (T20VA) is reduced to 2.90 eV, as shown in **Fig. 6.12(b)** and **Table 6.4**. Therefore, after vacuum annealing, the narrowing of the band gap results in the visible light sensitization of F-TiO_2 NFs. This may be extremely beneficial for the efficient visible light photocatalysis. In the case of T20VR, the whole absorption spectrum can be divided into three regions: up to 380 nm, 380-420 nm and beyond 420 nm. Absorption below 380 nm directly comes from the band to band transition, while the absorption in the range 380−420 nm arises due to the self-trapped excitons and shallow trap states Ti^{3+} centers. Santara et al.[23] showed that the absorption in the range 420−580 nm (blue, green, and yellow region) could be attributed to the deep trap F^+ centers

associated with the oxygen vacancies. Our results clearly show absorption beyond 420 nm, which can partly be due to the deep trap states, as confirmed from the PL analysis. The effective indirect band gap of T20VR is calculated to be 3.10 eV, which is lower than that of T20. The reduction in the bandgap is believed to be caused by the high electron concentration induced by the oxygen vacancy defects in the TiO_2 NCs.[24]

Table 6.4. *Details of the surface features, band gap and PL quantum yield (QY) of different mesoporous F-TiO_2 nanostructures.*

Sample code	*Shape of Self-grown TiO_2 NCs/ QDs (size)*	*Band gap (eV)*	*PL QY (%)*
T20	Arbitrary shape NCs (5.0 nm)	3.17	0.02
T60	Arbitrary shape NCs (8.4 nm)	3.17	0.07
T80	Arbitrary shape NCs (11.4 nm)	3.16	0.09
T20VR	Spherical QDs (4.2 nm)	3.10	5.76
T60VR	Spherical NPs (9.7 nm)	3.15	2.31
T80VR	Spherical NPs (12.8 nm)	3.14	2.73
T20VA	Arbitrary shape NCs	2.90	0.49
T20HR	Spherical QDs (4.5 nm)	3.15	0.21
Pure TiO_2 QDs	Spherical QDs (5.0 nm)	3.08	0.11

6.3.4.2. Photoluminescence Study

In order to confirm the nature of defects and their dependence on the annealing environment, PL study was carried out. **Fig. 6.13(a, b)** show the room temperature PL spectra of F-TiO_2 NCs/NFs grown at different molar concentration of HF and reaction duration, respectively under identical conditions of measurement. Due to the indirect band gap, no band edge emission was detected, and hence the possibility of free exciton recombination can be excluded. The observed broad visible PL band centered at ~560 nm is primarily related to self-trapped excitons and oxygen vacancy defects in TiO_2. PL intensity is found to be lowest for the sample prepared with the lowest HF concentration, and the intensity increases linearly with increasing HF concentration, as shown in the inset of **Fig. 6.13(a)**. PL intensity for 80 mM HF is about 4 times higher than that of 20 mM. Thus, the F-doping plays an important role in the PL emission efficiency of TiO_2

NCs. It is also observed that the PL intensity increases almost linearly with increasing the reaction duration, as shown in **Fig. 6.13(b)**.

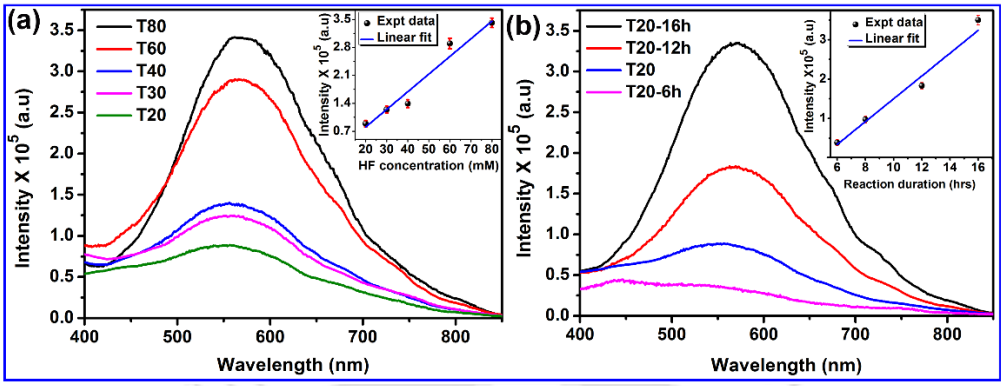

Fig. 6.13. A comparison of the room temperature PL spectra (excited with 355 nm laser) of F-TiO_2 NFs prepared with (a) different HF concentrations and (b) reaction durations. Inset in each case shows the variation of the PL intensity as a function of HF molar concentration as well as the reaction duration, along with the linear fit.

After the post-growth annealing of F-TiO_2 NFs, a major enhancement in the PL intensity is observed. After the RTA (furnace) annealing in air ambient, the PL intensity is increased by ~12 (7) times, without any major change in the nature of the spectrum. However, after RTA/furnace annealing under vacuum, a dramatic enhancement in PL intensity, blue shift (~90 nm) and lower FWHM are observed for the PL peak. As compared to the as-grown sample, vacuum RTA treated sample (T20VR) shows more than two orders of magnitude enhancement (~163 times) in the PL intensity, as shown in **Fig. 6.14(a)**. Though all the vacuum RTA treated samples exhibit highly intense PL spectra, the T20VR sample shows the maximum enhancement in the PL intensity, and it is about 5 times higher than that of T80VR. For the RTA treatment under vacuum, the size, as well as the density of TiO_2 QDs and concentration of defects, seem to be optimum in T20VR such that highest number of bound excitons are being generated and recombined, making it the most emission efficient. For a better understanding of the origin of broad PL emission and giant enhancement in PL intensity after vacuum RTA, each spectrum is deconvoluted with multiple Gaussian peaks. The broad PL spectrum of the as-grown sample (e.g., T20) could be fitted properly with three Gaussian peaks centered at 540 nm (peak 1), 625 nm (peak 2), and 745 nm (peak 3), as shown in **Fig. 6.14(c)**.[25] Peak 1 is ascribed to a single electron trapped oxygen vacancy (F^+ center), peak 2 is related to the intrinsic defects in TiO_2, may be induced by fluorine doping[26], and peak 3 is likely to be due to the hydroxyl (OH^-) species, as confirmed by the XPS analysis.

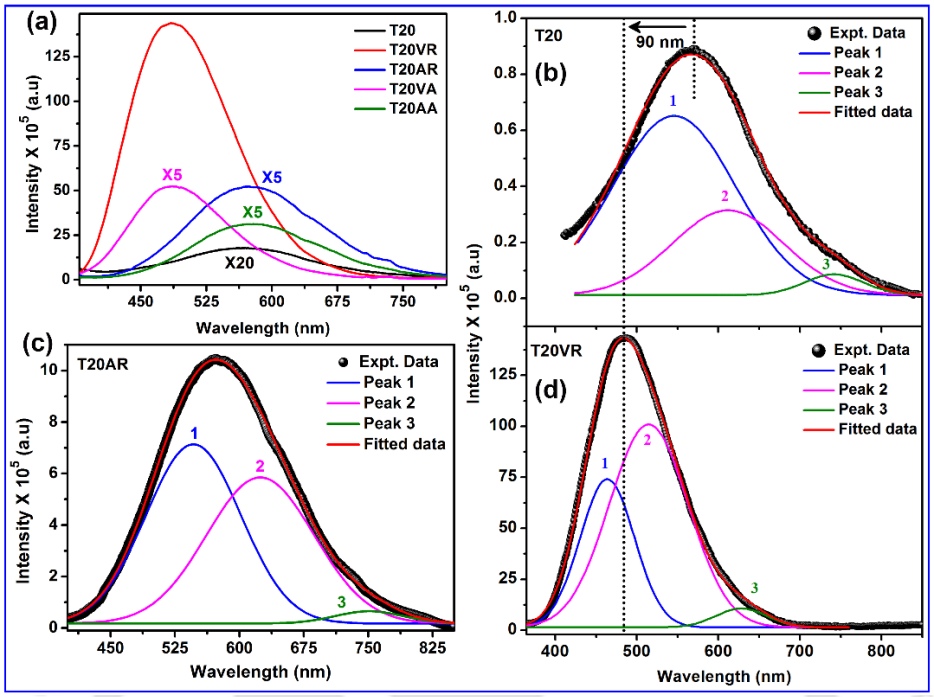

Fig. 6.14. (a) A comparison of PL spectra of T20 before and after annealing in different ambient. The spectra with low intensity are shown on a magnified scale, as indicated by the magnification factor in each case. (b) The Gaussian fit of the PL spectrum of T20AR. (c, d) The Gaussian fit of PL spectrum for T20 and T20VR, respectively. The vertical dotted lines are shown to visualize the blue shift of peak after vacuum RTA.

After RTA/furnace annealing in air, the PL spectrum can be again deconvoluted with three peaks with the similar peak identities of the as-grown sample, (see **Fig. 6.14(c)**). After vacuum RTA/furnace annealing, the PL spectra is blueshifted, and it can be deconvoluted with three Gaussian peaks (see **Fig. 6.14(d)**). Two major peaks observed at 464 nm (Peak 1) and 515 nm (peak 2) are related to oxygen vacancy-related trap states. Peak 3 at centered 627 nm is related to the defects due to F-doping in TiO_2 (see **Fig. 6.14(d)** for T20VR). Peak 1 corresponds to the emission from Ti^{3+} defect states, which is located just below the conduction band edge. Peak 2 corresponding to the 515 nm emission is due to deep trap states, which is associated with F^+ center, fully consistent with the ESR analysis. For the vacuum annealed (furnace) sample, the deconvoluted peak positions are similar to the sample T20VR. In T20VR, the integrated intensity corresponding to the F^+ centre is calculated to be nearly double of the Ti^{3+} center, supported by the XPS and ESR analyses. Thus, it can be concluded that the RTA treatment under vacuum is superior to the normal furnace annealing for the optimization of radiative centers and high PL yield from TiO_2 NPs/QDs.

For the T20VR, the room temperature PL QY is measured to be 5.76%, which is significantly higher than that reported in the literature for TiO_2 nanostructures (QY~ 0.05-3.5% or lower)[7, 27, 28] The details of PL QY of our as-grown and annealed samples are tabulated in **Table 6.4**. **Fig. 6.15(a)** shows the change in QY as a function of RTA duration for T20VR, while **Fig. 6.15(b)** shows the variation of PL QY for the samples grown with various HF concentrations (10 mM - 80 mM) after 3 min vacuum RTA treatment.

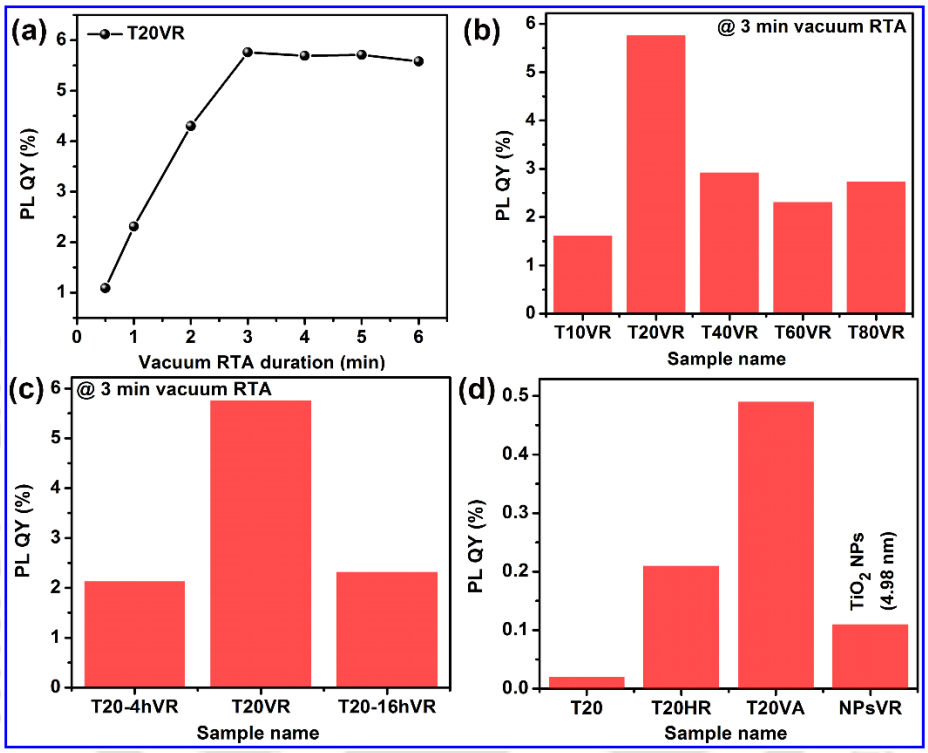

Fig. 6.15. (a) PL QY as a function of duration of vacuum RTA for T20. (b) Comparison of the PL QY of vacuum RTA treated samples synthesized at various HF concentrations (10 mM-80 mM). (c) A comparison of the PL QY of the samples synthesized for various reaction durations (4 h-16 h) followed by 3 min vacuum RTA. (d) A comparison of PL QY of T20, T20HR, T20VA and pure TiO_2 QDs after vacuum RTA.

It is clear that the sample T20VR grown with 20 mM HF and subsequently vacuum RTA treated for 3 min is found to be optimized for the maximum PL QY. A variation in PL QY with the change in the hydrothermal reaction duration is shown in **Fig. 6.15(c)** and T20VR with 8 h reaction is observed to be optimum. RTA treatment under hydrogen ambient was also performed to compare the QY, and it shows a PL QY 0.21% (see **Fig. 6.15(d)**). To understand the specific role of F^- doping and the interface of TiO_2 NCs/NFs in the PL enhancement, we prepared additional sets of bare TiO_2 QDs in purely anatase phase by sol-gel method and subsequently vacuum RTA treated for 3 min at the same temperature. The sizes were chosen to closely match

with that of the F-TiO_2 QDs prepared by the hydrothermal method. However, this sample (with average size ~5.0 nm) shows much lower PL intensity with the QY of ~0.11%, as shown in **Fig. 6.15(d)**. Thus, the F-doping of the QDs and its attachment to the mesoporous F-TiO_2 NF are crucial to achieve the high PL QY from the mesoporous TiO_2 NCs/NFs. We found that among the large number of samples studied here, T20VR is the best-optimized sample offering highest PL QY.

Here, biologically inert mesoporous F-TiO_2 nanostructures (500-800 nm) without using any kind of capping ligand or imposing toxicity into the material have been demonstrated for the first time. For further evidence of the intense fluorescence and high quantum yield of self-grown TiO_2 QDs on TiO_2 NFs, fluorescence confocal microscopy imaging was carried out. **Fig. 6.16** shows the laser confocal microscopy fluorescence image of T20VR. The bright spots clearly demonstrate strong PL from the F-TiO_2 QDs/NFs. Since the QDs are uniformly decorated on the TiO_2 NFs, the PL image shows an NF like pattern in the magnified image shown in the inset of **Fig. 6.16**, due to the limitation of spatial resolution (120 nm) of this technique. The absence of a continuously bright/illuminated region in the image further signifies that the self-grown F-TiO_2 QDs are the primary emitting species in the TiO_2 NF. This result clearly shows its suitability for bioimaging application as a fluorescent marker.

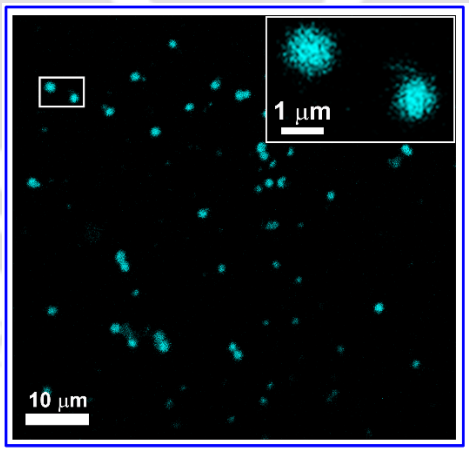

Fig. 6.16. Laser confocal fluorescence microscope image of the TiO_2 NFs decorated with self-grown TiO_2 QDs in T20VR showing strong whitish fluorescence. Inset shows a magnified view of the fluorescent TiO_2 NFs.

6.3.4.3. Time-Resolved Photoluminescence Study

In order to investigate the lifetime and recombination dynamics of photogenerated charge carriers, time-resolved photoluminescence (TRPL) measurement was performed on T20VA and

T20VR with 375 nm laser excitation, and the PL emission was monitored at 520 nm. **Fig. 6.17** shows the TRPL decay profiles of T20VR and T20VA samples.

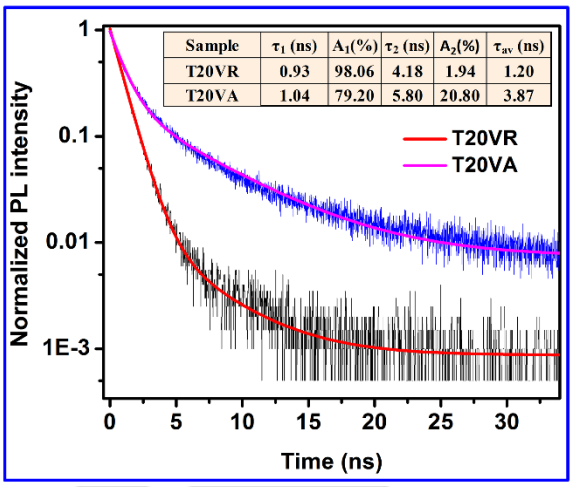

Fig. 6.17. Comparison of the TRPL spectra of T20VR and T20VA monitored at 520 nm (emission) with 375 nm excitation. The black and blue lines represent the experimental data, while the solid red and magenta lines represent the corresponding bi-exponential fit. The inset shows the details of lifetime (τ) components for different samples.

It's evident that the PL decay rate is much faster in vacuum RTA sample as compared to that of furnace annealed (vacuum) sample. The details of the time constants (τ) of T20VR and T20VA are shown in the inset of **Fig. 6.17**. The bi-exponential fit suggests that mainly two distinct states contribute to the TRPL spectra in each sample, which is fully consistent with the steady-state PL spectra. It can be noted that the average lifetime (τ_{av}) is considerably higher for the vacuum annealing case as compared to that of vacuum RTA. The τ_{av} of T20VR is found to be 1.20 ns, which is more than three times faster than that of T20VA sample (τ_{av}=3.87 ns). The lower τ_{av} in T20VR implies faster recombination and thus higher PL QY. The decay is monitored at 520 nm (emission wavelength), which is assigned to the F^+ (single electron trapped O_V) center. The contribution of F^+ center in the steady-state PL spectra is observed to be ~65% for T20VR and ~32.2% for T20VA. This may be due to the much higher defect density in T20VR than in T20VA, fully consistent with the ESR and PL analyses.

6.3.4.4. Temperature Dependent PL Study

In order to investigate the contribution of radiative and non-radiative processes, we have studied the temperature dependence of the PL spectra for T20VR, recorded in the range 80–300 K. It is observed that the intensity of the peak systematically increases with decreasing temperature, as

shown in **Fig. 6.18(a)**. The room temperature PL spectrum of T20VR has a broad peak centered at ~485 nm (2.56 eV). With the decreasing temperature, it shows a slight redshift, as indicated by the vertical line (dashed) in **Fig. 6.18(a)**. The vertical line indicates the peak position at ~300 K. The inset of **Fig. 6.18(a)** shows the variation of the integrated PL intensity as a function of temperature. At low temperature, the integrated PL intensity is much higher than that at room temperature. This is due to the activation of non-radiative recombination channels at room temperature, which results in the decrease in PL intensity.

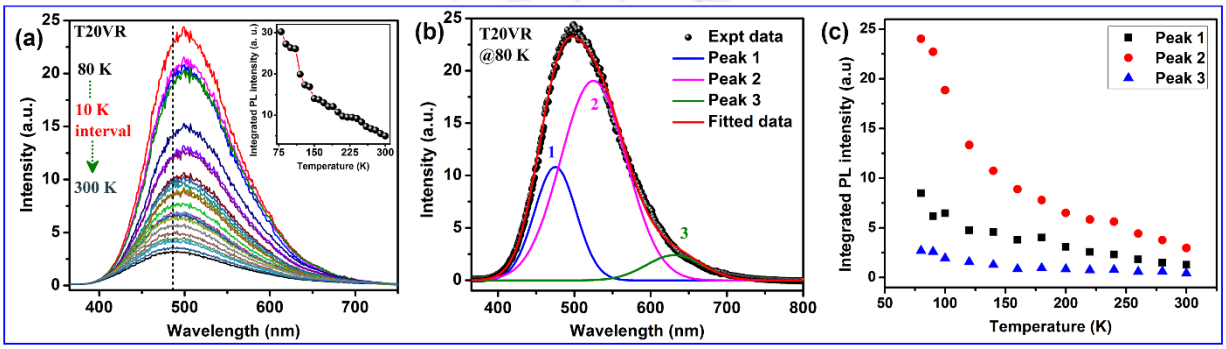

Fig. 6.18. (a) Low-temperature PL spectra of T20VR at different temperatures. The vertical dotted line is shown to indicate the red-shift of the center of PL peak with lowering temperature. The inset shows a change in integrated PL intensity as a function of temperature. (b) Gaussian fit of PL spectrum of T20VR at 80 K. (c) Change in integrated PL intensity of each peak as a function of temperature for sample of T20VR.

The temperature dependence of peak position and intensity could be ascribed to the interplay of radiative recombination of strongly localized excitons confined in the TiO_2 QDs and the temperature dependent non-radiative exchange interactions[29] between electrons and holes via the defect states due to the nonstoichiometric oxygen vacancies. At any temperature T, the effective decay constant (τ_{eff}) of the carrier is related to the radiative (τ_R) and non-radiative (τ_{NR}) lifetime of the transition from excited state to ground state by the equation:

$$\frac{1}{\tau_{eff}(T)} = \frac{1}{\tau_R(T)} + \frac{1}{\tau_{NR}(T)} \qquad (6.1)$$

Here, the variation of integrated intensity with temperature can be divided into two regimes: τ_R domination over τ_{NR} for 80 K < T < 150 K and τ_{NR} dominated for T > 150 K. The transition from τ_{NR} domination to τ_R domination results in the red-shift of the peak center from ~2.56 eV to ~2.48 eV.

Additionally, the PL efficiency η_R can be calculated following the expression:

$$\eta_R = \frac{1}{1 + \frac{\tau_R}{\tau_{NR}}} \qquad (6.2)$$

It suggests that for $\tau_R \ll \tau_{NR}$, η_R approaches to unity, which indicates the maximum possible efficiency of emission. On the other hand, if $\tau_R \gg \tau_{NR}$, $\eta_R \to 0$ (very small) the light emission is very inefficient in this case.[30] Thus, the necessary condition for the efficient luminescence is to have much shorter radiative lifetime than the non-radiative lifetime. In the case of vacuum RTA treatment, the radiative lifetime (τ_R) is indeed found to be much shorter than the case of furnace annealing case. This results in very high PL QY (5.76%) for the vacuum RTA sample (T20VR). Further, due to the size dependency of TiO_2 NCs on the radiative decay time, smaller size NCs tend to have a much shorter lifetime. Hence, TiO_2 QDs with smaller size exhibits faster decay time and consequently the higher PL emission efficiency. **Fig. 6.18(b)** shows the Gaussian fit of the PL spectrum of T20VR (centered at ~500 nm) recorded at 80 K. The peak consists of three peaks (peak 1, 2, 3) and change in relative intensity of each peak with temperature results in the shift of the mean position of the peak at a lower temperature. **Fig. 6.18(c)** shows a plot of the relative intensities (integrated) of each peak with temperature. Note that the change in PL intensity is more dramatic for peak 2 (F^+ center) and observed to be ~2.8 times higher than that of peak 1. At lower temperature, more carrier relaxation from conduction band or Ti^{3+} state to F^+ state is expected, since the capture cross-section of F^+ center is considered to be higher than that of Ti^{3+} state, which also may result in the ultra-high efficiency of visible PL emission associated with the F^+ center. Note that individual peak position remains nearly unchanged with temperature, the relative intensities change substantially. Prior to the radiative recombination, the carriers may expend some of their energy in a multi-step recombination process rather than a direct recombination to satisfy the energy and momentum conservation laws.[30, 31]

6.3.5. Mechanism of PL Enhancement in F-TiO_2 QDs/NFs

After the RTA treatment, we observe the shape evolution of the arbitrary shaped self-grown TiO_2 NCs (on the TiO_2 NFs) to spherical TiO_2 QDs. For T20, vacuum RTA creates TiO_2 NPs/QDs with a mean size of ~4.2 nm. Monticone et al.[10] studied the quantum size effect of anatase TiO_2 NPs and found the exciton Bohr radius (r_{Bohr}) as 0.8 nm. They also showed that the weak confinement regime extends up to the size ~ $8r_{Bohr}$, i.e., 6.4 nm even though no shift was observed in the band gap (or in the optical absorption edge) beyond the size $2r$ = 2 nm[32]. In the

present case, ESR and XPS studies confirm the highest concentration of O_V defects in sample T20VR. As the size of the NPs are very small with the high surface area and are uniformly distributed over the surface of TiO_2 NFs, the surface defects associated with oxygen vacancies are extremely high on the surface of TiO_2 NPs, which are almost covering the TiO_2 NF surface. Thus, the generation of surface defects by the vacuum RTA is mostly confined to the self-grown NPs and due to high electron density, the bandgap of TiO_2 NPs is slightly reduced. Consequently, the conduction band in the NP side tends to go little down as compared to that of NF side and the population density in the Ti^{3+} and F^+ centers is extremely high. Self-grown highly defective TiO_2 NPs/QDs falling in weak confinement regime exhibits a 0.07 eV reduction in the effective band gap compared to its as-grown counterpart sample. Thus, instead of an enlarged band gap in TiO_2 QDs[33], a straddling type (type-I) band arrangement at the interface of NF and QD can be expected, as illustrated in **Fig. 6.19**.

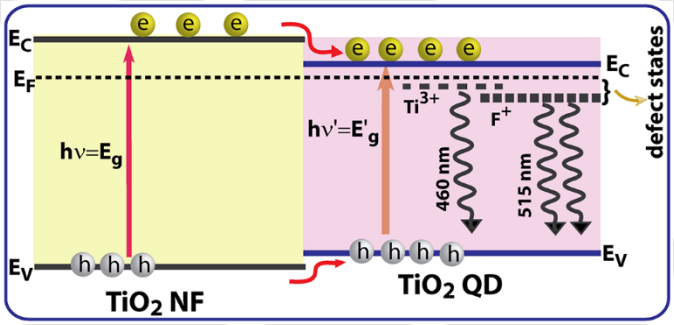

Fig. 6.19. Schematic illustration of the band structure of F-TiO_2 NPs/NFs homojunction and the PL mechanism mediated by different defects (Ti^{3+}, F^+ centers) in T20VR.

With the laser excitation (355 nm), both the NF and NPs are excited, and the straddling type band arrangement at the interface facilitates the migration of photoexcited charge carriers from the TiO_2 NF to NP side thermodynamically. Additionally, the electron capture cross-section, as well as defect density of F^+ center, may be higher and a relaxation of the electron from conduction band as well as Ti^{3+} tarp states to F^+ center may be favorable in T20VR. As the decay time constant, τ, is inversely proportional to the defect density, the average excited state carrier lifetime associated with the transition from F^+ state is much faster in T20VR than that in T20VA. This leads to very high intensity PL emission (QY≈5.76%) from the T20VR with 65% emission from F^+ center and 32% emission from the Ti^{3+} center. In the other samples (vacuum RTA treated), the size of NPs is much larger than that in T20VR, which leads to the lower surface coverage of NF and thus lower defect density in the NPs. Consequently, the PL QY is lower for

bigger NPs case, which happens for higher HF concentration as well as higher reaction durations. Note that despite the presence of TiO_2 NPs/QDs, the band edge PL intensity was negligibly low in all the samples due to the indirect gap nature of the TiO_2. However, the defect-mediated high yield and stable PL from the F-TiO_2 NPs is extremely important for its bioimaging and drug delivery applications.

6.4. Summary and Conclusions

1. Arbitrary shaped self-grown TiO_2 NCs decorated on mesoporous F-TiO_2 NFs are successfully synthesized by a single step hydrothermal method.
2. Shape evolution of arbitrary shaped TiO_2 NCs into spherical QDs with optimum defect density is demonstrated by vacuum RTA technique.
3. F-TiO_2 QDs/F-TiO_2 NFs shows a strong PL emission (~163 fold) associated with shallow and deep traps, and a record high PL QY of ~5.76% is achieved for indirect gap TiO_2 at room temperature.
4. Temperature-dependent PL and time-resolved PL studies reveal the ultrafast radiative carrier lifetime on the F-TiO_2 QDs, resulting in highly efficient PL emission.
5. PL enhancement is explained by the formation of a type-I junction at the F-TiO_2 QD/TiO_2 NF interface and efficient charge transfer from F-TiO_2 NF to F-TiO_2 QD side.

References

1. M. Liu, L. Piao, W. Lu, S. Ju, L. Zhao, C. Zhou, H. Li and W. Wang, *Nanoscale*, 2010, **2**, 1115-1117.
2. J. Miao and B. Liu, *RSC Adv.*, 2013, **3**, 1222-1226.
3. Q. Xiang, J. Yu and M. Jaroniec, *ChemComm*, 2011, **47**, 4532-4534.
4. H. G. Yang, G. Liu, S. Z. Qiao, C. H. Sun, Y. G. Jin, S. C. Smith, J. Zou, H. M. Cheng and G. Q. Lu, *J. Am. Chem. Soc.*, 2009, **131**, 4078-4083.
5. E. J. W. Crossland, N. Noel, V. Sivaram, T. Leijtens, J. A. Alexander-Webber and H. J. Snaith, *Nature*, 2013, **495**, 215.
6. S. Ding, F. Huang, X. Mou, J. Wu and X. Lu, *J. Mater. Chem.*, 2011, **21**, 4888-4892.
7. O. Cleary, F. Purcell-Milton, A. Vandekerckhove and Y. K. Gun'ko, *Adv. Opt. Mater*, 2017, **5**, 1601000-n/a.
8. A. Folger, P. Ebbinghaus, A. Erbe and C. Scheu, *ACS Appl. Mater. Interfaces*, 2017, **9**, 13471-13479.
9. Z. Su, Y. Zhu, Z. Wu, X. Peng, C. Gao, K. Xi, C. Lai and R. V. Kumar, *RSC Adv.*, 2014, **4**, 22989-22994.
10. S. Monticone, R. Tufeu, A. V. Kanaev, E. Scolan and C. Sanchez, *Appl. Surf. Sci.*, 2000, **162-163**, 565-570.

11. J. K. Bording and J. Taftø, *Phys. Rev. B*, 2000, **62**, 8098-8103.
12. N. T. K. Thanh, N. Maclean and S. Mahiddine, *Chem. Rev.*, 2014, **114**, 7610-7630.
13. H. G. Yang, C. H. Sun, S. Z. Qiao, J. Zou, G. Liu, S. C. Smith, H. M. Cheng and G. Q. Lu, *Nature*, 2008, **453**, 638.
14. B. Santara, P. K. Giri, K. Imakita and M. Fujii, *Nanoscale*, 2013, **5**, 5476.
15. D. Bersani, P. P. Lottici and X.-Z. Ding, *Appl. Phys. Lett.*, 1998, **72**, 73-75.
16. J. C. Yu, Yu, Ho, Jiang and Zhang, *Chem. Mater.*, 2002, **14**, 3808-3816.
17. M. N. Iliev, V. G. Hadjiev and A. P. Litvinchuk, *Vib. Spectrosc*, 2013, **64**, 148-152.
18. K. K. Paul, R. Ghosh and P. K. Giri, *Nanotechnology*, 2016, **27**, 315703.
19. B. Santara, P. K. Giri, K. Imakita and M. Fujii, *J. Phys. D: Appl. Phys.*, 2014, **47**, 215302.
20. G. Li, L. Li, J. Boerio-Goates and B. F. Woodfield, *J. Am. Chem. Soc.*, 2005, **127**, 8659-8666.
21. G. Wu, J. Wang, D. F. Thomas and A. Chen, *Langmuir*, 2008, **24**, 3503-3509.
22. T. E. Jones, T. C. R. Rocha, A. Knop-Gericke, C. Stampfl, R. Schlogl and S. Piccinin, *Phys. Chem. Chem. Phys.*, 2015, **17**, 9288-9312.
23. B. Santara, P. K. Giri, K. Imakita and M. Fujii, *J. Phys. Chem. C*, 2013, **117**, 23402.
24. C. Dette, M. A. Pérez-Osorio, C. S. Kley, P. Punke, C. E. Patrick, P. Jacobson, F. Giustino, S. J. Jung and K. Kern, *Nano Lett.*, 2014, **14**, 6533-6538.
25. D. Li, H. Haneda, S. Hishita and N. Ohashi, *Chem. Mater.*, 2005, **17**, 2596-2602.
26. D. Li, H. Haneda, S. Hishita and N. Ohashi, *Chem. Mater.*, 2005, **17**, 2596-2602.
27. A. S. Susha, A. A. Lutich, C. Liu, H. Xu, R. Zhang, Y. Zhong, K. S. Wong, S. Yang and A. L. Rogach, *Nanoscale*, 2013, **5**, 1465-1469.
28. Y. Li, C. Song, Y. Wang, Y. Wei, Y. Wei and Y. Hu, *Luminescence*, 2007, **22**, 540-545.
29. R. Ghosh, P. K. Giri, K. Imakita and M. Fujii, *Nanotechnology*, 2014, **25**, 045703.
30. J. Zhang, X. Chen, Y. Shen, Y. Li, Z. Hu and J. Chu, *Phys. Chem. Chem. Phys.*, 2011, **13**, 13096-13105.
31. A. V. Emeline, V. K. Ryabchuk and N. Serpone, *J. Phys. Chem. B*, 2005, **109**, 18515-18521.
32. N. Satoh, T. Nakashima, K. Kamikura and K. Yamamoto, *Nat. Nanotechnol.*, 2008, **3**, 106.
33. L. Pan, J.-J. Zou, S. Wang, Z.-F. Huang, A. Yu, L. Wang and X. Zhang, *ChemComm*, 2013, **49**, 6593-6595.

Chapter 7

In-Situ Chemical Vapor Deposition Growth of Monolayer MoS_2 on TiO_2 Nanostructures: Trion Inhibited Strong Excitonic Emission and Broadband Giant Photoresponsivity

In this chapter, we demonstrate an in-situ chemical vapor deposition growth of MoS_2@TiO_2 core-shell heterojunction with single layer MoS_2 (1L-MoS_2) as shell and 3D TiO_2 nanoflower (NF) as core for multifunctional optoelectronic applications. We explore a powerful approach to switch the trions in 1L-MoS_2 into neutral excitons through the migration of excess electrons in MoS_2@TiO_2 heterostructure and demonstrate a giant photoluminescence (PL) enhancement in the 1L-MoS_2 shell. The charge transfer induced p-doping effect in 1L-MoS_2 is verified from the oxygen plasma treatment. Further, the 1L-MoS_2@TiO_2 p-n heterojunction is demonstrated as a high performance broadband photodetector owing to it favorable band alignment and high absorption in the broad spectral range. The heterojunction photodetector exhibits a record high responsivity and detectivity with fast photoresponse, which is attributed to the fast photogenerated carrier transport at the p-n heterojunction due to the large built-in electric field.

7.1. Introduction

Despite several advantageous properties, monolayer MoS_2 (1L-MoS_2) possesses intrinsic n-type doping usually because of the substrate effect, resulting into a low photoluminescence (PL) quantum yield, which is reported to be quenched/enhanced further after the n-type/p-type doping.[1] Several techniques have been reported to manipulate the various exciton populations in the 1L-MoS_2 to enhance its PL intensity efficiently, such as chemical doping,[2] defect engineering by plasma irradiation,[3] negative gate-bias tuning,[1, 4] and plasmonic enhancement[5]. Usually, incorporation of single layer/few layer TMDs with other suitable semiconductors (ZnO, TiO_2) develops a type-II heterojunction facilitating efficient charge separation at the interface and quenching of its PL emission. These special type-II heterostructures (HSs) are extremely advantageous for photodetectors, photovoltaics and photocatalysis applications.[6, 7] Kim et al.[8] demonstrated an enhancement in the room temperature (RT) PL of the chemical vapor deposition (CVD) grown 1L-MoS_2 simply by transferring it on a ZnO film. In this case, the heterojunction

of 1L-MoS_2 with ZnO thin film was developed by post growth typical wet transfer method, which may lead to poor interfacial coupling and high charge transfer resistance at the interface. This in turn may hamper the transfer process of excess electrons leading to an incomplete conversion of trion to neutral exciton, which results into low overall PL efficiency.

1L-MoS_2 possesses high absorption coefficient with a broad spectral window (visible to near-infrared) and thus regarded as the advantageous candidate for the fabrication of efficient photodetector. A favorable approach is to fabricate a hybrid structure of 1L-MoS_2 and TiO_2 for the broadband photodetection. Yusin et al.[9] demonstrated that the performance of MoS_2 photodetector improves by depositing TiO_2 by atomic layer deposition process in between exfoliated MoS_2 and the electrode which leads to a significant enhancement in the photoresponsivity and response speed. Recently, Dhyani et. al.[10] demonstrated a simple and scalable fabrication process of Si/MoS_2 p-n heterojunction photodetector. However, the device showed a broadband responsivity with a peak value of only 8.75 A W^{-1} and thus needs further investigation to improve the overall performance.

In this chapter, we demonstrate a simple physical route to grow 1L-MoS_2 shell over a hydrothermally prepared TiO_2 core by an in-situ CVD technique for the multifunctional optoelectronic applications. The enormous PL enhancement from the 1L-MoS_2 after the formation of heterojunction is explained in the light of p-doping effect in MoS_2, which is further verified by oxygen plasma treatment. We also demonstrate a high performance broadband and fast photodetection by the 1L-MoS_2@TiO_2 p-n heterojunction photodetector. The heterojunction photodetector exhibits record high responsivity as well as the detectivity over the UV-visible-NIR region of the solar spectrum.

7.2. Experimental Details

7.2.1. Sample Preparation

7.2.1.1. Preparation of 3D TiO_2 NFs on Titanium Foil

3D TiO_2 NFs were synthesized by a typical hydrothermal process, as described in **Chapter 6, Section 2.2.1.1**., with a fixed HF molar concentration (20 mM) and reaction duration (8 h). 3D nature of the TiO_2 nanostructure was confirmed by the FESEM imaging.

7.2.1.2. Direct Growth of Single Layer MoS_2 on Various Substrates by CVD Method

Single layer MoS_2 was grown on various substrates (Ti, sapphire and TiO_2 NFs) by a one-step CVD process. MoO_3 (99.5%, Sigma-Aldrich) and sulfur powder (99.95%, Sigma-Aldrich) were used as source materials for the in-situ CVD growth of MoS_2 in a quartz tube (diameter ~2 inches) based two-zone muffle furnace. 200 mg sulfur and 15 mg MoO_3 powder were separately loaded in two ceramic boats. Different substrates were mounted over the boat containing MoO_3 powder facing downward and these were supported from the bottom by a quartz mask, placed in zone 2, while S source was placed upstream in zone 1 (see **Fig. 7.1(a)**). The design of the quartz mask is based on report by Mohapatra et al.[11] and it is crucial for the growth of monolayer MoS_2 only in the masked region.

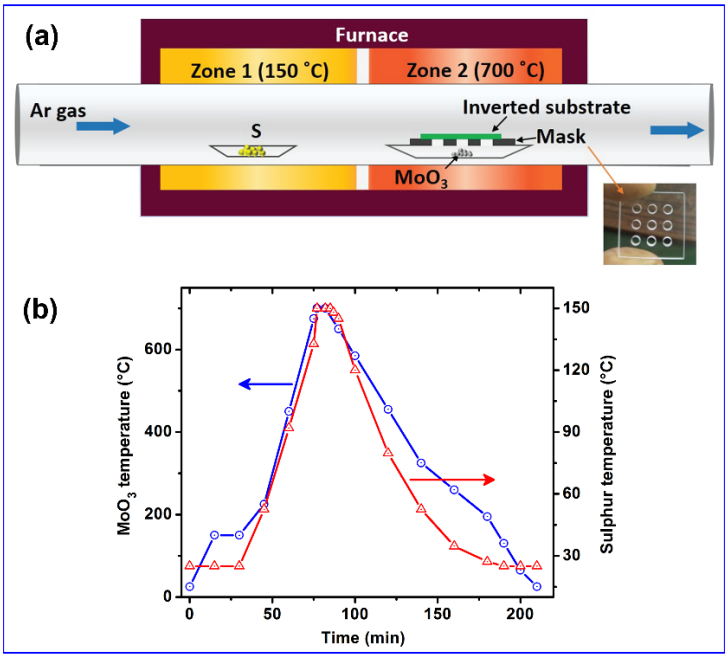

Fig. 7.1. (a) Chemical vapor deposition (CVD) setup for the fabrication of monolayer MoS_2 on various substrates (Ti, sapphire and TiO_2 NFs). (b) Variation of temperature as a function of time at the MoO_3 source and sulfur source positions during the CVD growth.

For both the zones, the temperatures were separately monitored, and to control the sulfur vapor pressure at the growth temperature of MoS_2 the temperature ramping profiles of the two zones were coordinated. High purity (99.999%) argon (Ar) was used as the carrier gas throughout the experiment. Prior to the growth, a high flow rate of Ar (~300 sccm) was used to purge inside the quartz tube for 30 min to remove the surface adsorbed impurities. Afterwards, MoO_3 and S source temperature was raised to 700 °C and 150 °C at a rate of 15 °C/min and 3.5 °C/min,

respectively, and maintained for 5 min for the growth at an Ar flow rate of 10 sccm. The furnace was then allowed to cool down at 6.5 °C/min till the temperature goes down to room temperature. The details of the time-temperature profile of MoO_3 and sulfur precursors over the entire experiment are shown in **Fig. 7.1(b)**. Interestingly, the single layer MoS_2 film was grown on each substrate only on the portions of the substrate covered by the quartz mask, while the directly exposed regions are observed to be deposited with few-layer and multi-layer MoS_2. We obtained a large area monolayer MoS_2 growth on all the substrates and the samples grown on Ti foil, sapphire and TiO_2 NFs are named as 1L-MoS_2@Ti, 1L-MoS_2@Sapphire and 1L-MoS_2@TiO_2, respectively.

7.2.2. Device Fabrication for Photocurrent Measurements

Here, as-grown TiO_2 NFs, 1L-MoS_2@Ti and 1L-MoS_2@TiO_2 core-shell heterojunctions are basically fabricated on the metallic Ti foil. Thus, the conducting Ti substrate acts as the bottom electrode for the photoresponse measurements. For the front contact, 100 nm thick Al layer was deposited through a mask on the top of the sample by thermal evaporation method (base pressure of ~1×10^{-6} torr). The device was illuminated from the top and the atomically thin 1L-MoS_2 shell ensures the photoexcitation from both the MoS_2 shell and TiO_2 core. Photocurrent response was measured using a microprobe station (ECOPIA EPS−500) connected to a source measure unit (Keithely 2400, USA) for current−voltage characteristics and a 250 W Xenon lamp (Newport, USA) was used to illuminate the device. The excitation wavelength was chosen using a monochromator (Oriel Instruments, USA) attached to the lamp. The light pulse was generated using a standard chopper (SRS, USA) and current response was digitized using the LabTracer software.

7.2.3. Characterization Techniques

Crystal phase, number of layers, defects and nature of doping present in the as-synthesized MoS_2 as well as its core-shell HSs with TiO_2 NFs were studied by a high resolution micro-Raman spectrometer (LabRam HR800, Jobin Yvon) with an Ar ion laser excitation of wavelength (λ_{ex}) 488 nm. The PL measurement was also carried out using the above instrument with the same laser excitation (λ_{ex} ~488 nm) from the same spot used for the Raman measurement. In both the measurements, the laser light was focused on the sample with a 100× objective lens to a spot size ~1 μm and the signal was collected by a CCD in a back scattering geometry sent through a

multimode fiber grating of 1800 grooves mm^{-1}. The laser power at the source was kept at ~1.5 mW, which discards the possibility of laser heating induced damage of the sample. The PL measurement at low temperature (83-300 K) was performed using the same system on a liquid nitrogen cooled low-temperature Linkam stage with 1 °C temperature accuracy and stability. The details of the FESEM, TEM, EDS and UV-Vis diffuse reflectance spectroscopy (DRS) measurement were described in **Chapter 2, Section 2.2.3**. For the confirmation of defect and doping effect on the PL enhancement, some samples were treated with mild oxygen plasma exposure (10 W) for different time durations using a miniature plasma cleaner (Harrick plasma, PDC-32G).

7.3. Results and Discussion

7.3.1. Morphology and Composition Studies

To investigate the typical surface morphology and microstructural properties of the as-prepared TiO_2 NFs and its heterojunction with single layer MoS_2, each sample was analyzed with FESEM and FETEM and the results are shown in **Fig. 7.2**. The FESEM image of pristine TiO_2 nanostructure grown on Ti foil reveals a 3D symmetric flower like structures with size ~1 μm, as shown in **Fig. 7.2(a)**.[12] FETEM image of a single and symmetric TiO_2 NF is shown in **Fig. 7.2(b)**. **Fig. 7.2(c)** shows the HRTEM lattice fringe pattern of pristine TiO_2. The lattice spacing of 0.36 nm corresponds to (101) planes of anatase TiO_2. The growth of single crystal tetragonal anatase phase TiO_2 is confirmed from the selected area electron diffraction (SAED) pattern shown as inset of **Fig. 7.2(c)**. **Fig. 7.2(d, e)** show the TEM images of TiO_2 NF covered with a 1L-MoS_2 film confirming the formation of core-shell HS. The SAED pattern of 1L-MoS_2@TiO_2 HS shows the diffraction spots of both the crystalline MoS_2 and TiO_2 layers confirming the co-existence of the two components, as shown in inset of **Fig. 7.2(e)**. From the HRTEM lattice fringe pattern shown in **Fig. 7.2(f)**, it is observed that the MoS_2 shell thickness is ~0.60 nm, which corresponds to the monolayer MoS_2. The IFFT image (see inset of **Fig. 7.2(f)**) confirms the (101) crystallographic plane of TiO_2 NF at the interface of 1L-MoS_2 shell. To further confirm the formation of core-shell HS, STEM mapping analysis of the MoS_2@TiO_2 HS was performed. **Fig. 7.2(g)** shows a dark-field STEM image of 1L-MoS_2@TiO_2 HS on which elemental mapping analysis was performed. The EDS elemental mapping reveals that the core of the HS is composed of Ti and O elements confirming the uniform growth of TiO_2, as shown in **Fig. 7.2(h,**

i). **Fig. 7.2(j, k)** exhibit the elemental mapping for Mo and S, respectively, which shows a uniform growth of MoS_2 film over the 3D TiO_2 platform.

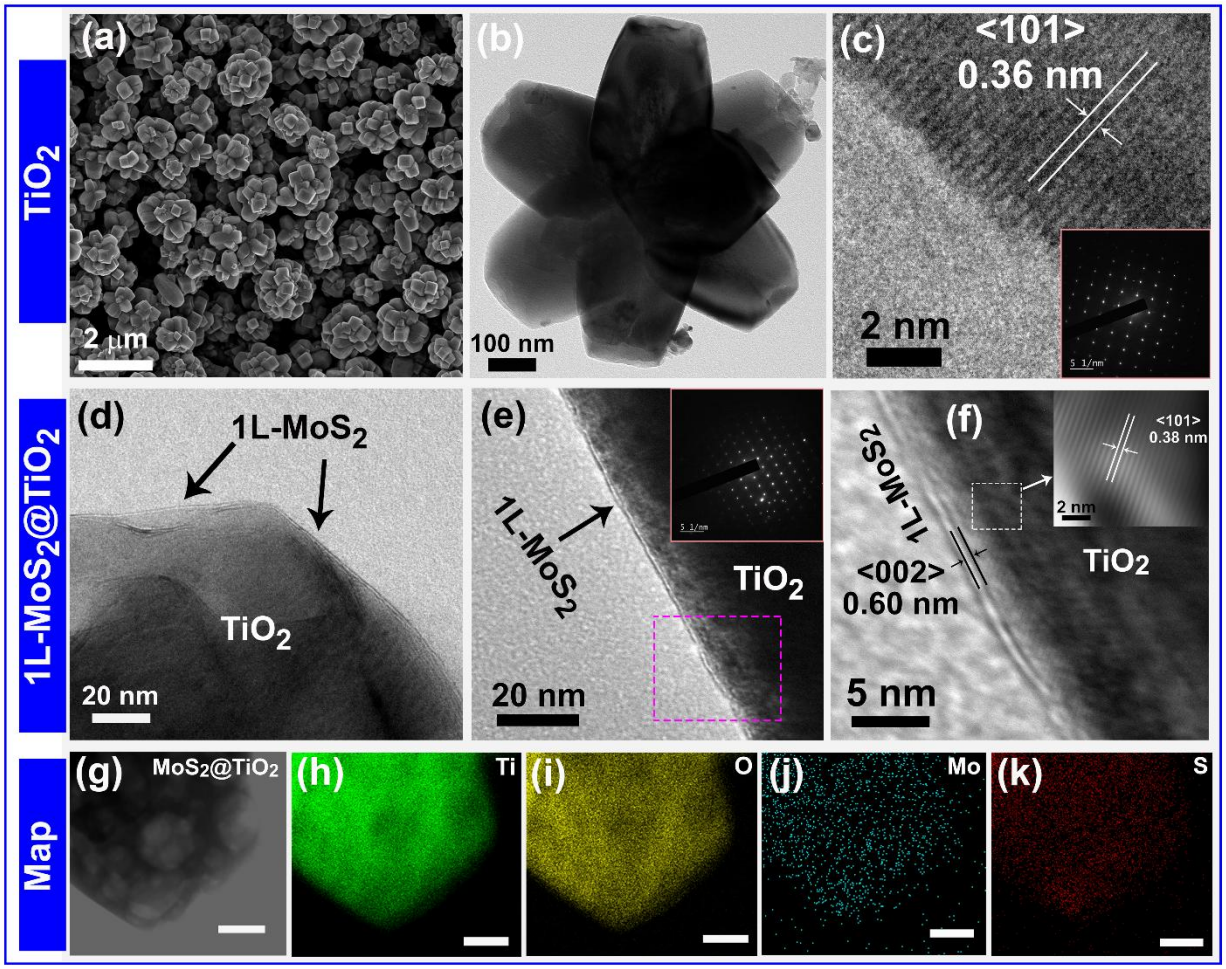

Fig. 7.2. (a) FESEM image of TiO_2 NFs, (b) TEM image of a TiO_2 NF, (c) HRTEM image of TiO_2 petal. Inset shows the SAED pattern of TiO_2 crystal. (d) TEM image of MoS_2@TiO_2 showing a monolayer shell over the TiO_2 core. (e) A magnified view of 1L-MoS_2@TiO_2. Inset shows the SAED pattern exhibiting MoS_2 and TiO_2 crystal lattices. (f) HRTEM lattice fringe pattern at the selected region of (e) showing the monolayer MoS_2 shell of thickness ~0.6 nm at the interface with TiO_2. Inset shows the IFFT image of TiO_2 at the interface with (101) plane. (g) STEM image of 1L-MoS_2@TiO_2 HS and (h-k) elemental mapping results of the core-shell HS showing Ti, O, Mo and S, respectively. The scale bar in each case is 100 nm.

7.3.2. Structural Analysis

7.3.2.1. Raman Analysis

In order to confirm the large area growth of monolayer MoS_2 on the different substrates, i.e., Ti, sapphire and TiO_2 NFs, position dependent Raman studies were carried out, as shown in **Figs. 7.3** and **7.4** and **Table 7.1**. **Fig. 7.3(a)** shows a digital photograph of MoS_2 layer grown on Ti substrate (MoS_2@Ti) by CVD technique. The exposed area of substrate to the MoO_3/S source is

found to be circular dark spot, while the covered portions are light greenish in color. **Fig. 7.3(b)** shows an optical microscope image of MoS_2@Ti at the marked region shown in **Fig. 7.3(a)**.

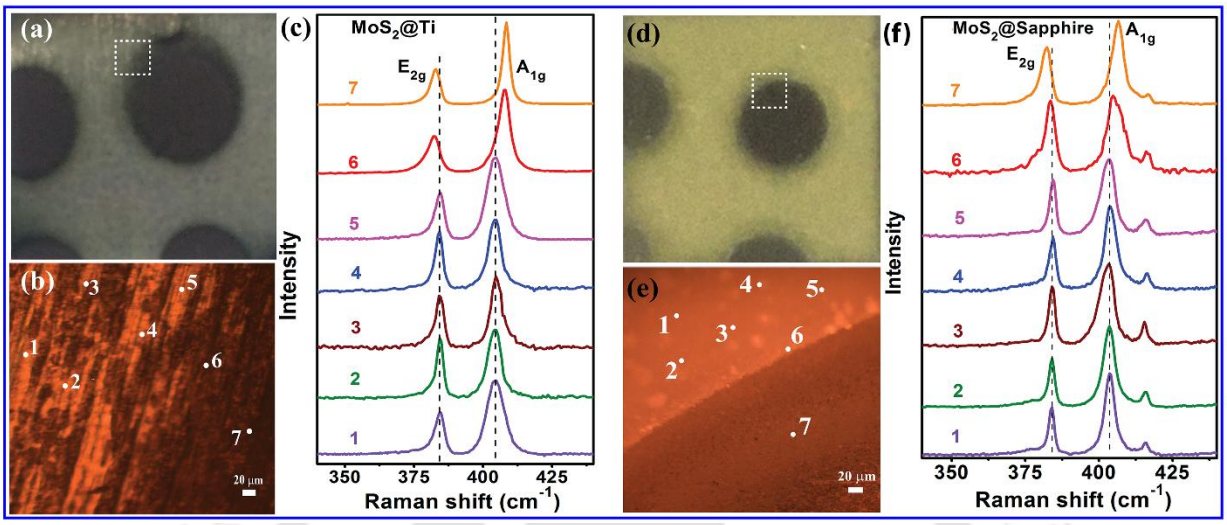

Fig. 7.3. (a, d) Digital photographs of MoS_2 layer grown on Ti foil (MoS_2@Ti) and sapphire (MoS_2@Sapphire), respectively by CVD technique. (b, e) The optical microscope images of MoS_2@Ti and MoS_2@Sapphire, respectively at the marked region of (a, d). (c, f) The Raman spectra of MoS_2@Ti and MoS_2@Sapphire, respectively recorded at different positions shown in (b, e). The vertical dashed line is drawn to indicate the shift of the Raman peak for spot 7 due to the formation of multilayer MoS_2.

For the detailed understanding about the structure and layer number of MoS_2, we have recorded Raman spectra at various positions of the sample, as shown in **Fig. 7.3(b)** and **Fig. 7.3(c)**. It is evident from the Raman data that outside the dark circular region, monolayer MoS_2 is formed while the dark region contains higher number of layers, as tabulated in **Table 7.1**. The CVD growth of MoS_2 on sapphire substrate was also investigated for a better comparison of the MoS_2 growth on other substrates. Similar to the Ti substrate, sapphire also shows dark circular regions in the exposed region and light greenish layer in the masked/covered region (see **Fig. 7.3(d)**). The recorded Raman spectra at different locations (see **Fig. 7.3(e)**) confirm the growth of monolayer MoS_2 outside the dark circular region, while it is multilayer MoS_2 at the dark region, as shown in **Fig. 7.3(f)** and **Table 7.1**. Similar growth of MoS_2 layers is also observed for the TiO_2 NFs substrate. **Fig. 7.4(a)** shows the digital photograph of CVD grown MoS_2@TiO_2. The exposed area of substrate appears as circular dark spot, while the covered portions are light greenish in color.

Table 7.1: *The position of E_{2g} and A_{1g} Raman peaks, their separation and corresponding layer number for MoS_2@Ti, MoS_2@Sapphire and MoS_2@TiO_2 at different positions.*

Spot no.	E_{2g} (cm^{-1})			A_{1g} (cm^{-1})			Δk (cm^{-1})			No. of layers
	MoS_2 @Ti	MoS_2@ Sapphire	MoS_2@ TiO_2	MoS_2 @Ti	MoS_2@ Sapphire	MoS_2@ TiO_2	MoS_2 @Ti	MoS_2@ Sapphire	MoS_2@ TiO_2	
1	384.3	384.2	384.4	404.3	403.6	404.9	20	19.4	20.5	1L
2	384.4	384.2	384.4	404.4	403.3	405	20	19.1	20.6	
3	384.4	384.3	384.4	404.6	403.6	405.1	20.2	19.3	20.7	
4	384.3	384.3	384.4	404.4	403.8	405.2	20.1	19.5	20.8	
5	384.3	384.4	384.4	404.4	403.5	405	20.1	19.1	20.6	
6	382.3	383.3	383.9	407.7	404.9	405.7	25.4	21.6	21.8	2L/ML
7	382.5	382.2	382.6	408.2	406.6	407.3	25.7	24.4	24.7	

Position dependent Raman spectra were recorded at different spots shown in the optical microscope image (see **Fig. 7.4(b)**) and are plotted in **Fig. 7.4(c)**. To discern clearly the layer number of MoS_2, the shaded region of Raman spectra in **Fig. 7.4(c)** is shown in **Fig. 7.4(d)** in the range 340-440 cm^{-1}. Similar to the above case, outside the dark circular region, monolayer MoS_2 (1L) is formed, while the dark region contains higher number of layers (ML), as tabulated in **Table 7.1**.

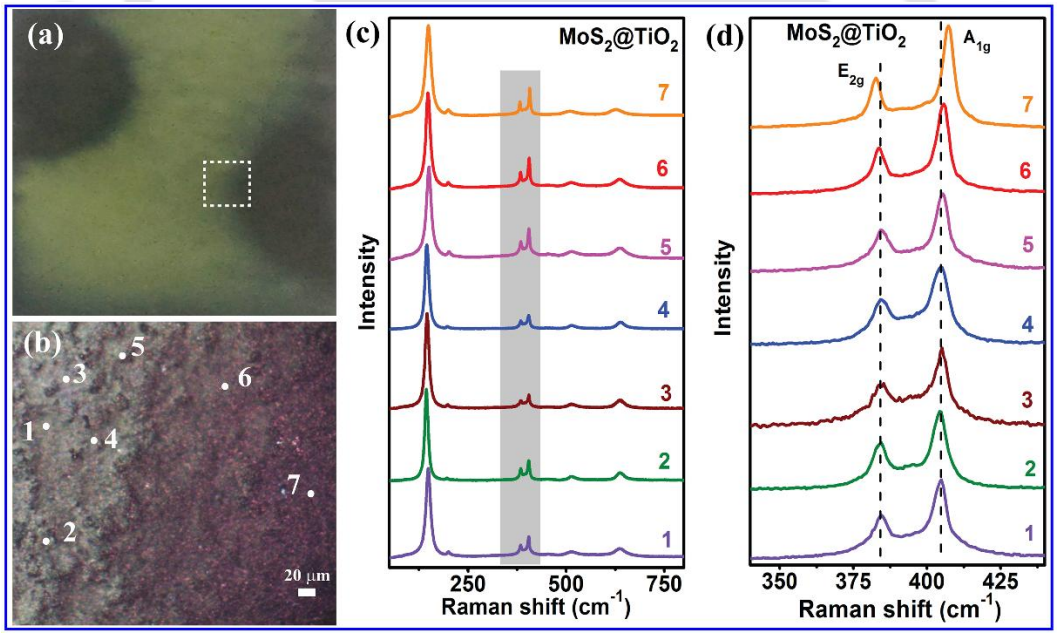

Fig. 7.4. (a) Digital photograph of MoS_2 layer grown on TiO_2 NFs (MoS_2@TiO_2) by CVD technique. (b) The optical microscope image of MoS_2@TiO_2 at the marked region of (a). (c) The Raman spectra of MoS_2@TiO_2 recorded at different positions shown in (b). (d) Raman spectra of shaded region shown in (c), in the range 340-440 cm^{-1}.

Fig. 7.5(a) shows a comparison of the Raman spectra of as-grown TiO_2 NFs, 1L-MoS_2@Ti and 1L-MoS_2@TiO_2 core-shell HS. Purely anatase TiO_2 NF exhibits six first-order Raman active

modes, namely, $E_g(1)$, $E_g(2)$, $B_{1g}(1)$, $A_{1g}/B_{1g}(2)$ and $E_g(3)$ identified at 145, 198, 397, 517 and 640 cm^{-1}, respectively. As observed in both the 1L-MoS$_2$@Ti and 1L-MoS$_2$@TiO$_2$ HS, two major first-order Raman modes, E_{2g} and A_{1g} are detected at ~384.4 and ~404.4 cm^{-1}, respectively, which correspond to 1L-MoS$_2$ based on the separation of these modes.[13]

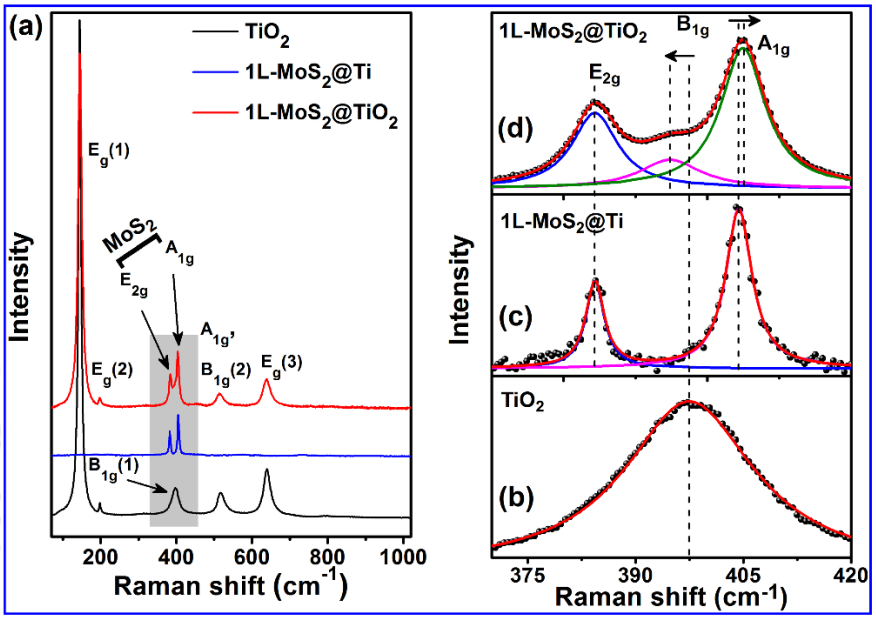

Fig. 7.5. (a) A comparison of Raman spectra of TiO$_2$ NFs, 1L-MoS$_2$@Ti and 1L-MoS$_2$@TiO$_2$ HS. The peaks in the shaded region correspond to 1L-MoS$_2$ layer and $B_{1g}(1)$ mode of anatase TiO$_2$. (b-d) Lorentzian fitting of Raman spectra in the range of 370-420 cm^{-1} for the different samples. The vertical dashed lines are used to indicate the shift in Raman modes after the formation of HS.

The successful growth of single-layer MoS$_2$ film on Ti as well as 3D TiO$_2$ NFs is verified by calculating the frequency difference (Δk) between the E_{2g} and A_{1g} modes of MoS$_2$. The Δk is found to be 19.9 cm^{-1} for 1L-MoS$_2$@Ti and 20.6 cm^{-1} for 1L-MoS$_2$@TiO$_2$ HS. The Raman spectrum of the HS comprises of the characteristic peaks of both MoS$_2$ and TiO$_2$ without any major changes in the line shape, confirming their co-existence in the HS sample. As the Raman peak $B_{1g}(1)$ of TiO$_2$ lies between the two characteristic Raman peaks of MoS$_2$, each Raman spectrum in the range of 370-420 cm^{-1} is fitted with Lorentzian line shapes in order to identify the individual peak contribution. **Fig. 7.5(b, c)** show the Lorentz fittings of Raman spectra for pristine TiO$_2$ and 1L-MoS$_2$@Ti, respectively. The deconvolution of the Raman spectrum for 1L-MoS$_2$@TiO$_2$ in the selected range confirms the presence of E_{2g} and A_{1g} modes of 1L-MoS$_2$ and $B_{1g}(1)$ mode of TiO$_2$, as shown in **Fig. 7.5(d)**. It may be noted that the $B_{1g}(1)$ mode of HS shows a red shift by 2.7 cm^{-1} with respect to that of pristine TiO$_2$ NFs, which may be due to the release

of compressive strain during the formation of HS, consistent with the XPS analysis (discussed in **Section 7.3.2.3**). The A_{1g} peak of 1L-MoS_2 in the HS is observed to be blue shifted by ~0.7 cm^{-1} with a higher FWHM as compared to that of the 1L-MoS_2@Ti, while no shift is detected in E_{2g} peak. It was reported that a blue shift and broadening of A_{1g} peak of MoS_2 originates from the change of electron-phonon interactions caused by p-type doping in the MoS_2 lattice.[14, 15] The p-type doping in the 1L-MoS_2@TiO_2 HS may occur due to the decrease in the electron density in MoS_2 resulting from the transfer of electrons from the MoS_2 to the TiO_2 layer.[3, 8] The unaltered E_{2g} peak implies that the crystal structure of MoS_2 is not affected by its growth on TiO_2 NFs. Note that due to the competing effects of lattice strain and doping on the Raman shift, the overall blue shift of the A_{1g} peak is relatively small.

7.3.2.2. Growth Mechanism of Monolayer MoS_2 over Various Substrates

Monolayer MoS_2 was grown on different substrates (sapphire, Ti foil and TiO_2 NFs), particularly on the region covered by quartz mask, following the report by Mohapatra et al.[11] As the substrates are placed just above the MoO_3 source and Sulfur is placed at a certain distance away from the substrates, the vapor pressure of MoO_3 is found to be much higher than that of Sulfur at the substrate position during the early phase of the growth, as shown in **Fig. 7.6(a, b)**.

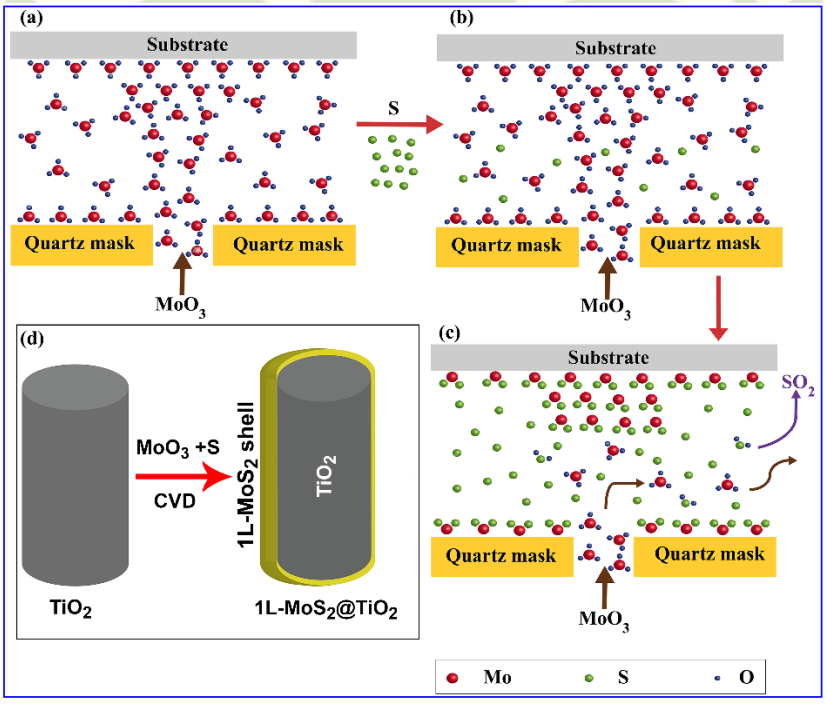

Fig. 7.6. (a-c) Schematic illustration showing the different steps of the growth process of monolayer MoS_2 film by CVD process. (d) Schematic diagram of a 1L-MoS_2@TiO_2 core-shell nanostructure grown by the CVD process.

However, the vapor pressure is much lower at the quartz masked region of the substrate. At this point, the masked region (covered with quartz) is exposed to low vapor pressure of MoO_3 and the MoO_3 molecules get attached to the surface of the substrate (see **Fig. 7.6(a)**). With the increase of temperature, there is also an increase in the vapor pressure of Sulfur, which arrives later near the MoO_3 molecules and it reacts with the MoO_3 molecules on the surface of the substrate, leading to the formation of monolayer MoS_2 ($2MoO_3 + 7S \rightarrow 2MoS_2 + 3SO_2$). No further reaction takes place as the vapor pressure of Sulfur is way higher than that of MoO_3 and therefore it flushes out the remaining MoO_3 molecules from the cavity, as shown in **Fig. 7.6(c)**. On the other hand, high vapor pressure exists at the exposed region of the substrate, which results in the growth of multilayer MoS_2 (see **Fig. 7.6(c)**). In case of TiO_2 NFs as substrate, due to the random orientation of the nanoflower petals, all the facets of the petals are exposed to the MoO_3 and S vapor pressure. **Fig. 7.6(d)** shows a schematic illustration of the pristine TiO_2 NF and 1L-MoS_2@TiO_2 core-shell HS with monolayer shell of MoS_2 over its surface.

7.3.2.3. XPS Analysis

In order to investigate the chemical valence state, presence of defects and impurities associated with the as-grown system, core level XPS spectra of different samples are studied and the results are shown in **Fig. 7.7**.

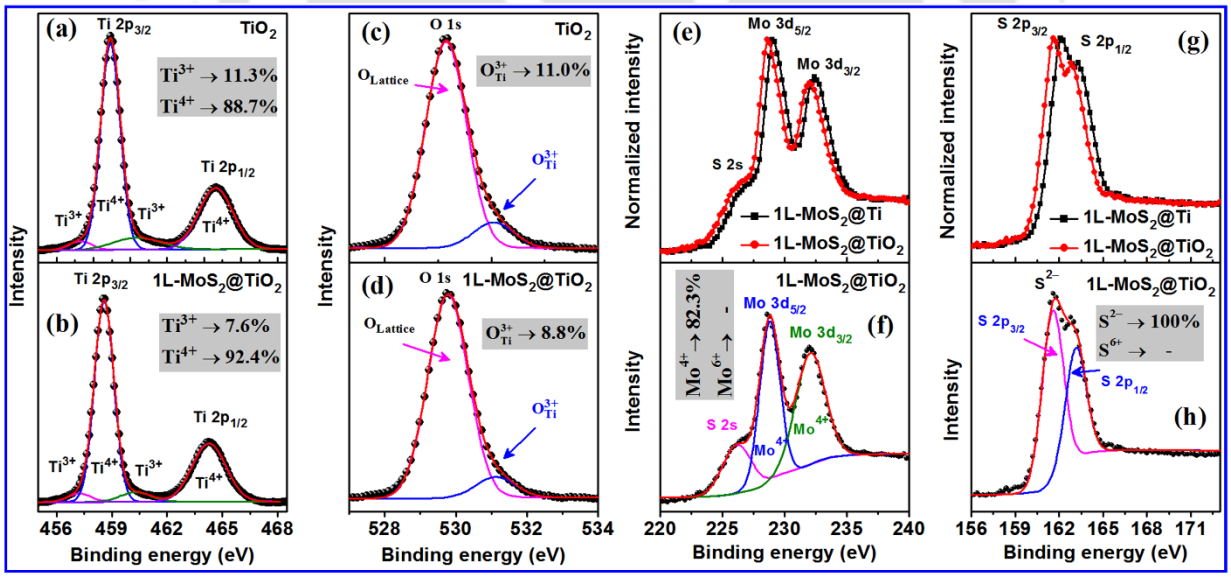

Fig. 7.7. Core level XPS spectra: (a, b) Ti 2p and (c, d) O 1s for as-grown TiO_2 and 1L-MoS_2@TiO_2 HS, respectively. (e) A comparison of Mo 3d core level XPS spectra (normalized) for 1L-MoS_2@Ti and 1L-MoS_2@TiO_2 HS, while (f) shows corresponding Gaussian deconvolution for 1L-MoS_2@TiO_2. (g) A comparison of S 2p core level XPS spectra (normalized) for 1L-MoS_2@Ti and 1L-MoS_2@TiO_2 HS, while (h) shows corresponding Gaussian deconvolution for 1L-MoS_2@TiO_2.

Fig. 7.7 (a, b) exhibit the Ti 2p core level XPS spectra for pristine TiO_2 NFs and 1L-MoS_2@TiO_2 HS, respectively, while the corresponding O 1s XPS spectra are shown in **Fig. 7.7(c, d)**, respectively. It is observed that the concentration of O_V as well as the relative Ti^{3+}% are reduced after the formation of heterojunction, may be due to the defect filling and relaxation of TiO_2 lattice strain, which is consistent with the Raman analysis. Note that the pristine TiO_2 NFs sample behaves as n-type layer due to the presence of O_V defects, as revealed from the Hall effect measurement. A comparison of Mo 3d XPS spectra for 1L-MoS_2@Ti and 1L-MoS_2@TiO_2 is shown in **Fig. 7.7(e)**, while that for S 2p is depicted in **Fig. 7.7(g)**. In both the cases, Mo and S peaks in 1L-MoS_2 in the 1L-MoS_2@TiO_2 HS show a red shift (~0.6 eV) with respect to that of 1L-MoS_2@Ti, which may be due to the reduced electron density in 1L-MoS_2 after the heterojunction formation with TiO_2.[8] **Fig. 7.7(f)** shows the Gaussian deconvolution of Mo 3d core level XPS spectra of 1L-MoS_2@TiO_2 showing two strong peaks at ~228.8 eV (Mo $3d_{5/2}$) and ~232.0 eV (Mo $3d_{3/2}$), attributed to the 4+ valence state of Mo, and it confirms the formation of MoS_2. It may be noted that the 1L-MoS_2@Ti as well as the HS do not contain any Mo^{6+} valence state, which discards the possibility of oxidation of Mo. **Fig. 7.7(h)** shows a Gaussian deconvolution of S 2p XPS spectra corresponding to the 1L-MoS_2@TiO_2 HS with the peaks at ~161.7 eV (S $2p_{3/2}$) and ~163.0 eV (S $2p_{1/2}$) attributed to the divalent sulfide ions (S^{2-}).

7.3.3. Optical Analysis

7.3.3.1. UV-Vis Absorption Study

Fig. 7.8 shows a plot of the Kubelka-Munk (K-M) function F(R) for various samples corresponding to their UV-visible diffuse reflectance spectra (DRS). An enlarged view of the spectra of 1L-MoS_2@Ti and 1L-MoS_2@TiO_2 is shown as an inset of **Fig. 7.8** in the range of 550-690 nm, clearly revealing two absorption peaks of MoS_2 corresponding to the direct excitonic transitions A, B. Pristine TiO_2 shows a high band-edge absorption in the UV region, which goes down significantly at 400 nm and beyond. The as-grown 1L-MoS_2@Ti shows the excitonic A and B absorption bands at 655 nm and 608 nm, respectively, corresponding to the direct excitonic transitions from valence band spin-orbital coupling with the energy splitting.[16] Two additional minor absorption peaks are also observed at 427 nm (C peak) and 285 nm (D peak), associated with van Hove singularities of MoS_2.[17] Besides the strong absorption in the UV region by the TiO_2 core, each characteristic absorption peak of MoS_2 shell is also identified in the 1L-MoS_2@TiO_2 HS identical to that of 1L-MoS_2@Ti, as shown in the inset of **Fig. 7.8**.

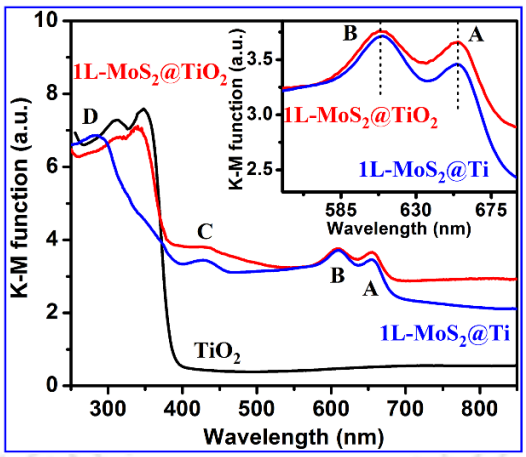

Fig. 7.8. Kubelka–Munk plot of as-grown TiO_2 NF, 1L-MoS_2@Ti and 1L-MoS_2@TiO_2 HS derived from the diffuse reflectance spectra. Inset shows the magnified view in the range 550-690 nm. A, B, C and D are the characteristic absorption bands of MoS_2. The vertical dotted lines indicate the negligible shift in the excitonic absorption band of 1L-MoS_2 after the HS formation.

Note that prior to the DRS measurement, we have removed the dark regions of the sample, which contains multi-layer MoS_2 in order to realize the absorption only from the monolayer MoS_2. This clarifies that a large area monolayer MoS_2 growth is achieved over both the substrates.

7.3.3.2. Photoluminescence Study

To determine the uniformity of the 1L-MoS_2 on different substrates, PL mapping (integrated over the 600 to 740 nm region) was performed at 300K (RT) under the ambient condition. **Fig. 7.9(a)** shows the PL intensity map for the 1L-MoS_2@Ti, which is almost uniform, signifying a uniform 1L-MoS_2 growth. Similarly, the PL intensity map of 1L-MoS_2@TiO_2 HS shown in **Fig. 7.9(b)** exhibits an overall uniformity throughout its surface, which confirms the formation of monolayer MoS_2 shell over the TiO_2 NFs. Interestingly, the integrated PL intensity of 1L-MoS_2@TiO_2 HS is observed to be much stronger than that of the 1L-MoS_2@Ti. **Fig. 7.9(c)** shows a comparison of the RT PL spectra of as-grown 1L-MoS_2@Ti, 1L-MoS_2@Sapphire and 1L-MoS_2@TiO_2 HS. The PL peak intensities corresponding to the as-grown 1L-MoS_2@Ti and 1L-MoS_2@TiO_2 are measured to be ~1.1k and ~243.0k (in arbitrary unit), respectively, as shown in **Fig. 7.9(c)**. Thus, the in-situ CVD grown 1L-MoS_2 shell over the 3D TiO_2 NFs facilitates a giant PL enhancement (~220 fold) as compared to that of 1L-MoS_2@Ti. From the comparison of the intensities of Raman modes of MoS_2 in 1L-MoS_2@Ti and 1L-MoS_2@TiO_2, it is observed that the larger area/volume of 1L-MoS_2 is exposed in case of 1L-MoS_2@TiO_2 than that in 1L-MoS_2@Ti due to the hierarchical/aligned 3D structure of TiO_2 NFs. Thus, the obtained PL

intensity as well as the enhancement factor in 1L-MoS_2@TiO_2 need to be normalized with respect to the respective Raman intensities. Taking the normalization factor into account, the PL enhancement in 1L-MoS_2@TiO_2 is ~83 fold as compared to that of 1L-MoS_2@Ti.

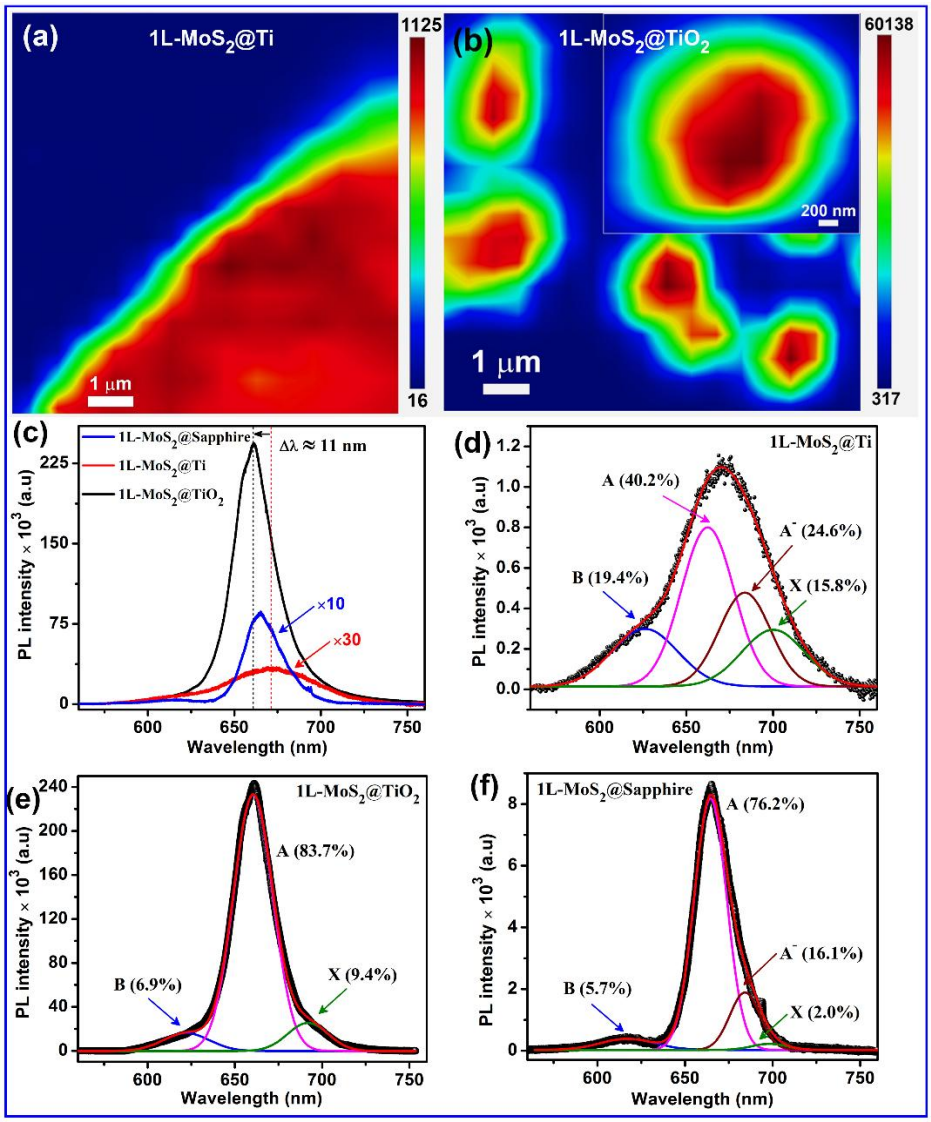

Fig. 7.9. (a, b) Total PL intensity (integrating from 600 to 740 nm) map of 1L-MoS_2@Ti and 1L-MoS_2@TiO_2 HS, respectively. Inset of (b) shows the enlarged view of a single 1L-MoS_2@TiO_2 NF. The laser beam (488 nm) is focused by the 100× objective lens. The HS sample was allowed to expose with only 25% of the incident radiation. (c) A comparison of room temperature PL spectra of 1L-MoS_2@Sapphire, 1L-MoS_2@Ti and 1L-MoS_2@TiO_2 HS. The Gaussian deconvolution of room temperature PL spectra of (d) 1L-MoS_2@Ti, (e) 1L-MoS_2@TiO_2 HS and (f) 1L-MoS_2@Sapphire. The relative percentage of each peak is shown in each case.

Additionally, the PL peak position is significantly blue shifted in the 1L-MoS_2@TiO_2 HS, by 11 nm (31 meV), as compared to that of 1L-MoS_2@Ti (see **Fig. 7.9(c)**). In order to investigate the origin of the representative PL emission, each spectrum is deconvoluted with multiple Gaussian

peaks, which are identified as the neutral exciton (A), negative trion (A^-), B exciton, and the bound exciton (X), as shown in **Fig. 7.9(d, e)**. The RT PL spectral weight of A exciton peak in the 1L-MoS_2@Ti is estimated to be 40.2%, which is enhanced enormously to 83.7% in the HS sample. Interestingly, the contribution of trion peak in 1L-MoS_2@Ti is observed to be 24.6%, which almost vanishes to zero in the HS. Spectral weight of the defect bound excitons (X) also diminishes from 15.8% to 9.4% in the HS, as shown in **Fig. 7.9(d, e)**. The A and B exciton peaks originate from the direct radiative transition from the minima of conduction band to the upper and lower-level valence band, respectively.[16] The A^- exciton peak arises due to the transition from the trions, formed after the bonding of an electron with a neutral exciton, caused by n-type doping in the CVD grown MoS_2 film[3] and the X exciton peak is attributed to the radiative recombination of bound excitons[18]. Note that the as-grown 1L-MoS_2 layer in 1L-MoS_2@Ti is intrinsically n-type doped (~25% of trion) may be due to the effect of Ti substrate, as reported by Zhong et al.[19] The PL spectrum of 1L-MoS_2@TiO_2 is also compared with the 1L-MoS_2@Sapphire. In case of 1L-MoS_2@TiO_2, we observe a blue shift by 5 nm (~14 meV) and the PL enhancement factor is ~30 fold in comparison to 1L-MoS_2@Sapphire. The Gaussian deconvolution of the PL spectrum shown in **Fig. 7.9(f)** reveals the higher spectral weight of neutral exciton (A) and lower spectral weight of negative trion (A^-) as well as bound exciton (X) as compared to that of 1L-MoS_2@Ti, which indicates the relatively lower defect density in 1L-MoS_2@Sapphire. The dramatic modification in the PL spectrum of 1L-MoS_2@TiO_2 HS with no trion peak can be attributed to the depletion of excess electrons from the single layer MoS_2 to the TiO_2 due to the special band alignment (type-II) at the interface.[8] Thus, the migration of excess electrons essentially induces p-doping effect in the 1L-MoS_2 shell, as evidenced from the blue shift in Raman and PL spectra, and it converts the trions to neutral excitons, leading to an enormous enhancement of PL intensity from 1L-MoS_2 shell in the HS.

The enormous enhancement in PL intensity in the core-shell HS is rather interesting since the heterojunction between MoS_2 and TiO_2 usually forms type-II heterojunction, which facilitates efficient charge transfer, resulting generally in PL quenching and it is regarded as efficient candidate for the photocatalysis.[20] However, in the present case, the charge transfer at the interface of MoS_2 and TiO_2 seems to occur mostly by the trions (excess electron bound to the neutral exciton) in intrinsically n-type doped 1L-MoS_2, while the neutral excitons are not separated. Thus, the charge transfer through the interface of the HS acts like typical p-doping

process by various chemical and physical treatments,[2] leading to a conversion of light-inefficient trions to light-efficient neutral excitons, which results in an enormous PL enhancement.[8, 21] The selective charge transfer from trion may be due to its much lower binding energy (~30 meV) as compared to that of neutral exciton (~600 meV), generated in the 1L-MoS_2 by the photo-excitation.[22] Thus, the p-doping of 1L-MoS_2 by the formation of heterojunction with TiO_2 leads to nearly complete conversion of negative trion into neutral exciton, facilitating the enormous PL enhancement.[3]

The giant PL enhancement in the HS cannot be fully accounted simply by the transfer of excess electrons from the 1L-MoS_2 to TiO_2, which promotes the neutral exciton recombination by suppressing the trion recombination.[1] It may partly be associated with the very high PL quantum efficiency of the excitons in the 1L-MoS_2 shell of the HS.[3] In order to investigate the role of radiative and nonradiative recombination rates in the RT PL spectra, we have recorded the PL spectra for both the 1L-MoS_2@Ti and 1L-MoS_2@TiO_2 HS at lower temperatures (83-300 K), and the results are shown in **Fig. 7.10(a, b)**, respectively. The excitation laser beam was focused on the sample with a 50× objective lens and the signal was collected through the same. Considering the very low thermally activated carrier trapping in MoS_2 at low temperatures, the PL intensity can be expressed as:[3]

$$I_{PL}(T) = \frac{I_0 \times K_{rad}(T)}{K_{rad}(T) + K_{nonrad}(T)} \qquad (7.1)$$

where I_0 is the maximum PL intensity at low temperature, $K_{rad}(T)$ and $K_{nonrad}(T)$ are the temperature dependent radiative and nonradiative recombination rates, respectively. Generally, trapping and relaxation of the photogenerated excitons at the defect states of a semiconductor are known to be associated with the nonradiative recombination rate K_{nonrad}.[16] With the increase of temperature, the PL intensity of a semiconductor reduces drastically, attributed to the thermally activated nonradiative recombination leading to the lower quantum efficiency. The PL intensity of the as-grown 1L-MoS_2@Ti is observed to be reduced to ~12% of its initial value with increasing the temperature from 83K to 300K, because of the switching of radiative to nonradiative recombination, as shown in **Fig. 7.10(a)**. It is noteworthy that the PL intensity of 1L-MoS_2@TiO_2 HS remains almost unaffected with the increase of temperature, as shown in **Fig. 7.10(b)**. The PL intensity decreases by only 0.42% of its initial value in the HS when temperature increases from 83K to 300K, see the inset of **Fig. 7.10(b)**. Based on the analysis of the PL spectra of 1L-MoS_2@TiO_2 HS recorded at various temperatures, it is found that the

K_{nonrad} is negligibly small in the HS even at RT and thus the above equation suggests that $I_{PL}(T) \approx I_0$, at all temperatures in the range 83-300K.[3] Thus, the PL emission of 1L-MoS_2 in the HS is mainly contributed by the radiative recombination of excitons, which is one of the major factors contributing to the giant PL enhancement.

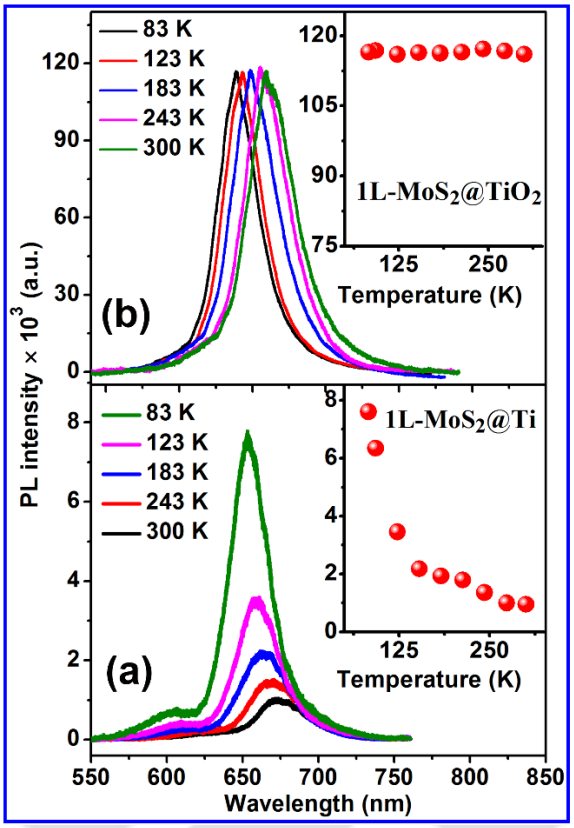

Fig. 7.10. (a, b) PL spectra recorded at different temperatures in the range of 83-300 K for 1L-MoS_2@Ti and 1L-MoS_2@TiO_2, respectively. Insets show the variation of PL intensity with the temperature.

7.3.4. Effect of Oxygen Plasma Treatment

7.3.4.1. Raman Study

S-vacancies in MoS_2 are reported to be introduced easily by controlled plasma treatment.[23] Here, we adopted a mild oxygen plasma treatment to different samples in order to elucidate the giant PL enhancement in the HS. **Fig. 7.11(a)** displays the Raman spectra for 1L-MoS_2@Ti after oxygen plasma exposure for various time durations. With the increasing plasma exposure time, A_{1g} mode is systematically blueshifted up to 1.5 cm^{-1} for 60s exposure time, while the E_{2g} mode is not influenced. Here, the stiffening of A_{1g} mode indicates an effective p-doping in the MoS_2 lattice introduced by oxygen bonding (Mo=O bonds) due to the plasma treatment, facilitating the

delocalization of electrons from Mo to chemically bonded O, which results in the conversion of negative trion to neutral exciton.[24, 25] Beyond 60s of plasma exposure, no further shift in A_{1g} mode was observed, though the Raman intensity of the MoS_2 characteristic peaks decreases monotonically, which confirms the physical damage of the film by overexposure of plasma. **Fig. 7.11(b)** shows the Raman spectra of 1L-MoS_2@TiO_2 HS before and after oxygen plasma exposure.

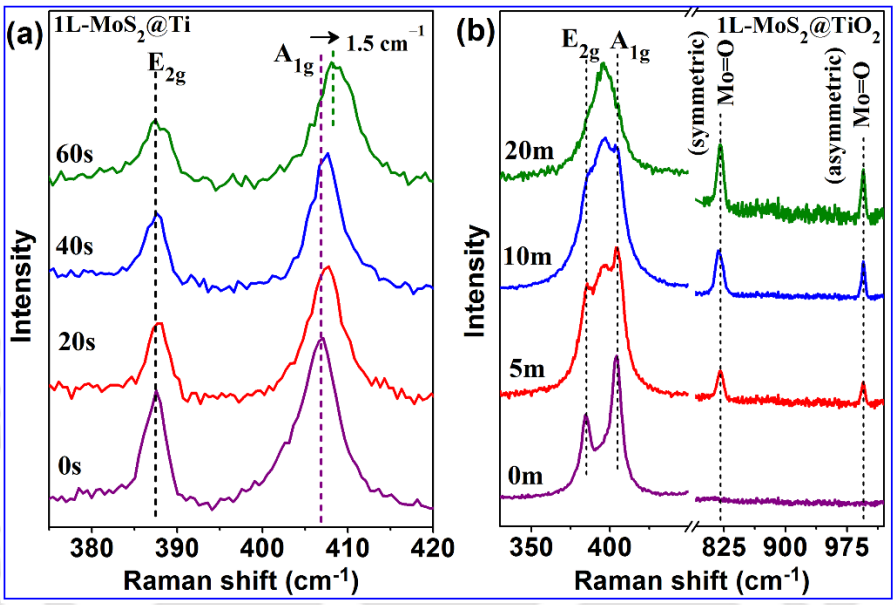

Fig. 7.11. (a) Raman spectra of 1L-MoS_2@Ti before and after oxygen plasma exposure for durations 20-60s. (b) Raman spectra of 1L-MoS_2@TiO_2 HS before and after oxygen plasma exposure. The dashed vertical lines indicate the shift in the Raman mode with plasma exposure.

Unlike the 1L-MoS_2@Ti, the 1L-MoS_2 shell on TiO_2 shows an exceptionally good stability under the plasma up to several minutes and then a gradual decrease in the intensity of both E_{2g} and A_{1g} modes. But, no detectable shift in the E_{2g} or A_{1g} Raman mode is observed after plasma exposure, which implies that the as-grown MoS_2 shell is optimally p-doped and oxygen plasma does not introduce any further doping in it. With the plasma exposure two additional Raman peaks are observed to be evolved at ~820 cm^{-1} and ~994 cm^{-1}, which may be assigned to the symmetric and asymmetric stretching vibration of terminal Mo=O bonds, respectively. Intensity of both the Raman peaks increases systematically with increasing the plasma exposure duration, confirming the formation of more Mo=O bonds, as shown in **Fig. 7.11(b)**.[26]

7.3.4.2. XPS Study

In order to investigate the change in MoS_2 structure after oxygen plasma treatment and its influence in the PL spectra, the core level XPS spectra of various oxygen plasma treated samples were recorded, as shown in **Fig. 7.12**. It is observed from **Fig. 7.12(a)** that the intensity of the O 1s XPS spectrum for as-grown 1L-MoS_2@Ti is very low, which becomes much stronger after 60s oxygen plasma exposure. The peak is centered at ~532 eV, and it is assigned to the adsorbed –OH group and oxygen molecules.[3] Thus, it is clear that the oxygen plasma induces higher oxygen content at the MoS_2 surface.

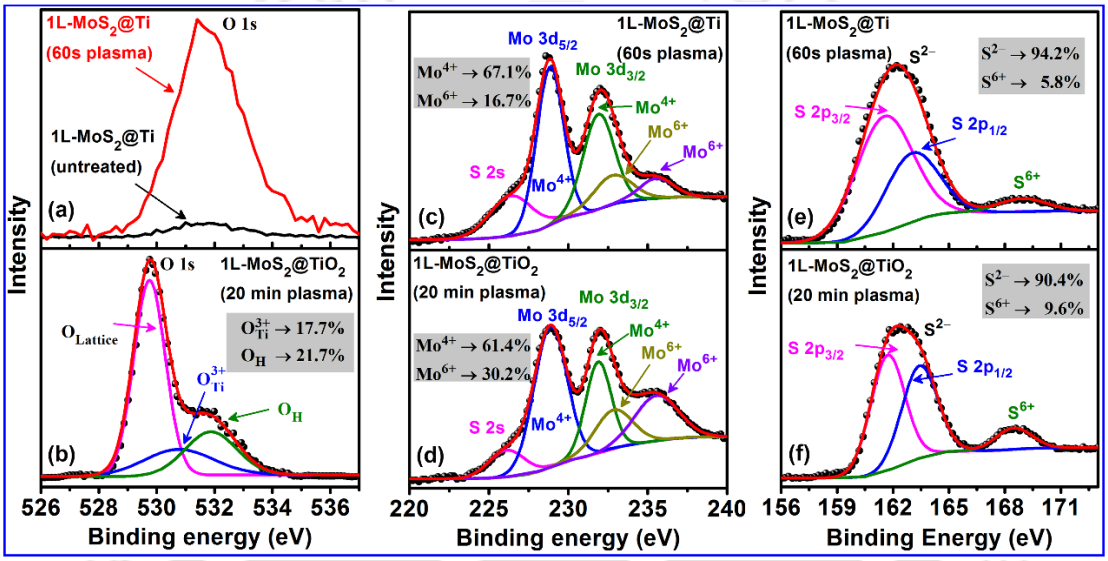

Fig. 7.12. (a) A comparison of core level O 1s XPS spectra of 1L-MoS_2@Ti: as-grown and after 60s oxygen plasma exposure. Core level XPS spectra: (b) O 1s, (d) Mo 3d and (f) S 2p, for 1L-MoS_2@TiO_2 HS after 20 min of oxygen plasma exposure. (c) Mo 3d, (e) S 2p, for 1L-MoS_2@Ti after 60s of plasma exposure. The symbols are experimental data and the solid curves are Gaussian fittings. The inset of each graph shows the relative percentage of various chemical valence states in the respective system.

Fig. 7.12(b) shows the O 1s XPS spectrum of 1L-MoS_2@TiO_2 after 20 min of oxygen plasma exposure. The Gaussian deconvolution of the spectrum reveals that the relative percentage of adsorbed –OH group/oxygen molecules reaches to 21.7% after the plasma exposure. It may also be noted that the longer duration plasma exposure creates more O_V defects in the TiO_2 lattice. **Fig. 7.12(c)** shows the Mo 3d core level XPS spectra of 1L-MoS_2@Ti after 60s of oxygen plasma exposure. Unlike the untreated MoS_2, 60s oxygen plasma treated MoS_2 shows two additional doublets located at ~232.7 and ~235.6 eV attributed to the Mo^{6+} valence state (with 16.7% spectral weight), which is also observed in the 1L-MoS_2@TiO_2 HS after 20 min of oxygen plasma exposure (with 30.2% spectral weight, see **Fig. 7.12(d)**). **Fig. 7.12(e)** and **Fig.**

7.12(f) exhibit the S 2p XPS spectra of 1L-MoS_2@Ti and 1L-MoS_2@TiO_2 HS after 60s and 20 min of oxygen plasma exposure, respectively, and the peaks at ~161.7 eV (S $2p_{3/2}$) and ~163.0 eV (S $2p_{1/2}$) are attributed to the divalent sulfide ions (S^{2-}). In addition to these peaks, each of the oxygen plasma treated samples shows a trace of oxidized S. In oxygen plasma environment, the S atom attached to the terminal Mo atom may be substituted by the O atom and forms terminal Mo=O bond and the delocalization of electrons from Mo to chemically bonded O results in the formation of Mo^{6+} valence state.[24, 27]

7.3.4.3. Photoluminescence and Photoresponse Study

In order to develop a deeper understanding about the PL enhancement in 1L-MoS_2@TiO_2, PL spectra were recorded for oxygen plasma treated 1L-MoS_2@Ti and 1L-MoS_2@TiO_2, and analyzed. The PL intensity of 1L-MoS_2@Ti increases systematically with increasing plasma exposure time and attains the maximum intensity (~8 times of as-grown 1L-MoS_2@Ti) at 60s, beyond which it gradually decreases, as shown in **Fig. 7.13(a)** and its inset. A gradual blue shift is also observed in the PL peak with increasing the plasma exposure time.

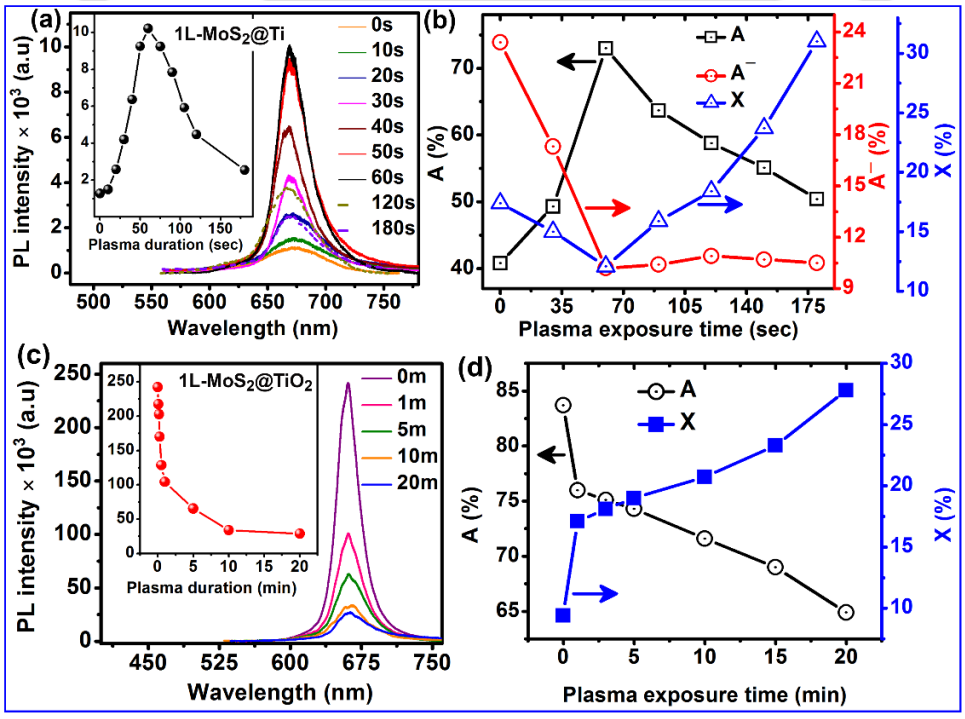

Fig. 7.13. (a) Evolution of the PL spectra of 1L-MoS_2@Ti with oxygen plasma exposure time. Inset shows the change in PL intensity with plasma exposure time. (b) Variation in relative spectral weight percentage of A, A^- and X peaks with the plasma exposure time, estimated from the Gaussian fittings of the respective PL spectrum. (c) Evolution of the PL spectra of 1L-MoS_2@TiO_2 with various oxygen plasma exposure time. Inset shows the change in PL intensity with plasma exposure time. (d) Change in relative spectral weight percentage of A and X with the plasma exposure time, estimated from the Gaussian fittings of the respective PL spectrum.

Fig. 7.13(b) shows the change in the relative percentage of A, A^- and X peaks in 1L-MoS_2@Ti with the plasma exposure time, estimated from the Gaussian fittings of the respective PL spectrum. With the increase of exposure time, contribution of trions in the PL emission decreases sharply, while the contribution of neutral exciton increases systematically and attains the maximum value at 60s, leading to a direct switch from trion to neutral exciton. Additionally, the defect peak (X) contribution in the PL decreases marginally with the plasma exposure time up to 60s and beyond which it increases dramatically. Thus, after 60s of plasma exposure, presence of excess defect trapping states reduces the recombination of neutral excitons, leading to the low overall PL intensity. **Fig. 7.13(c)** shows the comparative PL spectra for 1L-MoS_2@TiO_2, before and after oxygen plasma exposure. The PL intensity decreases drastically with increasing plasma exposure time, as shown in the inset of **Fig. 7.13(c)**. **Fig. 7.13(d)** shows the change in relative percentage of A and X with the plasma exposure time, estimated from the Gaussian fittings of their respective PL spectra. In the HS sample, the contribution of trions in the PL emission is negligible irrespective of the plasma treatment time. With increasing the plasma exposure time, the contribution of neutral exciton in the PL emission decreases, while the defect peak contribution increases monotonically. Thus, it is believed that the plasma treatment creates structural defects and trapping states in the HS, consequently the neutral exciton peak as well as the overall PL emission decreases, clearly showing the deterioration of MoS_2 film.

In order to investigate the influence of oxygen plasma exposure on defects in MoS_2, photocurrent response of 1L-MoS_2@Ti and 1L-MoS_2@TiO_2 heterojunction are recorded before and after 60s plasma exposure with a pulsed optical excitation (λ_{ex} =488 nm) at an applied bias of −5 V, as shown in **Fig. 7.14(a, b)**. In both the cases, the photocurrent is observed to be decreased after the plasma treatment. The decrease in photocurrent is caused by the trapping of the charge carriers by the defects created by the plasma treatment. This further confirms the introduction of oxygenated defects and chemical adsorption of oxygen molecules in MoS_2 lattice in the course of plasma treatment.[28] In case of 1L-MoS_2@Ti, during the oxygen plasma treatment, O_2 /H_2O molecules are adsorbed chemically with Mo at the S-vacancy sites and forms Mo=O bondings, to which electrons can be migrated from MoS_2 side, introducing a p-doping effect in MoS_2, as shown schematically in **Fig. 7.14(c, d)**. Consequently, the trions are eliminated and the neutral exciton emission dominates, resulting to an overall PL enhancement with a blue shift.[29] However, in case of as-synthesized 1L-MoS_2@TiO_2 heterojunction (type-II),

the excess electrons may favorably be migrated from the conduction band of MoS_2 to that of TiO_2, introducing heavy p-doping in the MoS_2, and thus leading to extremely high PL emission, as shown in the schematic of **Fig. 7.14(e)**. As the trion contribution in the as-grown HS is negligibly low, there is very little scope for the conversion of trion to neutral exciton with the plasma exposure. Thus, the oxygen plasma creates only oxygenated defects in the system and degrades the structural quality of the film.[29]

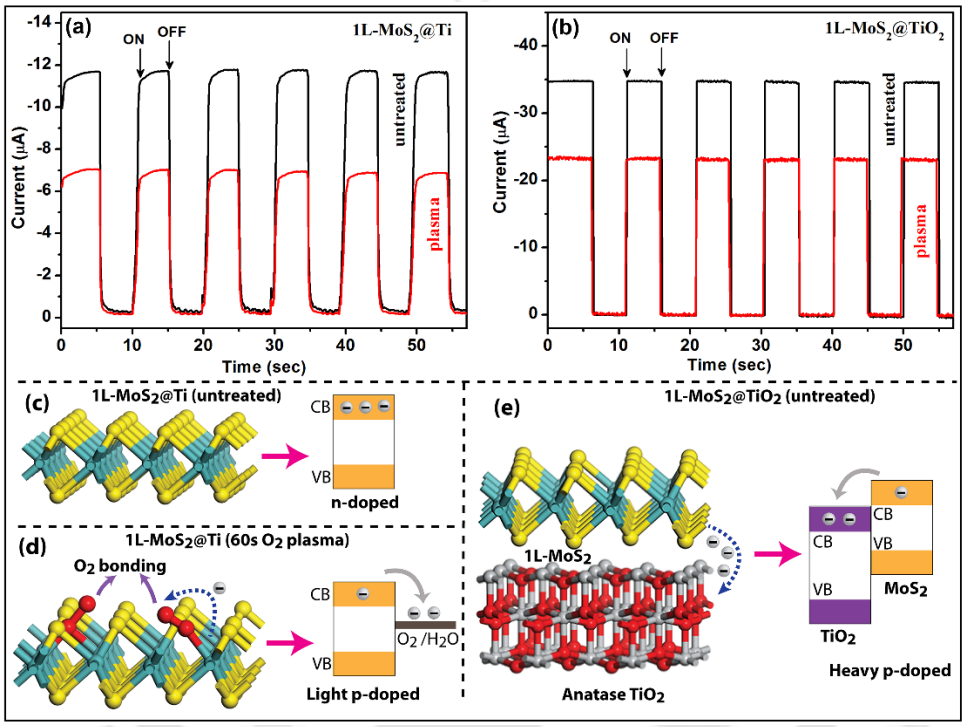

Fig. 7.14. Time dependent photoresponse of (a) 1L-MoS_2@Ti and (b) 1L-MoS_2@TiO_2 heterojunction before and after oxygen plasma treatment (60 sec) under a pulse light with λ_{ex}=488 nm. Schematic representation of electron transfer in (c) as-grown 1L-MoS_2@Ti, (d) 1L-MoS_2@Ti after oxygen plasma treatment for 60s and (e) as-grown 1L-MoS_2@TiO_2.

7.3.5. Performance Study of 1L-MoS_2@TiO_2 Heterojunction Photodetector

In this section, the 1L-MoS_2@TiO_2 heterojunction is utilized to demonstrate it as an efficient photodetector over a wide spectral range. At first, the performance of pristine TiO_2 and 1L-MoS_2@Ti as photodetectors is studied for the comparison. **Fig. 7.15(a)** depicts a schematic representation of the device structure under reverse bias condition. The current-voltage (I–V) characteristics of pristine TiO_2 and as-grown 1L-MoS_2@Ti in the dark and under the photoexcitation at λ_{ex}=370 nm and 570 nm are presented in **Fig. 7.15(b, c)**, respectively. Note that the excitation wavelength is chosen based on the respective absorption peaks. The I-V

characteristics of pristine TiO_2 and 1L-MoS_2@Ti both in dark and light are observed to be nearly symmetric at the negative and positive biases, suggesting the formation of back-to-back Schottky contact. A typical I–V characteristic of 1L-MoS_2@TiO_2 heterojunction is shown in **Fig. 7.15(d)** under the dark and illumination condition (λ_{ex}=570 nm).

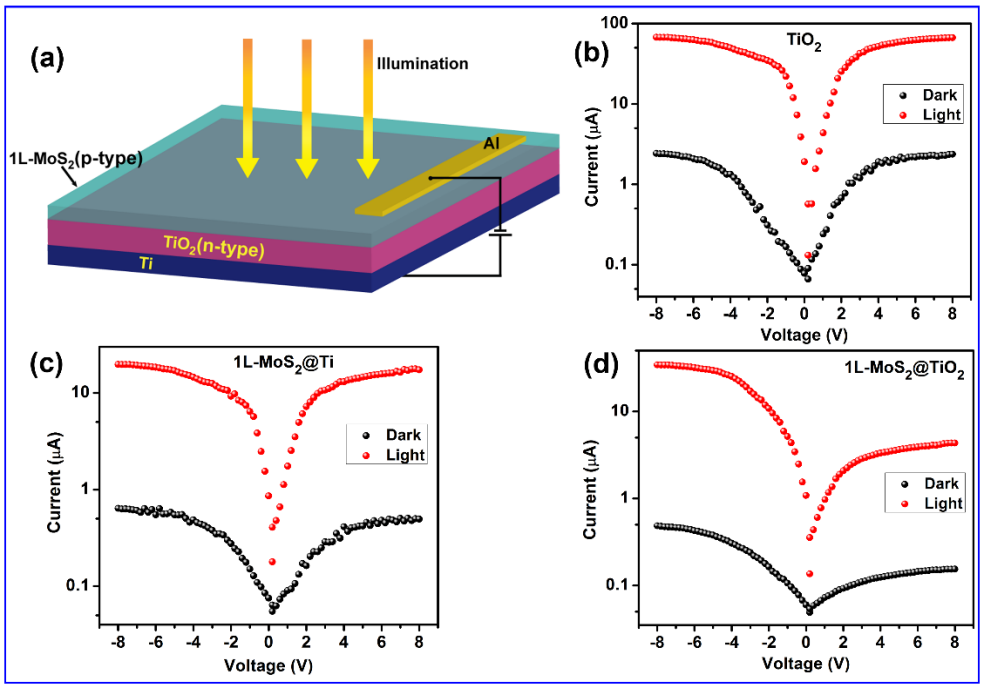

Fig. 7.15. (a) Schematic representation of the photoconductivity measurement on 1L-MoS_2@TiO_2 core-shell heterojunction device under reverse bias. Dark- and photo-current vs. voltage characteristics of (b) as-grown TiO_2 nanostructure (with λ_{ex}=370 nm), (c) 1L-MoS_2@Ti (with λ_{ex}=570 nm) and (d) 1L-MoS_2@TiO_2 p-n heterojunction photodetector (with λ_{ex}=570 nm).

In contrast to the as-grown TiO_2@Ti and 1L-MoS_2@Ti, the high asymmetric nature of the I–V characteristics of 1L-MoS_2@TiO_2 heterojunction clearly indicates the formation of rectifying p-n junction between the p-type MoS_2 and n-type TiO_2 at the interface. Note that the conducting Ti substrate enables to make good Ohmic back contact in the TiO_2 layer. At an applied reverse bias of -5V, the 1L-MoS_2@TiO_2 heterojunction possesses a dark current density of ~440 nA/cm^2, which increases by nearly 80 times to 35 μA/cm^2 upon illumination at 570 nm light. In contrast, 1L-MoS_2@Ti shows about 33 times enhancement under the same condition, while TiO_2 shows ~34 times enhancement under the illumination at 370 nm.

To characterize the performance of the as-fabricated photodetectors, responsivity and detectivity were measured in the spectral range 300-900 nm. Spectral responsivity represents the efficiency of a photodetector for a specific optical signal, which is directly proportional to its

internal gain. Responsivity (R) of a photodetector can be defined as the photocurrent generated in the photodetector per unit power of the light incident on its effective area and can be expressed as follows[30]:

$$R = \frac{I_L - I_D}{PA} \qquad (7.2)$$

Here I_L and I_D are the current under light and dark conditions, respectively, while P is the incident optical power density, and A is the effective illuminated area (0.84 cm^2). **Fig. 7.16(a)** depicts the spectral responsivity of pristine TiO_2, 1L-MoS_2@Ti and 1L-MoS_2@TiO_2 p-n heterojunction device at a bias of -5 V. Pristine TiO_2 exhibits excellent UV photoresponse with a peak responsivity ~25.3 A W^{-1} at 370 nm, while 1L-MoS_2@Ti shows relatively broad spectral response with a peak responsivity ~8.6 A W^{-1} at 570 nm. A prominent peak centered at ~370 nm and a steep fall beyond 400 nm are observed for pristine TiO_2 due to its absorption mainly in the UV region. In contrast, 1L-MoS_2@Ti photodetector shows a broad peak centered at ~570 nm, due to the absorption by the MoS_2 film in the entire visible region, as shown in **Fig. 7.8**. Interestingly, the 1L-MoS_2@TiO_2 heterojunction shows a broad spectral response from UV to near-IR region with two prominent peaks centered at ~370 nm and ~570 nm, attributed to the photo-absorption in TiO_2 core and 1L-MoS_2 shell, respectively. It is noteworthy that the p-n heterojunction shows much higher spectral responsivity (up to 35.9 A W^{-1}) at each wavelength compared to its individual counterparts, due to the formation of high quality interface during the in-situ CVD growth that facilitates efficient charge transfer. Note that the commercial Si photodiode (THORLABS, USA) has a typical peak responsivity of 0.48 A W^{-1} (at 750 nm), which is about 75 times lower than the peak responsivity of the present 1L-MoS_2@TiO_2 photodetector in the similar wavelength range.

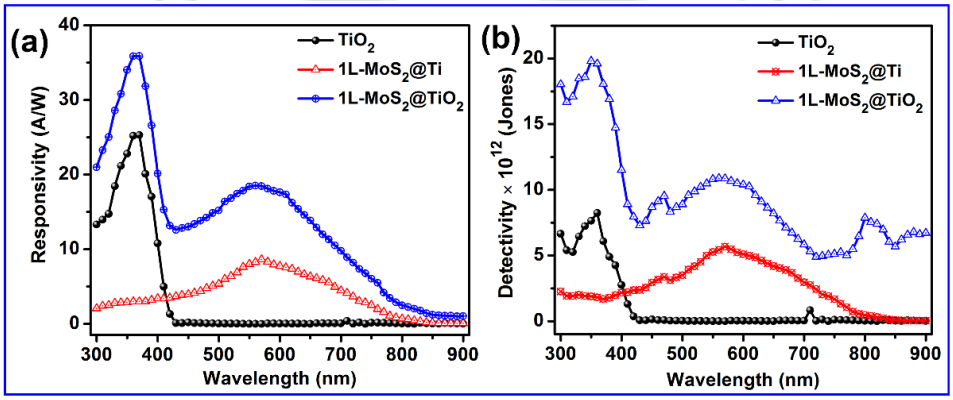

Fig. 7.16. (a, b) A comparison of spectral responsivity and detectivity of TiO_2, 1L-MoS_2@Ti and 1L-MoS_2@TiO_2 heterojunction, recorded at a bias of −5 V.

The figure of merit of a photodetector can be expressed in terms of detectivity (D*), which is related to responsivity (R) as follows[10]:

$$D^* = R \times \left(\frac{A}{2qI_D}\right)^{1/2} \qquad (7.3)$$

where A is the effective area of detector in cm^2, R is the responsivity, I_D is the dark current and q is the electronic charge. The above equation suggests that high responsivity and low dark current are desirable to achieve high detectivity in a photodetector. **Fig. 7.16(b)** depicts the detectivity of pristine TiO_2, 1L-MoS_2@Ti and 1L-MoS_2@TiO_2 p-n heterojunction device at a bias of -5 V. The peak detectivity of pristine TiO_2 and 1L-MoS_2@Ti photodetectors are estimated to be 8.2×10^{12} and 5.7×10^{12} Jones, respectively. The 1L-MoS_2@TiO_2 heterojunction photodetector exhibits broad detectivity in the spectral range of 300-900 nm, with peak values of 19.8×10^{12} and 10.9×10^{12} Jones at 370 nm and 570 nm, respectively, which are ~2 fold higher than its individual counterparts. A comparison of the improved responsivity and detectivity performances of our 1L-MoS_2@TiO_2 heterojunction with other MoS_2 based photodetectors is given in **Table 7.2**.

Table 7.2: *Comparison of the performance of MoS_2 based heterojunction photodetectors reported in the literature and this work.*

Heterojunction photodetector structure	Measurement condition (voltage/ wavelength)	Responsivity (AW^{-1})	Detectivity (Jones)	Ref.
Si/MoS_2 QD p-n	-10 V/ 520 nm	2.80	0.8×10^{12}	[31]
Si/MoS_2 p-n	-3V/ 580 nm	8.75	1.4×10^{12}	[10]
MoS_2/Si n-n	2 V/ 650 nm	11.90	2.1×10^{10}	[32]
a-Si/MoS_2 M-S-M	1 V/ 550 nm	0.21	-	[33]
1L-MoS_2/SiO_2/Si planar	1.5 V/ 514 nm	0.001	-	[34]
MoS_2/pentacene	-15 V/ 655 nm	0.31	1.55×10^{13}	[35]
1L-MoS_2@TiO_2 p-n	-5 V/ 570 nm	18.50	1.09×10^{13}	*This work*
1L-MoS_2@TiO_2 p-n	-5 V/ 370 nm	35.90	1.98×10^{13}	*This work*

Fig. 7.17(a) depicts the time dependent photocurrent responses of 1L-MoS_2@Ti and 1L-MoS_2@TiO_2 p-n heterojunction photodetectors upon the pulsed optical excitation (λ_{ex} =570 nm) at an applied bias of −5 V. For 1L-MoS_2@TiO_2 heterojunction device, the current is observed to be increased sharply and stabilized at a high conductivity state (29.5 μA) upon illumination and quickly switched back to the low conductivity state under dark condition.

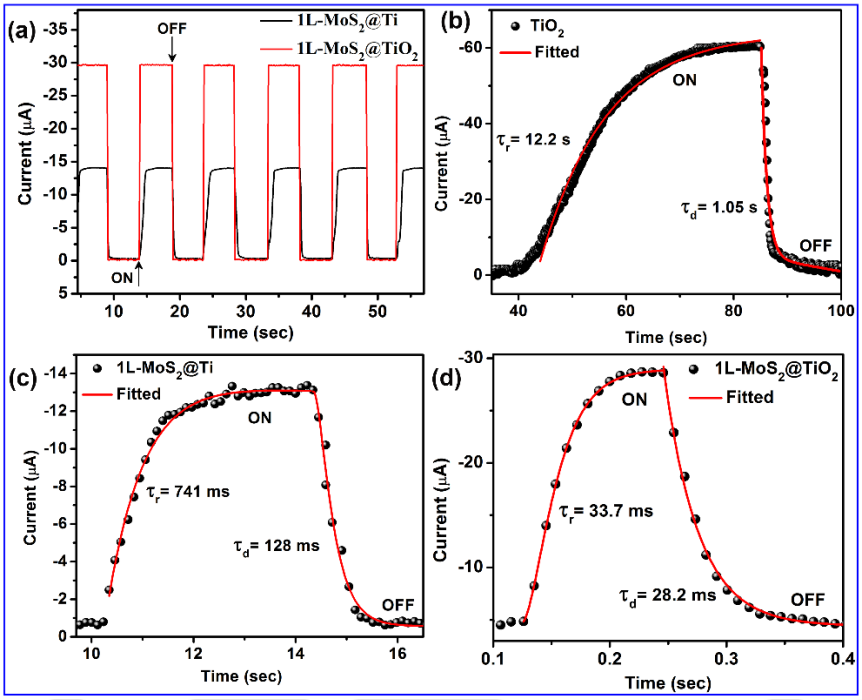

Fig. 7.17. (a) Typical time dependent photoresponses of 1L-MoS_2@Ti and 1L-MoS_2@TiO_2 heterojunction under a pulse light with λ_{ex}=570 nm. Temporal response of the photocurrent for: (b) pristine TiO_2 NFs, (c) 1L-MoS_2@Ti and (d) 1L-MoS_2@TiO_2 heterojunction photodetectors, measured at a reverse bias of 5 V. Solid lines are the fit to their respective experimental data points (black circle).

The steep rise and fall of photocurrent indicate a fast response speed, resulting from the effective generation and separation of electron–hole pairs at the seamless interfaces of 1L-MoS_2@TiO_2 heterojunction. To further investigate the response and recovery times of various photodetectors, photoresponse measurements are performed under pulsed light (λ_{ex} =370 nm for TiO_2, λ_{ex} =570 nm for 1L-MoS_2@Ti and 1L-MoS_2@TiO_2) for a single cycle as shown in **Fig. 7.17(b-d)**, respectively. In order to estimate the characteristic growth and decay time constants, the photoresponse data are fitted with exponential function.[36] The time constants of photocurrent growth/decay for pristine TiO_2 are estimated to be 12.20/1.05 s (see **Fig. 7.17(b)**), while that for 1L-MoS_2@Ti are found to be relatively faster 741/128 ms (see **Fig. 7.17(c)**). In contrast, in the 1L-MoS_2@TiO_2 heterojunction the growth/decay time constants are found to be much faster 33.7/28.2 ms (see **Fig. 7.17(d)**). Note that the measured time constants are limited by the instrument (source-measure unit) response time, which is of the similar order. It is believed that the actual time constants for the heterojunction sample would be much shorter than the measured values. Thus, the 1L-MoS_2@TiO_2 heterojunction possesses very fast photoresponse. Note that the pristine TiO_2 possesses very slow photoresponse due to the

presence of intrinsic oxygen vacancy defects/trap centers, while as-grown 1L-MoS_2@Ti shows comparatively faster photoresponse due to the high in-plane mobility of photogenerated carriers in the MoS_2 layer, facilitating the high speed path for electron transport. In case of heterojunction photodetector, the time constants are extremely small, i.e., extremely fast response due to the strong built-in electric field at the MoS_2 and TiO_2 interface, facilitating the separation and efficient transport of the photogenerated charge carriers.[10] Additionally, due to the lower density of oxygen vacancy defects in TiO_2 and S-vacancy defects in MoS_2, it facilitates much faster response than that of the pristine TiO_2 and 1L-MoS_2@Ti.

7.3.6. Photodetection Mechanism

The proposed mechanism of fast photodetection by 1L-MoS_2@TiO_2 p-n heterojunction can be illustrated better with the energy band diagrams shown in **Fig. 7.18(a-c)**. The conduction and valence band edges TiO_2 (with various defect related trap states) and 1L-MoS_2 are shown in **Fig. 7.18(a)** in proper energy scale, facilitating the band alignment of type-II heterojunction. The band diagram of 1L-MoS_2@TiO_2 heterojunction under the zero bias condition (equilibrium), develops a potential barrier Φ_B at the interface of p-type 1L-MoS_2 and n-type TiO_2 with their Fermi level (E_F) aligned at the same energy value, as shown in **Fig. 7.18(b)**. Thus, at equilibrium upon illumination of 1L-MoS_2@TiO_2 heterojunction with 488 nm laser (in case of PL measurement) mostly MoS_2 is photoexcited.

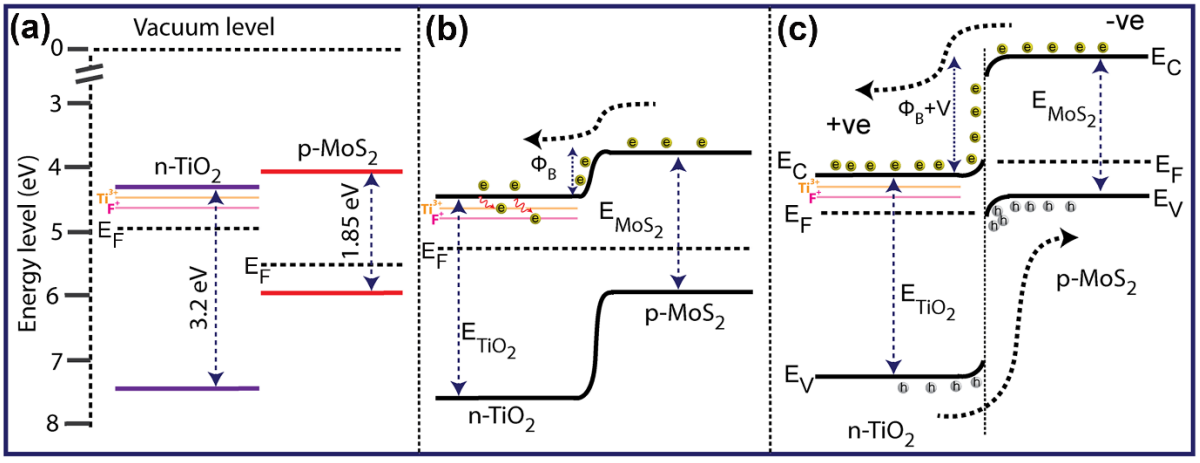

Fig. 7.18. (a) Schematic of the band edge positions of n-type TiO_2 and p-type MoS_2. Energy band diagram of 1L-MoS_2@TiO_2 heterojunction (type-II) under (b) equilibrium (zero bias) and (c) reverse bias condition.

The excess electron in trion is considered to be relatively loosely bound and may be migrated from the conduction band of MoS_2 to that of TiO_2 while the neutral excitons having higher binding energy are not affected by the zero bias potential. Therefore, the p-n heterojunction converts trion into neutral exciton through the interfacial charge transfer resulting into high PL enhancement. Under the reverse bias, the Fermi level (E_F) of p-MoS_2 is lifted to higher values, see **Fig. 7.18(c)**, resulting in the enhanced electric field as well as the expanded barrier potential across the depletion region. Due to the high potential developed at the interface, the photo-excitons are drifted towards the opposite electrodes, resulting in the high photocurrent. Thus, electrons and holes are injected into n-type TiO_2 and p-type MoS_2, respectively having a large number of accessible states and are collected by the electrodes. Additionally, the high carrier mobility in 1L-MoS_2 assists to enhance the fast photoresponse.

7.4. Summary and Conclusions

1. An in-situ CVD growth of MoS_2@TiO_2 core-shell heterojunction is demonstrated with single layer MoS_2 as shell and 3D TiO_2 NF as core.
2. Position dependent Raman analysis confirms the large area single layer growth of MoS_2 over various substrates and the growth mechanism is also revealed.
3. The 1L-MoS_2 shell in the MoS_2@TiO_2 HS exhibits a large enhancement (up to ~83 fold) in PL intensity as compared to the 1L-MoS_2@Ti and 1L-MoS_2@Sapphire, which is explained on the basis of heavy p-doping of the MoS_2 layer, resulting from the migration of excess electrons from 1L-MoS_2 to TiO_2 layer.
4. A controlled oxygen plasma treatment testifies the p-doping effect in MoS_2 layer due to the charge delocalization.
5. The low temperature PL study reveals the absence of nonradiative recombination channels in the HS sample even at the RT, which is responsible for the high PL quantum yield of 1L-MoS_2 shell.
6. The in-situ CVD grown 1L-MoS_2@TiO_2 p-n heterojunction acts as a high performance broadband photodetector. The heterojunction photodetector exhibits record high responsivity and detectivity with peak values of ~35.9 A W^{-1} and 1.98×10^{13} Jones, respectively.

7. The 1L-MoS_2@TiO_2 heterojunction shows fast photoresponse with rise time/fall time of 33.7/28.2 ms, which is 22 fold faster than that of 1L-MoS_2@Ti.
8. The fast and high photoresponse of 1L-MoS_2@TiO_2 photodetector is explained on the basis of fast photogenerated carrier transport at the p-n heterojunction due to the high built-in-potential.

References

1. K. F. Mak, K. He, C. Lee, G. H. Lee, J. Hone, T. F. Heinz and J. Shan, *Nat. Mater*, 2012, **12**, 207.
2. S. Mouri, Y. Miyauchi and K. Matsuda, *Nano Lett.*, 2013, **13**, 5944-5948.
3. H. Nan, Z. Wang, W. Wang, Z. Liang, Y. Lu, Q. Chen, D. He, P. Tan, F. Miao, X. Wang, J. Wang and Z. Ni, *ACS Nano*, 2014, **8**, 5738-5745.
4. D. Prasai, A. R. Klots, A. K. M. Newaz, J. S. Niezgoda, N. J. Orfield, C. A. Escobar, A. Wynn, A. Efimov, G. K. Jennings, S. J. Rosenthal and K. I. Bolotin, *Nano Lett.*, 2015, **15**, 4374-4380.
5. X. Li, J. Zhu and B. Wei, *Chem. Soc. Rev.*, 2016, **45**, 3145-3187.
6. Y. Tang, Y. Zhang, J. Deng, D. Qi, W. R. Leow, J. Wei, S. Yin, Z. Dong, R. Yazami, Z. Chen and X. Chen, *Angew. Chem. Int. Ed. Engl.*, 2014, **53**, 13488-13492.
7. T. Du, N. Wang, H. Chen, H. He, H. Lin and K. Liu, *J. Power Sources*, 2015, **275**, 943-949.
8. M. S. Kim, S. Roy, J. Lee, B. G. Kim, H. Kim, J.-H. Park, S. J. Yun, G. H. Han, J.-Y. Leem and J. Kim, *ACS Appl. Mater. Interfaces*, 2016, **8**, 28809-28815.
9. P. Yusin, P. Woojin, M. Somak, S. D. A. Aravindh, L. Kalaivanan, K. Yogeenth, K. Yonghun, C. Byungjin, J. Gun-Young, H. M. M. and R. I. S., *Small*, 2018, **14**, 1703176.
10. V. Dhyani and S. Das, *Sci. Rep*, 2017, **7**, 44243.
11. P. K. Mohapatra, S. Deb, B. P. Singh, P. Vasa and S. Dhar, *Appl. Phys. Lett.*, 2016, **108**, 042101.
12. M. Liu, L. Piao, W. Lu, S. Ju, L. Zhao, C. Zhou, H. Li and W. Wang, *Nanoscale*, 2010, **2**, 1115-1117.
13. H. Li, Q. Zhang, C. C. R. Yap, B. K. Tay, T. H. T. Edwin, A. Olivier and D. Baillargeat, *Adv. Funct. Mater.*, 2012, **22**, 1385-1390.
14. C. Lee, H. Yan, L. E. Brus, T. F. Heinz, J. Hone and S. Ryu, *ACS Nano*, 2010, **4**, 2695-2700.
15. L. Sun, J. Yan, D. Zhan, L. Liu, H. Hu, H. Li, B. K. Tay, J.-L. Kuo, C.-C. Huang, D. W. Hewak, P. S. Lee and Z. X. Shen, *Phys. Rev. Lett.*, 2013, **111**, 126801.
16. A. Splendiani, L. Sun, Y. Zhang, T. Li, J. Kim, C.-Y. Chim, G. Galli and F. Wang, *Nano Lett.*, 2010, **10**, 1271-1275.
17. D. Dumcenco, D. Ovchinnikov, K. Marinov, P. Lazić, M. Gibertini, N. Marzari, O. L. Sanchez, Y.-C. Kung, D. Krasnozhon, M.-W. Chen, S. Bertolazzi, P. Gillet, A. Fontcuberta i Morral, A. Radenovic and A. Kis, *ACS Nano*, 2015, **9**, 4611-4620.
18. S. Tongay, J. Suh, C. Ataca, W. Fan, A. Luce, J. S. Kang, J. Liu, C. Ko, R. Raghunathanan, J. Zhou, F. Ogletree, J. Li, J. C. Grossman and J. Wu, *Sci. Rep*, 2013, **3**, 2657.
19. H. Zhong, R. Quhe, Y. Wang, Z. Ni, M. Ye, Z. Song, Y. Pan, J. Yang, L. Yang, M. Lei, J. Shi and J. Lu, *Sci Rep.*, 2016, **6**, 21786.
20. W. Zhou, Z. Yin, Y. Du, X. Huang, Z. Zeng, Z. Fan, H. Liu, J. Wang and H. Zhang, *Small*, 2013, **9**, 140-147.
21. M. S. Kim, C. Seo, H. Kim, J. Lee, D. H. Luong, J.-H. Park, G. H. Han and J. Kim, *ACS Nano*, 2016, **10**, 6211-6219.
22. L. P. L. Mawlong, K. K. Paul and P. K. Giri, *J. Phys. Chem. C*, 2018, **122**, 15017-15025.

23. H.-P. Komsa, J. Kotakoski, S. Kurasch, O. Lehtinen, U. Kaiser and A. V. Krasheninnikov, *Phys. Rev. Lett.*, 2012, **109**, 035503.
24. K. K. Ghuman, S. Yadav and C. V. Singh, *J. Phys. Chem. C*, 2015, **119**, 6518-6529.
25. X. Wei, Z. Yu, F. Hu, Y. Cheng, L. Yu, X. Wang, M. Xiao, J. Wang, X. Wang and Y. Shi, *AIP Adv.*, 2014, **4**, 123004.
26. Q. Pang, Y. Zhao, X. Bian, Y. Ju, X. Wang, Y. Wei, B. Liu, F. Du, C. Wang and G. Chen, *J. Mater. Chem. A*, 2017, **5**, 3667-3674.
27. X. Yang, W. Fu, W. Liu, J. Hong, Y. Cai, C. Jin, M. Xu, H. Wang, D. Yang and H. Chen, *J. Mater. Chem. A*, 2014, **2**, 7727-7733.
28. S. Dhara and P. K. Giri, *J. Appl. Phys.*, 2011, **110**, 124317.
29. L. P. L. Mawlong, K. K. Paul and P. K. Giri, *J. Phys. Chem. C*, 2018, DOI: 10.1021/acs.jpcc.8b03957.
30. J. Li, S. Yuan, G. Tang, G. Li, D. Liu, J. Li, X. Hu, Y. Liu, J. Li, Z. Yang, S. F. Liu, Z. Liu, F. Gao and F. Yan, *ACS Appl. Mater. Interfaces*, 2017, **9**, 42779-42787.
31. S. Mukherjee, R. Maiti, A. K. Katiyar, S. Das and S. K. Ray, *Sci. Rep.*, 2016, **6**, 29016.
32. Y. Zhang, Y. Yu, L. Mi, H. Wang, Z. Zhu, Q. Wu, Y. Zhang and Y. Jiang, *Small*, 2016, **12**, 1062-1071.
33. M. R. Esmaeili-Rad and S. Salahuddin, *Sci. Rep.*, 2013, **3**, 2345.
34. P.-L. Néstor, L. Zhong, R. P. Nihar, I.-R. Agustín, E. Ana Laura, M. Amber, L. Jun, M. A. Pulickel, T. Humberto, B. Luis and T. Mauricio, *2D Materials*, 2014, **1**, 011004.
35. Y. Peng, R. Ding, Q. Ren, S. Xu, L. Sun, Y. Wang and F. Lu, *Appl. Surf. Sci.*, 2018, **459**, 179-184.
36. S. Dhara and P. Giri, *Nanoscale Res. Lett.*, 2011, **6**, 504.

Chapter 8

Summary and Outlooks

This chapter presents a summary of the significant contributions of the thesis and highlight the new findings on the fabrication of shape tailored TiO_2 nanostructures and TiO_2 based hierarchical heterostructures with plasmonic nanoparticles (NPs), two dimensional (2D) g-C_3N_4 and MoS_2 nanosheets, and their applications in visible light photocatalysis, photoelectrocatalysis, light emission and broadband photodetection. Open questions and the scope for the future works are discussed at the end.

8.1. Summary and Highlights of the Thesis Contribution

In this dissertation, we have presented the fabrication of mesoporous TiO_2(B) nanorods (NRs) by a hydrothermal method and controlled growth of Ag_2O NPs on the TiO_2(B) NRs in order to elucidate the ultrahigh visible light photodegradation of organic dye on the basis of ionic interactions (Chapter 2). Next, we have considered anatase TiO_2 NRs decorated with plasmonic Ag NPs and investigated the origin of the multi-step sequential degradation kinetics of an organic dye, Rhodamine-B (RhB), under the visible light illumination, for the first time (Chapter 3). Further, we have synthesized plasmonic ternary hybrids Ag-TiO_2(B), and Au-TiO_2(B) nanostructures decorated on g-C_3N_4 nanosheets and demonstrated its superior visible light driven photocatalysis. We have studied the temporal photoresponse systematically with monochromatic photoexcitation near the plasmonic absorption peaks to explain the enhanced photocatalysis (Chapter 4). Next, we have fabricated a unique ternary composite, Pt@MoS_2/TiO_2(B) with edge-site exposed few-layer MoS_2 nanoflowers (NFs) grown on porous TiO_2(B) NBs, followed by the Pt NPs selectively decorated on the edge-sites/defect-sites. We have demonstrated its outperformance in visible light photoelectrocatalytic hydrogen evolution reaction (HER) over the commercial Pt/C electrode and investigated its mechanism systematically (Chapter 5). Next, we have fabricated F-doped arbitrary shaped self-grown TiO_2 NCs decorated mesoporous 3D TiO_2 NFs by a single step hydrothermal method, for the first time. We have observed a shape evolution of arbitrary shaped F-TiO_2 NCs into spherical QDs by a controlled vacuum RTA treatment and demonstrated a record high photoluminescence quantum yield (PL QY) of ~5.76%

from the indirect bandgap TiO_2 QDs (Chapter 6). Finally, we have demonstrated an in-situ chemical vapour deposition (CVD) growth of single-layer MoS_2 (1L-MoS_2) shell wrapped over the 3D TiO_2 NF core, for the first time and elucidated the formation mechanism of seamless 1L-MoS_2 shell. 1L-MoS_2@TiO_2 p-n heterojunction acts as an efficient light emitter (photoluminescence) as well as a high-performance broadband photodetector (at a reverse bias), reported for the first time (Chapter 7).

The major contributions of the present thesis work are summarized below.

A. Elucidating the Mechanism of Strong Visible-Light Photocatalysis by TiO_2(B)/Ag_2O HSs

We have developed pure monoclinic B-phase TiO_2 (TiO_2(B)) NRs mesoporous in nature by a simple, cost-effective and versatile hydrothermal process. We have controlled the growth of Ag_2O NPs on the porous sites of TiO_2(B) NRs in order to get a uniform surface decoration of Ag_2O NPs with optimized size and number density. We have systematically characterized the as-grown catalysts to maximize the absorption in the entire solar spectrum and easy interfacial charge separation of the photoexcited carriers with prolonged lifetime. Using TiO_2(B)/Ag_2O HSs as the catalyst, we have observed highly stable visible light driven photodegradation of aqueous methyl orange (MO) (anionic) and methylene blue (MB) (cationic) as the reference dyes with one order enhanced efficiency than pristine components. We have achieved >94% photodegradation for both the dyes with high degradation rate constant in MO. The above results are explained on the basis of the formation of a type-II junction between the Ag_2O and TiO_2, strong coupling, band bending, easy interfacial charge transfer and the Coulombic interaction between the dye molecules and catalyst surface. *This work has been published in "Nanotechnology, 27, 315703 (2016)".*

B. On the Origin of Multi-Step Photocatalytic Decay by Defect Enriched Ag@TiO_2 NRs

We have developed pure anatase phase TiO_2 NRs using different growth parameters and decorated it with plasmonic Ag NPs by a simple in-situ photoreduction method. Raman and XPS studies provide a direct evidence of defect enrichment in the HS sample. Intrinsic surface defects and localized surface plasmon resonance (LSPR) in the optimized Ag@TiO_2 HS facilitate strong optical absorption in the entire visible region. We have observed that the photodegradation kinetics of the dye in presence of the HSs follows a sequential degradation process with two

distinct exponential decay functions/rate constants, for the first time. We have achieved ultrafast degradation rate constants up to 0.083 min^{-1} and 0.033 min^{-1} in the 2^{nd} and 1^{st} stage of degradation, respectively, which are way beyond that of the commercial P25 photocatalyst. The generation of hot electrons and their fast migration away from the interface facilitate the enhanced visible light photocatalysis, discussed in the light of the steady-state and time-resolved PL and photoconductivity studies. For the first time, we have proposed a multi-step sequential decay model which exactly fits the experimental data, simulated by Mathematica. The mechanism of the multi-step sequential degradation rate kinetics of RhB under visible light illumination was revealed by quantitative investigation of the following factors: (a) simultaneous photoreduction induced enhanced plasmonic effect of Ag NPs during photocatalysis and (b) fast N-de-ethylation of RhB. Ag@TiO_2 HS demonstrates long-term stability and superior performance over the bare TiO_2 NRs and other TiO_2 based photocatalysts for the solar light-driven detoxification of water. *This work has been published in "J. Phys. Chem. C., 121, 20016 (2017)".*

C. Trap State Mediated Plasmonic Hot Electron Injection and Efficient Charge Separation in Ag-TiO_2(B)-CN and Au-TiO_2(B)-CN with Superior Photocatalytic Performance

We have developed ternary plasmonic photocatalysts of Ag-TiO_2(B)-g-C_3N_4 and Au-TiO_2(B)-g-C_3N_4 by an in-situ chemical route and systematically investigated its superior photocatalytic performance in the degradation of RhB and phenol under the illumination of visible light. We have considered mesoporous monoclinic TiO_2(B) NRs with lower packing density and open channels as the platform to decorate the plasmonic metal NPs (Au and Ag). We have observed visible light photodegradation of RhB and phenol up to ~99% with first-order rate constants 1.3×10^{-3} and 1.5×10^{-3} min^{-1}, respectively, which is shown to be due to optimum charge transfer time and low charge transfer resistance. The scavenging test clearly reveals the major role of superoxide radicals (O^{2-}) in driving the enhanced photodegradation. We speculate that two synergetic plasmonic effects might regulate the enhanced photocatalytic activity in the ternary HSs: (a) localized electromagnetic field enhancement in the vicinity of the metal-semiconductor interface due to the presence of numerous plasmonic hotspots. (ii) Trap state mediated direct hot electron injection either through quantum tunnelling of low energy hot electrons through the interfacial barrier or via the coupling of the hot electrons with the interfacial defect states,

assisted by the narrow depletion layer width at higher cationic dopants, Ti^{3+}. The highly enhanced photocurrent due to the monochromatic photoexcitation near the plasmonic absorption peaks confirms the hot electron injection from plasmonic NPs and efficient interfacial separation via nitrogenated defects in 2D CN network.

D. Strong Photoelectrocatalytic Hydrogen Evolution Reaction in MoS_2/TiO_2(B) by Selective Decoration of Pt NPs at the MoS_2 Edge Sites

We have carried out a controlled growth of discrete few-layer MoS_2 nanoflowers (NFs) on the porous TiO_2(B) nanobelts (NBs) by a second stage hydrothermal treatment, following the selective decoration of platinum (Pt) NPs on the edge/defect sites of the MoS_2 layer and porous sites of TiO_2(B) NBs. The maximally edge-exposed MoS_2 NFs grown on and supported by the porous TiO_2 platform exhibits overall reduced layer numbers compared to the pristine MoS_2 layers and the MoS_2 NFs likely to be n-type doped, as revealed from the Raman analysis. Raman studies in conjunction with PL and XPS analyses provide a direct evidence of S-doping at the O-site in the TiO_2 lattice, which in turn enhances the absorption capability in the visible region. Quantitative XPS analysis reveals that the catalytically active bridging S_2^{2-}/apical S^{2-} increases up to ~72% after the formation of the ternary system (Pt@MoS_2/TiO_2(B). This ternary catalyst outperforms the commercial Pt/C electrode for the visible light driven photoelectrocatalytic hydrogen evolution reaction (HER), following the Volmer-Tafel mechanism. The marginal Pt loaded ternary system exhibits an extremely low charge transfer resistance, low overpotential as well as the Tafel slope with extremely high exchange current density, boosting the overall HER performance under the visible light. Chronopotentiometric measurements reveal the high stability of binary and ternary catalysts to sustain a 10 mA/cm^2 cathodic current up to 12 hours as well as 10,000 cycles. We have proposed a mechanism where the marginally-loaded Pt NPs activate the inert basal plane, edge sites of MoS_2 and porous sites of TiO_2, making an integrated network, facilitating an easy injection of the photogenerated electrons from the TiO_2 to MoS_2 and then to Pt NPs, realizing the superior HER activity under visible light. *This work has been published in "J. Mater. Chem. A, 6, 22681 (2018)" & "Sol. Energy Mater Sol. Cells., 185, 364 (2018)".*

E. High Photoluminescence Quantum Yield from Self-Grown TiO_2 QDs on F-Doped TiO_2 Nanoflowers

We have fabricated fluorine doped mesoporous 3D TiO_2 NFs uniformly decorated with arbitrary shaped self-grown TiO_2 NCs by a single step hydrothermal method, for the first time. We have performed systematic experiments to tune the size of the NCs simply by varying the reaction duration and HF concentration. We have observed a shape evolution of arbitrary shaped TiO_2 NCs into spherical NPs by a controlled RTA technique, and the growth mechanism is elucidated. For the first time, we have demonstrated a record high PL QY up to ~5.76% from the TiO_2 QDs/F-TiO_2 NFs thin film, despite its indirect bandgap. The strong PL emission from F-TiO_2 QDs (~163 times that of as-grown F-TiO_2 NCs) is associated with the shallow and deep trap states (Ti^{3+} and F^+ centers), confirmed by ESR and XPS studies. The as-grown sample contains a contribution of brookite phase, which increases linearly with the reaction duration and HF concentration but disappears after the post-growth annealing. We have further confirmed the fluorescence property of the F-TiO_2 QDs by confocal fluorescence microscopy imaging. The mechanism of high PL emission is elucidated from the low-temperature PL as well as the time-resolved PL analyses. It was proposed that the PL enhancement is partly due to the straddling type (type-I) band arrangement at the interface of NF and QD. Thus, a highly stable, biologically inert and highly fluorescent TiO_2 QDs/NFs thin film demonstrated for the first time is significant for emerging applications in optoelectronics and bioimaging. *This work has been published in "Part. Part. Syst. Charact., 35, 1800198 (2018)".*

F. Trion Inhibited Strong Excitonic Emission and Broadband High Photoresponsivity from 1L-MoS_2@TiO_2 Heterojunction

We have adopted a versatile physical route to grow 1L-MoS_2 shell wrapped over a hydrothermally prepared 3D TiO_2 NF core by an in-situ CVD technique. We have systematically investigated the large area single layer growth of MoS_2 on various substrates including sapphire, Ti and TiO_2 NFs by position dependent Raman analysis and high-resolution TEM imaging. The growth mechanism of 1L-MoS_2 over a large area has been elucidated. We have demonstrated a high PL enhancement (up to ~83 fold) from the 1L-MoS_2 shell in MoS_2@TiO_2 HS as compared to the 1L-MoS_2 grown on Ti and sapphire substrates. A detailed investigation reveals the heavy p-doping effect in the MoS_2 lattice, resulting from the migration of excess electrons from 1L-

MoS_2 to TiO_2, which may be responsible for the high PL yield, further supported by the low-temperature PL studies. We have verified the charge delocalization induced p-doping in MoS_2 and the PL enhancement by the controlled oxygen plasma exposure to the samples.

Further, we have demonstrated the 1L-MoS_2@TiO_2 p-n heterojunction as a high-performance broadband photodetector in the spectral range 300-900 nm. The I–V characteristics of 1L-MoS_2@TiO_2 heterojunction confirms the formation of rectifying p-n junction between the p-type MoS_2 and n-type TiO_2 at their interface. The heterojunction photodetector exhibits record high responsivity and detectivity with two prominent peaks in the UV (~370 nm) and the visible (~570 nm) region. The heterojunction photodetector displays a fast photoresponse due to the fast transport of photogenerated carriers driven by the high built-in-potential at the heterojunction. *This work has been published in "ACS Appl. Mater. Interfaces, 10, 42812 (2018)".*

8.2. Scope of Future Work

The present thesis is focused on the growth of various shape tailored mesoporous TiO_2 nanostructures followed by the fabrication of TiO_2 based heterostructures with metal and metal-oxide NPs, 2D C_3N_4 and few-layer MoS_2 nanosheets for the visible light photocatalysis, photoelectrocatalysis, light emission and broadband photodetection applications. The present work can be extended in several ways, as described below.

1. The present work has demonstrated enhanced visible light driven photocatalysis and photoelectrocatalysis for energy and environmental application using high-cost noble metal nanoparticles. However, finding a proper cost-effective alternative to the noble metal for the real-life application is an open challenge.

2. Considering the multi-step sequential decay model, the next-generation photocatalysts can be designed to explore its application.

3. MoS_2/TiO_2(B) composite with 1.4 wt% Pt NPs has outperformed commercial Pt/C electrode (20 wt% Pt) for the visible light photoelectrocatalytic hydrogen evolution with excellent stability. Thus, further optimization of the system with even lower Pt concentration can be explored as a next-generation photoelectrocatalytic device at the industrial scale.

4. Recently various 2D transition metal dichalcogenide (TMDC) nanosheets are receiving a considerable attention for the high adsorption of pollutants. The mesoporous TiO_2(B) NBs integrated with few-layer MoS_2/WS_2 nanosheets can be promising candidates for the high adsorption study, and the modelling of their kinetics may be investigated.

5. Tunable and highly fluorescent TiO_2 QDs as well as 1L-MoS_2@TiO_2 HSs can be studied further for bioimaging applications due to its nontoxicity and biocompatibility.

6. 1L-MoS_2@TiO_2(B) heterojunction exhibited extremely high absorption in the entire visible region and good photodetection behavior. This system can be an excellent choice for the visible light photoelectrocatalytic hydrogen generation. Further optimization of multijunction and number of TMDC layers on TiO_2 nanostructures may be investigated.

7. Fabrication and optimization of other TMDCs ($MoSe_2$, WS_2, WSe_2, etc.) layers on TiO_2 nanostructure can be explored to further broaden its application potential in light emission, photodetection, hydrogen generation etc.